

# UC Riverside

## UC Riverside Electronic Theses and Dissertations

### Title

Optical Spectroscopy of Excitonic States and Interlayer Phonons in Atomically Thin Transition Metal Dichalcogenides

### Permalink

<https://escholarship.org/uc/item/77j5c9zq>

### Author

van Baren, Jeremiah

### Publication Date

2020

Peer reviewed|Thesis/dissertation

UNIVERSITY OF CALIFORNIA  
RIVERSIDE

Optical Spectroscopy of Excitonic States and Interlayer Phonons  
in Atomically Thin Transition Metal Dichalcogenides

A Dissertation submitted in partial satisfaction  
of the requirements for the degree of

Doctor of Philosophy

in

Physics

by

Jeremiah van Baren

December 2020

Dissertation Committee:

Dr. Chun Hung Lui, Chairperson  
Dr. Yongtao Cui  
Dr. Vivek Aji

Copyright by  
Jeremiah van Baren  
2020

The Dissertation of Jeremiah van Baren is approved:

---

---

---

Committee Chairperson

University of California, Riverside

## Acknowledgments

Each path to completing a PhD is distinct, and mine has been no exception. Throughout, I have had the privilege of meeting, working with, and befriending a number of remarkable people and scientists. Although this process has been significantly different than any expectation, it has been the experience of a lifetime to work alongside so many talented and hard-working people. You have all taught me a good deal about being better scientist and a better person, and for that I cannot thank you enough.

I would like to thank a number of people, starting with those who supported this work:

Prof. Joshua Lui, who has been my doctoral advisor for the last five years. It has been a different experience than either of us expected. Building a research lab together was a humbling and life-changing experience. You have always been patient and supportive and for that I am tremendously grateful.

Erfu Liu, without whom much of this work would not exist. You have made an outstanding contributions to lab and it has been an enormous pleasure to work with you, particularly during our numerous visits to Tallahassee. We worked closely to improve the lab and to conduct the experiments in Chapters 3 and 4. The 2D heterostructure devices used in those chapters were fabricated by Erfu, to whom I provided some assistance.

Prof. Yia-Chung Chang, who provided critical theory support, modeling, and discussion for the exciton-related research in Chapters 3 and 4. Your input and conversation were crucial to the success of our research efforts and our understanding of excitonic states in 2D materials. Thank you to Ching-Tarng Liang for the model calculations in Chapter 4.3.

The current and former members of the Lui lab: Mashaël Altaïary, Matthew Wilson, Mohammed Alghamdi, Xian Wang, Ao Shi, Jeremy Valdecanas, Liang Xu, Benjamin Leong, Aaron Magpayo, and Donovan Dikitanan. Thank you all for your support, patience, and hard work. I owe you each a debt of gratitude in making this lab function.

Prof. Nathan Gabor, Prof. Yongtao Cui, Trevor Arp, Jacky Wan, Fatemeh Barati, Mina Rashetnia, and the other members of the QMO Lab and Cui Group who provided feedback, support, and compelling conversation throughout this research.

Prof. Rui He, Gaihua Ye, Zhipeng Ye, and Pouyan Rezaie, who conducted the low-frequency Raman experiments in Chapter 5, Prof. Jia-An Yan who provided the Raman calculations in Chapter 5. Prof. Xiaoxang Xi who fabricated the NbSe<sub>2</sub> samples in Chapter 5.2, and Prof. Zheng Liu and Prof. Peng Yu who grew the 3R-MoS<sub>2</sub> crystals used in Chapter 5.1.

Dmitry Smirnov, Zhengguang Lu, and Stephen McGill, who supported our experimental measurements at the National High Magnetic Field Laboratory, and the National Science Foundation and the State of Florida which support the user program.

Prof. Harry W.K. Tom, who provided advice during a difficult time, and was generous in providing experimental equipment which enabled much of this work.

Prof. Qiong Ma and the Jarillo-Herrero group for the opportunity to learn a great deal about 2D heterostructure fabrication which informed and inspired our efforts in Riverside.

Sonia Godinez, Jazmin Chavez, and the other departmental staff, as well as Mike Fournier and the CNAS Machine Shop staff who supported our lab development efforts.

Before joining the Lui laboratory, I was a member of two other research groups whose members I owe significant gratitude:

Prof. Roland Kawakami, Beth McCormick, Walid Amamou, Dante O'Hara, Kelly Luo, Sara Mueller, and the rest of the Kawakami group, who first introduced me to optics and 2D materials. You were fantastic colleagues throughout the ups and downs, and my time in Columbus is something I will never forget.

Prof. Karsten Pohl, Amanda Larson, Jun Wang, and the rest of the Pohl Lab, who first introduced me to experimental physics. Without this experience as an undergraduate, my life today would be very different. You exposed me to a career option and world which I barely knew existed, and almost certainly would not have pursued. Thank you for always treating me with respect and providing so much encouragement to follow this path.

I would also like to acknowledge those other friends in Ohio and California who have been so supportive, inspiring, and kept me sane, especially Carola, Christina, and Trevor.

Finally, I would like to express my utmost gratitude to my parents, Kate and Herb, my sister, Caroline, and long-time friends Benjamin, Ben, Bodhi, Kevin, and Mallika. You have all been an unwavering source of support, encouragement, and reality outside of academia. In all of the ups and downs of the last few years, you have been a constant and for that I cannot be more thankful.

Acknowledgement of Previously Published Material:

Chapter 3 is, in part, reproduced from two publications:

E. Liu, J. van Baren, T. Taniguchi, K. Watanabe, Y. C. Chang, and C. H. Lui.

*Physical Review Letters* 99, 205420 (2019).

E. Liu\*, J. van Baren\*, T. Taniguchi, K. Watanabe, Y. C. Chang, and C. H. Lui.

*Physical Review Letters* 124, 097401 (2020).

Chapter 4 is, in part, reproduced from three publications:

E. Liu, J. van Baren, Z. Lu, M. M. Altairy, T. Taniguchi, K. Watanabe, D. Smirnov, and

C. H. Lui. *Physical Review Letters* 123, 027401 (2019)

E. Liu, J. van Baren, T. Taniguchi, K. Watanabe, Y. C. Chang, and C. H. Lui.

*Physical Review Research* 1, 032007(R) (2019)

E. Liu\*, J. van Baren\*, C. T. Liang, T. Taniguchi, K. Watanabe, N. M. Gabor, Y. C.

Chang, and C. H. Lui. *Physical Review Letters* 124, 196802 (2020)

Chapter 5 is, in part, reproduced from two publications:

R. He, J. van Baren, J.-A. Yan, X. Xi, Z. Yi, G. Ye, I-H. Lu, S. M. Leong, and C. H. Lui.

*2D Materials* 3, 031008 (2016)

J. van Baren, G. Ye, J. A. Yan, Z. Ye, P. Rezaie, P. Yu, L. Zheng, R. He, and C. H. Lui.

*2D Materials* 6, 025022 (2019)

To my family and friends - for your continued support and patience.

## ABSTRACT OF THE DISSERTATION

Optical Spectroscopy of Excitonic States and Interlayer Phonons  
in Atomically Thin Transition Metal Dichalcogenides

by

Jeremiah van Baren

Doctor of Philosophy, Graduate Program in Physics  
University of California, Riverside, December 2020  
Dr. Chun Hung Lui, Chairperson

Atomically thin transition metal dichalcogenides (TMDs, e.g. MoS<sub>2</sub>, MoSe<sub>2</sub>, WSe<sub>2</sub>, and NbSe<sub>2</sub>) exhibit remarkable properties which are relevant for science and novel applications, such as robust excitonic effects and well-defined valley degree of freedom. These electronic and vibrational properties are highly dependent on the layer number, stacking configuration, and charge density in the sample system and may be probed and manipulated through applied electromagnetic fields. As the quality and complexity of TMD-based devices has improved, so too has our ability explore the novel physics of these systems. In this dissertation, we probe exceptionally high-quality TMD devices to explore the detailed excitonic physics in monolayer WSe<sub>2</sub> and the interlayer phonons in MoS<sub>2</sub> and NbSe<sub>2</sub>.

First, we study monolayer WSe<sub>2</sub> devices encapsulated in boron nitride. The WSe<sub>2</sub> optical spectra exhibit diverse excitonic features, including the bright states, both the intra- and inter-valley dark states, and a collection of phonon replicas. We systematically study these spectral features and identify novel excitonic physics. For the bright states, we observe the 1s – 4s Rydberg excitons and measure their binding energy and exciton radii.

When subject to high magnetic field, the bright trions (or exciton polarons) further exhibit pronounced charge-density-dependent oscillations due to Landau quantization. For the dark states, we identify the dark trions and demonstrate their distinct valley Zeeman effect and enhanced lifetime compared to bright trions. We further observe the intervalley exciton and characterize the intra- and inter-valley relaxation pathways available to the dark states. Finally, we investigate the exciton-phonon interactions and observe a collection of phonon-mediated relaxation processes. We demonstrate that these phonon replicas enable valley-selective optical detection of the dark excitons (trions).

Beyond the monolayer, we study the interlayer shear and breathing mode phonons in multilayer MoS<sub>2</sub> and NbSe<sub>2</sub>. We compare the phonon spectra of 2H- and 3R-stacked MoS<sub>2</sub> crystals and observe strong dependence of the shear modes on the layer stacking order. We further simulate the Raman spectra with a concise analytical model that considers the layer-by-layer structure of 2D crystals. Our Raman results provide an effective method to characterize the layer number and stacking order in 2D materials.

# Contents

|  |             |
|--|-------------|
| <b>List of Figures</b>   | <b>xiv</b>  |
| <b>List of Tables</b>  | <b>xvii</b> |
| <b>1 Introduction</b>  | <b>1</b>    |
| 1.1 Transition Metal Dichalcogenides (TMDs)                                  | 6           |
| 1.1.1 Optical Excitation of Monolayer WSe <sub>2</sub>                       | 9           |
| 1.1.2 Bright Excitons  | 13          |
| 1.1.3 Bright Trions  | 15          |
| 1.1.4 Exciton Energy with Finite Charge Density                              | 17          |
| 1.1.5 Monolayer WSe <sub>2</sub> under Out-of-Plane Magnetic Field           | 20          |
| <b>2 Sample Fabrication and Experimental Methods</b>                         | <b>24</b>   |
| 2.1 van der Waals Heterostructure Device Fabrication                         | 24          |
| 2.1.1 Transfer Microscope Design   | 26          |
| 2.1.2 2D Material Fabrication Process  | 28          |
| 2.2 Optical Microscope System  | 34          |
| 2.2.1 Light Sources  | 34          |
| 2.2.2 Beam Pathway, Optics   | 38          |
| 2.2.3 Sample Stage, Electrical Interface                                     | 41          |
| 2.2.4 Measurement Automation   | 41          |
| 2.3 Magneto-Optical Experiment   | 42          |
| 2.3.1 31-T Resistive Magnet  | 42          |
| 2.3.2 17.5-T Superconducting Magnet  | 44          |
| 2.4 Reflection-Contrast Spectroscopy   | 47          |
| 2.5 Quantitative Analysis of Reflection-Contrast Spectra                     | 50          |
| 2.5.1 Transfer-Matrix Formalism for Thin-Film Interference                   | 51          |
| 2.5.2 Parameterization of Unknown Layer Dielectric Function                  | 53          |
| 2.5.3 Optimization of Dielectric Function <i>via</i> Nonlinear Least-squares | 58          |
| 2.6 Photoluminescence Spectroscopy   | 61          |
| 2.6.1 Time-Resolved Photoluminescence Spectroscopy                           | 63          |

|          |   |            |
|----------|---|------------|
| <b>3</b> | <b>Bright Excitons and Trions in Monolayer WSe<sub>2</sub> under High Magnetic Field</b>              | <b>67</b>  |
| 3.1      | Magnetophotoluminescence of Exciton Rydberg States in Monolayer WSe <sub>2</sub>                      | 68         |
| 3.1.1    | Methodology . . . . .   | 69         |
| 3.1.2    | Experimental Results . . . . .  | 69         |
| 3.1.3    | Analysis of Exciton Zeeman and Diamagnetic Shifts . . . . .   | 74         |
| 3.1.4    | Quantitative Model Calculations . . . . .   | 78         |
| 3.1.5    | Conclusion . . . . .  | 80         |
| 3.2      | Landau-Quantized Photoluminescence and Absorption in Monolayer WSe <sub>2</sub>                       | 80         |
| 3.2.1    | Methodology . . . . .   | 83         |
| 3.2.2    | Gate-Dependent Reflectance Contrast . . . . .   | 83         |
| 3.2.3    | Electronic Quantization Observed <i>via</i> Optical Conductivity . . . . .                            | 89         |
| 3.2.4    | Landau-Fan-Type Analysis of Optical Conductance Oscillation . . . . .                                 | 93         |
| 3.2.5    | Landau-Quantization Observed <i>via</i> Photoluminescence . . . . .                                   | 97         |
| 3.2.6    | Divergence from the Single-particle Model . . . . .   | 103        |
| 3.2.7    | Conclusion . . . . .  | 105        |
| <b>4</b> | <b>Dark Excitonic States and Phonon Replicas in Monolayer WSe<sub>2</sub></b>                         | <b>106</b> |
| 4.1      | Optical Selection Rules for the Dark Trion in Monolayer WSe <sub>2</sub>                              | 108        |
| 4.1.1    | Optical Detection of In-Plane-Emission Photoluminescence . . . . .                                    | 109        |
| 4.2      | Gate-Tunable Dark Trions in Monolayer WSe <sub>2</sub>  | 110        |
| 4.2.1    | Methodology . . . . .   | 110        |
| 4.2.2    | Gate-Dependent Photoluminescence at Zero-Field . . . . .  | 111        |
| 4.2.3    | Temperature Dependent Photoluminescence . . . . .   | 113        |
| 4.2.4    | Gate-dependent Magnetophotoluminescence . . . . .   | 114        |
| 4.2.5    | Gate-Dependent Photoluminescence Lifetime of Dark Trions . . . . .                                    | 116        |
| 4.2.6    | Conclusion . . . . .  | 119        |
| 4.3      | Valley-selective Chiral Phonon Replicas of Dark Excitons and Trions in Monolayer WSe <sub>2</sub>     | 120        |
| 4.3.1    | Methodology . . . . .   | 122        |
| 4.3.2    | Gate-Dependent Photoluminescence at Zero-Field . . . . .  | 122        |
| 4.3.3    | Gate-Dependent Magnetophotoluminescence . . . . .   | 124        |
| 4.3.4    | Measurement of Exciton Dipole-Orientation . . . . .   | 127        |
| 4.3.5    | Phonon Replica Optical Selection Rules . . . . .  | 128        |
| 4.3.6    | Chiral Phonons in Monolayer WSe <sub>2</sub> . . . . .  | 130        |
| 4.3.7    | Conclusion . . . . .  | 133        |
| 4.4      | Multipath Optical Recombination of Intervalley Dark Excitons and Trions in Monolayer WSe <sub>2</sub> | 133        |
| 4.4.1    | Methodology . . . . .   | 134        |
| 4.4.2    | Observation of the Intervalley Exciton . . . . .  | 136        |
| 4.4.3    | Signatures of Intervalley Excitons . . . . .  | 138        |
| 4.4.4    | <i>K</i> -point Phonon Replica Photoluminescence . . . . .  | 142        |
| 4.4.5    | Intervalley Phonon Replica Selection Rules . . . . .  | 144        |
| 4.4.6    | Multipath Radiative Relaxation of Dark Trions . . . . .   | 145        |
| 4.4.7    | Conclusion . . . . .  | 148        |

|          |   |            |
|----------|---|------------|
| <b>5</b> | <b>Interlayer Phonons in Transition Metal Dichalcogenides</b>           | <b>150</b> |
| 5.1      | Stacking-Dependent Interlayer Phonons in 3R- and 2H-MoS <sub>2</sub>    | 151        |
| 5.1.1    | Rhombohedral (3R) MoS <sub>2</sub>                                      | 152        |
| 5.1.2    | Interlayer Phonons  | 153        |
| 5.1.3    | Methodology   | 154        |
| 5.1.4    | Experimental Low-Frequency Raman Spectra                                | 155        |
| 5.1.5    | Frequency Analysis <i>via</i> Linear Chain Model                        | 159        |
| 5.1.6    | Calculation of Interlayer Force Constant and Elastic Moduli             | 161        |
| 5.1.7    | Group-Theory Analysis   | 162        |
| 5.1.8    | Qualitative Description of Raman Activity                               | 163        |
| 5.1.9    | Quantitative Bond Polarizability Model                                  | 164        |
| 5.1.10   | Conclusion  | 171        |
| 5.2      | Interlayer Breathing and Shear Modes in NbSe <sub>2</sub> Atomic Layers | 171        |
| 5.2.1    | Methodology   | 172        |
| 5.2.2    | Crystal Structure of NbSe <sub>2</sub>                                  | 173        |
| 5.2.3    | Broadening of Interlayer Phonon Raman from Sample Degradation           | 175        |
| 5.2.4    | Layer-dependent Interlayer Raman Peak Broadening                        | 181        |
| 5.2.5    | Conclusion  | 183        |
| <b>6</b> | <b>Conclusion</b>   | <b>184</b> |
|          | <b>Bibliography</b>   | <b>187</b> |

# List of Figures

|      |  |    |
|------|--|----|
| 1.1  | Illustration of layered materials and an example 2D heterostructure device.  | 2  |
| 1.2  | Crystal structure of monolayer WSe <sub>2</sub> .  | 7  |
| 1.3  | Schematic band structure of monolayer WSe <sub>2</sub> .   | 8  |
| 1.4  | Optical valley selection in monolayer WSe <sub>2</sub> .   | 12 |
| 1.5  | Excitons and related optical absorption in monolayer WSe <sub>2</sub> .  | 14 |
| 1.6  | Monolayer WSe <sub>2</sub> gating device and schematic of hole trion ( $A^+$ ).  | 16 |
| 1.7  | Schematic of intervalley ( $A_1^-$ ) and intravalley ( $A_2^-$ ) electron trions in monolayer WSe <sub>2</sub> .             | 17 |
| 1.8  | Gate-dependent optical conductance in monolayer WSe <sub>2</sub> gating device.  | 18 |
| 1.9  | Valley Zeeman effect in monolayer WSe <sub>2</sub> and single-particle band $g$ – $factors$ .                                | 21 |
| 1.10 | Valley Zeeman shift of the neutral $A$ exciton ( $A^0$ ) in monolayer WSe <sub>2</sub> .                                     | 22 |
| 2.1  | Photograph and schematic of transfer microscope stage.   | 27 |
| 2.2  | Illustration of the simple dry transfer fabrication process.   | 31 |
| 2.3  | Time series of stamp approach to 2D flake.   | 32 |
| 2.4  | Optical image of Representative BN-encapsulated monolayer WSe <sub>2</sub> gating device.                                    | 33 |
| 2.5  | Schematic of multi-technique optical microscope system.  | 35 |
| 2.6  | Fiber-based magneto-optical schematic.   | 43 |
| 2.7  | Free-space magneto-optical schematic.  | 45 |
| 2.8  | Absorption and corresponding reflectance spectra for isolated and encapsulated monolayers.                                   | 48 |
| 2.9  | Comparison of raw reflection and reflectance contrast spectra for monolayer WSe <sub>2</sub> gating device.                  | 50 |
| 2.10 | Dielectric function from Drude-Lorentz oscillator model.   | 55 |
| 2.11 | Multi-Lorentzian parameterization of monolayer WSe <sub>2</sub> dielectric function and representative fitting result.       | 57 |
| 2.12 | Optimization of the BN-encapsulated monolayer WSe <sub>2</sub> dielectric function at intermediate electron doping.          | 59 |
| 2.13 | Gate-dependent reflection contrast spectrum and fitted optical conductance map for monolayer WSe <sub>2</sub> gating device. | 60 |
| 2.14 | Photoluminescence of exciton internal energy levels.   | 62 |

|      |   |     |
|------|---|-----|
| 2.15 | Experimental gate-dependent photoluminescence map of a monolayer WSe <sub>2</sub> gating device at $T = 5$ K. . . . .   | 63  |
| 2.16 | Time-resolved photoluminescence and deconvolution with instrument response function. . . . .  | 65  |
| 3.1  | BN-encapsulated monolayer WSe <sub>2</sub> device schematic; Internal energy levels of $A$ exciton and PL spectrum of $n = 1s - 4s$ energy levels. . . . .  | 70  |
| 3.2  | PL of $A$ -exciton Rydberg states in monolayer WSe <sub>2</sub> under magnetic field at temperature $T = 4$ K . . . . .   | 72  |
| 3.3  | The total, Zeeman, and diamagnetic energy shifts of $A$ -exciton Rydberg states in monolayer WSe <sub>2</sub> under magnetic field. . . . .   | 75  |
| 3.4  | The energy and radii of Rydberg excitons in monolayer WSe <sub>2</sub> . . . . .  | 79  |
| 3.5  | Schematic Landau levels in monolayer WSe <sub>2</sub> ; comparison of single-particle model and experimental results. . . . .   | 81  |
| 3.6  | Trion configuration at intermediate hole doping and gate-dependent reflection contrast maps at $B = 0$ T and $B = 17.5$ T for the $K$ - and $K'$ -valleys in monolayer WSe <sub>2</sub> . . . . . | 85  |
| 3.7  | Optical sheet conductivity maps of monolayer WSe <sub>2</sub> for $B = 0 - 17.5$ T. . . . .   | 88  |
| 3.8  | Gate-dependent oscillation of $A^0$ ; comparison of experimental data and semi-empirical calculation results. . . . .   | 90  |
| 3.9  | Landau-level-related oscillation of $K$ -valley intervalley electron trion $A_1^-$ . . . . .  | 92  |
| 3.10 | Step-like energy shift and FWHM oscillations of $K$ -valley $A^0$ for $B = 0 - 17.5$ T. . . . .   | 94  |
| 3.11 | Landau-level-induced kinks in peak conductivity and peak photon energy of $K$ -valley $A_1^-$ for $B = 0 - 17.5$ T. . . . .   | 95  |
| 3.12 | Landau fan diagram of magnetic-field-dependent Landau level half-filling gate-voltages from $A^0$ and $A_1^-$ oscillations. . . . .   | 96  |
| 3.13 | Landau-level-induced oscillations of photoluminescence intensity in the $K$ - and $K'$ -valley excitons and trions. . . . .   | 98  |
| 3.14 | Gate-dependent photoluminescence maps of the $K'$ -valley in monolayer WSe <sub>2</sub> for $B = 0$ to $17.5$ T. . . . .  | 102 |
| 4.1  | Schematic configurations of bright exciton, spin dark exciton, and dark trions. . . . .   | 107 |
| 4.2  | Gate-dependent photoluminescence of BN-encapsulated monolayer WSe <sub>2</sub> highlighting dark exciton and dark trions. . . . .   | 112 |
| 4.3  | Temperature-dependent PL of bright and dark trions in monolayer WSe <sub>2</sub> . . . . .  | 114 |
| 4.4  | Magnetic-field- and gate-dependent photoluminescence of monolayer WSe <sub>2</sub> ; bright (dark) exciton (trion) $g$ -factors. . . . .  | 116 |
| 4.5  | Time-resolved PL of the bright trion ( $A^+$ ) and dark trion ( $D^+$ , at $V_g = -0.8$ V and $V_g = -3.0$ V) in BN-encapsulated monolayer WSe <sub>2</sub> . . . . .                             | 118 |
| 4.6  | Band configurations, transition dipole, and optical emission of the bright exciton, dark exciton, and dark exciton chiral phonon replica. . . . .   | 121 |
| 4.7  | Gate-dependent photoluminescence map of BN-encapsulated monolayer WSe <sub>2</sub> gating device. . . . .   | 123 |
| 4.8  | Analysis of exciton PL features from gate-dependent PL map in Figure 4.2. . . . .   | 124 |

|      |   |     |
|------|---|-----|
| 4.9  | Magnetic-field-dependent second-derivative PL map ( $d^2I/dE^2$ ) of BN-encapsulated monolayer WSe <sub>2</sub> at charge neutrality, electron doping, and hole doping. . .                     | 126 |
| 4.10 | Photoluminescence intensity of bright, dark, and phonon replica states; $g$ -factors and dipole orientation. . . . .  | 128 |
| 4.11 | Chiral phonons and schematic of chiral-phonon-mediated dark exciton relaxation. . . . .   | 131 |
| 4.12 | Schematic intervalley electron-hole recombination processes in monolayer WSe <sub>2</sub> . . . . .   | 135 |
| 4.13 | Gate-dependent photoluminescence map of BN-encapsulated monolayer WSe <sub>2</sub> gating device. . . . .   | 137 |
| 4.14 | Excitation power dependent photoluminescence intensity and FWHM of bright, dark, and replica excitons (trions). . . . .   | 138 |
| 4.15 | Analysis of exciton features in gate-dependent PL map in Figure 4.13. . .   | 139 |
| 4.16 | Intervalley exciton $g$ -factor measurement <i>via</i> magnetophotoluminescence. .  | 141 |
| 4.17 | Magnetic-field-dependent, helicity-resolved PL map in BN-encapsulated monolayer WSe <sub>2</sub> with electron doping or hole doping. . . . .   | 143 |
| 4.18 | Splitting of intra- and inter-valley trion emission under a magnetic field; schematic diagram and gate-dependent magnetophotoluminescence of dark trion in monolayer WSe <sub>2</sub> . . . . . | 147 |
| 4.19 | Zeeman splitting of intra- and inter-valley relaxation pathways of the dark exciton. . . . .  | 148 |
|      |   |     |
| 5.1  | Crystal structure of 2H and 3R MoS <sub>2</sub> . . . . .   | 152 |
| 5.2  | Experimental and calculated Raman spectra of the interlayer shear and breathing modes for 2H- and 3R-MoS <sub>2</sub> bilayer. . . . .  | 156 |
| 5.3  | Parallel-polarized (VV) and cross-polarized (HV) Raman spectra of the shear modes and breathing modes for 3R-MoS <sub>2</sub> and 2H-MoS <sub>2</sub> with layer number $N = 1L-13L$ . . . . .  | 157 |
| 5.4  | Frequencies of the observed shear modes and breathing modes in Figure 5.3 as a function of MoS <sub>2</sub> layer number. . . . .   | 160 |
| 5.5  | Layer displacement of the two shear modes and comparison of experimental and calculated cross-polarized Raman spectra in 3R- and 2H-MoS <sub>2</sub> trilayers. .                               | 165 |
| 5.6  | Schematic representation of interlayer bonds for 3R- and 2H-MoS <sub>2</sub> . . . . .  | 167 |
| 5.7  | Experimental and simulated cross-polarized shear-mode Raman spectra for 5L and 9L 3R- and 2H-MoS <sub>2</sub> . . . . .   | 169 |
| 5.8  | Experimental and simulated parallel-polarized spectrum of 10L 3R MoS <sub>2</sub> . .   | 170 |
| 5.9  | Comparison of the crystal structure of bilayer 2Ha-NbSe <sub>2</sub> and 2Hc-MoS <sub>2</sub> . .   | 174 |
| 5.10 | Optical image of an exfoliated NbSe <sub>2</sub> flake on a SiO <sub>2</sub> /Si with partial BN capping. Low frequency Raman spectra of 1L and 2L uncapped NbSe <sub>2</sub> . . .             | 175 |
| 5.11 | Low-frequency Raman spectra of NbSe <sub>2</sub> with layer number $N = 2 - 15$ and bulk NbSe <sub>2</sub> . . . . .  | 178 |

# List of Tables

|     |  |     |
|-----|--|-----|
| 3.1 | PL energy ( $E_{PL}$ ), binding energy ( $E_b$ ), $g$ -factor, diamagnetic coefficient ( $\sigma$ ), and root-mean-square radius ( $r$ ) of the exciton Rydberg states in BN-encapsulated monolayer WSe <sub>2</sub> . . . . . | 71  |
| 5.1 | Elastic parameters of 2H- and 3R-MoS <sub>2</sub> calculated from the interlayer phonon frequencies. . . . .   | 162 |

# Chapter 1

## Introduction

When thinned to a single layer, extraordinary mechanical, electronic, and optical properties can emerge from otherwise unremarkable bulk layered crystals. Graphite is the prototype example whose layered structure is illustrated in Figure 1.1(a). Each sheet-like layer, called graphene, has exceptionally strong in-plane bonds and excellent thermal and electrical conductivity but is weakly bonded to its neighbors by the van der Waals interaction. Graphite has thus found widespread use as the “lead” in our pencils and as a dry lubricant. Beyond the myriad uses of graphite, its dull, gray exterior hid another remarkable secret: a single layer of graphene, isolated from its neighbors, exhibits remarkable properties which emerge due to its intrinsic two-dimensionality [1]. Moreover, the isolation of high-quality graphene flakes with lateral dimension  $\leq 100 \mu\text{m}$  does not require expensive instrumentation or complex processes. The so-called “scotch tape method” of micromechanical exfoliation requires only a bulk crystal, adhesive tape, and an optical microscope. In strict terms of single-material fabrication, the barrier to entry in 2D materials research

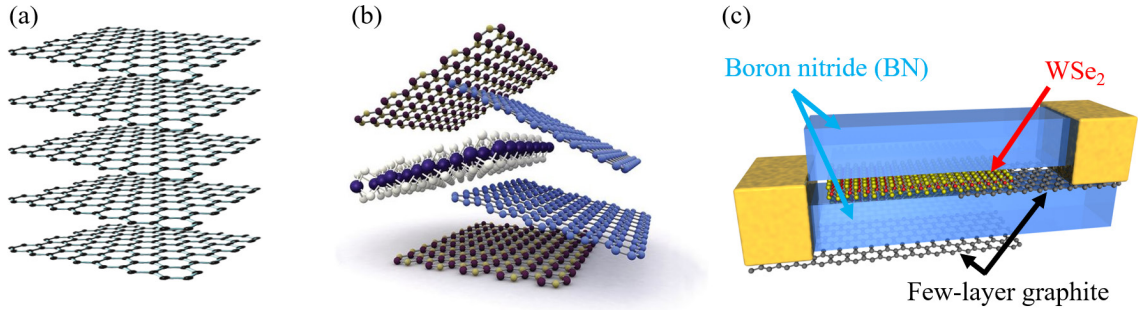


Figure 1.1: (a) Graphite, composed of individual graphene layers. (b) Schematic illustration of arbitrary hetero-layer stacking of van der Waals materials (Adapted from K.S. Novoselov, *et al.* [2]). (c) Example schematic of an all-2D gating device composed of monolayer tungsten diselenide (WSe<sub>2</sub>) based, graphene, and hexagonal boron nitride (BN).

is low. As a result, the field has rapidly expanded in the intervening 15 years and has grown beyond graphene to an entire family of 2D materials which include semiconductors, insulators, ferromagnets, and more exotic classes such as superconductors and topological insulators. Importantly, many members of this 2D catalog exhibit similar stability, ease of few-layer exfoliation, and emergence of novel properties in the monolayer limit which have attracted such interest to graphene.

The intrinsic layered nature of van der Waals materials which allows straightforward isolation of single layers is also advantageous in reverse. Just as constituent layers may be peeled apart, so too can individual layers be assembled like building blocks into an arbitrary 2D heterostructures [3] as illustrated in Figure 1.1(b). Figure 1.1(c) shows a schematic diagram of a 2D gating device composed of few-layer graphite as electrical contact and gate electrode, insulator hexagonal boron nitride (BN) as gate dielectric, and monolayer WSe<sub>2</sub> as the semiconductor channel. This example device uses only three members, but our catalog of 2D materials is far more extensive. Generally, we can imagine a large number of

possible 2D heterostructures whose characteristics may be finely tailored by specific material choice and arrangement. Further, the properties of each layer are not fixed but can be significantly altered through interlayer and interfacial interactions. In contrast to 3D materials where the electronic properties are dominated by the interior bulk material with little influence from the surface, 2D materials are essentially all-surface. These 2D materials are thus highly susceptible to extrinsic effects on a large scale from fine-tuning to fundamental renormalizing their material properties. This remarkable phenomenon is perhaps best illustrated by the notable influence of interlayer stacking configuration on electronic properties and recent demonstrations of “magic angle” graphene [4] and the observation of long-lived interlayer valley excitons [5]. To realize the full potential of such *designer* heterostructures whose properties can be finely controlled and targeted for specific technological or scientific interests, we must first establish several key foundations: a fundamental understanding of the properties of each individual 2D material, the consequences of layer-by-layer stacking in both homo- and heterostructure configurations, and more broadly the influence of various extrinsic effects which may induce desired properties.

In this dissertation, we use optical spectroscopy to investigate excitonic physics in individual monolayers and the influence of few-layer stacking on the subgroup of 2D materials called transition metal dichalcogenides (TMDs) with form  $\text{MX}_2$  ( $\text{M} = \text{Mo}, \text{W}$ ;  $\text{X} = \text{S}, \text{Se}$ ). Group-*IV* monolayer TMDs exhibit two time-reversal electronic valleys with direct band gap and host exceptionally robust excitonic phenomena and strong light-matter interactions [6]. These materials therefore attract significant scientific and technological interest as a promising platform to explore excitonic physics and optoelectronic manipulation of the

exciton, spin, and valley-pseudospin states among other properties [6–8]. We will briefly introduce this family of materials below and discuss those optical and electronic properties which are essential to the research results presented in the remainder of this work.

In Chapter 3 we explore the behavior of excitons and trions in high-quality monolayer WSe<sub>2</sub> gating devices under high out-of-plane magnetic field ( $B \leq 31$  T). We first discuss the internal energy levels structure of the bright, neutral *A*-exciton and characterize the non-hydrogenic Rydberg series emission ( $n = 1s$  to  $n = 5s$ ) *via* photoluminescence spectroscopy. The exciton states exhibit linear valley Zeeman shift and quadratic diamagnetic shift under magnetic field from which we deduce the per-state exciton binding energies, *g*-factors, and spatial radii. Next, we utilize electrostatic gating together with high magnetic field to study the influence of Landau quantization on the exciton and trion. We observe charge-density-dependent quantum oscillations of the various excitonic species in both reflectance contrast and photoluminescence spectroscopy. Our results highlight the complex interaction between excitons and ambient carriers which may be controlled by Landau level filling and which diverges from the standard single-particle model in the regime of moderate charge density. This divergence suggests the presence of significant many-body interactions in monolayer WSe<sub>2</sub> which make this material a promising system in which to explore correlated quantum phenomena.

In Chapter 4, we go beyond the well-studied bright exciton (trion) and develop a more complete picture of the *dark* excitonic states in monolayer WSe<sub>2</sub>. We measure the photoluminescence of the spin-forbidden dark exciton and related trions which may be continuously tuned by electrostatic gating. At zero magnetic field, our results show the

binding energies of the dark exciton (trion) states and demonstrate the exceptionally long recombination lifetime of the dark trion in comparison to the bright trion (up to 1.2 ns vs. 10 ps). Using magneto-optical PL, we confirm the spin-triplet configuration of the dark states and resultant valley-independent optical selection rules. We expand upon this analysis to explore the multi-pathway radiative relaxation of the dark exciton (trion) states mediated by phonon and lattice defect scattering. We first show valley-selective PL of the dark exciton (trion) states *via* chiral phonon emission and rigorously establish their optical selection rules. In this way, we demonstrate the optical detection of dark state valley pseudospin. We further discuss the optical detection of the intervalley exciton and intervalley-relaxation of the dark trion through chiral phonon and defect scattering. Totally, we produce a more complete experimental and theoretical picture of the complex excitonic landscape in monolayer WSe<sub>2</sub> at the charge neutrality point and under moderate electron (hole) doping.

Finally, in Chapter 5, we explore the influence of layer-by-layer stacking in MoS<sub>2</sub> and NbSe<sub>2</sub> homostructures by probing the interlayer vibrations *via* ultralow-frequency Raman spectroscopy. We measure the interlayer phonon spectra in two chemically-identical stacking configurations (3R and 2H) of MoS<sub>2</sub> from the monolayer to bulk crystal from which we determine the stacking-dependent elastic properties. We further develop a concise model based on bond polarizability to calculate the interlayer phonon Raman intensities. Together with our experimental results, this provides a clear fingerprint with which to efficiently identify the thickness and stacking configuration of 2D materials *via* Raman spectroscopy.

Before discussing the detailed research results that comprise the majority of this dissertation, however, we present a brief introduction to the optical and electronic properties of TMDs which are essential to the research results presented in the remainder of this work followed by discussion of the experimental techniques used throughout.

## 1.1 Transition Metal Dichalcogenides (TMDs)

In contrast to the atomically-thin graphene, TMD monolayers are composed of a transition metal atom sandwiched between two chalcogen atoms in a trigonal prismatic structure, as shown in Figure 1.2(a) [6]. The most common group-VI  $\text{MX}_2$  TMDs ( $\text{M} = \text{Mo}, \text{W}$ ;  $\text{X} = \text{S}, \text{Se}$ ) adopt a similar hexagonal lattice to graphene but with reduced  $D_{3h}$  symmetry (Figure 1.2(b)). Out-of-plane mirror symmetry ( $\sigma_h$ ) is preserved but in-plane inversion symmetry (i) is broken and rotational symmetry is reduced from  $C_6$  to  $C_3$ . When stacked,  $\text{MX}_2$  TMDs most commonly adopt an A-A'-A-A'... stacking order (2H) where adjacent layers are inversion symmetric. We discuss a symmetry-based analysis of the 2H structure and discuss our experimental results regarding the influence of stacking order on TMD interlayer coupling in Chapter 5.

Although TMDs have been studied for over 50 years, both as bulk materials and thin flakes, monolayer TMDs were only successfully isolated and characterized in the last decade. These monolayer TMD systems have since become a subject of immense research interest, largely motivated by two foundational results in  $\text{MoS}_2$ . First, Mak, *et al.* [9] and Splendiani *et al.* [10] confirmed in 2010 that TMDs have a direct band-gap and thus strong optical coupling in the monolayer limit, as opposed to the indirect band gap and weak

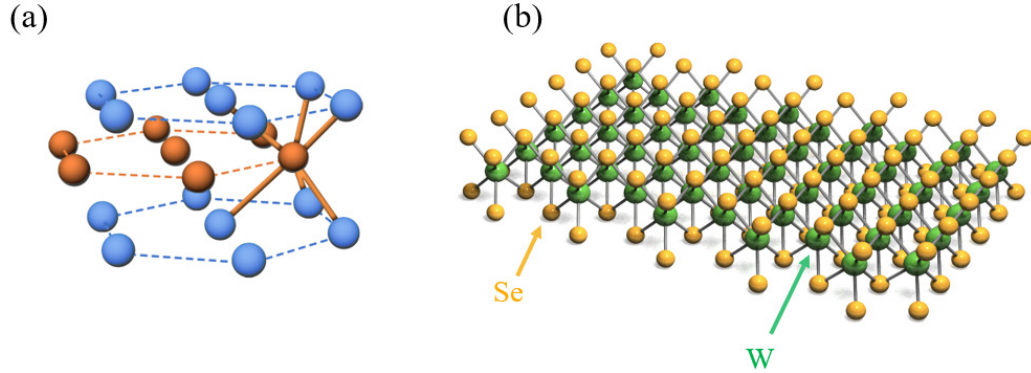


Figure 1.2: Illustration of the trigonal prismatic and hexagonal crystal structure of monolayer tungsten diselenide ( $\text{WSe}_2$ ).

optical coupling in few-layer and bulk samples. As illustrated schematically in Figure 1.3, the direct gap is located at  $K$  and  $K'$  points in the Brillouin zone, which are referred to as the  $K$ - and  $K'$ -valleys. They further demonstrated the presence of robust excitonic effects due to the two-dimensional electronic confinement which persist up to room temperature. Shortly afterward, in 2012, Cao, *et al.* [11] and Xiao *et al.* [12] demonstrated experimentally that the optical transition across this direct band gap could be selectively excited at the  $K$ - and  $K'$ -valleys by right- and left-circularly polarized light, respectively. Together, these results established monolayer TMDs as a remarkable system which simultaneously exhibits strong light interaction, robust excitonic effects, and optical valley-selection which gives a momentum-based degree of freedom.

We use the  $\text{WSe}_2$  as a representative example to understand the electrical and optical properties of monolayer group-VI TMDs as it is the subject of Chapter 3 and Chapter 4. Similar to  $\text{MoS}_2$ ,  $\text{WSe}_2$  transitions in the monolayer limit to a direct gap with  $E_g \sim 1.8 - 2.0$  eV [14–16], located the  $K$ - and  $K'$ -valleys in momentum space. Figure 1.3(a)

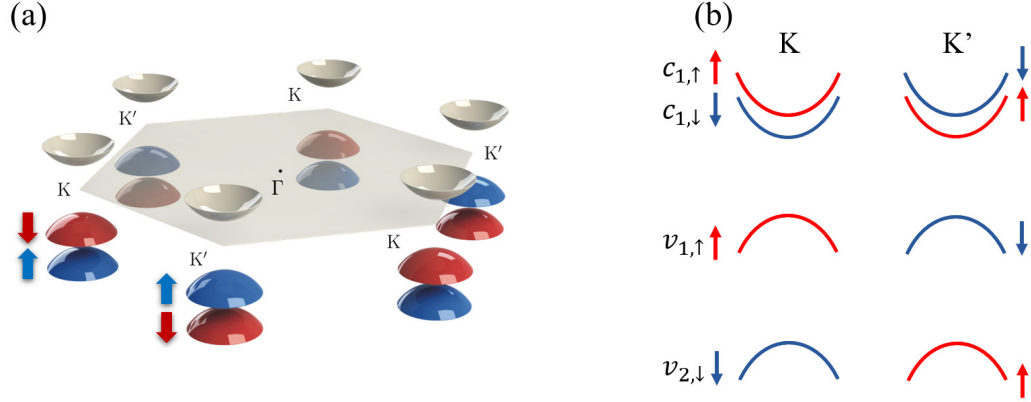


Figure 1.3: (a) Hexagonal Brillouin zone of monolayer WSe<sub>2</sub>. (b) Schematic band configuration at the  $K$  ( $K'$ ) valley in monolayer WSe<sub>2</sub> (Adapted from E.J. Sie [13]). The arrows and color indicate the electron spin (up, down) of the band.

shows a schematic view of the local band structure at the  $K$ - and  $K'$ -points. Specifically, we highlight the parabolic conduction and valence bands near to the charge neutrality point. These bands comprise the direct band gap and thus largely determine the electrical and optical properties of the material. Due to the strong spin-orbit coupling in WSe<sub>2</sub>, the spin-degeneracy of each band is intrinsically broken and each band is split into two sub-bands with opposite spin configuration, labeled in Figure 1.3(b). The conduction band is split by  $\sim 30$  meV ( $c_1$ ), while the valence band is split by  $\sim 450$  meV ( $v_1$ ) [6]. We note that the conduction band spin-splitting is relatively small ( $\sim k_B T = 300$  K), and thus both sub-bands play a significant role in the electronic properties. The valence band splitting, however, is over  $10\times$  larger so the influence of the lower energy sub-band is much reduced. For the remaining discussion, we largely focus on the three sub-bands ( $v_{1,\uparrow}$ ,  $c_{1,\downarrow}$ ,  $c_{1,\uparrow}$ ) closest to the charge neutrality point as this three-band picture is sufficient to describe the relevant properties.

### 1.1.1 Optical Excitation of Monolayer WSe<sub>2</sub>

We now describe the general process of photoexcitation in monolayer WSe<sub>2</sub> at charge neutrality and the formation of excitonic states. We can limit our discussion to the  $K$ -valley for simplicity, as the two valleys are time-reversal partners. Identical analysis under time-reversal can be applied to the  $K'$ -valley.

At charge neutrality, the valence band is fully occupied by electrons and the conduction bands are fully unoccupied. An electron in the valence band may be excited to an available state in the conduction band through absorption of an incident photon with appropriate energy. For example, a direct transition between  $v_{1,\uparrow}$  and  $c_{1,\uparrow}$ . As the photon has vanishingly small momentum, the electron can be photoexcited only to those conduction band states with nearly identical momentum which corresponds to a vertical transition in the band diagram. The lowest energy free-particle transition across the band gap will thus be between a valence band maximum and a conduction band minimum at the  $K$  point. Importantly, the original electron state in the valence band is left unoccupied by the photoexcitation process. This unoccupied valence band state modifies the electron interactions and acts as an effective positive charge carrier - a *hole*. Thus, each photoexcitation event produces a single excited electron-hole pair. We note that this is a slight generalization but is broadly accurate for our purposes. Photoexcitation between two states away from the band minimum is still allowed, but requires higher photon energy and leaves the excited electron-hole pair above their band minima (the hole will naturally relax to the top of the valence band which is its energy minimum). These so-called *hot* carriers will rapidly relax on the femtosecond timescale, either towards the band minimum through scattering

with other charge carriers and lattice vibrations (phonons), or directly to the valence band through another pathway (e.g., hot luminescence, Auger scattering).

So far, we have discussed the general process of photoexcitation and exciton formation in a two-dimensional material semiconductor without much consideration of the electronic structure in monolayer WSe<sub>2</sub>. As mentioned above, however, the distinct optical selection rules and band configuration in this material are central to our interest and the details of the results in Chapter 2 and Chapter 3 of this work.

### Valley-Dependent Optical Selection

Beyond satisfying energy conservation, the photoexcitation of an electron between two bands must also satisfy further properties of those bands such as the electron spin and orbital symmetry. By considering the symmetry of each band in monolayer WSe<sub>2</sub> ( $v_{1,\uparrow}, c_{1,\downarrow}, c_{1,\uparrow}$ ), we can derive the valley-dependent optical selection rules mentioned above.

The electronic transition by photon absorption can be expressed in terms of the Bloch states of the involved bands,  $|\psi_\alpha\rangle$  ( $\alpha = v_{1,\uparrow}, \dots$ ) and the momentum operator,  $\hat{P}_\gamma$ , for the incident photon where  $\gamma$  indicates the photon polarization. For example, a transition from  $v_{1,\uparrow}$  to  $c_{1,\uparrow}$  the transition rate (proportional to oscillator strength) is given from first-order perturbation theory by:

$$I_{v_{1,\uparrow} \rightarrow c_{1,\uparrow}} \propto \left| \langle \psi_{c_{1,\uparrow}} | \hat{P}_\gamma | \psi_{v_{1,\uparrow}} \rangle \right|^2 \quad (1.1)$$

As mentioned at the beginning of this section, the monolayer WSe<sub>2</sub> crystal has  $D_{3h}$  symmetry and therefore the Brillouin zone-corner  $K$ -point states have slightly reduced  $C_{3h}$  symmetry - threefold rotation ( $C_3$ ) and out-of-plane mirror reflection ( $\sigma_h$ ). For the oscil-

lator strength to be non-zero (a dipole-allowed transition), the above expression must be unchanged under these symmetry operations at the  $K$ -point [17].

$$\langle \psi_{c_{1,\uparrow}} | \hat{P}_\gamma | \psi_{v_{1,\uparrow}} \rangle \rightarrow \langle \psi_{c_{1,\uparrow}} | C_3^{-1} C_3 \hat{P}_\gamma C_3 C_3^{-1} | \psi_{v_{1,\uparrow}} \rangle = \langle C_3 \psi_{c_{1,\uparrow}} | C_3 \hat{P}_\gamma C_3^{-1} | C_3 \psi_{v_{1,\uparrow}} \rangle \quad (1.2)$$

$$\langle \psi_{c_{1,\uparrow}} | \hat{P}_\gamma | \psi_{v_{1,\uparrow}} \rangle \rightarrow \langle \psi_{c_{1,\uparrow}} | \sigma_h^{-1} \sigma_h \hat{P}_\gamma \sigma_h \sigma_h^{-1} | \psi_{v_{1,\uparrow}} \rangle = \langle \sigma_h \psi_{c_{1,\uparrow}} | \sigma_h \hat{P}_\gamma \sigma_h^{-1} | \sigma_h \psi_{v_{1,\uparrow}} \rangle \quad (1.3)$$

From previous density functional theory (DFT) calculation [6], the valence and conduction bands at the  $K$ -point near the charge neutrality point are primarily composed of the  $d$ -orbitals of the  $W$  atoms with a sufficiently small contribution from the  $p$ -orbitals of  $Se$  which we can neglect. The  $d$ -orbitals are split energetically into three orbits,  $d_0 = d_{z^2}$ ,  $d_{\pm 1} = \sqrt{2}^{-1}(d_{xz} \pm id_{yz})$ , and  $d_{\pm 2} = \sqrt{2}^{-1}(d_{x^2-y^2} \pm id_{xy})$ , where the subscripts ( $d_{\pm m}$ ) indicate the magnetic angular momentum quantum number,  $m$ . The valence band,  $v_1$ , is dominated by the  $d_{+2}$  orbital and the conduction bands ( $c_{1,\downarrow}, c_{1,\uparrow}$ ) are dominated by the  $d_0$  orbital. Recall, as well, that  $v_{1,\uparrow}$  and  $c_{1,\uparrow}$  are spin up and  $c_{1,\downarrow}$  is spin down. We can therefore determine how the functions transform under the symmetry operations, as the total state transforms as the product of the orbital and spin transformations.

$$C_3 |v_{1,\uparrow}\rangle = e^{-i\frac{\pi}{3}} |v_{1,\uparrow}\rangle, \quad \sigma_h |v_{1,\uparrow}\rangle = i |v_{1,\uparrow}\rangle \quad (1.4)$$

$$C_3 |c_{1,\downarrow}\rangle = e^{-i\frac{2\pi}{3}} e^{i\frac{\pi}{3}} |c_{1,\downarrow}\rangle = e^{-i\frac{\pi}{3}} |c_{1,\downarrow}\rangle, \quad \sigma_h |c_{1,\downarrow}\rangle = -i |c_{1,\downarrow}\rangle \quad (1.5)$$

$$C_3 |c_{1,\uparrow}\rangle = e^{-i\frac{2\pi}{3}} e^{-i\frac{\pi}{3}} |c_{1,\uparrow}\rangle = e^{-i\frac{3\pi}{3}} |c_{1,\uparrow}\rangle, \quad \sigma_h |c_{1,\uparrow}\rangle = i |c_{1,\uparrow}\rangle \quad (1.6)$$

Similarly, we can examine the photon momentum operator for in-plane, linear polarization ( $\hat{P}_\gamma = \hat{P}_z$ ) and out-of-plane, circular polarization ( $\hat{P}_\gamma = \hat{P}_\pm = \hat{P}_x \pm i\hat{P}_y$ ) under  $C_3$  and  $\sigma_h$  transformation:

$$C_3 \hat{P}_z C_3^{-1} = \hat{P}_z, \quad \sigma_h \hat{P}_z \sigma_h^{-1} = -\hat{P}_z \quad (1.7)$$

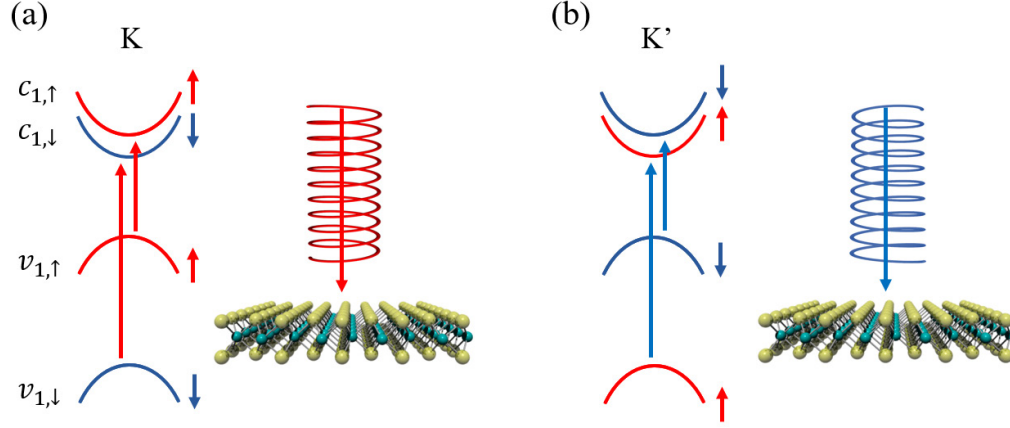


Figure 1.4: Circularly polarized valley-specific optical selection rules for electronic photo-transitions in the (a)  $K$ -valley and (b)  $K'$ -valley in monolayer  $\text{WSe}_2$ .

$$C_3 \hat{P}_\pm C_3^{-1} = e^{\mp i \frac{2\pi}{3}} \hat{P}_\pm, \quad \sigma_h \hat{P}_\pm \sigma_h^{-1} = \hat{P}_\pm \quad (1.8)$$

Using the above transformations, we can evaluate Equation 1.2 and Equation 1.3 for each permutation of band-to-band transition and photon polarization / propagation direction to determine the optical selection rules. We show the case of a transition from  $v_{1,\uparrow} \rightarrow c_{1,\uparrow}$  with right-circularly polarized photon:

$$\langle C_3 \psi_{c_{1,\uparrow}} | C_3 \hat{P}_+ C_3^{-1} | C_3 \psi_{v_{1,\uparrow}} \rangle = e^{-i \frac{\pi}{3}} e^{-i \frac{2\pi}{3}} e^{+i \frac{3\pi}{3}} \langle \psi_{c_{1,\uparrow}} | \hat{P}_+ | \psi_{v_{1,\uparrow}} \rangle = \langle \psi_{c_{1,\uparrow}} | \hat{P}_+ | \psi_{v_{1,\uparrow}} \rangle \quad (1.9)$$

$$\langle \sigma_h \psi_{c_{1,\uparrow}} | \sigma_h \hat{P}_+ \sigma_h^{-1} | \sigma_h \psi_{v_{1,\uparrow}} \rangle = (-i)(i) \langle \psi_{c_{1,\uparrow}} | \hat{P}_+ | \psi_{v_{1,\uparrow}} \rangle = \langle \psi_{c_{1,\uparrow}} | \hat{P}_+ | \psi_{v_{1,\uparrow}} \rangle \quad (1.10)$$

Thus, the transition  $v_{1,\uparrow} \rightarrow c_{1,\uparrow}$  is only allowed with absorption of a normally incident right-circularly polarized photon ( $\hat{P}_+$ ). Similar analysis shows that the equivalent transition in the opposite ( $K'$ ,  $v_{1,\downarrow} \rightarrow c_{1,\downarrow}$ ) valley is allowed with absorption of a left-circularly polarized photon. These are the valley-dependent optical selection rules, as illustrated in Figure 1.4. We note that the higher energy transition  $v_{1,\downarrow} \rightarrow c_{1,\downarrow}$  (and equivalent in  $K'$ -valley) also satisfies the same selection rules and is allowed.

### 1.1.2 Bright Excitons

The photoexcited electron-hole pair are (quasi-)particles with opposite charge in close proximity to each other and will therefore experience attractive Coulomb interaction, analogous to the electron and proton in a hydrogen atom. In the weakly interacting limit, the relaxation of the electron-hole pair will be dominated by rapid recombination with energy equal to the free particle energy gap of the corresponding bands.

If the Coulomb interaction is strong, however, the electron-hole pair can form a bound state - an *exciton* - with lower energy than the free-particle state (the exciton binding energy) and extended lifetime. Although excitons can form between electrons and holes throughout conduction and valence bands, respectively, we necessarily focus on those exciton states which have strong light coupling and can be experimentally excited and detected. The above discussion of optical selection rules in monolayer WSe<sub>2</sub> involves only the single-particle electronic transition, but the results can be extended to the exciton. Near the  $K$  ( $K'$ ) points, the exciton inherits the symmetry of the single-particle transition and thus has identical optical selection rules. We define two species of *bright* exciton which correspond to the allowed optical transitions near the band gap at the  $K$ -valley: the lower energy transition ( $v_{1,\uparrow} \rightarrow c_{1,\uparrow}$ ) is the  $A$  exciton, while the higher energy transition ( $v_{1,\downarrow} \rightarrow c_{1,\downarrow}$ ) is the  $B$  exciton. The  $A$  and  $B$  exciton are shown schematically in Figure 1.5(a,b), respectively. As both  $A$  and  $B$  excitons inherit the valley-dependent optical selection we may selectively excite exciton populations in the  $K$ - and  $K'$ -valleys by resonant absorption of right- and left-handed circularly polarized light, respectively [12]. A representative optical absorption spectrum of monolayer WSe<sub>2</sub> is shown in Figure 1.5(c).

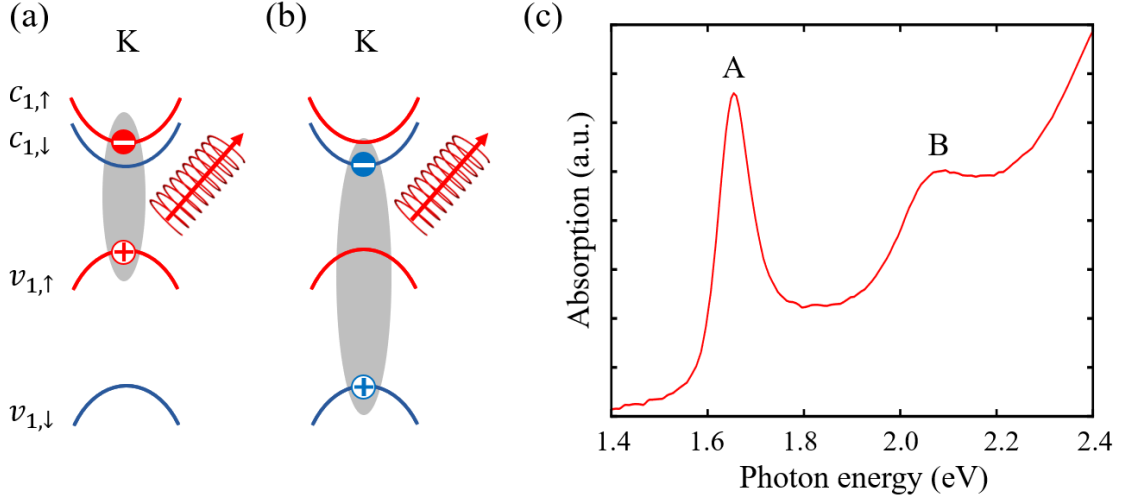


Figure 1.5: Schematic of  $K$ -valley (a)  $A$  and (b)  $B$  excitons with right-circular polarized optical selection in monolayer  $\text{WSe}_2$ . (c) Representative absorption spectrum with peaks corresponding to the  $A$  and  $B$  exciton resonances [18].

In addition to the valley-dependent optical selection rules, the 2D excitons in monolayer  $\text{WSe}_2$  are energetically distinct from those in bulk materials. The electron-hole interaction is enhanced due to the two-dimensional confinement of the electron and hole and reduced Coulomb screening due to the dielectric environment surrounding the 2D plane [19]. The electron and hole are confined to the plane, but the electric field which governs their interaction is not. The combined effects are reflected in the large exciton binding energy ( $\sim 0.17 - 0.5$  eV) [7, 15, 16] which is approximately two orders of magnitude larger than that in traditional 3D semiconductors, and one order of magnitude larger than in bulk TMDs (quasi-2D). We note that the external screening effect is the primary cause of the large variation in reported exciton binding energies and optically-derived free-particle band gaps in monolayer TMDs. Like the hydrogen Rydberg series, the exciton hosts a complex series of internal energy levels. The arrangement of energy levels in 2D excitons diverges from the Rydberg equation, however, due to the 2D confinement and dielectric screening

discussed above. We note, as well, that the  $A$  exciton in monolayer WSe<sub>2</sub> has Bohr radius  $\sim 1.6$  nm which is  $4-5\times$  larger than the lattice constant ( $\sim 0.33$  nm) [15,16] The exciton is thus spatially delocalized (a *Wannier-Mott* exciton) and can diffuse through the crystal. As a further consequence of the Bohr radius and large binding energy, the exciton must have relatively large extent in momentum space and therefore includes contributions from states throughout the corresponding conduction (valence) bands. We investigate the detailed properties of the neutral  $A$ -exciton and its internal energy levels in Chapter 3.

### 1.1.3 Bright Trions

Due to its two-dimensionality, the charge density in the monolayer can be continuously tuned *via* electrostatic gating as depicted in Figure 1.6(a). With negative (positive) *gate voltage* ( $V_g$ ) between the gate electrode and WSe<sub>2</sub>, ambient holes (electrons) are injected into the monolayer. These ambient holes progressively fill the valence bands and thus shift the WSe<sub>2</sub> Fermi energy ( $E_F$ ). We note that the 2D density of states is constant for the conduction and valence bands near the band gap at the  $K$  ( $K'$ ) valley, so the shift in  $E_F$  is proportional to  $V_g$  and the state-degeneracy (e.g.,  $\Delta E_F \propto 2V_g$  when filling the valley-degenerate valence bands). The presence of ambient carriers has several significant effects on the excitonic behavior. We discuss the low- to intermediate-charge-density regime where the ambient carrier separation is much greater than the exciton radius (charge density,  $n < 5 \cdot 10^{12}$  cm<sup>-2</sup>) as the excitonic picture breaks down at high charge density.

In the single-particle picture, an exciton can capture an ambient carrier and form a three-particle bound state with finite charge called a *trion*. The positive (hole) trion,  $A^+$ ,

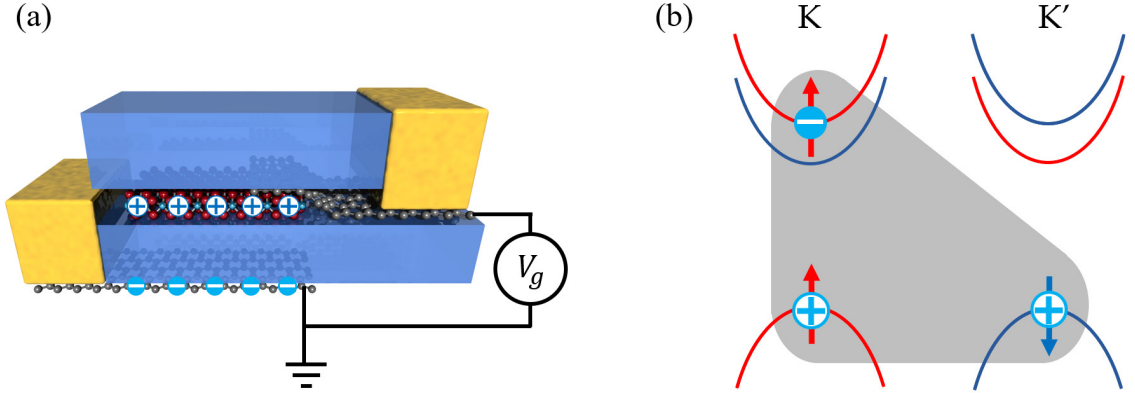


Figure 1.6: (a) Schematic of a monolayer WSe<sub>2</sub> gating device. WSe<sub>2</sub> is encapsulated in hexagonal boron nitride (BN), with few-layer graphite as electrical contact and gate electrode. A gate-voltage is applied between the few-layer graphite sheets to inject charge into the WSe<sub>2</sub> monolayer. (b) Schematic of the bright hole trion ( $A^+$ ) configuration in monolayer WSe<sub>2</sub>.

in monolayer WSe<sub>2</sub> is depicted in Figure 1.6(b). The trion has an additional binding energy relative to the neutral exciton and therefore its absorption resonance is at lower energy. In monolayer WSe<sub>2</sub>, similar to other 2D systems, the trion binding energy is  $\sim 10\%$  of the neutral exciton binding energy. For example, the neutral exciton ( $A^0$ ) and hole trion ( $A^+$ ) have binding energies  $\sim 180$  meV and  $\sim 20$  meV, respectively, when encapsulated by thick BN as in Figure 1.6(a). The possible configurations of trion depend on the arrangement of valence and conduction bands. The exciton (trion) state is not simply a combination of three discrete electron (hole) states - it includes contributions from many states near the band minima. The constituent states are fermionic and are subject to Pauli exclusion; thus, the trion cannot be composed of two electrons (holes) which occupy the same band. For reasonable hole doping, only an *intervalley* trion configuration is allowed as the exciton-forming hole already occupies the valence band of one valley. The intervalley trion ( $A^+$ ) is depicted in Figure 1.6(b). For electron doping, however, both intervalley and intravalley

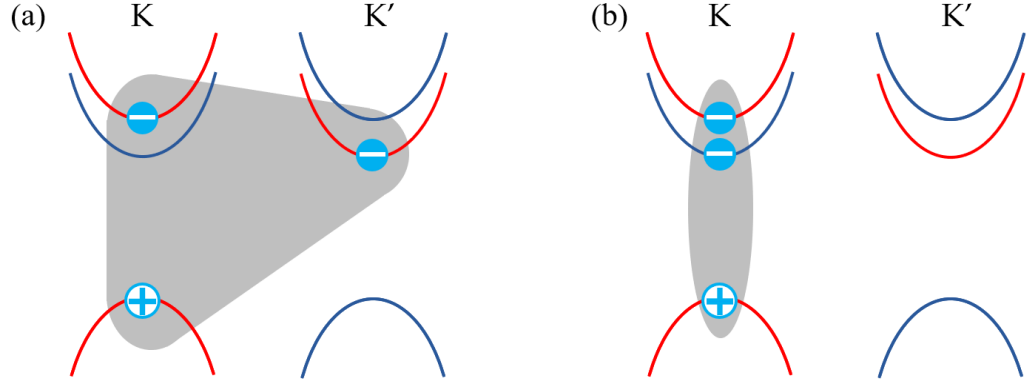


Figure 1.7: Schematic configurations of the (a) intervalley electron trion ( $A_1^-$ ) and (b) intravalley electron trion ( $A_2^-$ ).

trion configurations are allowed. The exciton-forming electron occupies the higher spin-split conduction band in one valley which leaves the lower sub-bands in both valleys available for trion formation. The intervalley ( $A_1^-$ ) and intravalley ( $A_2^-$ ) are depicted in Figure, respectively. We note that the binding energy of  $A_1^-$  is reduced relative to  $A_2^-$  due to the intervalley exchange interaction from the  $A_1^-$  spin-triplet configuration.

#### 1.1.4 Exciton Energy with Finite Charge Density

The injected charge carriers will modify the exciton (trion) through two primary mechanisms. First, the ambient charge will effectively screen the exciton Coulomb interaction and more broadly renormalize the electronic band structure. Increased screening of the exciton binding will reduce its binding energy, increase the effective exciton radius, and therefore decrease the oscillator strength. All else constant, the screening effect on the exciton absorption produces increased resonance energy (blue shift) and decreased absorption intensity. However, the free particle interaction also experiences increased screening. For the bands of interest at the  $K$  ( $K'$ ) point, the free particle band gap is reduced with

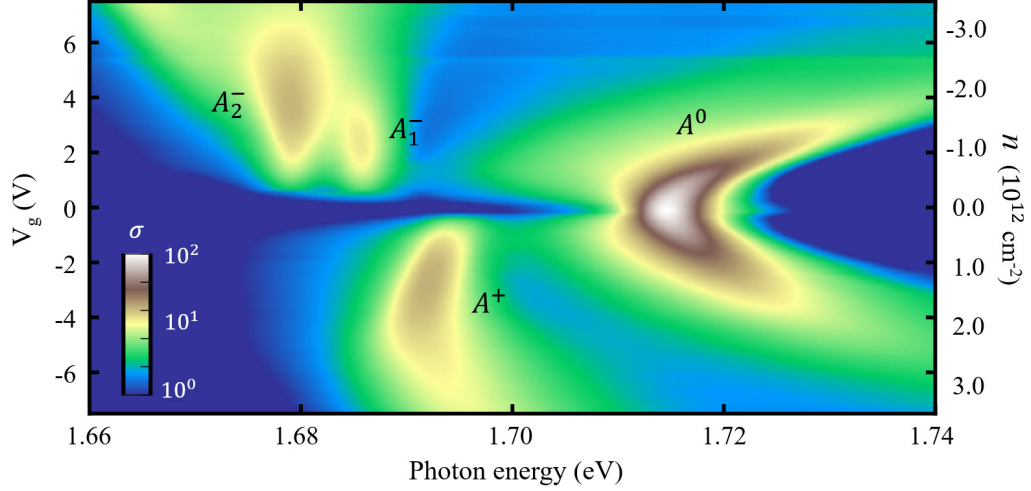


Figure 1.8: Representative gate-dependent optical conductance map measured in a monolayer WSe<sub>2</sub> gating device. The optical absorption is proportional to the optical conductance.

increasing charge density [7]. The exciton energy is given by the free particle band gap minus the exciton binding energy, so the band gap renormalization and binding energy reduction compete with each other. In monolayer WSe<sub>2</sub>, the magnitude of both effects is approximately equal. Therefore, the net screening effect on the exciton is a small shift in energy and significant decrease in oscillator strength where both effects are proportional to the charge density.

Second, and slightly more subtle, is the filling by ambient carriers of states which otherwise contribute to the exciton at charge neutrality. This so-called phase-space filling (PSF) effect [7] reduces the phase space available for photoexcitation and exciton formation due to Pauli exclusion. Overall, the PSF increases the absorption resonance energy (decreases the exciton binding energy). We note that this effect requires filling phase space which is occupied by the exciton-forming electron (hole). As shown in Figure 1.5(a), the exciton-forming hole for the *A*-exciton occupies the highest energy valence band. The *A*-

exciton will thus experience increasing PSF immediately upon hole injection. In contrast, the lowest energy conduction subbands are not directly involved in  $A$ -exciton formation. The exciton-forming electron occupies the higher energy spin-split subband. Therefore, the  $A$  exciton will not experience PSF with electron injection until this higher energy subband begins to fill. The  $B$ -exciton (Figure 1.5(b)), however, will experience PSF immediately upon electron injection as its exciton-forming electron occupies the lower energy conduction subband.

A representative map of the optical conductivity (proportional to absorption) of the exciton and trion species ( $A^0, A^+, A_1^-, A_2^-$ ) as a function of ambient charge density in monolayer WSe<sub>2</sub> is shown in Figure 1.8. At charge neutrality ( $n \sim 0 \text{ cm}^{-2}$ ), only the neutral exciton ( $A^0$ ) appears in the absorption spectrum within the energy range 1.66 – 1.78 eV. With increasing hole density (negative  $V_g$ ), the  $A^0$  absorption shifts to higher energy and decreases in intensity. The  $A^+$  resonance appears immediately upon hole injection. The  $A^+$  absorption initially increases in intensity as it gains oscillator strength from  $A^0$ , but begins to decrease at intermediate charge density ( $\sim 2.5 \cdot 10^{12} \text{ cm}^{-2}$ ). At this point, the binding energy is significantly reduced and the exciton effect is suppressed. Similarly,  $A^0$  is blue shifted and suppressed with electron injection while  $A_1^-$  and  $A_2^-$  appear.

### Limits of Trion Picture and the Exciton-Polaron

As a final note, we emphasize that the trion picture of a discrete three-body state discussed above is not accurate beyond the single-particle scenario, but is nonetheless useful to qualitatively describe the excitonic behavior at finite charge density. For this reason, the trion picture has been widely used to describe the charge-density-dependent optical

spectra in monolayer TMDs in the low-density-limit. A more realistic picture is given by the exciton-polaron model [20–24] . Here, the exciton interacts with the broader Fermi surface of ambient carriers and forms a complex, many-body state. The exciton can excite electron-hole pairs across the Fermi surface; the exciton is thus dressed by this polarized Fermi surface to form an exciton-polaron. This model converges to the trion picture in the single-particle limit but the distinction becomes increasingly important with increasing charge density. The detailed physics of the exciton-polaron and its divergence from the trion is a subject of significant ongoing research. We use the terms interchangeably throughout this work for ease of discussion, particularly where the distinction is not crucial to the data interpretation, but for clarity emphasize that the exciton-polaron is the more accurate picture.

### 1.1.5 Monolayer WSe<sub>2</sub> under Out-of-Plane Magnetic Field

Another important consequence of the distinct band structure in monolayer WSe<sub>2</sub>, which produces the optical valley selection discussed above, is the valley-specific evolution of the electronic band structure under out-of-plane magnetic field. The out-of-plane magnetic field breaks the time-reversal symmetry and lifts the valley degeneracy of each band. In the single-particle picture, the shift of each band at the  $K$ - ( $K'$ -) valley is described by the valley Zeeman effect. Each band experiences a rigid energy shift,  $\Delta E_\alpha$ , which is the combined effect of the spin, orbital magnetic moment, and Berry curvature contributions to the net magnetic moment of the band states [8].

$$\Delta E_\alpha = \mu_B B \left[ 2 \cdot \mathbf{S}_\alpha + \mathbf{m}_\alpha + \tau \cdot \frac{m_0}{m_\alpha^*} \right] \quad (1.11)$$

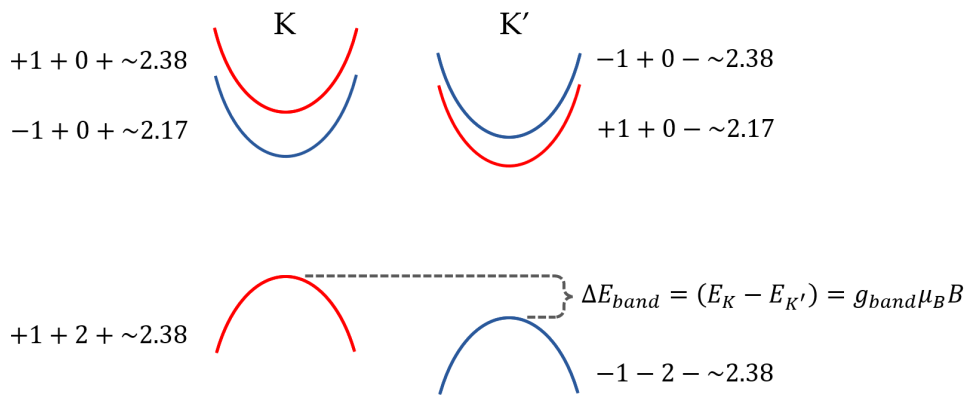


Figure 1.9: Schematic band structure of monolayer WSe<sub>2</sub> under out-of-plane magnetic field. Band shift is illustration of the valley Zeeman effect. The electron spin, orbital magnetic moment, and Berry curvature contributions to the  $g$ -factor of each band from the single-particle model are labeled. The upper conduction subband and valence band have similar effective mass ( $m^* \approx 0.42m_0$ ) [25–27]. Our results in Chapter 4 show that the lower conduction subband has larger effective mass ( $m^* \approx 0.46m_0$ ) [28].

where  $\alpha = v_{1,\downarrow}, \dots$  is the band index,  $\mu_B = e\hbar/2m_0$  is the Bohr magneton,  $m_0$  is the electron mass, and  $B$  is the out-of-plane magnetic field strength. The first bracketed term describes the contribution of the electron spin to the total magnetic moment, where  $\mathbf{S}_\alpha = \pm 1/2$ . The second term arises from the orbital character of the band. As in our discussion of the optical selection rules, we can identify the dominant magnetic angular momentum quantum number,  $\mathbf{m}_\alpha$ , for each band from DFT calculation [6]. The final term arises from the finite Berry curvature of the band near the  $K$  ( $K'$ ) point which produces an effective magnetic moment. Here,  $\tau = \pm 1$  is the valley index of  $K$  ( $K'$ ) and  $m_\alpha^*$  is the electron (hole) effective mass.

We can thus estimate the energy shift of each band under out-of-plane magnetic field, which we illustrate in Figure 1.9. We list the spin, orbital angular momentum, and

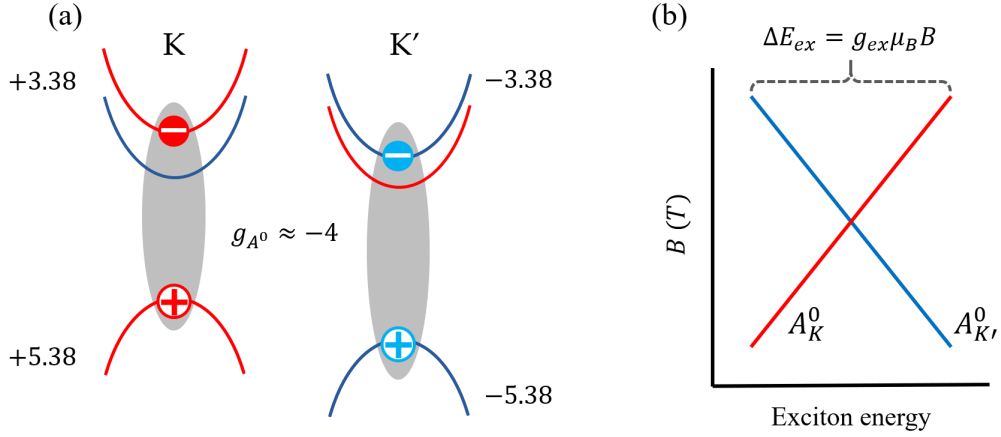


Figure 1.10: (a) Illustration of exciton valley degeneracy breaking under out-of-plane magnetic field. The total single-particle  $g$ -factor for the relevant bands are labeled. The exciton  $g$ -factor is the difference between the relative shift in each valley ( $g \approx -4$  for the  $A^0$  exciton shown). (b) Energy splitting of the  $A^0$  exciton in the  $K$  (red) and  $K'$  (blue) valleys. The magnitude of energy splitting is proportional to the exciton  $g$ -factor and magnetic field intensity.

Berry curvature contributions next to each subband. Each subband is approximately a spin eigenstate with  $\mathbf{S} = \pm 1/2$  indicated by red and blue, respectively. The conduction band is primarily composed of W orbitals  $d_0 = d_{z^2}$  with  $m = 0$ , while the valence band is primarily composed of W orbitals  $d_{+2} = 1/\sqrt{2} (d^{x^2-y^2} \pm id_{xy})$  with  $m = \pm 2$  for the  $K$ - and  $K'$ -valley, respectively. These first two terms are known to fairly high confidence. The final term is related to the carrier effective mass  $m^*$ . Here we assume the upper conduction subband and valence band have similar effective mass ( $m^* \approx 0.42m_0$ ) [25–27]. Our results in Chapter 4 show that the lower conduction subband has larger effective mass ( $m^* \approx 0.46m_0$ ) [28]. By convention, the valley Zeeman shift is defined in terms of a  $g$ -factor which is related to the difference in energy between corresponding bands in the  $K$ - and  $K'$ -valley as shown for the valence band in Figure 1.9.

Using the neutral exciton  $A^0$  as an example, we can see that the valley Zeeman shift necessarily breaks the exciton valley degeneracy, as well.  $A^0$  is shown for both valleys under out-of-plane magnetic field in Figure 1.10(a). If we assume that the exciton binding energy is not modified by the magnetic field, then the exciton absorption energy will shift with the difference between the conduction and valence bands. We note that this assumption is accurate only in the low-magnetic-field limit where the magnetic length  $l_B = \sqrt{\hbar/eB}$  is much larger than the exciton radius. We discuss this further in Chapter 3. Regardless,  $A^0$  will experience an energy shift of  $\pm 2\mu_B B$  in the  $K$ - and  $K'$ -valley, respectively, as illustrated in Figure 1.10(b). The total valley energy splitting of  $A^0$  will be  $\approx 4\mu_B B$  producing an exciton  $g$ -factor,  $g_{A^0} \approx -4$ . Importantly, the valley-dependent optical selection rules are maintained under out-of-plane magnetic field. As the exciton valley degeneracy is broken, we can distinguish the exciton (trion) in each valley *via* circularly-polarized optical probe.

## Chapter 2

# Sample Fabrication and Experimental Methods

### 2.1 van der Waals Heterostructure Device Fabrication

As discussed earlier, the 2D van der Waals materials have two universal, powerful traits. “Stackability”, due to their weak out-of-plane bonding relative to those in-plane, and exceptional influence of interface effects as 2D materials are essentially all-interface. Owing to these fundamental characteristics, we can fabricate optoelectronic devices with desirable properties by stacking vdW layers in a particular fashion. The layers can be assembled like building blocks and add new functionality (e.g., gate electrodes) or modify the functionality of other layers (e.g., dielectric layers, heterojunctions, moiré-pattern-based restructuring). For example, encapsulating an active layer (e.g., monolayer  $\text{WSe}_2$ ) within flakes of few-layer hexagonal boron nitride (BN) largely insulates it from environmental influence (e.g., surface

adsorbates, strain) and modifies the surrounding dielectric environment [29]. BN is a wide-bandgap insulator which can be relatively free of in-gap defect states which means that it will not directly interact with incident visible light in a substantial way and is relatively homogeneous. On the other hand, a stack of two WSe<sub>2</sub> monolayers with a small twist angle results in significant renormalization of the physical and electronic structure, essentially producing an entirely new system with its own emergent physics [30]. We can imagine, with an entire catalogue of 2D materials at our disposal, the possibility to design unique vdW material heterostructure devices which may fulfill a large range of technological and scientific needs.

We therefore need a tool which allows arbitrary stacking of vdW materials with high precision and in such a way that minimizes damage and introduction of other undesired external influences to the materials of interest. So-called “micromechanical transfer” tools have been progressively developed over the last decade and there is significant literature that illustrates noteworthy advancements in that time (e.g., development of dry-transfer method [31, 32], tear-and-stack method for twisted homostructures [33]). Broadly, the transfer microscope holds a polymer stamp which can controllably pick up and deposit 2D material flakes through the well-known dry transfer process. The microscope allows accurate placement of the 2D flakes to assemble arbitrary van der Waals structures. We discuss the details of the microscope design and transfer process as of December 2020.

### 2.1.1 Transfer Microscope Design

We first discuss the design of our transfer microscope and note several aspects which diverge from those found in literature. A photograph of the microscope and a corresponding schematic illustration are shown in Figure 2.1(a,b). The transfer stage consists of two major parts: the Base and the Transfer Arm. During transfer, the substrate onto which 2D material flakes have been exfoliated (purple, Figure 2.1(b)) is placed on the top surface of the Base and is fixed in place by vacuum. The surface has a small hole in the center which is connected to a vacuum line. Embedded within the Base are two DC resistive cartridge heaters and a thermocouple which sits very close to the top surface. The heaters and thermocouple are connected to a high-power DC voltage source and a temperature PID controller. The PID controller regulates the DC voltage output to heat the base to an input target temperature. We note that the PID is tuned to ensure sufficiently slow heating that the Base surface has roughly uniform temperature and the heaters are unlikely to be damaged. We thermally isolate the Base from the rest of the transfer assembly by mounting it on ceramic standoffs. Beneath these standoffs, the full Base stage can be freely rotated translated in plane  $(x, y)$ . Above the Base is an optical microscope assembly which images the plane parallel to the Base surface with interchangeable long-working distance objective lens (50x and 10x shown).

Between the Base and the objective lens is a Transfer Arm, which holds the polymer stamp and must be sufficiently translucent so the optical microscope can image the Base through the Transfer Arm. Conventionally, the Transfer Arm is a standard glass microscope slide; however, the thickness of the glass slide can cause significant optical ab-

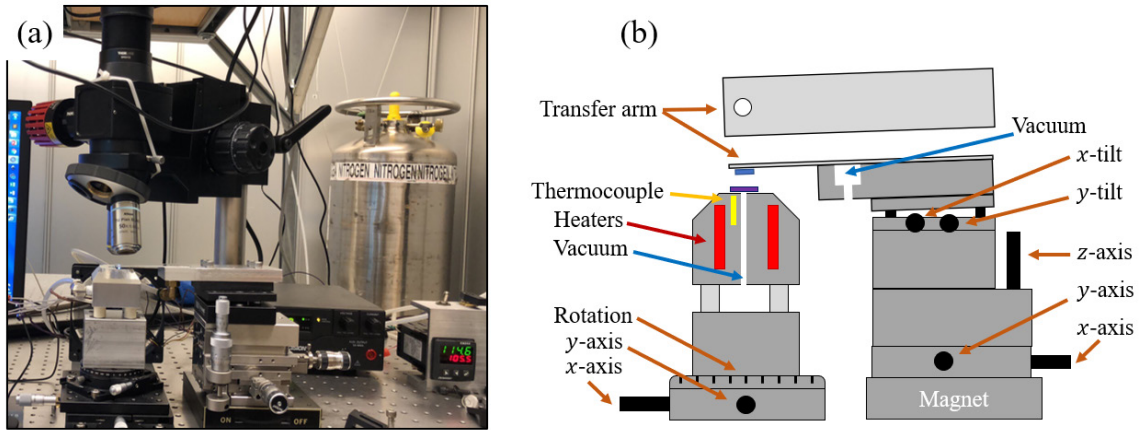


Figure 2.1: (a) Photograph and (b) schematic drawing of the transfer microscope system described in text.

berations when the microscope images through it to the Base. To alleviate this problem, we instead use a thin aluminum Transfer Arm with a small hole covered by a standard microscope cover slip. The cover slip holds the polymer stamp and is  $\approx 10\times$  thinner than a glass slide which significantly reduces the aberrations. The Transfer Arm is held in place to the larger Transfer Army assembly by vacuum. To allow high-precision alignment of the polymer stamp and the sample on the Base, and to bring the stamp into contact with the Base, the Transfer Arm assembly features a 3D linear translation stage and a tip-tilt stage. The entire Transfer Arm assembly is ultimately held in place on the optical table by a magnetic base. The magnetic can be withdrawn to allow free positioning of the Transfer Arm assembly. Altogether, the transfer assemblies allow  $\approx 1 \mu\text{m}$   $x, y$  alignment accuracy, rotational alignment, and controllable  $x, y$  tilt of the stamp relative to the Base surface.

## 2.1.2 2D Material Fabrication Process

### 2D Flake Preparation

First, the desired 2D material is exfoliated from bulk crystal (or otherwise prepared, e.g., by chemical vapor deposition) onto an initial substrate using silicone-free semiconductor tape. We note the common substrate of choice for clear optical contrast is a SiO<sub>2</sub>(250-320 nm)/Si wafer due to the strong interference of reflected visible light. Other substrates may be used, such as quartz, however sample identification may be significantly more challenging. Each of the to-be-stacked flakes is similarly prepared so that all are available prior to the transfer process. Flakes of interest on the as-exfoliated substrates are identified and imaged by optical microscopy. We image the flakes at the highest-available magnification and at least one larger scale (e.g., 100x, 10x). The high-magnification image is used for heterostructure design, e.g., by digitally overlaying images the component flakes; the low magnification image is saved to aid precise location of the flake of interest in the transfer microscope. Further imaging via dark-field microscopy is also useful to estimate the ideality of the flakes in question – this technique collects only light scattered at angles larger than the central imaging cone of the microscope objective, and thus allows identification of “roughness” in a flake due to wrinkles, bumps, and other inhomogeneities in the ideal 2D plane. Flake edges and steps can also be distinguished.

We note, as well, that post-exfoliation treatment can be critical to achieving the highest quality vdW heterostructures, but optimal procedures vary significantly from material to material. Generally, we find that post-exfoliation annealing of common transition metal dichalcogenide flakes at  $T \approx 350$  K in a low pressure tube furnace with an inert

carrier gas reduces the incidence of interfacial bubbles in the final monolayer TMD heterostructure devices. Flakes may also experience noticeable aging effects with long time delay between exfoliation and use in fabrication which negatively impact heterostructure quality and transfer success, but again this varies on a per-material and per-environment basis. For most materials, storage in an inert environment is sufficient.

### **Polymer Stamp Preparation**

We next fabricate the polymer stamp which will be used to pick up and manipulate the flakes of interest. This stamp consists of two layers: a translucent, viscoelastic polymer base, e.g., polydimethylsiloxane (PDMS), and a translucent, thermoplastic polymer top layer which is soluble in a common solvent (e.g., acetone, chloroform). Choice of this top layer is important as it must controllably pick up the flakes of interest and cleanly separate from the base polymer when the final transfer step is completed. Common stamp materials are polypropylene carbonate (PPC) and poly(bisphenol A carbonate) (PC). We believe that PC is superior in most respects, but requires significantly higher temperatures throughout the transfer process as compared to PPC. Thus, PPC is preferably for materials which degrade under heating. To ensure the stamp conforms well to the flake, it is ideal to control the stamp polymer glass transition. This temperature must be above room temperature, achievable by the transfer microscope heating element, and low enough to not damage the flakes of interest. We fabricate the stamp using thin commercial PDMS as a base and PC as the active layer. A thin film of PC is prepared from liquid stock (PC in chloroform, 6% w/t) by sandwiching the liquid between two standard glass slides. The top slide is quickly removed with minimal downward pressure such that a uniform film remains on the bottom

slide. After the PC film dries, we mechanically stack it with a sacrificial PDMS layer for structural rigidity. The final stamp is formed by stacking a small square of PC film on top of fresh PDMS and placing the stamp on the Transfer Arm (cover slip) to be used.

### **Dry Transfer Procedure**

For brevity, we will describe only the first, second, and final mechanical transfer steps. The intermediate steps are largely identical to the second step. The transfer process is illustrated in Figure 2.2, but we discuss it in more detail in the text. The transfer microscope Base begins at room temperature. The substrate containing the first flake to be transferred is affixed to the Base, and the flake of interest is roughly centered in the microscope field of view by translating the Base (a). The Base is then heated to just below ( $\approx 150$  °C for PC) the glass transition temperature of the active polymer layer. The flake may need to be repositioned during or after the heating process due to the thermal expansion of the Base. The stamp is then lowered until it is very near the sample surface. We move the focal plane of the microscope to a height between the flake and the surface of the stamp. The stamp is further lowered until it intersects the current focal plane, thus controllably approaching the flake surface. This process is repeated until the stamp is immediately above, but not touching, the sample surface.

Next, the stamp is slowly contacted with the substrate. This may be accomplished by fine mechanical control or via thermal expansion of the Base. In the latter case, we use lower initial temperature of the Base to allow for the required thermal expansion without significantly exceeding the polymer glass transition temperature. For either method, we

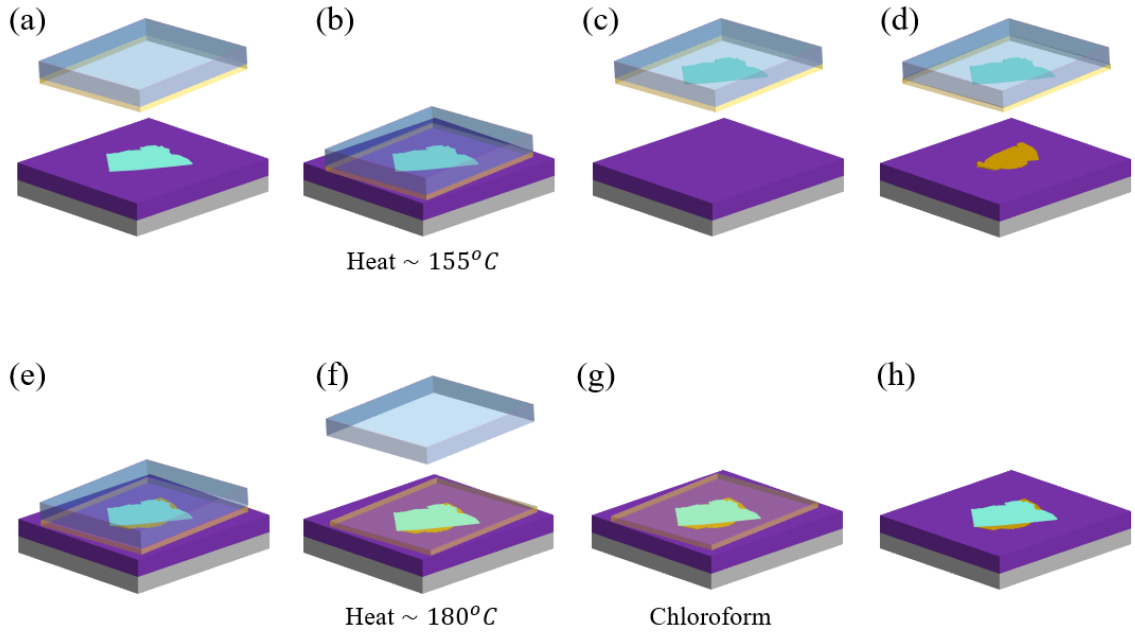


Figure 2.2: Illustration of the simple dry transfer fabrication process. (a) Polymer stamp is positioned above to-be-picked flake. (b) Stamp in contact with flake, sample heated to polymer glass transition. (c) Sample cooled, stamp lifted with attached flake. (d) Second 2D flake positioned. (e) Stamp stacks the two 2D flakes. (f) Sample is heated to high temperature to separate polymer stamp, PC left behind. (g) PC is dissolved in chloroform. (h) Completed simple stack.

attempt to contact the polymer and substrate such that the area immediately surrounding the flake of interest is covered by the stamp but contact elsewhere between the stamp and substrate is minimized. In this way we ensure good, conformed contact with the flake while minimizing the overall contact area and thus total adhesion force between the stamp and substrate. As the contact area increases, so does the difficulty in lifting the stamp from the substrate and the likelihood of other issues such as stamp tearing or flake damage. We accomplish this by tilting the stamp by  $\approx 3^\circ$  relative to the Base. This ensures that initial contact between the stamp and the substrate is along a single line with controllable position. As the stamp is brought closer to the substrate, the area of contact will expand

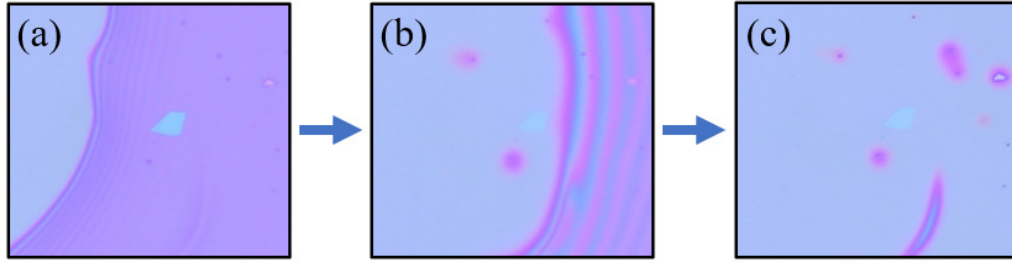


Figure 2.3: (a-c) Time series of microscope images showing the angled polymer stamp (light colored area, left side of image) slowly covering a BN flake as the polymer stamp is contacted with the sample substrate.

linearly (Figure 2.3) such that the total contact area can be controlled. This also suppresses the formation of "bubbles" in the contact area due to deformation of the polymer stamp - inhomogeneity in the stamp is naturally pressed out by the unidirectional contact spread.

While in contact with the stamp, we reduce the Base temperature below the glass transition. The stamp and attached flake are then lifted from the substrate via thermal compression of the Base or mechanical control. It is crucial to perform both the stamp contact and liftoff in as smooth and controlled a fashion as possible to minimize mechanical stress and subsequent damage to the flake. We note, as well, that BN is an ideal choice for the first flake pickup / top heterostructure layer as it has relatively strong vdW interactions with other 2D materials, is comparatively easy to pick up, and can be mostly inert to functionality of the device.

Subsequent flakes are transferred in a similar manner, but at a lower Base temperature below the glass transition. While the first layer relies solely on adhesion to the polymer stamp, subsequent flakes may be picked up via interaction with the previous layer. This is particularly true if most of the flake area is in contact with a previous layer, rather

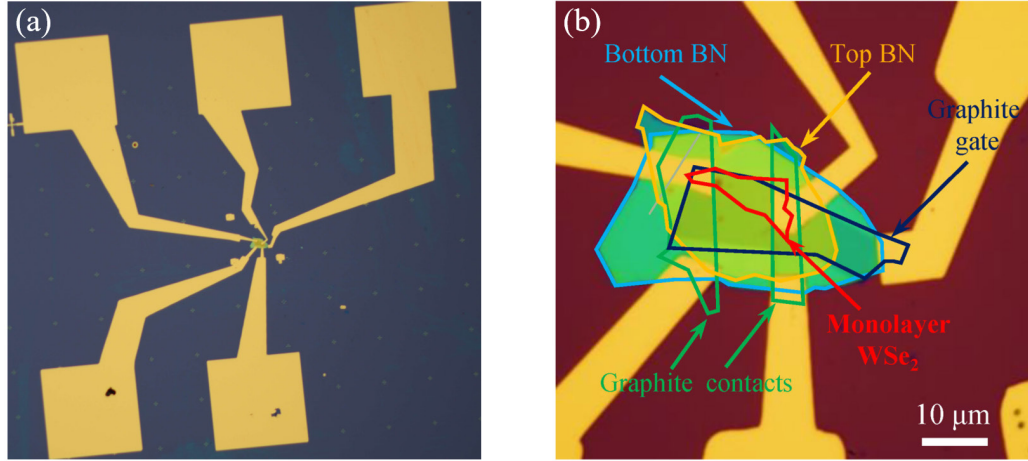


Figure 2.4: Optical image of Representative BN-encapsulated monolayer  $\text{WSe}_2$  gating device used for the experiments in Chapter 3 and Chapter 4. (a) Image showing complete device with gold contacts deposited *via* electron beam lithography and electron beam evaporation. (b) Magnified image of 2D heterostructure with constituent layers outlined and labeled. The device is composed of  $\text{BN}/\text{WSe}_2/\text{BN}/\text{FLG}/\text{SiO}_2/\text{Si}$ .

than the polymer. In the case of a small overlap with the previous layer, the heating process described in step one may be repeated; however, there is a risk of releasing those layers already picked up by the stamp. Regardless, the stamp containing the already-picked-up flakes is lowered near to the surface of the new flake. We adjust the focal plane between the stamp and the flake substrate to properly align the layers. This alignment process is repeated as the stamp is lowered to the substrate. Even with our thin stamp and substrate, there is observable distortion of the microscope image viewed through the stamp. Aligning the two flakes at a distance and blindly approaching will result in a misaligned structure.

After all layers have been sequentially aligned and picked up using the above method, the desired heterostructure is complete but suspended from the polymer stamp. As a final step, we carefully lower the completed heterostructure onto a target substrate again ensuring a smooth and controlled approach. In contrast to previous steps, we maximize

the contact area between the stamp and substrate. The Base is then heated substantially above the polymer glass transition to ensure maximum adhesion between the active polymer and the final substrate. The temperature is then lowered and the stamp lifted. The active polymer adheres more strongly to the substrate than the PDMS, thus separating the stamp and depositing the complete heterostructure and active polymer layer on the final substrate. This sample is then immersed in an appropriate solvent (e.g., chloroform for PC) to dissolve the active polymer leaving behind the completed heterostructure. Optical images of a representative BN-encapsulated monolayer WSe<sub>2</sub> gating device with few-layer graphite (FLG) contacts is shown in Figure 2.4.

## 2.2 Optical Microscope System

In this section, we provide an overview of the multi-technique experimental setup which is used for much of the zero-magnetic-field measurement. A comprehensive experimental schematic for the work in this dissertation is shown in Figure 2.5. Solid lines of various colors denote laser or broadband light pathways. Dashed lines are digital connections between electronics and the control computer. Thin black lines between components are analog electrical connections. We present a brief overview of the components used in the experimental procedures, starting with available light sources.

### 2.2.1 Light Sources

The schematic in Figure 2.5 includes three laser sources and a broadband lamp which can be used interchangeably *via* flip mirrors. Each continuous wave (CW) laser source

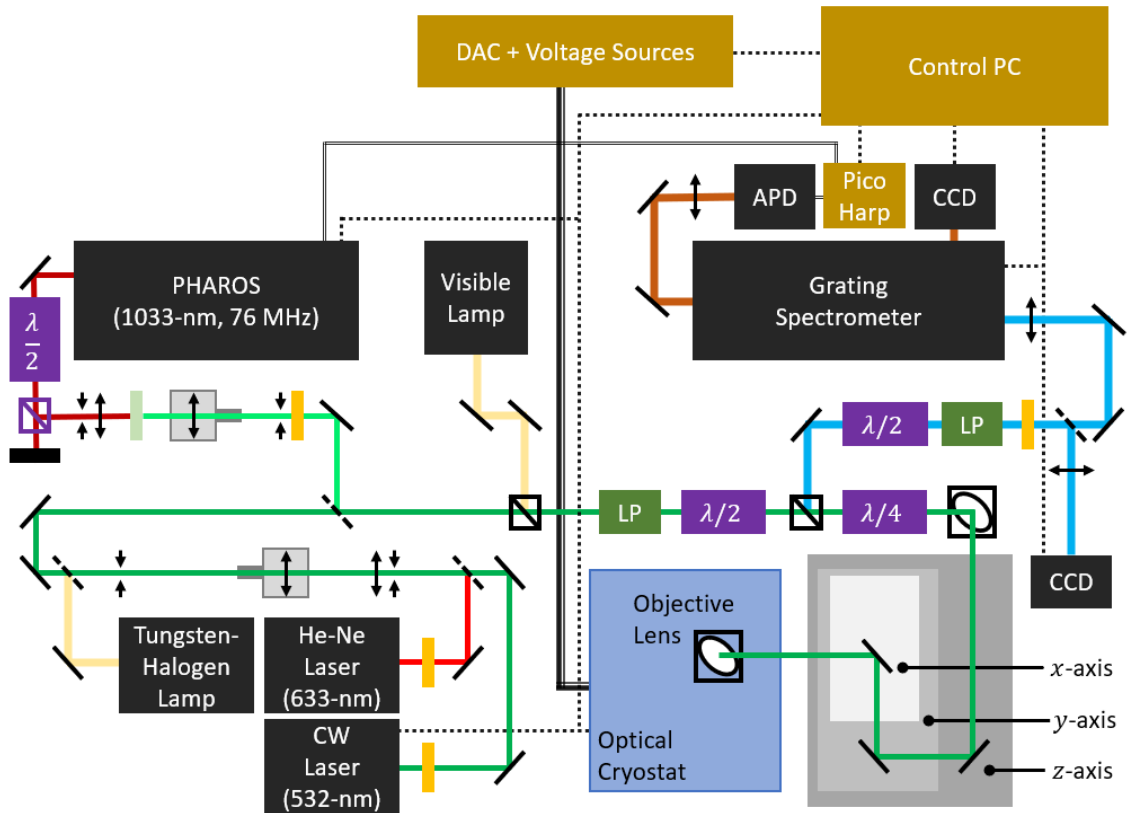


Figure 2.5: Schematic of multi-technique optical microscope system described in text. Colored lines indicate optical pathways. Angled solid (dashed) black lines are (flip) mirrors. Gold rectangles are transmissive frequency filters. Solid black lines connecting components are analog electrical connections. Dotted black lines are digital connections.

has linearly polarized emission with vertical orientation relative to the optical table, while the broadband lamp is unpolarized. Each laser source is collimated and magnified by a lens pair with adjustable separation distance.

### **Continuous-wave (CW) Laser Sources**

1. 532.14-nm continuous wave laser (torus 532, Laser Quantum)
2. 632.8-nm continuous wave helium-neon gas laser (HNL210LB, Thorlabs)

The primary emission mode of both CW lasers has narrow bandwidth, but a sharp transmissive band-pass filter (yellow rectangle, Figure 2.5) is placed immediately after the laser exit to remove any sidebands present in the emission spectrum. We note that any secondary laser emissions are exceptionally weak compared to the primary lasing wavelength. However, our experimental signals have intensity  $\geq 10^{-9}$  relative to the primary laser peak, so may have comparable intensity to even weak laser sidebands. The final intensity of each laser is controlled by reflective neutral density filters. Laser (1) has high initial output power ( $\leq 125$  mW) and features additional electronic control of the output power which may be adjusted on the laser head or *via* external computer control.

### **Ultrafast Laser Source**

1. 1030-nm, 76 MHz, 80 fs Nd:YAG oscillator (PHAROS, Light Conversion)  
(frequency doubled *via* second harmonic generation to 515-nm)

The PHAROS laser pathway shown in Figure 2.5 is the direct output of a high power oscillator ( $\approx 2.2$  W) used to pump a 250 KHz regenerative amplifier system. The power must

be immediately attenuated before continuing along the beam path for safety. The output passes first through a variable-angle half-wave plate which rotates the linear polarization and then a polarizing beam splitter which sends only the vertically polarized component along the rest of the beam path. The horizontally polarized component terminates at a beam block. In this work, we study excitons with absorption energy in the visible to near-infrared range, so we double the output frequency of the ultrafast laser by second harmonic generation (1030-nm to 515-nm). The 1030-nm laser is focused through a 1.9 mm lithium triborate (LBO; EKSPA Optics LBO-602H) crystal with type-1 phase matching between the fundamental 1030-nm pulse and 515-nm second harmonic pulse. We choose a thin crystal to minimize temporal walk-off due to group-velocity mismatch (GVM) of the fundamental and SHG pulses. This allows us to tightly focus the laser in the crystal to maximize conversion efficiency. For the same reason, we choose LBO over the more common barium borate (BBO) as it exhibits significantly lower group-velocity mismatch for SHG at 1030-nm (51 fs/mm vs. 94 fs/mm). The distance over which phase-matching between the fundamental and SHG pulses is satisfied can be approximated by the quasistatic interaction length ( $L_{qs} = \tau/\text{GVM}$ ). For SHG at 1030-nm with 90 fs pulse width  $L_{qs}$  is  $\approx 1.8$  mm for LBO and  $\approx 1.0$  mm for BBO. We therefore expect proportionately higher conversion efficiency in LBO vs. BBO. We note that LBO also exhibits reduced group delay dispersion relative to BBO which will minimize temporal broadening of the SHG pulse relative to the fundamental pulse width. Overall, we observe SHG conversion efficiency of several percent which is more than sufficient given the available pump power.

## Broadband Light Sources

1. 360- to 2600-nm stabilized tungsten-halogen lamp (SLS201L, Thorlabs)
2. Visible LED lamp (for optical sample imaging)

For continuous, broadband optical measurement in visible and near-infrared wavelengths, we use a stabilized tungsten-halogen lamp. The light is collimated immediately after the lamp by two lenses with fixed separation length in a lens tube. The lamp is an extended light source, so the first lens (aspheric condenser lens) focuses the light through a small pinhole ( $\approx 5 \mu\text{m}$  diameter) placed at the focal point to approximate a point light source. The transmitted light is then collected and collimated at a diameter  $\approx 2 \text{ cm}$  by a biconvex lens. We note that the incoherent lamp output cannot be perfectly collimated but we achieve sufficiently low beam divergence for our path length. A diffusing element can be used, as well, to produce a more uniform image at the sample plane, rather than imaging the lamp filament. To image the sample for positioning, inspection, *etc.*, we use a basic LED lamp. The lamp output is roughly collimated with a biconvex lens and is coupled into the laser beam path with a beamsplitting element to allow simultaneous imaging of the reflected laser spot and sample *via* a basic CCD camera in the detection path.

### 2.2.2 Beam Pathway, Optics

#### Excitation Pathway

Following collimation and filtering, all light sources follow the same beam pathway. The excitation beam first passes through a linear polarizer (LP) with vertical orientation relative to the optical table, then a variable-angle half-wave plate which rotates the linear

polarization. Next, the excitation beam is transmitted through an unpolarized beamsplitter followed by a variable-angle quarter-wave plate. Together, the two wave-plates can produce any polarization of the excitation beam with circular basis. In this work, we exclusively use linear and circular (right- or left-handed) polarization. For linear polarized measurement, we remove the quarter-wave plate.

The excitation beam then passes through a series of perpendicularly oriented mirrors which allow translation of subsequent mirrors without translating the relative beam spot location on each mirror. Ultimately, this allows us to translate the objective lens, which focuses the excitation beam onto the sample, in three dimensions without changing the location of the beam spot in the objective entrance aperture. To maintain the relative beam spot location on each element, *all* subsequent elements are translated identically such that translation along one axis changes only the distance between two adjacent mirrors. Each translation axis includes one less mirror. Here, the 3D translation is accomplished by a series of successively smaller optical mounts and micrometer-actuated linear translation stages stacked on each other. Thus, we mechanically translate the excitation beam focal point in three dimensions with sub-micron resolution.

The excitation light is finally focused onto the sample surface using a high numerical aperture (N.A.  $\approx 0.6$ ) dry objective lens with long working distance (Nikon). The sample is contained inside an optical cryostat (described below) with the objective lens outside, so the focused light must pass through the cryostat windows. Due to the high N.A. and window thickness, the window dispersion produces significant aberrations which degrade the optical image and greatly increase the minimum laser spot size. To compensate for

these aberrations, we use an objective lens with a *correction collar* that allows adjustment of the central lens group position within the objective.

### **Detection Pathway**

The to-be-detected signal is collected by the objective lens and follows the excitation pathway in reverse through the translation stage and quarter-wave plate. The detected light is separated by the unpolarized beamsplitter and sent along the detection pathway labeled in blue in Figure 2.5. For linear or circular polarized detection, we use a variable-angle half-wave plate and linear polarizer (LP) in series to select the desired polarization. The linear polarizer has fixed vertical orientation, so the remainder of this pathway is vertically polarized. For Raman and photoluminescence measurement, the excitation laser is higher energy and significantly more intense than the detected PL signal. We use a transmissive long-pass filter (Semrock) to remove the excitation laser which is reflected onto a beam block to minimize scattered light. Immediately afterwards, a flip mirror is available to direct light towards a USB CCD camera which can image the sample. Finally, the detected light is focused into the entrance slit of a spectrometer (SpectraPro HRS 300, Princeton Instruments) which contains three diffraction gratings on a controllable turret. The monochromator has two exit slits which may be chosen by a computer-controlled mirror. A thermoelectric cooled CCD array (PIXIS 400BRX, Princeton Instruments) is mounted at the primary exit. The monochromator and CCD are controlled and calibrated by software (LightField, Princeton Instruments) for straight-forward spectral measurement. The secondary monochromator exit focuses the detected light within a chosen spectral window onto a single-element, single photon avalanche photodiode (APD; PDM Series, Micro Photon Devices).

### 2.2.3 Sample Stage, Electrical Interface

The sample is contained within a closed-cycle, low-vibration optical cryostat (Cryostation, Montana Instruments) with computer-controlled base temperature from 4 K to 350 K. The cryostat has two  $\text{CaF}_2$  windows: one exterior window and a second window in the interior heatshield. The 2D material device is mounted on a custom sapphire chip carrier which is placed close ( $\leq 2$  mm) to the inner surface of the heatshield window. We note that the true minimum sample temperature is higher than the base cryostat temperature of 4 K, likely due to reduced cooling power through the chip carrier. The chip carrier is connected to electrical feedthroughs in the cryostat through which we can apply and detect voltages from external electronics (DAC, voltage sources; National Instruments, Keithley Instruments) *via* computer control. The 2D device is wire-bonded to the chip carrier.

### 2.2.4 Measurement Automation

As some measurements require high acquisition rate (or, inversely, long total exposure time), we use software automation *via* LabVIEW and python for unattended control. For the research shown throughout this work, we use simple automation scripts which simultaneously control the DAC/Voltage Sources (National Instruments, Keithley) and Spectrometer/CCD Array (Princeton Instruments) for unattended gate-dependent measurement. For clarity, the gate-dependent measurements are conducted by sweeping the gate voltage at a fixed rate in equally-spaced voltage steps. At each step, the spectrometer entrance shutter and CCD acquisition are triggered for a set integration time *via* the Light-Field software API. The acquired spectrum is then read into the program memory. For the

small single-gate maps in this work ( $\leq 1200$  lines) it is sufficient to keep the entire map in memory and write an output file upon completion. We do note that our lab automation efforts include most of the major instrumentation and optomechanics in the lab but these capabilities were not utilized in this work.

## 2.3 Magneto-Optical Experiment

The magneto-optical data in this work was wholly collected at the National High Magnetic Field Laboratory (NHMFL) DC Field Facility in Tallahassee, FL over four user weeks from August 2019 to January 2020. We used two magneto-optical systems at the NHMFL whose experimental configuration we discuss here briefly.

### 2.3.1 31-T Resistive Magnet

Figure 2.6 illustrates the fiber-based optical path in this setup. First, the excitation laser is focused into a single-mode optical fiber which carries it into the sample chamber where the light is recollimated, sent through a transmissive laser line filter, 50/50 beam splitter, and then quarter waveplate which converts the linearly polarized excitation laser to circularly polarized with fixed helicity. The light is finally focused onto the sample using a cryogenic objective lens with N.A.  $\approx 0.67$ . The wider spectrum of emitted light (photoluminescence) is collected by the same objective lens, and passes through the quarter waveplate which converts right- (left-) handed circularly polarized PL to vertical (horizontal) linear polarization. The collected light then passes through the beam splitter and a low-pass transmissive long pass filter to remove the reflected excitation light. The collected

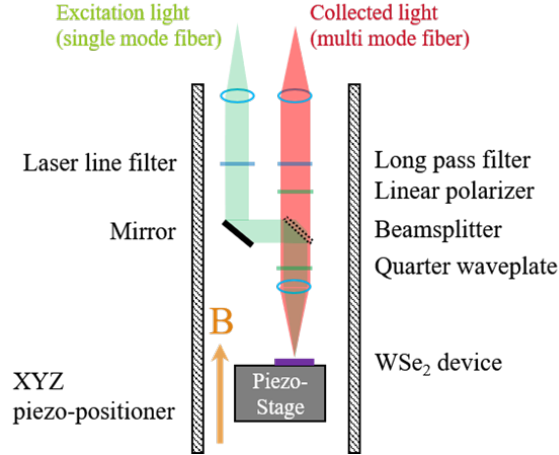


Figure 2.6: Fiber-based probe setup for photoluminescence (PL) measurement under high magnetic field. Cell 9, National High Magnetic Field Laboratory.

light is then focused into a multimode optical fiber to exit the cryostat. Outside of the cryostat, the light exits the optical fiber, passes through a linear polarizer, and is focused into spectrometer (Princeton Instruments ISOPlane 320) with charge coupled device (CCD) camera to measure the PL spectrum.

The sample device was mounted in a custom optical insert provided by the NHFML. The long insert arm carries the fiber-optic and electrical cables into the sample chamber of the cryostat. Sample positioning and focusing is enabled by an XYZ open-loop piezoelectric positioner (attocube) which holds the sample using a commercial chip carrier and socket. The cryostat uses a  $\text{He}^3$  exchange gas and thus easily achieves sample temperature  $T \leq 5$  K even under moderate laser irradiation. The magnet used here is a high power DC resistive magnet which produces fields up to 31-T. For all measurements our sample was oriented perpendicular to the magnetic field direction.

We make three notes with regard to this experimental setup. First, it exhibits exceptional sample stability at constant temperature and magnetic field – we were unable to observe any appreciable sample drift under these conditions. When sweeping the magnetic field, however, we noticed significant sample drift which required careful correction using the piezoelectric positioners. We attribute this behavior to a magnetic-field-induced force on some components (e.g., chip carrier) which causes slipping of the piezoelectric stage. This conclusion is supported by the exaggerated or unpredictable motion of the piezoelectric stage immediately after or during magnetic field sweep, the effects of which diminish quickly at constant magnetic field. Second, the optical setup is hard-wired for laser spectroscopy experiment. The single-mode fiber which carries the excitation light supports a limited spectrum and the TFF is fixed in the interior optical probe. Thus, we were unable to conduct complimentary broadband reflectance measurements due to experimental limitation. Finally, use time of the magnetic field is limited by power consumption - we are provided a power budget by the facility which can be used over one week. As a rough approximation, this entire power budget could be used in 9 hours of operation at the highest magnetic field (31-T). Thus, it was not feasible to conduct detailed gate-dependent PL mapping at constant high magnetic field as one such map can take several hours to acquire.

### **2.3.2 17.5-T Superconducting Magnet**

Figure 2.7 illustrates the free-space optical path in this setup. In contrast to the fiber-based configuration in Cell 9, the top and bottom of the Cell 3 magneto-cryostat bore feature transmissive windows so all optical elements besides the objective lens are outside of the cryostat on a standard optical table. For PL, the essentials are largely the same:

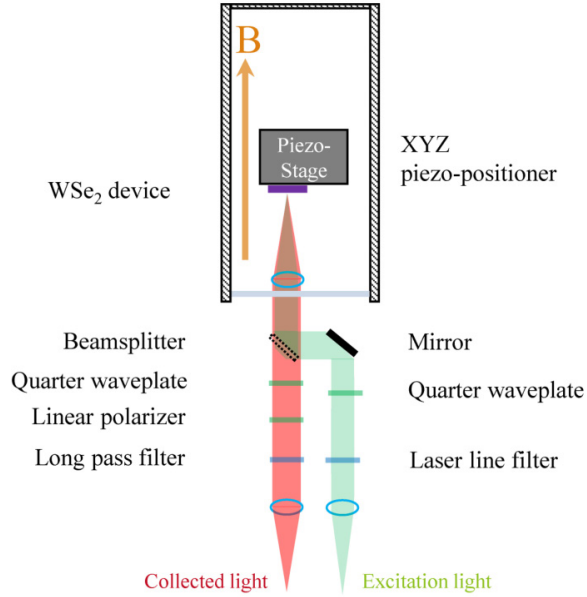


Figure 2.7: Free-space coupled setup for photoluminescence (PL) and reflectance measurement under high magnetic field. Cell 3, National High Magnetic Field Laboratory.

the excitation laser is first collimated and cleaned with a transmissive laser line filter. The laser then passes through a half-wave plate, then beamsplitter, and quarter-wave plate for circular polarization. The excitation laser is finally reflected vertically into the bore of the magneto-cryostat and aligned with an internal objective lens which focuses the light onto the sample. The same objective lens collects the signal light which follows an identical path in reverse out of the magneto-cryostat. The collected light passes through the quarter-wave plate, then beamsplitter, and linear polarizer. Finally, the collected light passes through a transmissive long pass filter which removes the reflected higher-energy excitation light and is focused into a multimode optical fiber which carries the signal into a spectrometer with CCD array (Princeton Instruments) for spectral measurement.

The sample device was mounted in a custom optical insert provided by the NHFML. The long insert arm carries the fiber-optic and electrical cables into the sample chamber of the cryostat. Sample positioning and focusing is enabled by an XYZ open-loop piezoelectric positioner (attocube) which holds the sample using a commercial chip carrier and socket. The cryostat uses a He<sup>3</sup> exchange gas and thus easily achieves sample temperature  $T \leq 5$  K even under moderate laser irradiation.

We make several notes about this experimental setup in contrast to the Cell 9 system. First, the open-bore configuration with free-space coupling to the internal objective lens allows significantly higher degree of experimental flexibility. In this system, both PL and reflectance contrast measurements are straightforward from an optics standpoint and it is feasible to conduct much more involved optical experiment (e.g., ultrafast). This is the benefit of the open-bore configuration. We note that this does come with drawbacks - the observed stability of the system is highly variable in terms of the beam spot location. The excitation laser must travel several meters through the microscope bore from the optical table to the internal objective lens. Thus, small variations in the angle or position of the cryostat optical probe due to thermal cycling or magnetic-field-induced force can have significant effects on the focusing conditions. This was the largest experimental hurdle to conducting comprehensive gate-dependent PL and reflectance mapping in this facility as it required active sample repositioning with the open-loop piezoelectric stage to maintain constant focal position.

## 2.4 Reflection-Contrast Spectroscopy

From the theoretical discussion in Chapter 1, we see that each exciton exhibits a peak-like resonance in the material absorption spectrum. For this reason, we seek to measure the absorption spectrum (equivalently, the optical conductance) of the target material as directly as possible to characterize the exciton resonance. The absorption is not a directly observable quantity, but it is closely related to the optical transmission and reflectance which are experimentally observable. If we completely isolate the partially transparent monolayer TMD, for example by suspension in vacuum, we can shine a broadband lamp directly onto the material and easily measure the transmitted and reflected power for each photon energy. Thus, we simply obtain the absorption spectrum. Due to experimental constraints (e.g., opacity of the sample substrate, sample mounting configuration), however, it is much more difficult to measure the transmitted spectrum than the reflected spectrum. Thus, we would prefer to use the reflected spectrum, alone, to characterize the material absorption.

For an isolated thin film of a single material, the qualitative relationship between the absorption and reflection spectrum is straightforward. A peak in absorption (Figure 2.8(a)) corresponds to a similar peak in the reflection spectrum (Figure 2.8(b), green). In reality, our gating device is not an isolated monolayer - it is a multilayer thin film structure composed of a 2D heterostructure (WSe<sub>2</sub>, BN, FLG) on a SiO<sub>2</sub>/Si substrate. Thus, the reflection spectrum will be complicated by significant interference effects. The reflection spectrum for the same peak-like absorption in Figure 2.8(a) is shown by the black line in Figure 2.8(b) for an example device structure. We note that the shape and intensity of the reflection spectrum is highly dependent on the dielectric function and thickness of each ma-

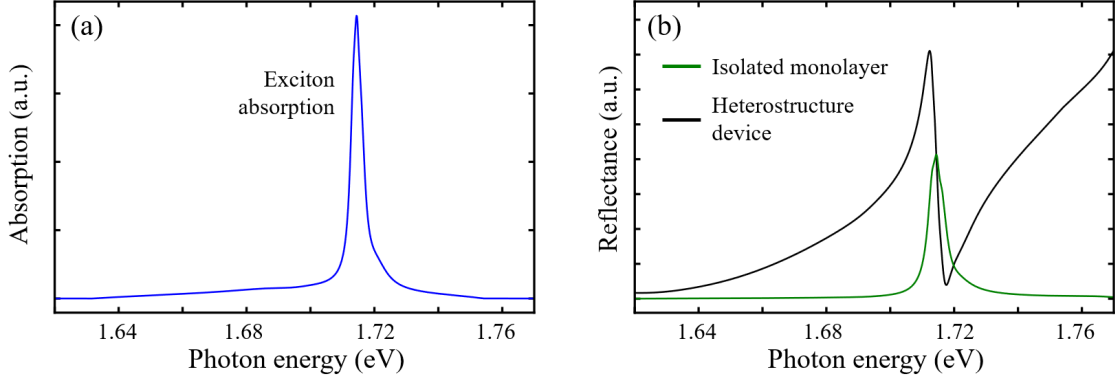


Figure 2.8: (a) Example absorption spectrum of monolayer WSe<sub>2</sub> in the vicinity of the A<sup>0</sup> exciton. (b) Corresponding reflectance contrast spectra calculated numerically from the absorption spectrum in (a) for a monolayer suspended in vacuum (green line) and a monolayer embedded in a realistic heterostructure (black line) of BN(20 nm)/WSe<sub>2</sub>/BN(40 nm)/FLG(8 nm)/SiO<sub>2</sub>(285 nm)/Si.

material in the sample. Regardless, the interference effects complicate quantitative analysis of the reflection spectrum but qualitative analysis of each "peak" is still fairly straightforward. We discuss a numerical approach to quantitatively analyze these reflection spectra later in this section.

A second complication is knowledge of the exact spectrum of the incident light whose reflected spectrum is measured. Experimentally, we measure the reflection spectra by illuminating the sample with a broadband light source and simultaneously measuring the complete reflection spectrum with a spectrometer and CCD array. The reflection spectra in Figure 2.8(b) are relative reflected power at each photon energy. To avoid this issue and maximize the signal contribution from the desired layer in the heterostructure sample we can normalize the reflected spectra measured at two spatial locations on the sample. This is *reflection contrast* spectroscopy. Specifically, we measure the reflected spectrum at two locations on each sample: first, including the entire heterostructure device; second, including

the entire heterostructure *minus* the layer of interest. We refer to the second spectrum as the *reference*. For the monolayer WSe<sub>2</sub> gating device, the WSe<sub>2</sub> is the layer of interest. We measure the reflected spectrum of the full heterostructure (BN(20 nm)/WSe<sub>2</sub>/BN(40 nm)/FLG(8 nm)/SiO<sub>2</sub>(285 nm)/Si) and the reference spectrum (BN/BN/FLG/SiO<sub>2</sub>/Si) which are shown in Figure 2.9(a) in black and red, respectively. The reflection contrast is found by the difference between the two spectra divided by the reference spectrum,  $\Delta R/R$ . We plot the reflection contrast thus obtained from Figure 2.9(a) in Figure 2.9(b).

### **Gate-Dependent Reflection-Contrast Spectroscopy**

To explore the charge-density-dependent exciton behavior in our monolayer WSe<sub>2</sub> gating device, we perform the above reflection-contrast measurement while varying the applied gate voltage. The gate voltage is varied between a maximum and minimum value in evenly-separated steps where a sample (full heterostructure) reflection spectrum is measured for each gate voltage step. A representative raw gate-dependent reflection map and the corresponding reflection-contrast map are shown in Figure 2.9(c,d), respectively. We note that the most rigorous approach requires measuring a reference spectrum for each gate voltage step, but we do not find that the reference spectra change significantly with gating in our monolayer WSe<sub>2</sub> gating device. Moreover, translating the measurement location back and forth between sample and reference locations results in a noticeable reduction in data quality due to accumulated positioning error and sample inhomogeneity. This decision should be evaluated on a system-by-system basis.

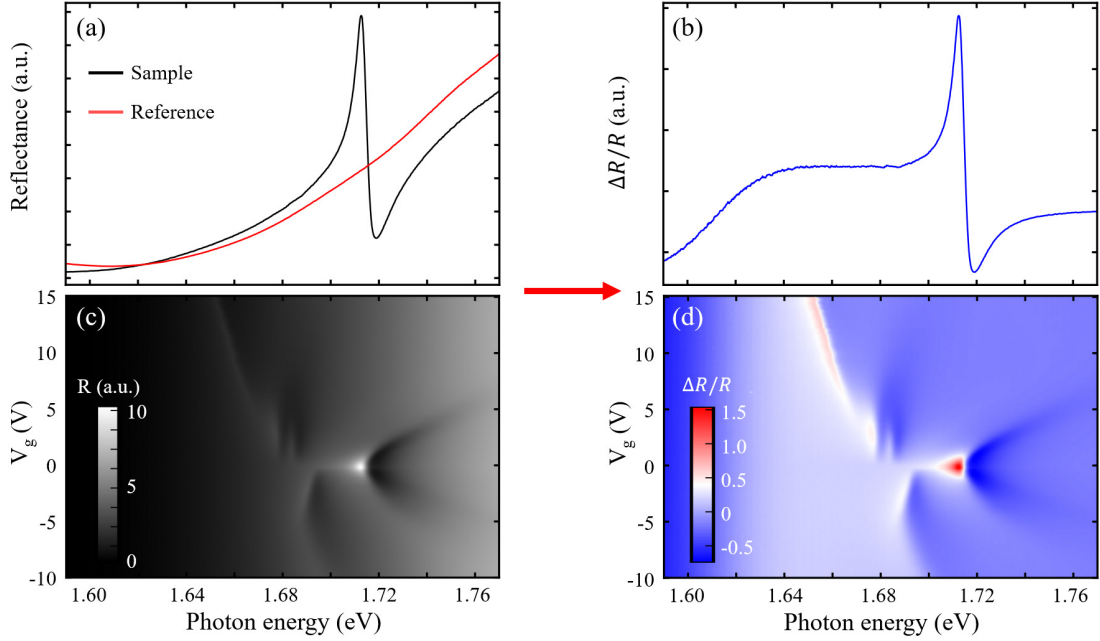


Figure 2.9: (a) Reflection spectra of a complete heterostructure (black line) and reference location (red line) without the semiconductor layer. (b) Reflection contrast spectrum calculated from the signal and reference spectra in (a). (c) Gate-dependent map of raw signal reflectance spectra (as in black line, (a)). (d) Gate-dependent map of reflectance contrast spectra generated from (c) and the reference spectrum in (a).

## 2.5 Quantitative Analysis of Reflection-Contrast Spectra

As mentioned above, quantitative analysis of our experimental reflection-contrast spectra is complicated by significant interference from the multi-layer sample structure. The problem of thin film interference is well-studied and can be found in electromagnetic texts, though, and can be easily applied to our sample system if we treat it classically. From a calculation perspective, the transfer matrix formalism for thin-film interference is particularly convenient. If the properties of each constituent layer in the thin film structure are fully specified, as well as the incident light spectrum, the reflected and transmitted spectra may be easily determined. With regard to our experimental heterostructure, we

ideally know the relevant properties of all but one unknown layer (or set of layers). Due to the interaction between layers, this is not strictly true, but it is a reasonable assumption if the relative interaction-induced change of the optical properties is not significant. We may then “guess” the optical properties (dielectric function) of the unknown layer and calculate a “test” reflection spectrum to be compared with our experimental data. The optical properties may then be optimized *via* non-linear least squares such that the calculated and experimental spectra are identical. Thus, the unknown optical properties are estimated.

### 2.5.1 Transfer-Matrix Formalism for Thin-Film Interference

Before discussing the details of our experimental analysis technique, we briefly summarize the transfer matrix formalism used to calculate thin-film interference spectra [34]. We assume a system of infinite, uniform thin films stacked in the  $z$  direction where we define  $z = 0$  as the first (top) surface. The incident light is approximated as plane waves, such that the electric field at any position  $z$  is the sum of forward and backward propagating plane waves.

$$E(x, y, z) = E_F(z)e^{-ik_x x} + E_B(z)e^{ik_x x} \quad (2.1)$$

In the simplest case of a single interface between two media, the forward and backward propagating waves before ( $z = 0$ ) and after ( $z = \delta$ ) the interface are related by a matrix operation,

$$\begin{bmatrix} E_F(z = 0) \\ E_B(z = 0) \end{bmatrix} = \hat{\mathbf{T}}_{1,2} \begin{bmatrix} E_F(z = L) \\ E_B(z = L) \end{bmatrix} = \frac{1}{t_{1,2}} \begin{bmatrix} 1 & r_{1,2} \\ -r_{1,2} & 1 \end{bmatrix} \begin{bmatrix} E_F(z = \delta) \\ E_B(z = \delta) \end{bmatrix} \quad (2.2)$$

Here,  $\hat{\mathbf{T}}_{1,2}$  is the transfer matrix which describes the interface between the two media (1,2).

The matrix elements of  $\hat{\mathbf{T}}_{1,2}$  can be expressed in terms of the Fresnel coefficients:

$$t_{ij} = \frac{2\tilde{n}_i}{\tilde{n}_i + \tilde{n}_j}, \quad r_{ij} = \frac{\tilde{n}_j - \tilde{n}_i}{\tilde{n}_i + \tilde{n}_j} \quad (2.3)$$

where  $\tilde{n}_i$  and  $\tilde{n}_j$  are the complex refractive indices of the two media, respectively. We note that the above coefficients are valid when the light is normally-incident on the interface, which is the case for our experimental backscattering geometry. We use this simple case for brevity, but expansion to the general case of arbitrary angle of incidence is straightforward. We can solve the above expressions and determine the relative reflected and transmitted power across the interface - these are the single interface Fresnel equations.

$$R = \left| \frac{r_{1,2}}{t_{1,2}} \right|^2, \quad T = \left| \frac{1}{t_{1,2}} \right|^2 \quad (2.4)$$

Our device structure is composed of many layers with finite thickness, however, so we must consider the influence of multiple interfaces and the accumulated phase,  $\phi$ , of the plane waves as they propagate through the bulk of each layer. Similar to interface treatment above, we can relate the electric fields at position  $z$  and  $z + \delta$  within the same medium by a matrix:

$$\begin{bmatrix} E_F(z) \\ E_B(z) \end{bmatrix} = \begin{bmatrix} e^{i\phi} & 0 \\ 0 & e^{-i\phi} \end{bmatrix} \begin{bmatrix} E_F(z + \delta) \\ E_B(z + \delta) \end{bmatrix}, \quad \phi = \frac{2\pi}{\lambda_0} \tilde{n} \delta \quad (2.5)$$

where the accumulated phase,  $\phi$ , is related to the vacuum wavelength,  $\lambda_0$ , and the complex index of refraction,  $\tilde{n}$ . Totally, we have two expressions with transfer matrices which relate the electric field as it propagates through interface and bulk media. For a series of stacked layers with finite thickness, the total transfer matrix for the multilayer system is simply the sequential product of the individual interface and bulk transfer matrices.

Thus, the electric field on either side ( $z = 0, z = L$ ) of the complete thin film structure with  $N$  layers and total thickness  $L$  are related by:

$$\begin{bmatrix} E_F(z = 0) \\ E_B(z = 0) \end{bmatrix} = \hat{\mathbf{T}}_{0,1} \hat{\mathbf{T}}_1 \hat{\mathbf{T}}_{1,2} \dots \hat{\mathbf{T}}_{N-1} \hat{\mathbf{T}}_{N-1,N} \begin{bmatrix} E_F(z = L) \\ E_B(z = L) \end{bmatrix} = \hat{\mathbf{T}}_{0,N} \begin{bmatrix} E_F(z = L) \\ E_B(z = L) \end{bmatrix} \quad (2.6)$$

Finally, we can solve for the relative reflected ( $R$ ) and transmitted ( $T$ ) power for the complete  $N$ -layer thin film system in terms of the matrix elements of the transfer matrix.

$$R = \left| \frac{\hat{\mathbf{T}}_{0,N}^{1,2}}{\hat{\mathbf{T}}_{0,N}^{1,1}} \right|^2, \quad T = \left| \frac{1}{\hat{\mathbf{T}}_{0,N}^{1,1}} \right|^2, \quad (2.7)$$

For a system of fully defined thin films, calculation of reflection spectra by the above method is trivial. The transfer matrices are wavelength dependent, both directly ( $\lambda_0$ ) and in the wavelength-dependent refractive indices  $\tilde{n}_i(\lambda_0)$  for the involved media. We calculate the transfer matrix for each wavelength in the desired spectrum, from which we determine the relative reflected power. The only parameters required are the complex refractive index and thickness of each layer. In our experimental system, most of these quantities are known within some margin of error - layer thicknesses can be measured *via* scanning probe (e.g., atomic force microscopy) technique and the wavelength-dependent refractive index of "known" layers may be measured independently or found in literature. Only the refractive index of the "active" layer (e.g, monolayer WSe<sub>2</sub>) is unknown.

### 2.5.2 Parameterization of Unknown Layer Dielectric Function

To perform non-linear optimization and thus estimate the wavelength-dependent refractive index,  $\tilde{n}_{active}$ , of the "active" layer, we must generate test reflection spectra which can be compared to experiment. In this problem,  $\tilde{n}_{active}$  is being optimized such

that the difference between the calculated reflection spectrum of the total sample and the experimental reflection spectrum (the *residual*, a 1D array) is minimized. Practically, we need to parameterize the  $\tilde{n}_{active}(\lambda_0)$  function and collectively optimize each parameter.

To generate test  $\tilde{n}_{active}(\lambda_0)$ , we use the well-known Drude-Lorentz oscillator model, which relates the complex dielectric function,  $\tilde{\epsilon} = \epsilon_1 + i\epsilon_2 = \tilde{n}^2$ , to a series of physical oscillators (e.g., exciton dipoles). Here, the imaginary component of the dielectric function,  $\epsilon_2(\omega)$ , is given by the sum of peak-like (e.g., Lorentzian) functions, where each function ideally corresponds to one physical oscillator. The real component,  $\epsilon_1(\omega)$ , is then found by Kramers-Kronig relations. The complex dielectric function is therefore:

$$\tilde{\epsilon}(\omega) = \epsilon_1 + i\epsilon_2 = 1 + \sum_i \frac{\omega_{p,i}^2}{\omega_{0,i}^2 - \omega^2 - i\omega\gamma_i} \quad (2.8)$$

$$\epsilon_1(\omega) = 1 + \sum_i \frac{\omega_{p,i}^2(\omega_i^2 - \omega^2)}{(\omega_{0,i}^2 - \omega^2)^2 + \omega^2\gamma_i^2}, \quad \epsilon_2(\omega) = \sum_i \frac{\omega_{p,i}^2\omega\gamma_i}{(\omega_{0,i}^2 - \omega^2)^2 + \omega^2\gamma_i^2} \quad (2.9)$$

The  $i$ -th oscillator in the imaginary component is described by the oscillator plasma frequency (proportional to oscillator strength),  $\omega_{p,i}$ , the oscillator frequency,  $\omega_{0,i}$ , and the oscillator linewidth (damping),  $\gamma_i$ .

Figure 2.10(a,b) depicts the imaginary ( $\epsilon_{2,i}$ ) and real ( $\epsilon_{1,i}$ ) components of a single oscillator. Figure 2.10(c,d) show the imaginary and real components for a series of oscillators. The magnitude of  $\epsilon_{2,i}$  is localized at the oscillator frequency,  $\omega_{0,i}$ . In contrast,  $\epsilon_{1,i}$  has significant magnitude over a larger energy range – particularly for  $\omega < \omega_{0,i}$ . Thus, the influence of each oscillator extends to energies significantly below its central frequency. To produce an accurate dielectric function for our experimental range of interest, then, we must include contributions from as wide an energy range as possible. In our model system of BN

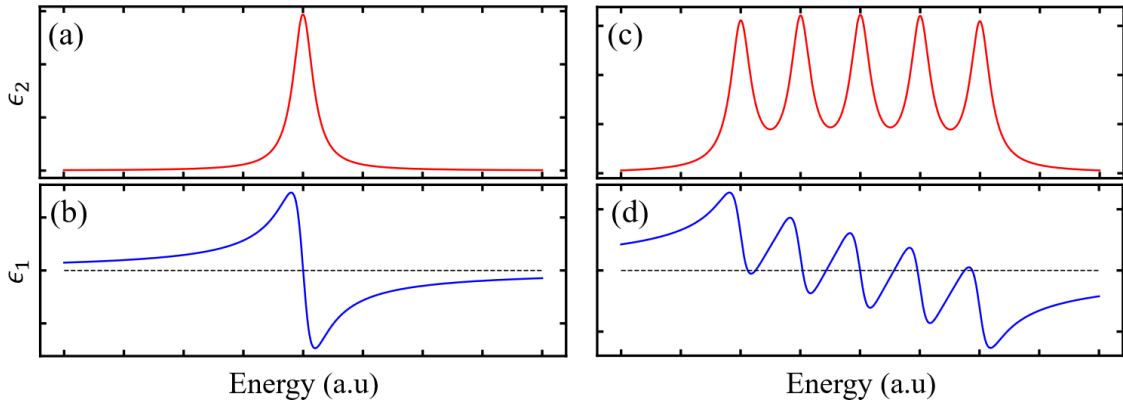


Figure 2.10: (a) Imaginary ( $\epsilon_2$ ) and (b) real ( $\epsilon_1$ ) components of the complex dielectric function for a single Drude-Lorentz oscillator (Equation 2.8). (c) Imaginary and (d) real components for a series of five oscillators.

encapsulated WSe<sub>2</sub>, such a comprehensive measurement would require reflection data in a large energy range from visible to ultraviolet. Experimental difficulty increases significantly as we widen the studied energy window. Without complete experimental data, we must approximate the contribution of oscillators outside of our experimental energy window. If we have prior knowledge of the unknown dielectric function (e.g., previous measurement, physical model), the extended spectrum can be estimated by discrete oscillators outside the measured energy range. For an oscillator distant in energy from the experimental data, however, large variation in the fitting parameters may have small or unexpected effects on the calculated reflection spectra. Without appropriate constraints, the optimization process will be unstable and likely fail. Further, we prefer to avoid excessive constraints in the fitting process as it may bias or otherwise affect the results.

Instead, we approximate the contribution of high frequency oscillators with a single fitting parameter. The low-energy tail of  $\epsilon_{1,i}(\omega)$  is approximately constant when  $\omega < \omega_{0,i} - 3\gamma_i$ . The total high energy contributions are estimated as a real constant  $\epsilon_\infty$ .

$$\tilde{\epsilon}(\omega) = \epsilon_\infty + \sum_i \frac{\omega_{p,i}^2}{\omega_{0,i}^2 - \omega^2 - i\omega\gamma_i} \quad (2.10)$$

For the remainder of this section, we use this expression to parameterize the unknown dielectric function. Finally, we must decide how many functions are necessary to fully parameterize the dielectric function and for each determine their initial parameters and any bounds.

### Defining Necessary Oscillators

In the simplest case of the neutral exciton at charge neutrality, the dielectric function is well described by a single Lorentzian function which directly corresponds to the physical exciton oscillator. This is shown clearly by comparing the calculated reflection spectrum in Figure 2.8(b, black line) with the experimental reflection spectrum in Figure 2.9(a, black line). The calculated spectrum is determined using the layer thicknesses and structure of the experimental device, and is qualitatively identical to the experimental result.

Away from charge neutrality, however, the absorption spectra may have many exciton (trion) resonances which require additional oscillators in the dielectric function to properly describe. Figure 2.11(b, black line) shows an experimental reflection contrast spectrum for monolayer WSe<sub>2</sub> with electron doping ( $V_g = 2$  V). Features which correspond to the neutral exciton ( $A^0$ ) and both electron trions ( $A_1^-$ ,  $A_2^-$ ) are present simultaneously,

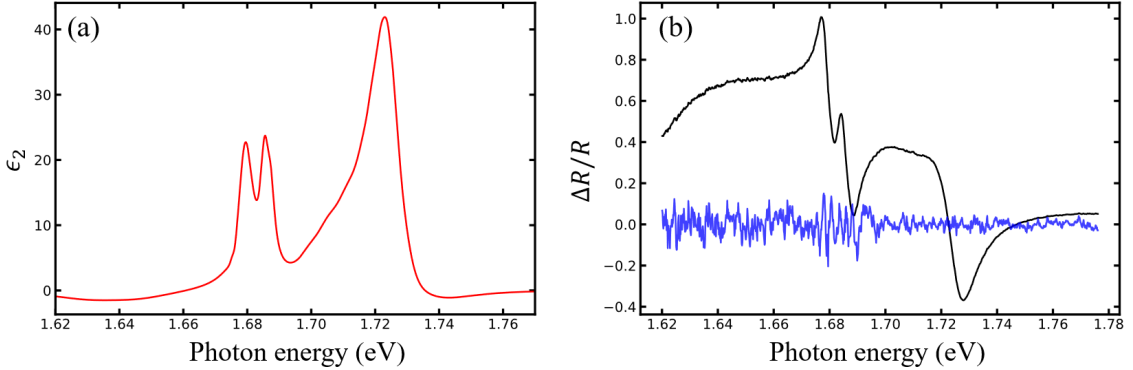


Figure 2.11: (a) Imaginary component of complex dielectric function for BN encapsulated monolayer WSe<sub>2</sub> with intermediate electron doping. Peaks correspond to exciton (1.72 eV) and electron trions ( $\approx 1.68$ ) absorption resonances. (b) Optimization of reflection contrast spectrum from experimental data (black line) for BN encapsulated monolayer WSe<sub>2</sub> with intermediate electron doping. The difference (blue line) between the experimental reflection contrast spectrum and that calculated from  $\epsilon_2$  in (a) is magnified by a factor of 10 to highlight the goodness of fit.

so the dielectric function must feature at least three oscillators. The situation is further complicated by the non-Lorentzian lineshape of these absorption features. To fully parameterize the non-Lorentzian shape, then, we must add additional Lorentzian oscillators which may sum together to form arbitrary line shape. For example, Figure 2.11(a) shows  $\epsilon_2$  for monolayer WSe<sub>2</sub> with electron doping ( $V_g = 2$  V) and is totally composed by the sum of  $\approx 20$  Lorentzian functions of varied width and intensity. The additional parameterization results in good fits to our experimental data. Figure 2.11(b, blue curve) shows the difference between the experimental reflection contrast spectrum and the spectrum calculated from Figure 2.11(a).

Unfortunately, this choice decouples the Lorentzian functions which parameterize the dielectric function from physical oscillators - for example, a trion absorption resonance may be described by the sum of five Lorentzian functions rather than one. This as a

reasonable trade-off as the exciton (trion) absorption features with arbitrary line shape can be quantitatively analyzed separately after the dielectric function is obtained. We finally note that the choice of Lorentzians as the basis functions for parameterization of  $\epsilon_2$  is somewhat arbitrary -in principle we can use as a basis any function with finite area. However, we find that the Lorentzian functions give good results with a low number of total fitting parameters and minimal fitting error. We note that this solution is sufficient for our purposes as we need  $\leq 20$  oscillators to describe our data. A more robust expanded approach for fine analysis is discussed by Kuzmenko. [35]

### 2.5.3 Optimization of Dielectric Function *via* Nonlinear Least-squares

The fitting process used here is a standard non-linear least squares fitting implemented in python using the lmfit package. We define a custom model function where the residual is the difference between the calculated and experimental reflection contrast spectra. The fitting parameters are the characteristics of each Lorentzian function from Equation 2.10:  $\omega_{p,i}^2$ ,  $\gamma_i$ , and  $\omega_{0,i}$  and the high frequency constant,  $\epsilon_\infty$ . We define upper and lower bounds based on reasonable physical constraints for each fitting parameter to reduce the search space of the fitting algorithm, reduce fitting time, and avoid instabilities. We note that the amplitude ( $\omega_{p,i}^2$ ) is allowed to have a negative value to better fit arbitrary functions with fewer parameters. This seems very unphysical, but as mentioned above we have disconnected the Lorentzians from physical oscillators so it is not unreasonable so long as  $\epsilon_2$  remains positive.

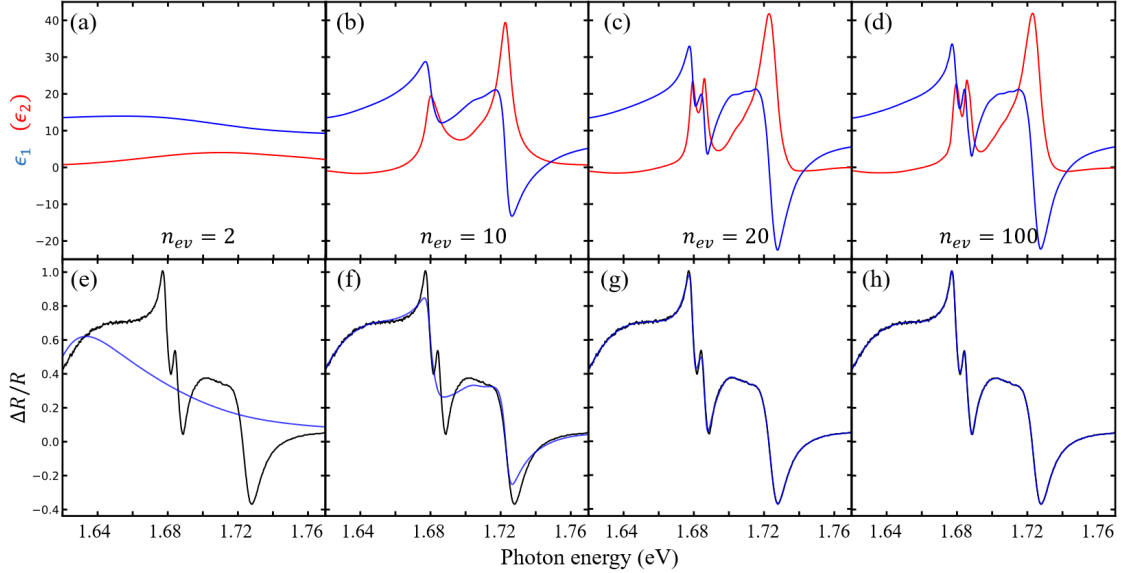


Figure 2.12: Optimization of the BN-encapsulated monolayer WSe<sub>2</sub> dielectric function at intermediate electron doping optimized using the described fitting procedure. (a-d) Optimized real and imaginary components of monolayer WSe<sub>2</sub>, (e-h) comparison of experimental reflectance contrast (black line) and calculated reflectance contrast (blue line) for increasing number of regression model evaluations.

For each model evaluation step, a reflection contrast spectrum is calculated given the test dielectric function and known characteristics of the layered structure (layer thickness, known dielectric functions of other layers). The fitting parameters are then optimized at each model step to minimize the residual using the least\_squares method in the scipy package. The optimized dielectric function for monolayer WSe<sub>2</sub> in the gating device (BN(20 nm)/WSe<sub>2</sub>/BN(40 nm)/FLG(8 nm)/SiO<sub>2</sub>(285 nm)/Si) is shown in Figure 2.12(a-d) for increasing optimization steps. As shown by the  $n_{ev} = 2$  panel, the initial conditions for the dielectric function is a series of broad features which produce a relatively flat spectrum. The optimized function quickly converges towards a peak like spectrum after a small number of evaluations; however, fine matching requires significantly more model evaluations. The corresponding experimental (black curve) and calculated reflection contrast spectra for

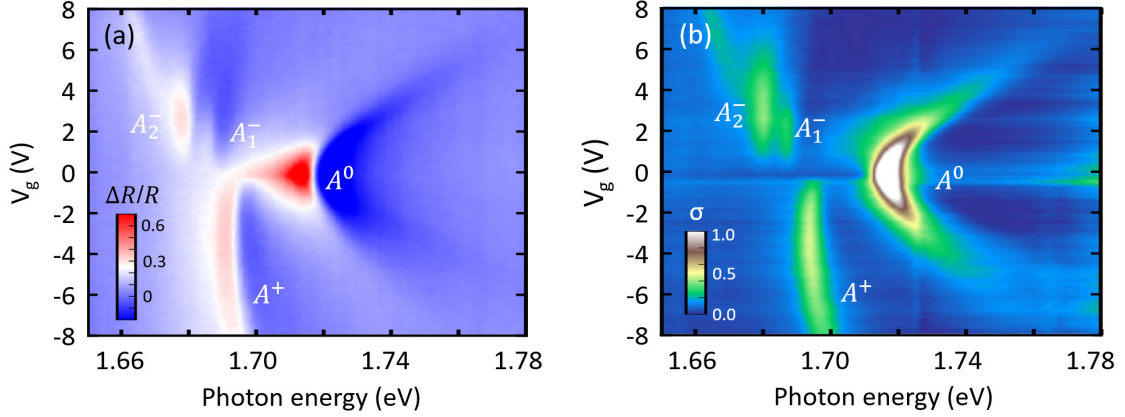


Figure 2.13: (a) Gate-dependent reflection contrast spectrum for monolayer WSe<sub>2</sub> gating device. (b) Gate-dependent optical conductance map generated from (a) using the described fitting procedure.

increasing model evaluation steps are shown in Figure 2.12(e-h). By  $n_e v = 100$ , the experimental and calculated reflection contrast spectra are nearly identical. Finally, we terminate the optimization when the relative change in the residual drops below a cutoff value.

We apply this optimization process to the gate- and magnetic-field-dependent reflection contrast data to produce two-dimensional maps of the monolayer WSe<sub>2</sub> optical conductivity. The process is identical for all spectra with the exception of the initial dielectric function. For example, in a gate-dependent map, we process the spectra sequentially in order of gate voltage. To minimize fitting time for successive gate voltages where the reflection contrast spectrum does not change enormously we use the optimized dielectric function from the previous gate voltage as the initial guess of the current spectrum. To avoid premature termination, we slightly perturb this initial dielectric function. An example gate-dependent reflection contrast map and corresponding optical conductance map generated from this fitting process are shown in Figure 2.13(a,b), respectively.

## 2.6 Photoluminescence Spectroscopy

In contrast to the reflection measurement which resonantly probes direct optical transitions, photoluminescence (PL) measures radiative relaxation. We are concerned with the behavior of excitons in monolayer WSe<sub>2</sub>, so we will briefly discuss the photoexcitation and radiative relaxation process in this class of 2D semiconductor. For PL, we excite the system with a narrow bandwidth laser source and collect the light radiated from the sample over a broad spectrum. There are thus two modes of photoexciting the exciton states: resonant and non-resonant. In this work we primarily use non-resonant excitation, where the photon energy of the laser source is higher than the resonant absorption energy. In the single-particle picture, a photon with above-gap energy is absorbed and photoexcites a hot electron-hole pair to states with energy above the band gap. The hot electron and hole will cool and relax towards the energy minimum (e.g., conduction (valence) band minima (maxima) through carrier-carrier and carrier-phonon scattering. As in the resonant process, the electron-hole pair can form an exciton state which itself will relax further towards the lowest energy state.

Depending on the state in question, the exciton may relax non-radiatively to another exciton state (or to the ground state *via* Auger scattering) [7] or radiatively to the ground state (annihilation) and emit a photon with energy corresponding to the recombination energy. We note that the exciton recombination energy and absorption energy need not be the same. The photoluminescence and excitation processes may differ and the resonantly excited exciton state may not be the minimum energy state. Experimentally, we collect the emitted photons to measure a PL spectrum. Each exciton emission process will emit light

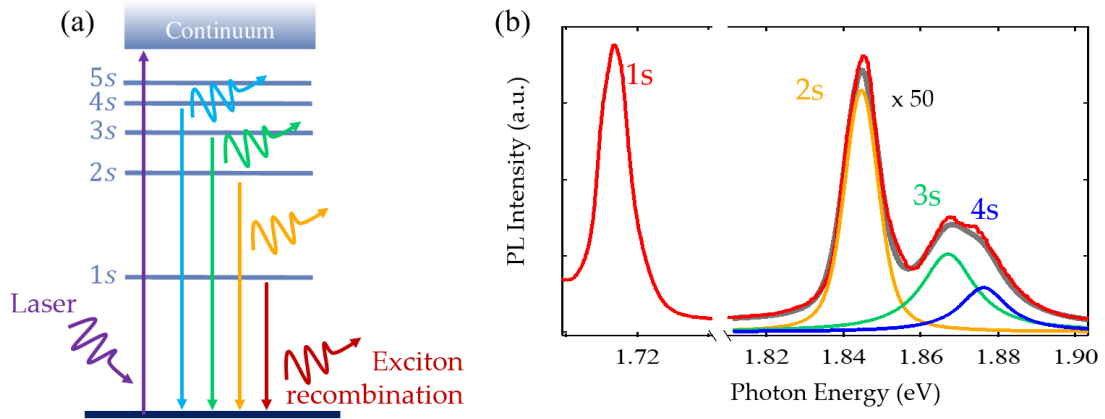


Figure 2.14: (a) Schematic of internal  $s$ -series Rydberg-like energy levels of the  $A^0$  exciton in monolayer  $\text{WSe}_2$ . (b) Experimental photoluminescence spectrum which shows contributions from the  $1s$  to  $4s$   $A^0$  exciton states. Each PL peak is fitted using a Lorentzian function.

with a peak-like spectral distribution (e.g., Lorentzian). Thus, the total PL spectrum is the sum of individual peak-like spectra from each exciton which can recombine radiatively. Importantly, the exciton radiative recombination is controlled by the same optical selection rules as the absorption process which we derive in Chapter 1 but the intensity depends on both the exciton oscillator strength *and* the steady-state exciton population. [7]

As an example, we show the  $s$ -series of internal exciton energy levels of the bright neutral exciton ( $A^0$ ) in Figure 2.14(a). The above gap incident laser excites a population of electrons and holes which form excitons and populate the various energy levels. Relaxation of the higher excited states is dominated by inter-level, non-radiative relaxation; however, each state has the same optical selection rules as the  $1s$  state and can recombine to emit light. Figure 2.14(b) shows the measured PL spectrum which is the sum of the various excited state PL.

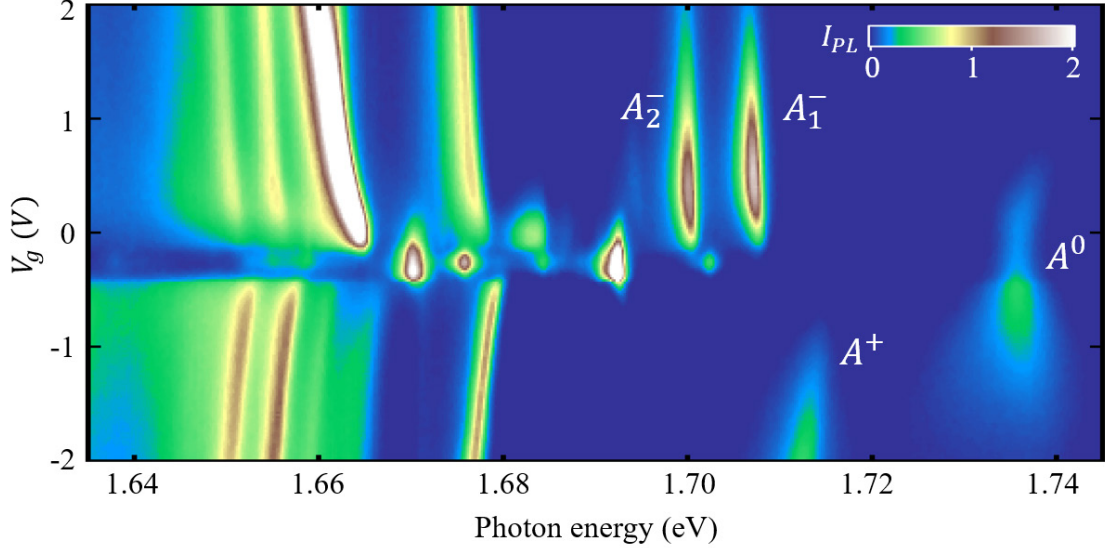


Figure 2.15: Experimental gate-dependent photoluminescence map of a monolayer WSe<sub>2</sub> gating device at  $T = 5$  K. The bright neutral exciton  $A^0$ , hole trion  $A^+$ , intervalley electron trion  $A_1^-$ , and intravalley electron trion  $A_2^-$  are labeled. The unlabeled PL features with energy  $< 1.70$  eV are the *dark* states and phonon replicas which we discuss in detail in Chapter 4.

As with reflection, the trions states will dominate the PL spectrum at non-zero charge density. We can thus measure a similar gate-dependent PL map in a monolayer WSe<sub>2</sub> gating device in which we identify the neutral exciton, electron trions, and hole trion. A representative gate-dependent PL map is shown in Figure 2.15. This gating map also shows another important difference between the reflection measurement and PL - we observe PL features with lower energy than the bright exciton which do not appear in the reflection map. These are the *dark* excitons which we discuss in more detail in Chapter 4.

### 2.6.1 Time-Resolved Photoluminescence Spectroscopy

The PL measurement above probes the steady-state exciton population. To resolve the time dynamics of the PL process, we use time-resolved photoluminescence (TRPL)

spectroscopy. Here, the sample is excited by an ultrafast pulsed laser (pulse width  $\approx$  100 fs) to semi-instantaneously excite a population of excitons. Some part of the exciton population will then decay radiatively with a characteristic lifetime - this PL emission is detected in a time-sensitive manner. We note that there are two modes of time-resolved detection commonly used to detect PL: streak camera imaging and single photon counting. For experimental availability reasons, we choose (time correlated) single photon counting (TCSPC).

In this scheme, the PL is directed into a monochromator in the same manner as the steady-state PL. In steady-state, the diffracted light is dispersed onto a CCD array where each CCD element corresponds to a detection wavelength depending on the diffraction angle. Here, we select a subset spectral window (e.g., several nm energy width) by passing the diffracted light through an exit slit. This spectrally narrow slice of the PL is focused onto a single-element avalanche photodiode (APD) which is configured for single-photon detection. When the APD detects a photon, it triggers the timing electronics along the detection channel. The timing electronics correlate this detection event with reference timing pulses from the excitation laser which allow determination of the time delay between the excitation laser pulse generation and the detected PL event. In this way, we generate a time-resolved plot of integrated PL intensity *vs.* time. Representative TRPL traces for excitons with different lifetime are shown in Figure 2.16(a). The APD has an intrinsic instrument response function (IRF) which is convoluted with the true time trace. We measure the IRF directly with a reflected ultrafast pulse and then numerically deconvolve the experimental data. The deconvoluted TRPL traces are shown in Figure 2.16(b).

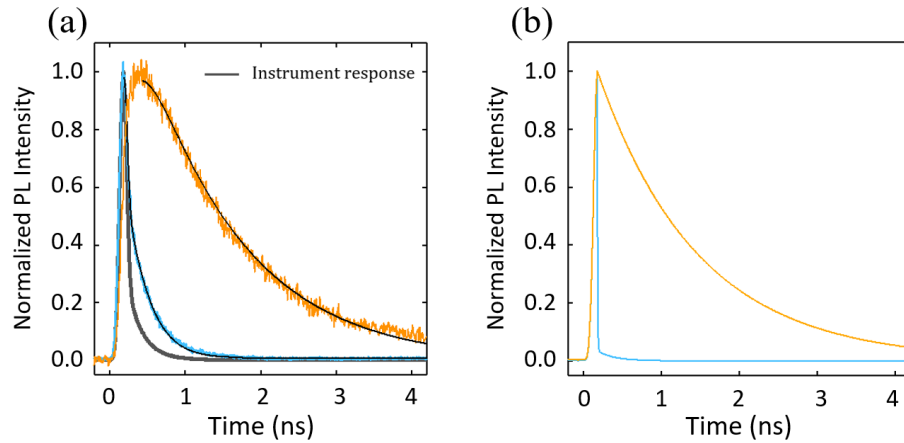


Figure 2.16: (a) Experimental time-resolved photoluminescence traces with different lifetime (blue line, orange line), and measured instrument response function (IRF, grey line). Data measured using time-correlated single photon counting procedure described in text. (b) Corresponding time-resolved photoluminescence traces after deconvolution with the instrument response function.

We note that the PL detection rate must be kept significantly below the excitation laser repetition rate to ensure accurate counting statistics. Following a detection event, there is a period of "dead time" in which incident photons will not be detected. This dead time can be significant compared to the measured lifetime. When multiple PL photons arrive at the detector within one period, then, we will always detect the first event but may not detect the second (or further). Thus, the detection will be biased towards PL events with shorter lifetime and the generated TRPL traces will not be representative. To avoid this "pulse pile-up", we keep the PL detection rate  $\leq 5\%$  relative to the laser repetition rate which significantly reduces the likelihood of multiply PL events per period.

## Choice of Ultrafast Laser Source for Single Photon Counting

Finally, we discuss the choice of ultrafast laser source used for TRPL. We study individual exciton species in monolayer WSe<sub>2</sub> with lifetime  $\approx < 10\text{ns}$ . Our choice of ultrafast laser source is thus subject to five key considerations: First, the peak instantaneous electric field and total power must be kept below respective thresholds to avoid laser-induced material damage. We maximize both thresholds by encapsulating the monolayer WSe<sub>2</sub> in BN and performing the measurements under vacuum at cryogenic temperatures. Nonetheless, it is still easy to irreparably damage the sample. Second, the per-pulse energy must be kept sufficiently low that exciton-exciton interactions are not significant. The initial population of excitons is positively related to the pulse energy, and it has been shown previously that multi-exciton interactions (e.g., biexcitons) arise with high exciton density [36–39]. Third, there is evidence of significant band renormalization under high intensity electric field [40–42]. Fourth, the pulse duration and inter-pulse period must be much less than and much greater than the exciton relaxation time, respectively. In this way, we “instantaneously” excite an initial population of excitons which fully relax within one period. Each of these limitations suggest we minimize the laser power, pulse energy, and repetition frequency as much as possible, converging to the single-photon limit. The final requirement is that we detect a sufficient number of exciton relaxation events to be a statistically representative population in a reasonable time frame. Practically, this means the average laser power should be as high as possible while satisfying the other requirements so the signal detection rate is much larger than the background count rate. We thus choose a 76 MHz ( $\approx 13\text{ ns}$  period *vs.* exciton lifetime  $\leq 10\text{ ns}$ ) excitation laser with pulse duration  $\approx 100\text{ fs}$ .

## Chapter 3

# Bright Excitons and Trions in Monolayer WSe<sub>2</sub> under High Magnetic Field

Application of external magnetic field is a powerful tool to manipulate and probe the electronic properties of two-dimensional materials. As discussed in Chapter 1 for monolayer WSe<sub>2</sub>, applied out-of-plane magnetic field breaks time-reversal symmetry in the 2D material and therefore breaks the energy degeneracy between the opposite  $K$ - and  $K'$ -valleys while preserving the valley-specific optical selection rules. This allows us to selectively probe the electronic transitions and excitonic states in each valley. The magnetic field also modifies the exciton energy which are related to its fundamental properties [15, 19, 43, 44] and interaction with other excitonic states, localization, and ambient carriers [45] within the material among many possible interactions.

In this chapter, we apply strong out-of-plane magnetic fields to monolayer WSe<sub>2</sub> gating devices and use photoluminescence (PL) and reflection contrast spectroscopies to examine the non-hydrogenic Rydberg series of the neutral exciton and explore the complex interaction between excitons and ambient carriers controlled by Landau level filling.

### 3.1 Magnetophotoluminescence of Exciton Rydberg States in Monolayer WSe<sub>2</sub>

The binding energy of the neutral exciton ( $A^0$ ) in monolayer WSe<sub>2</sub> and other monolayer TMDs has been reported in the large range 0.16 eV to 0.6 eV [7] which is mildly surprising at first glance. As briefly mentioned in Chapter 1, this is an expected consequence of the 2D nature of the material and its placement on various substrates and media. The Coulomb interaction, and therefore the excitonic effect, in monolayer WSe<sub>2</sub> is highly dependent on the surrounding dielectric environment so the choice of surrounding material (BN encapsulation, bare wafer, suspension) has a significant renormalizing effect on the electronic structure. It is therefore of interest to our further research efforts regarding the excitonic physics in this system to first thoroughly characterize the neutral exciton and the free particle electronic structure.

The exciton hosts internal energy levels similar to the Rydberg series of the hydrogen atom where the higher excited levels (e.g.,  $n = 2s, 3s, \dots$ ) have been shown to have larger radius and thus enhanced sensitivity to magnetic confinement and external screening effects. We can therefore study the magnetic-field-dependent of the entire series of exciton energy levels with an appropriate model to characterize the exciton and ground state (free

particle). In this section we apply this methodology to BN encapsulated monolayer WSe<sub>2</sub> samples and characterize the exciton under our specific sample conditions. The WSe<sub>2</sub> gating devices used in subsequent results have similar dielectric environment and thus these results inform our further work in this system.

### 3.1.1 Methodology

All samples were fabricated using the dry transfer method as described in Chapter 2. A schematic of the sample geometry is shown in Figure 3.1(b). In each sample, monolayer WSe<sub>2</sub> is encapsulated between two BN flakes with thickness 25 - 30 nm and deposited on a clean SiO<sub>2</sub>(285 nm)/Si wafer. Electrical contact with the WSe<sub>2</sub> flake was not required for this experiment but few-layer graphite (FLG) gate electrode and electrical contact were added for other data collection. This experiment was conducted at  $T = 4$  K in the 31 T cryogenic magneto-optical system (Cell 9) at the National High Magnetic Field Laboratory (NHMFL) in Tallahassee, FL which is described in Chapter 2.

### 3.1.2 Experimental Results

Figure 3.1(c) shows a representative photoluminescence spectrum of monolayer WSe<sub>2</sub> without applied magnetic field. The energy range 1.81 eV – 1.90 eV is magnified 50x for ease of viewing. Owing to the ultra-clean nature of our encapsulated samples, the PL lines are sharp and well-resolved. We identify the 1s – 4s features of the *A* exciton as informed by prior reflection-contrast measurement on similar WSe<sub>2</sub> samples. To quantitatively analyze and separate the overlapping 3s and 4s contributions, we fit the total

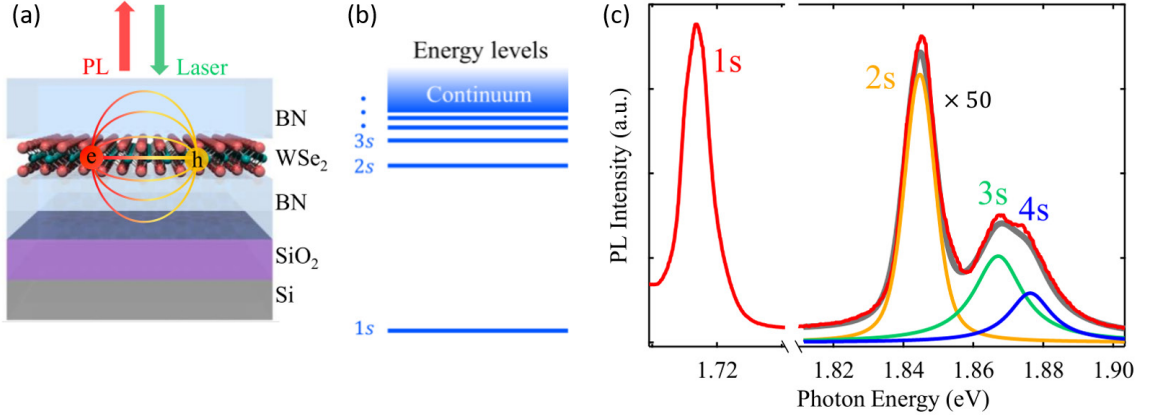


Figure 3.1: (a) Schematic diagram of an exciton in monolayer WSe<sub>2</sub> encapsulated by BN. The electric field (lines) between the electron (e) and hole (h) spreads into the surrounding BN medium. (b) Schematic internal energy levels of an exciton in monolayer WSe<sub>2</sub>. (c) PL spectrum of monolayer WSe<sub>2</sub> at temperature  $T = 4$  K and zero magnetic field under 532-nm continuous laser excitation. The spectrum at 1.81–1.90 eV is multiplied by 50 times for clarity. The red line is the experimental spectrum; the orange, green, and blue lines are the Lorentzian fits to reveal the 2s, 3s, and 4s exciton states, respectively. The gray line is the total fit spectrum.

spectrum with a series of Lorentzian functions from which we extract the center PL energies of each feature. The extracted PL energies,  $E_{PL}$ , are summarized in Table 3.1. Using a quantitative model, the details of which we discuss in Section 3.1.4, we extrapolate the free particle bandgap ( $E_g = 1.884$  eV) from our extracted A exciton PL energies. We thus obtain binding energies for each state 1s – 4s as  $E_g - E_{PL}$  which are shown in Table 3.1. These results are comparable to previous results of reflectance spectroscopy in similar BN-encapsulated WSe<sub>2</sub> samples [15]. We note that this project considered only the A exciton. In contrast to molybdenum-based TMD monolayers, the B 1S exciton is  $\sim 400$  meV above the A 1s energy and thus well-separated from the studied series of A excited states.

We further explore the A exciton energy levels by applying a strong out-of-plane magnetic field. We measure PL spectra for magnetic field  $B = -31 \text{ T} - 31 \text{ T}$ , shown with logarithmic color scale in Figure 3.2(a). As above, the energy range  $1.81 \text{ eV} - 1.90 \text{ eV}$  is magnified 50x. Figure 3.2(c) shows selected line cuts from the map in Figure 3.2(a). We observe significant magnetic-field-induced PL energy shift which are highlighted with dashed lines to trace the energy shift of each excited state. Notably, the higher excited states exhibit more significant energy shift which allows clear distinction between each feature. The 3s and 4s states, in particular, overlap at zero field but are cleanly separated at intermediate magnetic field.

We note the appearance of shoulder-like features just below the 1s and 2s exciton lines at  $B = -30 \text{ T}$ , labeled with an asterisk (\*) in Figure 3.2(c). At high negative magnetic field, the A exciton PL energy is much higher in the K valley than in the K' valley. Intervalley scattering processes will produce a valley population imbalance which favors the K' valley. The PL intensity of the K' valley will thus be much greater than that of the K valley as the total luminescence is proportional to population. We ideally measure the PL contribution of only one valley (K) via circular-polarization filtering but there is some transmission of the

Table 3.1: PL energy ( $E_{PL}$ ), binding energy ( $E_b$ ),  $g$ -factor, diamagnetic coefficient ( $\sigma$ ), and root-mean-square radius ( $r$ ) of the exciton Rydberg states in BN-encapsulated monolayer WSe<sub>2</sub>. The numbers in parentheses are the theoretical values from our model.

|    | $E_{PL}$ (eV) | $E_b$ (meV) | $g$               | $\sigma$ ( $\mu\text{eV}/\text{T}^2$ ) | $r$ (nm)               |
|----|---------------|-------------|-------------------|--|------------------------|
| 1s | 1.712         | 172 (172.1) | $-4.38 \pm 0.12$  | $0.21 \pm 0.1$ (0.31)                  | $1.6 \pm 0.4$ (1.68)   |
| 2s | 1.843         | 41 (43.8)   | $-4.60 \pm 0.10$  | $6.4 \pm 0.2$ (4.86)                   | $8.24 \pm 0.12$ (6.66) |
| 3s | 1.864         | 20 (19.5)   | $-4.22 \pm 0.14$  | $27.3 \pm 1.3$ (24.2)                  | $17.0 \pm 0.4$ (14.86) |
| 4s | 1.873         | 11 (11.0)   | $-45.06 \pm 0.21$ | $53.7 \pm 3.0$ (76.3)                  | $27.8 \pm 0.7$ (26.37) |

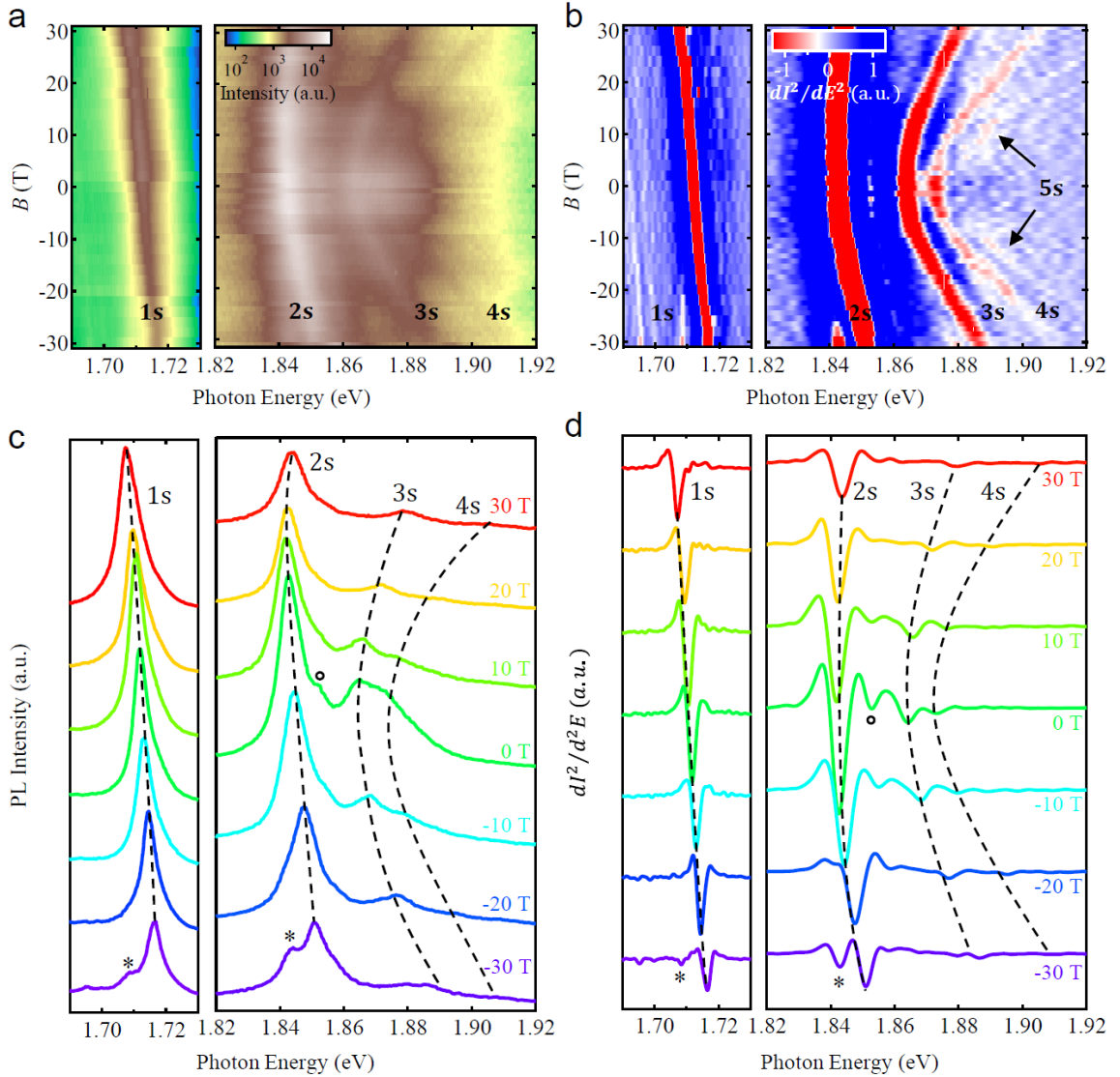


Figure 3.2: PL of A-exciton Rydberg states in monolayer WSe<sub>2</sub> under magnetic field at temperature  $T = 4$  K. (a) Logarithmic PL maps at magnetic fields  $B = -31$  to  $31$  T. (b) Color map of the second energy derivative of PL intensity ( $d^2I/dE^2$ ) in panel (a). (c) Cross-cut PL spectra from panel (a) at selective magnetic fields. (d) The cross-cut  $d^2I/d^2E$  spectra from panel (b) at selective magnetic fields. The dashed lines highlight the shift of Rydberg states. PL features marked by the “\*” symbol at  $B = -30$  T come from the other valley due to the imperfect helicity selection in the measurement.

opposite polarization due to misalignment or low extinction of the polarizing filter. Thus, when the intensity of our target polarization is very weak relative to that of the opposite polarization, as induced here by magnetic-field splitting, a small polarization leakage will be observable. We attribute the labeled features to this process.

To further enhance the weak, higher excited states, we plot the second derivative of the measured spectra with respect to energy ( $d^2I/dE^2$ ). For clarity, we take this derivative for spectra of each magnetic field, individually, and plot the results as a false color map in Figure 3.2(b). Maxima in the intensity map appear in the derivative map as sharpened minima which allow us to more effectively trace the magnetic-field-induced energy shift of each exciton state. Notably, an additional PL line appears at high energy above the 4s state for  $B > 5$  T. Although this feature is weak, we preliminarily identify it as the 5s *A* exciton. We note that a second small dip in the derivative spectra appears just above the 2s line and mimics the 2s magnetic-field shift. This feature is labeled in Figure 3.2(c, d) at  $B = 0$  T with an open circle. We do not definitely identify this feature but suggest that it may be an artifact of the interpolation / smoothing which is a part of the as-used numerical derivative calculation.

Prior absorption experiments of the Rydberg-like exciton states in monolayer TMD samples have shown notable absorption enhancement under out-of-plane magnetic field [15, 44]. This was attributed to an enhancement of the exciton oscillator strength due to magnetic-field-induced confinement. Due to their larger spatial extent, the higher-lying excited states exhibited larger absorption enhancement. In contrast, we observe notable PL suppression of the 2s–4s excitons at high magnetic field. The higher excited states appear to

exhibit stronger magnetic-field-induced PL suppression. Further, the preliminarily identified 5s state appears only at intermediate magnetic field. Exciton PL intensity is roughly proportional to the product of oscillator strength and lifetime. Thus, the observed PL suppression suggests that the oscillator-strength-based PL enhancement is overpowered by a significant reduction in exciton lifetime at high magnetic fields. We attribute this lifetime reduction to increased non-radiative recombination rates of the exciton when shifted to higher energy by the magnetic field.

### 3.1.3 Analysis of Exciton Zeeman and Diamagnetic Shifts

For a more quantitative analysis, we fit each spectrum with a series of Lorentzian functions corresponding to each PL line as illustrated in Figure 3.2(a). The extracted PL energies of each exciton state are plotted in Figure 3.3(a). According to prior research, the exciton energy shift can be described by two components in the low-magnetic-field limit – the valley Zeeman effect discussed in Chapter 1 and the diamagnetic shift. [15, 46]. The Zeeman effect is odd in magnetic field, so the associated energy shift is simply the difference in exciton PL energy in a single valley at opposite magnetic field or, identically, the difference in exciton PL energy of opposite valleys at fixed magnetic field. The diamagnetic shift is even under magnetic field – proportional to  $B^2$ . The diamagnetic shift is thus the average exciton PL energy in a single valley at opposite magnetic field. In this way, we extract the valley-Zeeman and diamagnetic shifts of the 1s – 4s excitons which we plot in Figure 3.3(b, c), respectively. Although we preliminarily identify a 5s peak, it appears only briefly with weak intensity. The 5s feature is thus excluded from further analysis.

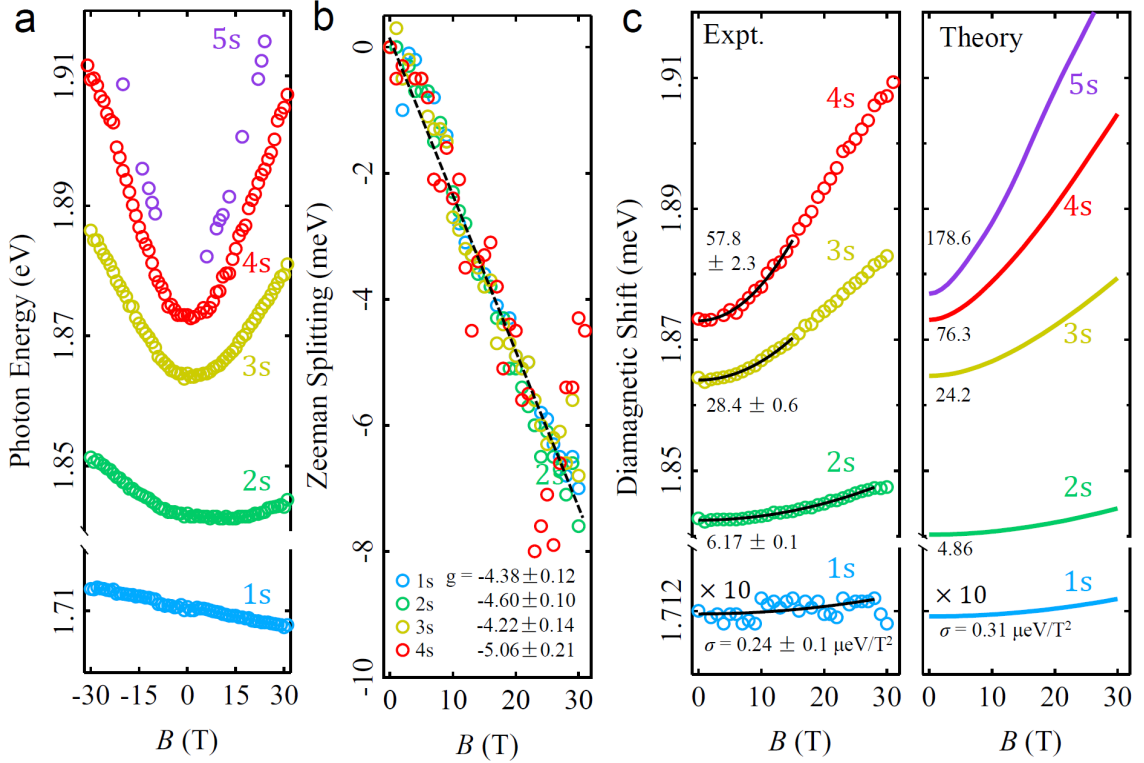


Figure 3.3: The energy shifts of A-exciton Rydberg states in monolayer WSe<sub>2</sub> under magnetic field. (a) The exciton PL energy as a function of magnetic field, as extracted from the data in Figure 3.2. (b) Zeeman shifts extracted from panel a. The  $g$ -factors are obtained from linear fits. (c) Diamagnetic shifts extracted from panel a. The lines are quadratic fits. (d) Predicted exciton diamagnetic shifts from our model. We denote both the measured and calculated diamagnetic coefficient ( $\sigma$ ) in units of  $\mu\text{eV}/\text{T}^2$ . The energy in panel (c) and (d) for 1s state is magnified by 10 times.

We first consider the valley-Zeeman effect as discussed in Chapter 1. The bright  $A$  exciton is composed on an electron in the lowest-energy conduction band and a hole in the highest-energy valence band – a spin singlet state. The total exciton spin is zero and does not contribute to the Zeeman shift. However, the highest-energy valence band is largely composed of d-type atomic orbital which has azimuthal quantum number  $m = \pm 2$  for the  $K$ - and  $K'$ -valley, respectively [7]. The Zeeman splitting is the difference between valley contributions. We thus estimate an effective  $g$ -factor,  $g = -4$ . In our experiment, the Zeeman splitting energies of the  $1s - 4s$  states are well-described by a linear fit. We extract  $g$  factors between 4.2 and 5.1, as shown in Figure 3.2(b) and summarized in Table 3.1, which are in good agreement with our estimate and previous reports [15, 47–50].

We next consider the diamagnetic shift contribution. In the weak-field limit, where the exciton binding energy is much greater than the Landau-level spacing, the diamagnetic shift of the exciton energy can be expressed as: [51]

$$\Delta E_{Dia.} = \frac{e^2}{8\mu} \langle r^2 \rangle B^2 = \sigma B^2 \quad (3.1)$$

where  $\mu = (m_e^{-1} + m_h^{-1})^{-1}$  is the exciton reduced mass,  $\sigma$  is the diamagnetic coefficient, and  $r$  is the radial coordinate of the exciton such that  $\langle r^2 \rangle = \langle \psi | r^2 | \psi \rangle$  is the expectation value of  $r^2$  over the exciton envelope function  $\psi$ . The root-mean-square radius is related as  $r = \sqrt{\langle r^2 \rangle} = \sqrt{8\mu\sigma}/e$ . The diamagnetic shift coefficient,  $\sigma$ , is proportional to  $r^2$ . Thus, a larger diamagnetic shift of exciton energy indicates a larger exciton size. Successive higher energy excited states have increasing spatial extent and are thus expected to exhibit larger diamagnetic shift than the low-lying excitons.

In the high-field limit, where the Landau-level spacing significantly exceeds the exciton binding energy, excitonic effects are suppressed. The optical spectra are instead dominated by direct optical transition between Landau levels in the valence and conduction bands. The Landau-level energy is approximately linear with magnetic field

$$E_{LL} = (N + \frac{1}{2})\hbar\omega_c \quad (3.2)$$

where  $\omega_c = eB/\mu$  is the interband transition cyclotron frequency. At intermediate magnetic field, where the Landau-level energy spacing and exciton binding energy are comparable, the rate of exciton energy shift will evolve continuously from low- to high-field descriptions. Assuming identical electron and hole effective mass,  $m_e = m_h = 0.4m_0$ , we estimated a reduced mass,  $\mu = 0.2$ . The Landau level energy spacing can be roughly estimated  $E_{LL} \approx 0.58meVT^{-1}$  which gives  $E_{LL}(B = 31 \text{ T}) \approx 18 \text{ meV}$ .

We plot the extracted diamagnetic shifts of 1s – 4s excitons in Figure 3.3(c). The 1s and 2s states exhibit small diamagnetic shift with approximately  $B^2$  dependence throughout the measured magnetic field range. As discussed above, and summarized in Table 3.1, we estimate the 1s and 2s binding energies as 171 meV and 41 meV, respectively. Both are significantly larger than our estimated Landau-level energy spacing and thus well within the weak-field limit. Using a quadratic fit, which we overlay as solid lines, we extract diamagnetic coefficients  $\sigma_{1s} = 0.24 \pm 0.1 \mu eVT^{-2}$  and  $\sigma_{2s} = 6.4 \pm 0.2 \mu eVT^{-2}$ . From the relationship  $r = \sqrt{8\mu\sigma}/e$ , we estimate the corresponding root-mean-square radii of the 1s and 2s exciton as  $r_{1s} = 1.6 \pm 0.4 \text{ nm}$  and  $r_{2s} = 8.24 \pm 0.13 \text{ nm}$ .

In contrast, the 3s and 4s PL lines exhibit  $B^2$  dependence only for  $B < 15 \text{ T}$ . Above this limit, both features transition to approximately linear magnetic field dependence. In

Table 3.1, we estimate the binding energies of the 3s and 4s states as 20 meV and 11 meV, respectively, which is comparable to the estimated Landau level energy spacing of 18 meV at  $B = 31$  T. By fitting the diamagnetic energy shift in the low-field regime (solid line overlay, Figure 3.3(c)), we extract diamagnetic coefficients  $\sigma_{3s} = 27.3 \pm 1.3 \mu\text{eV}/T^2$  and  $\sigma_{4s} = 53.7 \pm 3.0 \mu\text{eV}/T^2$ . The estimated exciton radii are thus  $r_{3s} = 17.0 \pm 0.4$  nm and  $r_{4s} = 27.8 \pm 0.7$  nm. The extracted diamagnetic coefficient and r.m.s radius values for all observed  $A$ -exciton states are summarized in Table 3.1. We note that these results are in agreement with prior magnetoabsorption measurements which measured the diamagnetic shift of the 1s - 3s  $A$ -exciton states in monolayer WSe<sub>2</sub> [15].

### 3.1.4 Quantitative Model Calculations

As mentioned above, we carried out model calculations to quantitatively analyze our data. We define the system as a 2D semiconductor with dielectric constant  $\epsilon_{1L-\text{WSe}_2} \approx 7.5$  embedded in a 3D medium of boron nitride with lower dielectric constant  $\epsilon_{BN} \approx 3.8$  [52]. As illustrated in Figure 3.1(b), the electron and hole which form the exciton are confined to the 2D plane of the WSe<sub>2</sub>, but the electric field which defines their interaction extends into the surrounding medium. When the spatial separation of electron and hole is increased (increased exciton radius), a larger portion of the electric field extends beyond the 2D plane. Thus, the screening effect from the surrounding material becomes more significant. In our geometry, the surrounding material has a lower dielectric constant and thus the total screening of the exciton interaction is inversely related to the exciton radius.

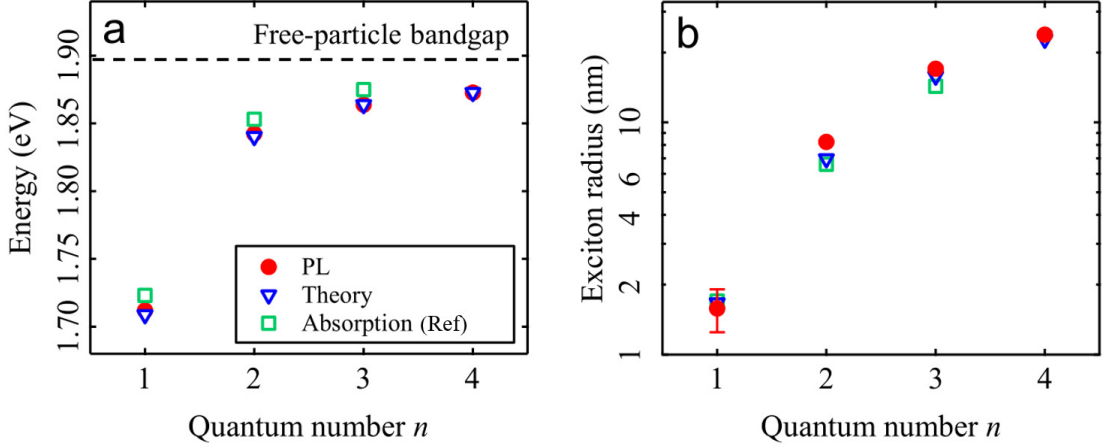


Figure 3.4: The energy and radii of Rydberg excitons for principle quantum number  $n$  in monolayer WSe<sub>2</sub>. (a) The recombination energy and (b) radii of  $A$ -exciton states (red dots) extracted from the PL data in Figure 3.3, in comparison with the theoretical predictions (blue triangles) and results from a prior absorption experiment (green squares [15]). The dashed line denotes the free-particle band gap predicted by our model.

The interaction potential is well-described by the Rytova-Keldysh potential: [53, 54]

$$V(r) = -\frac{e^2}{8\epsilon_0 r_0} \left[ H_0\left(\frac{\kappa r}{r_0}\right) - N_0\left(\frac{\kappa r}{r_0}\right) \right] \quad (3.3)$$

where  $H_0$  and  $N_0$  are the Struve and Neuman functions of zero-th order, respectively;  $r$  is the electron-hole separation;  $r_0$  is an effective screening length of monolayer WSe<sub>2</sub>, and  $\kappa$  is the effective static dielectric constant of the heterostructure. Both  $r_0$  and  $\kappa$  are fitting parameters in our model. In the long-range limit ( $r \gg r_0$ ), the screening is dominated by the 3D medium and the potential is proportional to  $1/\kappa r$ . In the short-range limit ( $r \ll r_0$ ), where the 2D layer contributes significantly to the total screening effect, the potential exhibits approximately  $\log(r)$  dependence.

We used the potential described above to fit our observed PL energies and radii of the 1s - 4s  $A$  excitons. We assume effective masses of the electron and hole obtained from density-functional theory (DFT). We obtain best-fit values for the fitting parameters,

$r_0 = 5$  nm and  $\kappa = 3.97$ . We further estimate a free-particle band gap of 1.884 eV for BN-encapsulated monolayer WSe<sub>2</sub>. Figure 3.4(a, b) show the calculated PL energies and exciton radii as compared to our experimental observations and prior magnetoabsorption study. We also plot the calculated diamagnetic shifts of the exciton states in Figure 3.3(d).

### 3.1.5 Conclusion

In summary, we measured the magnetophotoluminescence of BN-encapsulated monolayer WSe<sub>2</sub> samples under strong out-of-plane magnetic field. From the linear valley Zeeman shift of the exciton PL energies, we extracted the exciton  $g$ -factors for each excited states of the  $A^0$  exciton for  $n = 1s - 4s$ . We further measured the second order diamagnetic shift of the exciton PL energies which allowed us to determine the diamagnetic coefficients and exciton r.m.s radii for each excited state. Finally, we used the Rytova-Keldysh model to fit our data and estimate the binding energy of the  $n = 1s - 4s$   $A^0$  states, as well as the free-particle band gap. We also note that our results are in agreement with two similar publications [44, 50].

## 3.2 Landau-Quantized Photoluminescence and Absorption in Monolayer WSe<sub>2</sub>

As discussed in the previous section and in Chapter 1, the first-order effect of an out-of-plane magnetic field on the electronic structure of monolayer WSe<sub>2</sub> is the valley Zeeman shift. The two electronic valleys (K, K') exhibit opposite Zeeman shift under out-of-plane magnetic field. The relative energy shift of the valence and conduction bands at

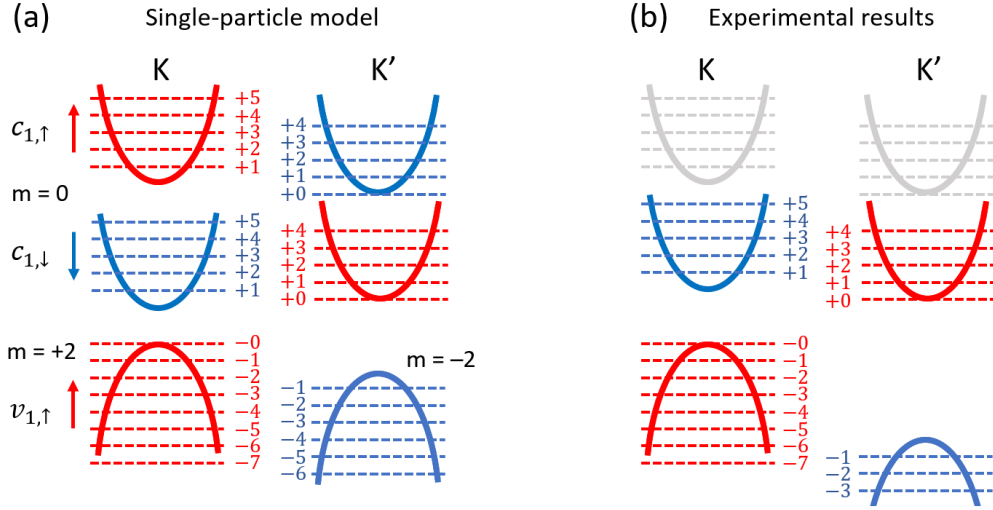


Figure 3.5: (a) Schematic Landau levels (dashed lines) in monolayer WSe<sub>2</sub> predicted by a single-particle model. The arrows and color denote the electron spin in the conduction bands and valence band.  $m = 0, \pm 2$  are the azimuthal quantum numbers of the atomic orbits in the conduction bands and valence band, respectively. (b) LLs revealed by our experiment, indicating strong enhancement of valley Zeeman shift by many-body interactions.

$B = 17.5$  T are illustrated in Figure 3.5(a) as predicted by the single particle model. For "positive" magnetic field, the band gap will decrease (increase) in the K (K') valley, which produces a exciton energy splitting proportional to the exciton  $g$ -factor.

The magnetic field will also quantize the electronic density of states into Landau levels (LL) whose degeneracy and energy spacing are proportional to the magnetic field intensity. At charge neutrality, the Landau quantization becomes significant for excitons in the intermediate-magnetic-field regime where the exciton binding energy is comparable to the Landau level spacing ( $B \approx 15$  T for  $A_{3s}$ ). We observed this transition for the  $A_{3s}$  and  $A_{4s}$  states. The  $A_{1s}$  binding energy is  $\approx 10$ x greater than  $A_{3s}$ , however. For the magnetic fields used in this section ( $B \leq 17.5$  T), the  $A_{1s}$  binding energy is much greater than the LL spacing; thus, the exciton is the superposition of many LLs.

## Landau-Quantization at Finite Charge Density

To this point, our discussion of Landau quantization on the excitonic behavior has been limited to charge neutrality. The situation changes significantly at non-zero charge density as we can form charged excitons (trions) and must fill the Landau levels sequentially in energy with ambient charge injection which produces Shubnikov-de Haas-type oscillations in conductivity in electrical transport [55–57]. In monolayer WSe<sub>2</sub>, the LLs inherit the spin-valley characteristics and subsequent valley Zeeman splitting of their parent band [58–60]. Thus, at least the zero-energy [23,61,62] (band edge) LL will begin filling in one valley before the other - these are so-called *valley-polarized* Landau levels. The order of LL filling depends on the relative Zeeman shift and the alignment of the LL in each valley. As illustrated in Figure 3.5(a), the single-particle model predicts three ( $n_K = -0$  to  $-2$ ) valley-polarized LLs in the K-valley valence band. As we will discuss later in this section, our results diverge significantly from this prediction.

The the valley-polarized LLs in monolayer WSe<sub>2</sub> have been studied previously by transport [55–57] scanning probe [63], and optical absorption [61] measurements, but each studied the LLs directly without consideration of excitonic effects. Further, transport study was limited to LLs with filling factor  $n \geq 17$  due to high contact resistance and low carrier mobility. Smolenski *et al.* [64] previously reported LL-related oscillation of the  $A_{1s}$  exciton in monolayer WSe<sub>2</sub>; however, their study was limited to optical absorption only for LLs with filling factor  $n \geq -1$ . We expand upon this study with comprehensive absorption and PL which shows LL-related oscillation of the  $A_{1s}$  excitons and trions (and further dark trions) in the conduction and valence bands, including the zero-energy  $n = \pm 0$  LL.

### 3.2.1 Methodology

Using high-quality BN-encapsulated monolayer WSe<sub>2</sub> gating devices as described in Chapter 2, we conducted comprehensive magneto-reflectance-contrast and magneto-PL measurements. Reflectance contrast and PL measurements are described in Chapter 2. All data shown in this section was taken at the National High Magnetic Field Laboratory DC Field Facility in Tallahassee, FL during two weeks March 18-25 and August 19-26, 2019. We used the 17.5 T superconducting magneto-optical system (Cell 3) with sample temperature  $T = 4$  K described in Chapter 2 for all measurements. For better comparison with theory calculation and qualitative analysis, we extract the single-layer optical conductivity of monolayer WSe<sub>2</sub> from reflectance contrast data using the approach in Chapter 2.

### 3.2.2 Gate-Dependent Reflectance Contrast

Figure 3.6(d) shows the reflectance contrast spectrum,  $\Delta R/R$ , of monolayer WSe<sub>2</sub> at zero magnetic field. For reference, we show a schematic band diagram in Figure 3.6(a). Immediately, we identify the neutral  $A_{1s}$  exciton ( $A^0$ ), the hole trion ( $A^+$ ), and intervalley ( $A_1^-$ ) and intravalley ( $A_2^-$ ) electron trions. As discussed in Chapter 1, the presence of ambient charges at  $V_g \neq 0$  transfers oscillator strength from the neutral exciton to the trion. In other words, it suppresses the neutral exciton and facilitates trion formation. To explore the influence of Landau quantization on the excitonic states, we apply large out-of-plane magnetic field ( $B \leq 17.5$  T) and selectively measure  $\Delta R/R$  for the  $K$  and  $K'$  valleys.

### Gate-Dependent Reflectance Contrast, $K'$ -valley

The  $K'$  valley reflection contrast map (left circularly polarized detection) is shown in Figure 3.6(e) at  $B = 17.5$  T. At first glance, this spectrum is qualitatively similar to that at  $B = 0$  T. Upon hole (electron) doping,  $A^0$  is suppressed and the corresponding positive (negative) trion appears. With closer inspection, we note three key differences. First,  $A^0$  is suppressed almost immediately with negative gating, rather than a prolonged transition where both  $A^0$  and  $A^+$  are visible simultaneously. Second,  $A^+$  appears to red-shift linearly with decreasing  $V_g$ . At  $B = 0$  T,  $A^+$  exhibits a more complex energy shift with decreasing  $V_g$  which initially red-shifts and then begins to blue-shift at  $V_g < -4$  V. Third, we clearly observe only one electron trion rather than the two observable at  $B = 0$  T. Each observation can be explained qualitatively by examining the energetic arrangement of constituent bands in the  $K$  and  $K'$  valleys as depicted schematically in Figure 3.6(b). We discuss the hole-side  $V_g < 0$  V data immediately below but return to discuss the electron-side data in Section 3.2.3.

First, the rapid suppression of  $A_{K'}^0$  with hole doping. With increasing hole density in the  $K$ -valley, oscillator strength is transferred from  $A_{K'}^0$  to  $A_{K'}^+$ , which suppresses the neutral exciton resonance.  $A_{K'}^+$  is depicted schematically in Figure 3.6(b). At  $B = 0$  T, the valence band is valley degenerate so we must simultaneously fill the both valleys upon hole doping. For  $B > 0$  T, however, the  $K$ -valley valence band lies at a higher energy than the opposite valley. All injected holes will therefore fill the  $K$ -valley valence band first, which means that the transition process from  $A_{K'}^0$  to  $A_{K'}^+$  will occur more rapidly.

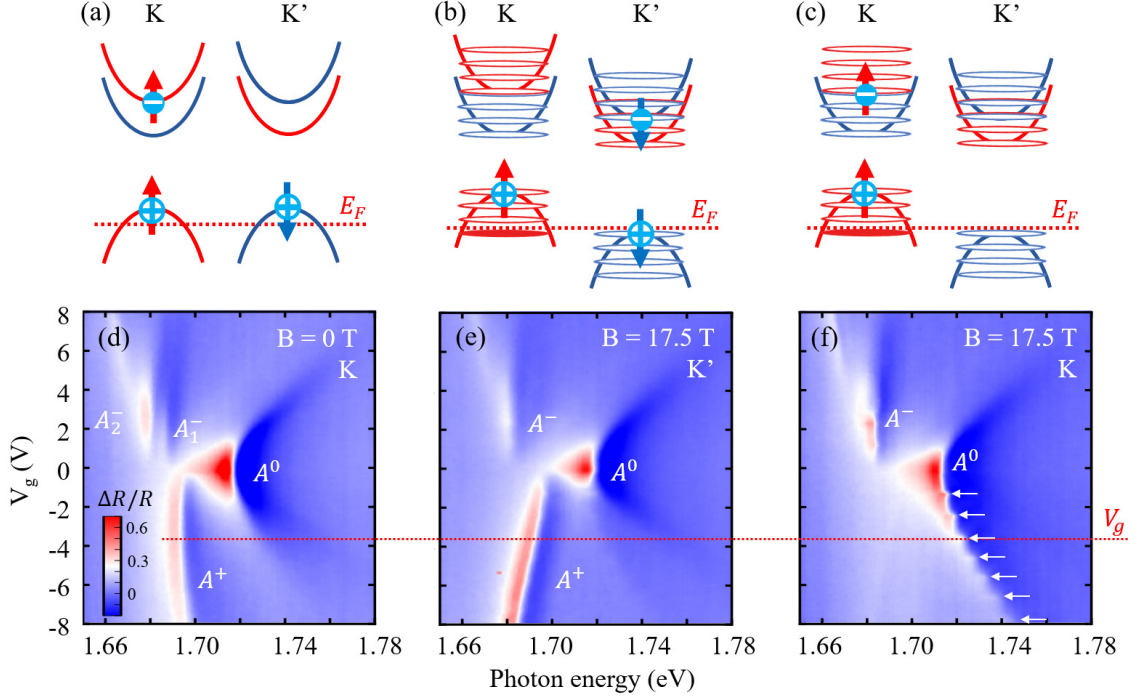


Figure 3.6: Schematic band structure with exciton (trion) configuration at intermediate hole doping and gate-dependent reflection contrast maps for (a,d)  $B = 0$  T, and  $B = 17.5$  T for the (b,e)  $K'$  and (c,f)  $K$ -valley. The red dashed lines indicate corresponding Fermi energy ( $E_F$ ) and gate-voltage ( $V_g$ ) to fill three  $K$ -valley valence band Landau levels. We note that the depicted size of each Landau level is purely aesthetic - each Landau level has identical degeneracy.

Second, the linear red-shift of  $A_{K'}^+$ . The presence of valley-polarized holes hints at the origin of the observed  $A_{K'}^+$  linear red-shift with decreasing  $V_g$ . As discussed in Chapter 1, excitonic states experience energy shift under electrostatic gating due to three primary sources - phase-space filling (PSF), screening, and band-gap renormalization [7]. The screening and band-gap renormalization (BGR) are related to the total ambient charge density and applied electric field intensity, but the PSF-based energy shift is sensitive only to filling of electronic states directly involved in the exciton formation. Thus, an exciton (trion) in the  $K'$  valley will always experience the screening and BGR effects with increasing

charge density, but will not experience PSF-based energy shift under hole doping until the  $K'$  valence band begins to fill. The PSF-effect causes an increase of the exciton energy, while the net effect of screening and BGR is a reduction in exciton energy. Thus, the presence of screening and BGR *without* PSF is consistent with the observed red shift of  $A^+$  throughout our studied gate voltage range. We see no indication of the PSF-related energy blue-shift even at the largest hole densities, which suggests that the Fermi energy does not reach the  $K'$  valence band.

Finally, the electron trion. The appearance of only one clear  $A^-$  resonance at high magnetic field can be attributed to similar valley-polarization of the conduction band. As discussed in Chapter 1,  $A_1^-$  and  $A_2^-$  correspond to inter- and intra-valley electron trions, respectively. For  $B > 0$  T, we expect to first fill the  $K'$  conduction band which immediately facilitates formation of  $A_2^-$ . The lack of ambient electrons in  $K$  for small positive gate voltages prevents efficient formation of  $A_1^-$ . We will discuss the behavior of the electron trions in more detail in Section 3.2.3.

### **Gate-Dependent Reflectance Contrast, $K$ -valley**

The  $K$  valley reflection contrast map (right circularly polarized detection) is shown in Figure 3.6(f) for  $B = 17.5$  T. We observe three primary differences in comparison to  $K'$ -valley data. First,  $A^0$  extends to a much larger negative gate voltage before suppression, whereas  $A^+$  is nearly completely suppressed within the studied  $V_g$  range.. At  $B = 17.5$  T,  $A^0$  persists with hole doping beyond our gating range . Second, we again observed one  $A^-$  resonance which appears at a higher energy than that in the  $K'$ -valley. Third,  $A^0$  exhibits step-like energy shifts (denoted by white arrows) which are equally-separated with inter-

step gate voltage separation of  $\approx 1.17$  V, and  $A^-$  exhibits two discernible intensity maxima which are separated by a nearly identical  $\Delta V_g$  to the step-like energy shifts in  $A^0$ .

First, the simultaneous suppression of  $A^+$  and persistence of  $A^0$  with hole doping. Just as  $A^0$  is efficiently suppressed in the  $K'$ -valley, the valley-polarized valence bands can explain the persistence of  $A^0$  to large negative gate voltage in the  $K$ -valley.  $A^0$  retains its oscillator strength until  $A^+$  formation becomes favorable - in the  $K$ -valley, this requires the filling of the  $K'$  valence band with ambient holes. As shown in Figure 3.6(c), the  $K$  valence band lies above  $K'$  in energy and will be preferentially filled upon hole injection. Thus  $A^0$  will persist and  $A^+$  will be suppressed until the Fermi energy reaches the  $K'$  valence band edge.

The valley-contrasting  $A^-$  behavior may be explained similarly. The  $K'$  conduction band lies below the  $K$  valley in energy and will fill first under electron doping. This favors formation of the intravalley  $A_1^-$  in contrast to the observation of the intervalley  $A_2^-$  in the  $K'$  valley reflectance map.

As further evidence of this qualitative picture, we examine the  $K$ -valley reflection data under varied magnetic field intensity. To clearly distinguish each exciton resonance, we calculate the monolayer WSe<sub>2</sub> optical conductivity from reflection contrast data using the method outlined in Chapter 2. The gate-dependent  $K$ -valley optical conductance maps are plotted in Figure 3.7 for magnetic fields between  $B = 0$  T and  $B = 17.5$  T. At  $B = 11.5$  T, which is the lowest non-zero magnetic field for which we have complete data,  $A^0$  is persists only to  $-6.5$  V. At this point,  $A^0$  is suppressed and a faint resonance appears at  $\approx 1.71$  eV which we identify as  $A^+$ . We interpret this as the gate voltage at which the

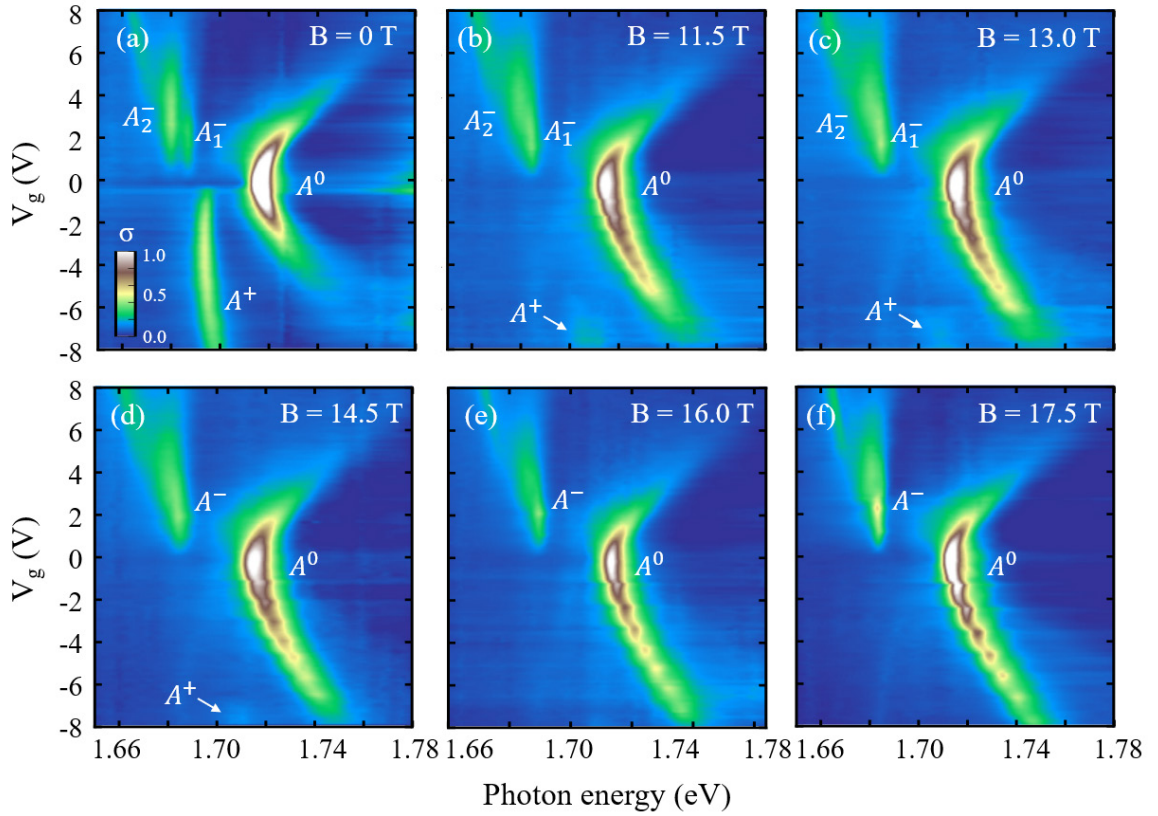


Figure 3.7: (a-f) The real part of the optical sheet conductivity ( $\sigma$ ) for the  $K$ -valley excitonic states in monolayer  $\text{WSe}_2$  for positive magnetic field  $B = 0$  T to 17.5 T. Optical sheet conductivity is proportional to the product of monolayer thickness and  $\epsilon_2$  derived from the reflectance contrast maps (as in Figure 3.6(f)) using the quantitative analysis process described in Chapter 2. The  $A^+$  trion is weakly visible at  $B < 15$  T, but is suppressed at  $B > 15$  T.

$K'$ -valley valence band begins to fill under hole doping. As the magnetic field increases, the  $K'$  valence band is further separated in energy from the  $K$  valence band due to the Zeeman shift. Correspondingly, the total charge density we must inject to bring the Fermi energy to the  $K'$  valence band edge increases with magnetic field and  $A^0$  may persist to ever larger gate voltages.

We note that each of the qualitative explanations discussed so far do not require quantization into Landau levels but rather appear due to the Zeeman shift. The observed step-like energy shift of  $A^0$  and intensity oscillation of  $A^-$ , however, cannot be explained without considering a quantized density of states.

### 3.2.3 Electronic Quantization Observed *via* Optical Conductivity

To further explore the step-like behavior of  $A_K^0$ , we examine the optical conductivity in detail at  $B = 17.5$  T. For each  $V_g$ , we extract the photon energy of maximum conductivity (eV), the full width at half maximum (FWHM), the peak conductivity, and the total integrated conductivity of the resonance. The results are shown in Figure 3.8(a-d). In contrast to the  $K'$ -valley, the valence band LLs which compose the  $A_K^0$  are the first to be filled under hole doping as shown schematically in Figure 3.6(c). Thus, the  $A_K^0$  will experience the combined effects of PSF, screening, and BGR. When the Fermi energy is within a partially-filled LL an increase in gate voltage will rapidly fill the LL with ambient carriers. The exciton will experience an energy shift dominated by the PSF-effect which increases the exciton absorption energy. When the Fermi energy is between LLs, an increase in gate voltage will not inject further ambient carriers.

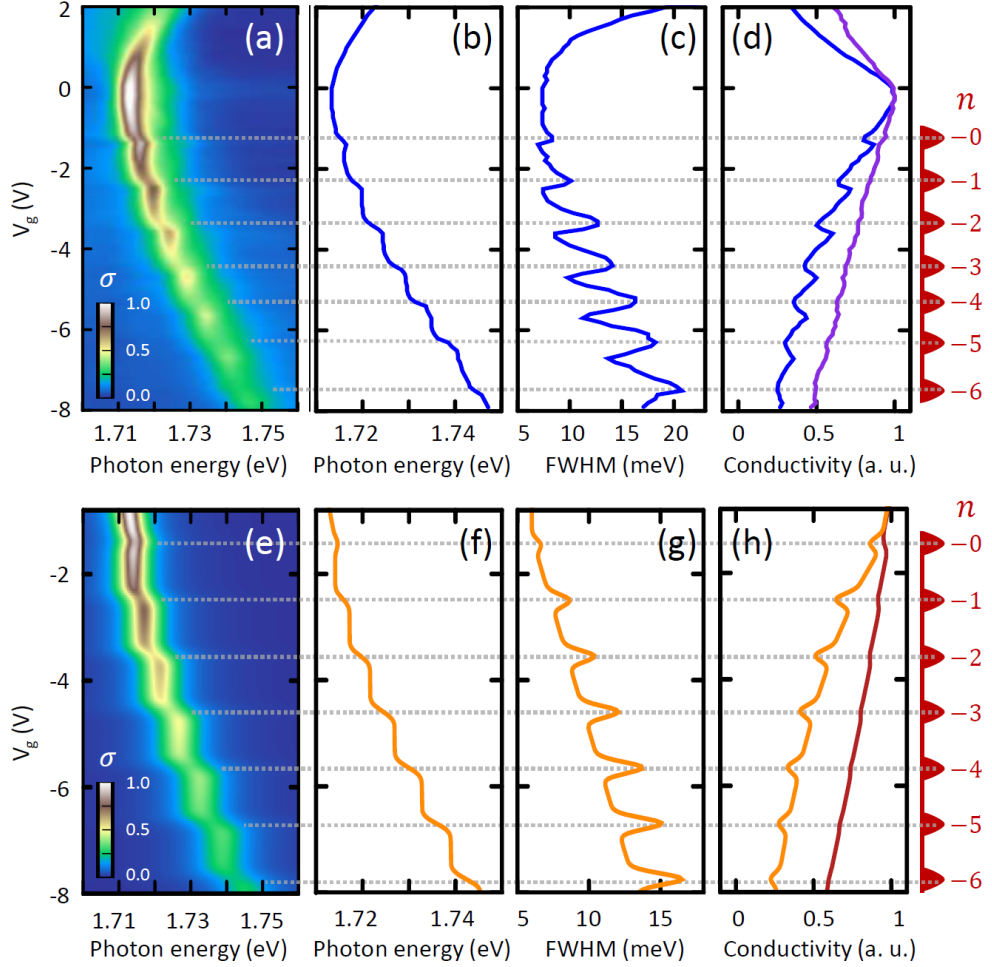


Figure 3.8: (a) The optical sheet conductivity of  $A^0$  exciton extracted from Fig. 2(d). (b) The exciton peak energy, (c) full width at half maximum (FWHM), (d) peak conductivity (blue) and integrated conductivity (purple), extracted from (a). (e) The theoretical exciton conductivity map, (f) peak energy, (g) FWHM, (h) peak conductivity (orange) and integrated conductivity (red). All conductivity values are normalized to 1. The dashed lines denote the half-filled LL positions.

The total effect of the sequential LL-filling on the exciton energy is thus a step-like behavior with decreasing  $V_g$  which alternates between rapid blue-shift while actively filling a LL and an energy plateau in the inter-LL gap. This behavior is reflected by our experimental data as shown in Figure 3.8(b). We note that the maximized phase-space near the Fermi energy at the LL half-filling point will also facilitate exciton-carrier scattering which will decrease the  $A^0$  coherence and homogeneously broaden the conductivity resonance. Thus, the local maxima in FWHM should coincide with the center of each "step" in the  $A^0$  energy shift and indicate the  $V_g$  for half-filling of each observed LL. We overlay horizontal lines in Figure 3.8 to show that this prediction is reflected by our data. We note that the total integrated conductivity of  $A^0$  slowly decreases with  $V_g$  and does not oscillate with the LL-filling. The maximum conductivity oscillates out of phase with the FWHM to preserve the total conductance. We use this evidence to identify the maxima in FWHM as the half-filling points for each LL.

This qualitative model can be quantified using semiempirical calculations. We calculated the exciton conductivity spectrum by solving the massive Dirac equation for the electron and hole, including the Coulomb interaction screening, for monolayer WSe<sub>2</sub> under magnetic field. For simplicity, we only consider the case of ambient hole injection in the  $K$  valley. As shown in Figure 3.8(e-h), our calculations reproduce the primary experimental observations and further confirm our identification of the half-filled LL gate voltages. For details of this calculation, see supplementary material of this publication [65].

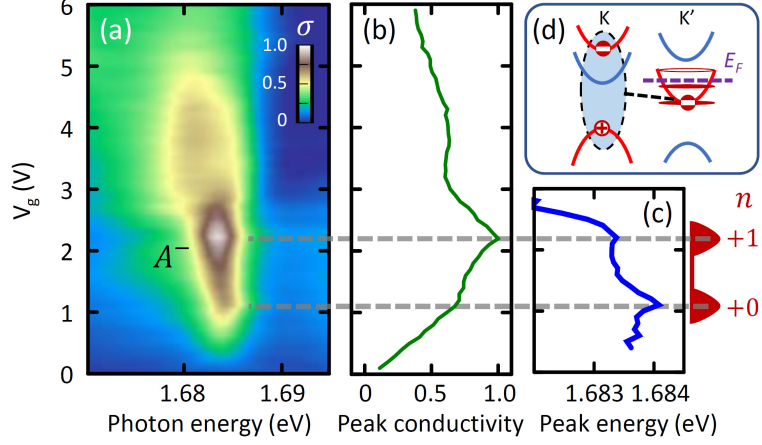


Figure 3.9: (a) The normalized optical sheet conductivity of  $A^-$ -trions extracted from 3.7(f). (b) The trion peak conductivity and (c) peak energy extracted from (a). The dashed lines denote the half-filled LL positions. (d) The schematic band configuration of intervalley  $A^-$ -trion with the relevant LLs and Fermi energy ( $E_F$ ).

### Landau-Quantization-Induced Oscillation of the Electron Trion

We now briefly discuss the LL-related behavior under electron doping ( $V_g > 0$  V). We first note that the neutral exciton  $A^0$  does not exhibit noticeable LL-related oscillations in this regime, in contrast to the clear oscillations with hole doping. The lower conduction bands ( $c_1$ ) which are filled first under electron injection are not directly involved in the  $A^-$  exciton formation, so the PSF which causes the hole-side oscillations does not occur. This provides further evidence that the overall carrier density only weakly influences the exciton binding energy in comparison to the PSF effect.

In contrast to the hole trion ( $A^+$ ), the electron trion ( $A_1^-$ ) in the  $K$ -valley does show oscillatory behavior which we attribute to the LL-filling of the  $K'$ -conduction band. Figure 3.9(a) shows the extracted  $K$ -valley optical conductivity in the vicinity of  $A_1^-$ . By careful inspection of  $A_1^-$ , we observe the appearance of two "kinks" in the peak conductivity and slight blue-shift of the resonance energy which appear at identical gate voltages

(Figure 3.9(b,c), respectively). We preliminarily assign these features as the gate-voltage locations of the half-filled LLs. We speculate that the availability of phase-space near the Fermi surface when the Fermi energy lies within a partially-filled LL will facilitate trion formation, enhance the trion oscillator strength, and renormalize the binding energy. However, this is very much a qualitative description and more study is warranted.

### 3.2.4 Landau-Fan-Type Analysis of Optical Conductance Oscillation

The above qualitative picture and supporting quantitative calculations support our assertion that electronic quantization is the driving factor in this oscillatory conductivity behavior; however, we have not provided compelling evidence that these are indeed Landau levels. A clear signature of Landau-quantization is the well-defined state degeneracy of each LL. For monolayer WSe<sub>2</sub> under out-of-plane magnetic field, which is essentially a spin-polarized 2D electron gas (more accurately, a massive Dirac fermion system), the density of available states in each LL is given by the ratio of magnetic field strength,  $B$ , to the fundamental flux quantum,  $\Phi_0 = h/e$ ,

$$n_{LL} = \frac{B}{\Phi_0} = \frac{eB}{h} \quad (3.4)$$

where  $h$  is the Planck constant and  $e$  is the electron charge. If we consider our monolayer WSe<sub>2</sub> gating device as an ideal capacitor with capacitance  $C$ , the total charge density,  $N$ , is related to the gate voltage,  $V_g$ , as  $N = CV_g/e$ . The gate voltage required to half-fill a LL with index  $n$  is thus,

$$V_g(n, B) = \left(n + \frac{1}{2}\right) \frac{e^2 B}{hC} + V_0 = \left(n + \frac{1}{2}\right) \frac{G_0 B}{2C} \quad (3.5)$$

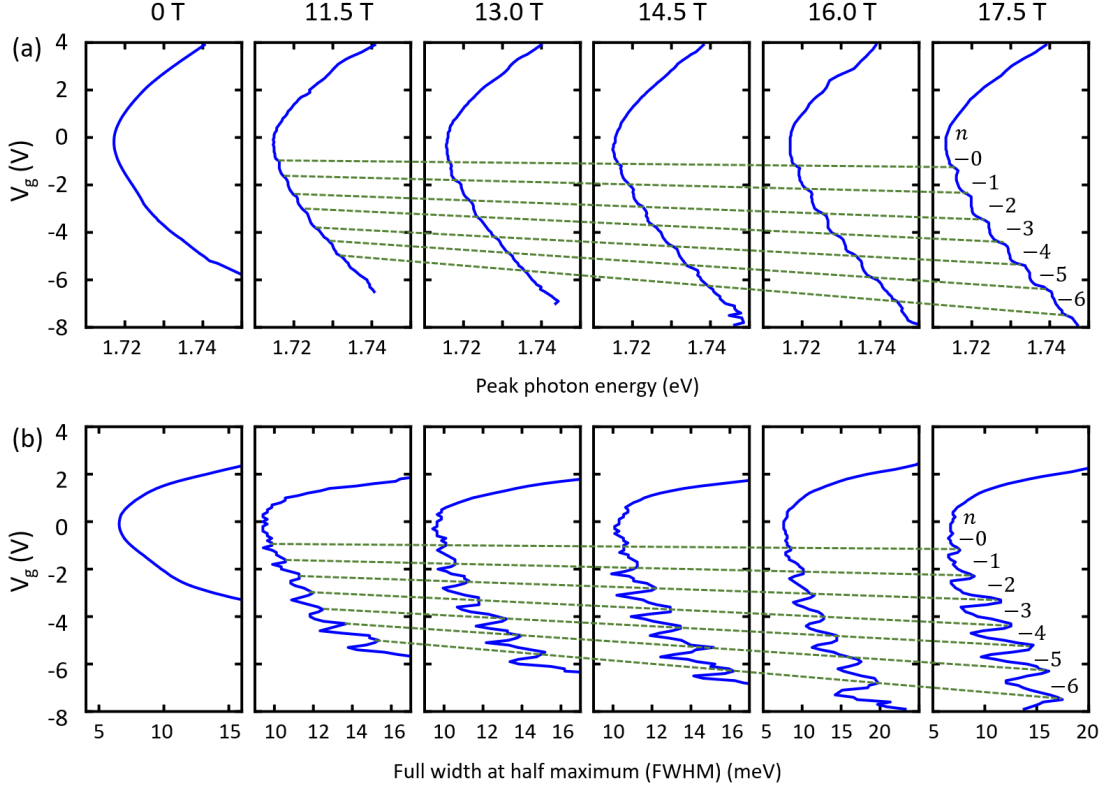


Figure 3.10: (a) Step-like energy shift and (b) FWHM oscillations of  $K$ -valley  $A^0$  extracted from optical conductivity maps (Figure 3.7) for  $B = 0 - 17.5$  T. Green dotted lines show the approximate location and linear shift of Landau level half-filling gate-voltage with increasing magnetic field.

Here,  $V_0$  is the gate voltage necessary to bring the Fermi energy to the edge of the valence (conduction) band from the charge neutrality point due to filling of defect states, *etc.*  $G_0 = 2e^2/h$  is the conductance quantum. We estimate the total device capacitance as the geometric capacitance  $C = \epsilon_0 \epsilon_{BN} / d$  where  $\epsilon_0$  is the vacuum permittivity,  $\epsilon_{BN}$  is the relative BN dielectric constant for a static field in the out-of-plane direction, and  $d = 42$  nm is the thickness of the bottom BN flake which serves as the gate dielectric measured by atomic force microscopy (AFM).

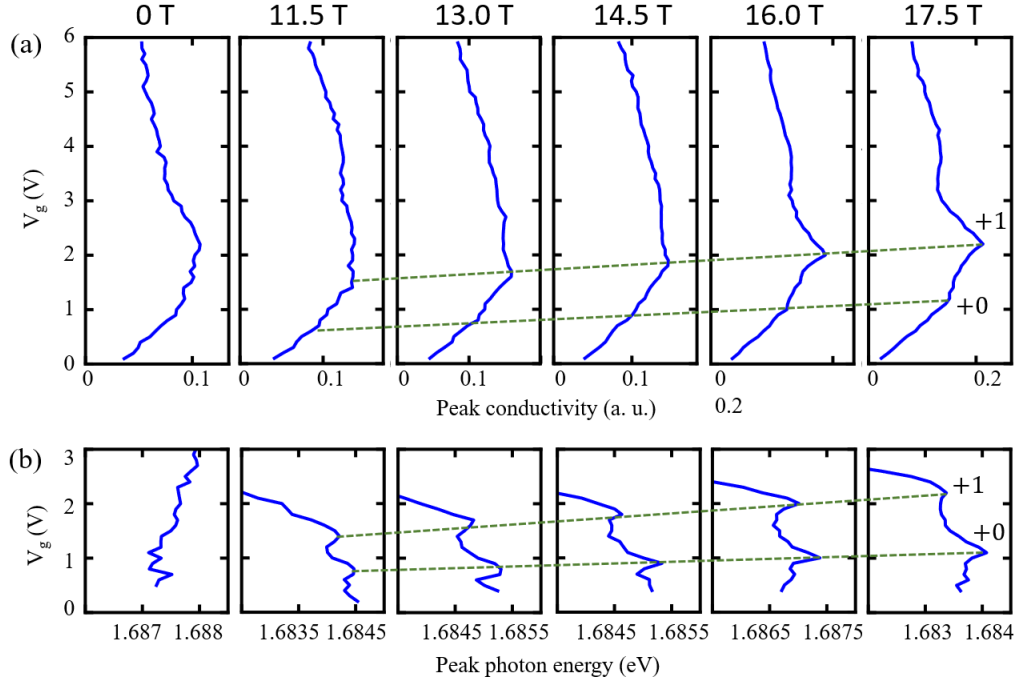


Figure 3.11: Landau-level-induced kinks in (a) peak conductivity and (b) peak photon energy of  $K$ -valley  $A_1^-$  (Figure 3.7) for  $B = 0 - 17.5$  T. Green dotted lines show the approximate location and linear shift of Landau level half-filling gate-voltage with increasing magnetic field.

If the observed step-like energy shift in  $A^0$  originates from Landau quantization, then we expect the steps to be equally separated in gate voltage and, further, that this separation voltage,  $\Delta V_g$ , should scale linearly with the magnetic field intensity. To confirm this prediction, we perform identical gate-dependent reflection constant measurements at varied  $B$  and extract the peak photon energy and FWHM as shown in Figure 3.10. We identify the gate voltage of half-filled LL,  $V_{g,LL}$ , in the valence band from the  $A^0$  FWHM maxima for each magnetic field. Similarly, we identify the gate voltage of half-filled LL in the conduction band from the local maxima of the  $A^-$  peak conductivity and energy shift as shown in Figure 3.11(a,b).

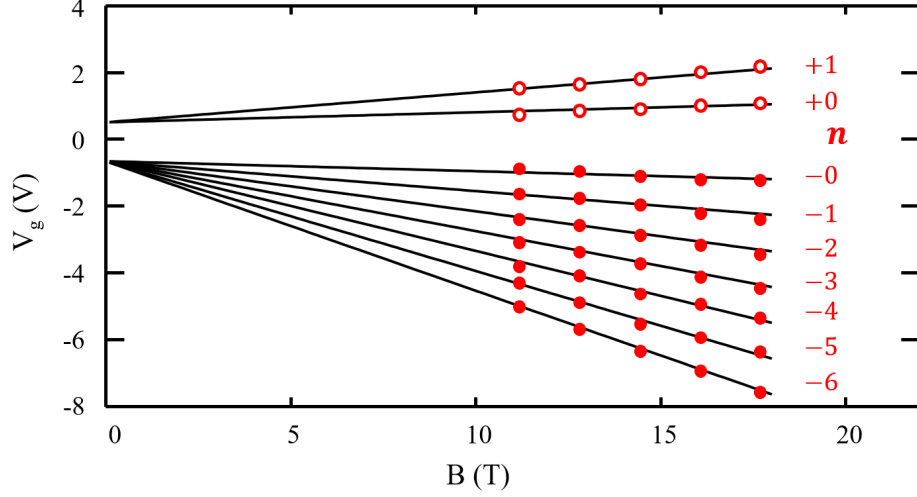


Figure 3.12: The measured gate voltages ( $V_g$ ) for Landau level (LL) half-filling in the  $K$ -valley valence band (red closed dots) and  $K'$ -valley conduction band (red open dots) as a function of magnetic field. Black lines depict the Landau fan diagram derived from fitting the data, where  $n$  is the filling factor of the corresponding LL. The fit includes a  $\Delta V_g \approx 1.2$  V gap between the half filling of  $n = \pm 0$  LLs at  $B = 0$  T which is partially due to filling of defect states inside the band gap.

We plot the collected  $V_{g,LL}$  in Figure 3.12, where red and yellow points indicate data  $A^0$  and  $A^-$ , respectively, and fit the total set of  $V_{g,LL}$  with Equation 3.5. For both electron and hole sides, we find remarkably good agreement where the observed LLs are identified as  $n = -0$  to  $-6$  in the  $K$  valence band and  $n = +0$  and  $+1$  in the  $K'$  conduction band for each  $B$ . We note that, beyond the LL index  $n$ , the only other fitting parameters are the gate-voltage offset  $V_0$  and the BN dielectric constant,  $\epsilon_{BN}$ . We find the best fit when  $V_0 = 0.5$  V and  $\epsilon_{BN} = 3.07$ . While  $V_0$  is highly device specific, depending on the defect density and electrical contact barrier, our value of  $\epsilon_{BN}$  is in excellent agreement with literature reports of thick BN flakes ( $d > 30$  nm) [66].

The observed linearity in  $B$  of the LL positions ( $V_{g,LL}$ ) in Figure 3.12 in agreement with Equation 3.5 is compelling evidence that the observed oscillations in  $A^0$  and  $A^-$

originate from *valley-polarized* LLs. Beyond the qualitative evidence linking the observed behavior to valley-polarized electronic quantization presented earlier in this section, the fitting results show quantitatively that we are filling LLs with no spin- and valley-degeneracy. The presence of either would modify the per-LL density of states. If our qualitative picture is correct, it further shows that each of the observed oscillations indicates sequential filling of LLs in a single valley without intermediate filling of the opposite valley LLs.

### 3.2.5 Landau-Quantization Observed *via* Photoluminescence

The discussion above is limited to the direct absorption (optical conductivity) properties which form only one part of the larger picture of excitonic behavior. For more comprehensive analysis, we study the effect of electronic quantization on the excitonic luminescence *via* gate-dependent magneto-PL as described in Chapter 2. PL maps of the  $K$  and  $K'$ -valley at  $B = 17.5$  T are shown in Figure 3.13(a,d), respectively. In both valleys, we label the bright exciton ( $A^0$ ) and trions ( $A^+, A_1^-, A_2^-$ ) seen in the above reflection contrast data, but also observe additional PL lines at lower energy. We identify these lower energy PL features as the *dark* excitons ( $D^0$ ), trions ( $D^\pm$ ), and associated phonon replicas which we discuss in more detail in Chapter 4. Regardless, we immediately observe clear oscillations in the PL intensity of the hole side trions without any significant oscillation of the PL energy. We note, as well, that such oscillations in PL intensity are conspicuously absent from the various electron trions with the possible exception of  $A_{1,K}^-$ . To understand the observed phenomena in detail, we examine the two valleys individually.

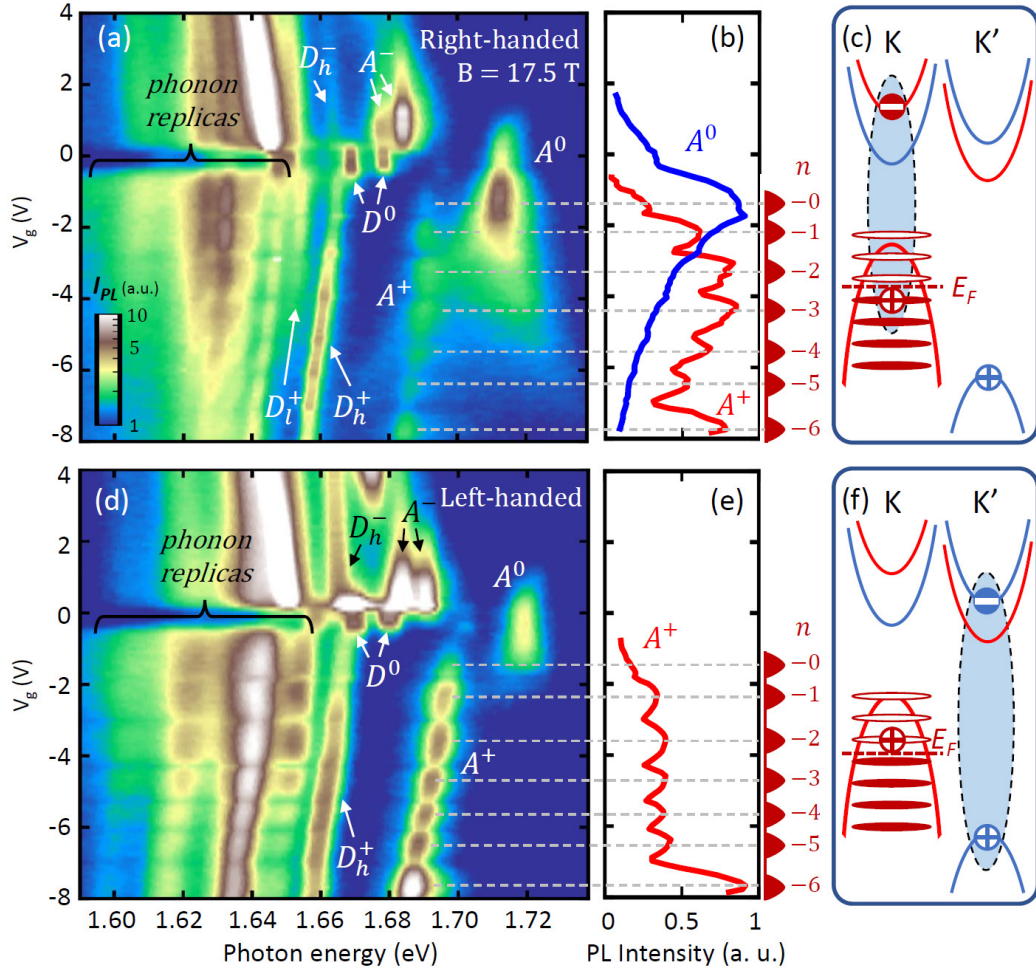


Figure 3.13: (a) The gate-dependent photoluminescence (PL) map with right-handed circular polarization, which shows the  $K$ -valley emission of bright excitonic states ( $A$ ), under 532-nm continuous laser excitation at  $B = 17.5$  T and  $T \approx 4$  k. (b) The normalized integrated PL intensity for the  $A^0$  exciton (blue) and  $A^+$  trion (red) in (a). The dashed lines denote the estimated half-filled LL positions. (c) The schematic band configuration of  $K$  valley  $A^+$  trion with the relevant LLs and Fermi energy ( $\epsilon_F$ ) under the magnetic field. The  $K'$ -valley hole comes from the laser excitation. (d)–(f) Similar figures as (a)–(c) for left-handed circular polarization, which reveals the  $K'$ -valley emission of bright excitonic states. In (a) and (d), which share the same color scale, we also observe the emission of dark excitonic states ( $D$ ) from both valleys due to their linear polarization as well as a series of phonon replicas of the dark states.

### Landau-Quantization Observed *via* PL, $K$ -valley

The  $K$ -valley PL map is shown in Figure 3.13(a). As in the optical conductivity, we observe similar persistence of  $A^0$  to high negative gate voltages as compared to the zero magnetic field case due to the valence band Zeeman splitting. The intervalley electron trion,  $A_1^-$ , is noticeably enhanced as compared to  $A_2^-$  due to the preferential filling of the  $K'$  conduction band, in good agreement with our earlier discussion. In contrast to the conductivity, however, we observe a weak signature of  $A^+$  simultaneously with  $A^0$ . The low intensity of  $A^+$  relative to  $A^0$  hints at its likely origin.

As depicted schematically in Figure 3.13(c), the  $K$ -valley  $A^+$  requires a population of holes in the  $K'$  valence band, but the Fermi energy ( $E_F$ ) cannot reach the  $K'$  valence within our studied  $V_g$  range due to the large Zeeman splitting. Thus there is no ambient population of holes to facilitate  $A^+$  formation. Unlike the direct absorption process in the reflectance contrast measurement, however, the PL measures the radiative emission of the exciton state which has a significantly longer timescale. Following above-gap photo-excitation, the *hot* electrons and holes will cool to the bottom of their respective bands (and between bands) on a much faster timescale than the exciton radiative lifetime. It is energetically favorable for a hole (electron) to relax to the highest (lowest) valence (conduction) band; however, interband relaxation processes have their own characteristic timescale. Thus, as we continuously photo-excite the system, we generate a population of transient electrons and holes which are distributed throughout the various bands. We suggest that this transient population of holes in the  $K'$  valence band allows the formation of a small  $A^+$  population despite the lack of ambient carriers.

For both the weak  $A^+$  and  $A^0$ , we observe oscillations in the PL intensity with  $V_g$ , but note that they have opposite phase. When the  $A^0$  PL is maximized, the  $A^+$  PL is minimized and vice versa. The integrated intensity of  $A^0$  and  $A^+$  are shown in Figure 3.13(b) as blue and red lines, respectively. As alluded to above, the PL intensity is proportional to the steady-state population of the corresponding exciton species. Thus, the alternating PL intensity of  $A^0$  and  $A^+$  with LL-filling suggests that the steady-state population of excitons and trions vary significantly depending on the position and extent of the Fermi energy relative to each LL. According to our discussion of the  $A^0$  conductivity linewidth oscillations, the  $A^0$  lifetime should be significantly reduced at the LL half-filling due to enhanced carrier scattering. This suggests the non-radiative relaxation rate from  $A^0$  to the lower energy  $A^+$  should be enhanced, and more generally that the direct formation of  $A^+$  should be favored. We study only the steady-state PL here and thus cannot distinguish these trion formation processes, but we suggest that this could be addressed through two-color pump-probe spectroscopy experiment under quantizing magnetic field. Regardless, this qualitative picture explains the contrasting PL intensity oscillations of  $A^0$  and  $A^+$  and allows use to identify the position of LL half-filling *via* PL to complement the reflection contrast experiment.

### **Landau-Quantization Observed *via* PL, $K'$ -valley**

Next, we examine the  $K'$ -valley PL. Figure 3.13(d) shows the  $K'$ -valley PL map at  $B = 17.5$  T. Similar to the optical conductance,  $A^0$  is suppressed and  $A^+$  appears immediately with negative gating. As shown schematically in Figure 3.13(f) and discussed above, the  $K$  valence band immediately accumulates ambient holes which allow efficient

$A^+$  trion formation. When the Fermi energy lies between two LL, however, the available phase space for carrier interactions is minimized which should suppress the  $A^+$  formation rate due to reduced carrier scattering. The predicted oscillatory behavior is reflected in our experimental data. The integrated intensity of  $A^+$  is shown in Figure 3.13(e) where we highlight the LL half-filling positions which coincide with PL maxima. Each of the  $A^+$  PL intensity maxima are relatively equal, but the last PL intensity maximum at  $V_g \approx -7.8$  V is significantly enhanced. We attribute this PL enhancement to the initial filling of the  $K'$  valence band, when the Fermi energy reaches the first  $K'$ -valley LL. In this scenario, the simultaneous filling of LL in both valleys facilitates inter-valley scattering which enhances trion formation and should smooth the observed LL-related PL intensity oscillations.

To study the evolution of the Zeeman shift and LL-formation in detail, we measure the  $K'$ -valley PL for a wide range of magnetic field intensity. PL maps highlighting the bright exciton and trions are shown in Figure 3.14 for  $B = 5.5$  T to  $B = 17.5$  T. We observe three phenomena with increasing magnetic field. First, the appearance and subsequent spreading in  $V_g$  of the LL-related oscillations in  $A^+$ . Second, The progressive suppression of  $A_1^-$  and enhancement of  $A_2^-$  as the  $K$  conduction band is shifted above that in  $K'$  thus favoring the formation of the intravalley  $A_2^-$ . Third, the gate voltage at which the  $A^+$  PL intensity suddenly increases and the LL-related oscillations are obscured,  $V_{g,K'}$ , shifts approximately linearly with  $B$ . This linear shift with  $B$  is in general agreement with our expectations for Zeeman-shift-related valence band splitting. We note that the transition between filling a single valley and filling both valleys varies significantly with  $B$ . For  $B = 10$  T, we observe a series of approximately equal-intensity oscillations before the

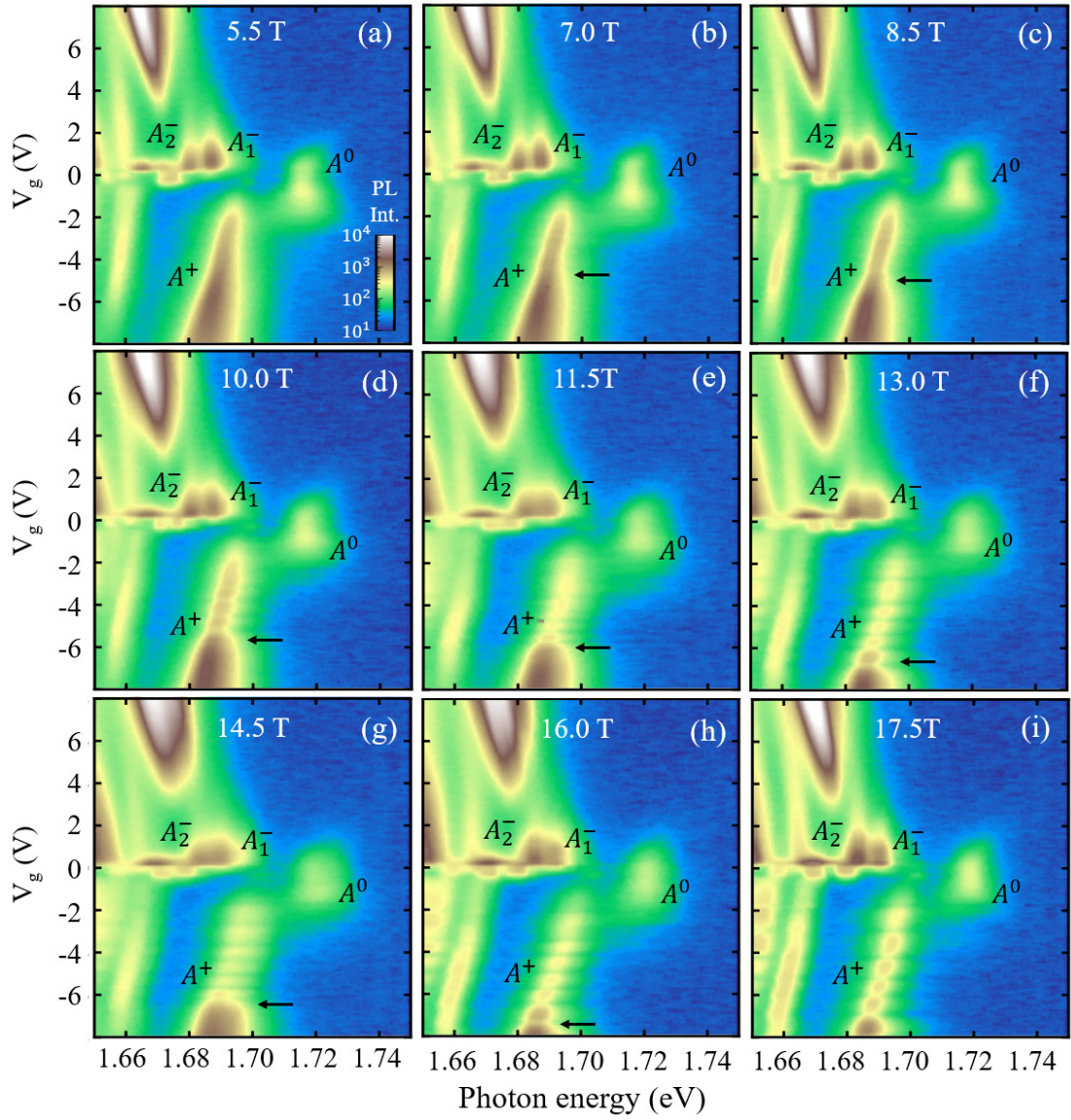


Figure 3.14: (a-l) Gate-dependent photoluminescence (PL) intensity maps for the K-valley states in monolayer WSe<sub>2</sub> under magnetic field  $B = 0$  to 17.5 T. The sample temperature is  $T = 4$  K. All of the maps share the same logarithmic color scale bar in panel (a). The black arrows denote an increase of the  $A^+$  PL intensity.

$A^+$  PL intensity suddenly increases and the observed oscillations vanish. For  $B = 13$  T and  $B = 16$  T, the final PL intensity maximum ( $n = -6$ ) is enhanced relative to the others but is followed by a final local intensity minimum. Qualitatively, this behavior suggests a complex overlap of the final  $K$ -valley polarized LL and the  $n = -1$  LL in the  $K'$ -valley which depends on  $B$  and the charge density.

### 3.2.6 Divergence from the Single-particle Model

Figure 3.5(a) schematically shows the relative band configuration and Landau level arrangement as predicted by the single particle model for monolayer TMDs which we discussed in Chapter 1. In the model, the Zeeman shift of an electronic band,  $\Delta E_{band}$  is proportional to the band  $g$ -factor,  $g_{band}$ :

$$\Delta E_{band} = \mu_B B \left( 2 \cdot \mathbf{S} + \mathbf{m}_{\text{orbital}} + \tau \frac{m_e}{m^*} \right) \quad (3.6)$$

Here,  $\mathbf{S} = \pm 1/2$  is the spin of the band,  $\mathbf{m}_{\text{orbital}} = \pm 2$  (0) is the orbital magnetic quantum number for the valence (conduction) bands,  $\tau = \pm 1$  is the valley index for the  $K$  ( $K'$ ) valley,  $m_e$  is the electron mass, and  $m^*$  is the carrier effective mass. The Landau levels are separated in energy proportional to the cyclotron frequency,  $\omega_c$ . The energy separation between each LL is:

$$\Delta E_{LL} = \hbar \omega_c = \hbar \frac{eB}{m^*} = 2 \frac{m_0}{m^*} \mu_B B \quad (3.7)$$

where  $e$  is the elementary charge. If we add the effect of the Zeeman shift to the LL energy, we can derive expressions for the valence band LL energies in each valley where we define  $E = 0$  as the charge neutrality point.

$$E_{LL,K}(n_K, B) = \mu B \left[ 5 + (1 + n_K) \frac{m_0}{m^*} \right] \quad (3.8)$$

$$E_{LL,K'}(n_{K'}, B) = -\mu B \left[ 5 + (n_{K'}) \frac{m_0}{m^*} \right] \quad (3.9)$$

Here,  $n_K$  ( $n_{K'}$ ) are the LL indices for the  $K$  ( $K'$ ) valence band. Using the valence band hole effective mass,  $m_h^* \approx 0.4$ , we find that three  $K$ -valley LLs lie above the  $K'$ -valley band-edge LL ( $n = -1$ ). We thus predict the three  $K$ -valley polarized valence band LLs as depicted in Figure 3.5(a).

However, as discussed above and summarized in Figure 3.5(b), our experimental results suggest the presence of at least *seven*  $K$ -valley polarized LLs in the valence band. In both reflection contrast Figure 3.7 and Figure 3.14 measurements we identify valley-polarized valence band LLs with index  $n = -0$  to  $n = -6$ . This implies a significant enhancement ( $\geq \times 2.3$ ) of the valence band  $g$ -factor as compared to the predictions of the single particle model. We note that Equation 3.6 is well-tested near the band edge. Divergence from this model in our gate-tunable device at moderate injected charge density suggests the presence of significant multi-body interactions which modify the valence band  $g$ -factor.

Likewise, the single particle model predicts one valley-polarized LL in the conduction band, but we observe at least two valley-polarized LLs in the optical conductivity of  $A_K^-$ . This suggests that significant  $g$ -factor enhancement occurs in the conduction bands with electron doping, as well.

### 3.2.7 Conclusion

In summary, we used high-quality monolayer WSe<sub>2</sub> gating devices with variable carrier density under high magnetic field to study the influence of Landau quantization on the exciton and trion. We observed charge-density-dependent quantum oscillations of the bright and dark exciton (trion) species in both reflectance contrast and photoluminescence spectroscopy. Our results highlight the complex interaction between excitons and ambient carriers which may be controlled by Landau level filling and which diverges from the standard single-particle model in the regime of moderate charge density. This divergence suggests the presence of significant many-body interactions in monolayer WSe<sub>2</sub> which make this material a promising system in which to explore correlated quantum phenomena.

## Chapter 4

# Dark Excitonic States and Phonon Replicas in Monolayer WSe<sub>2</sub>

In the gate-dependent photoluminescence (PL) data shown in the earlier chapters, we notice the presence of several excitonic features with lower PL energy than the bright exciton (trion) species identified thus far. A closer examination of the band configuration near bandgap at the  $K$ - and  $K'$ -points strongly hints at the origin of these PL features. Figure 4.1(a) shows a schematic of the  $K$ -valley bright exciton ( $A^0$ ) configuration - we notice that the separation between the lower conduction subband (spin down) and the valence band (spin up) form the lowest energy band gap. Exciton (and, for that matter trions) formation is not forbidden for an electron-hole pair between these bands. For clarity, we show the configurations of possible exciton, electron trion, and hole trion formed from the lower conduction subband in Figure 4.1(b-d).

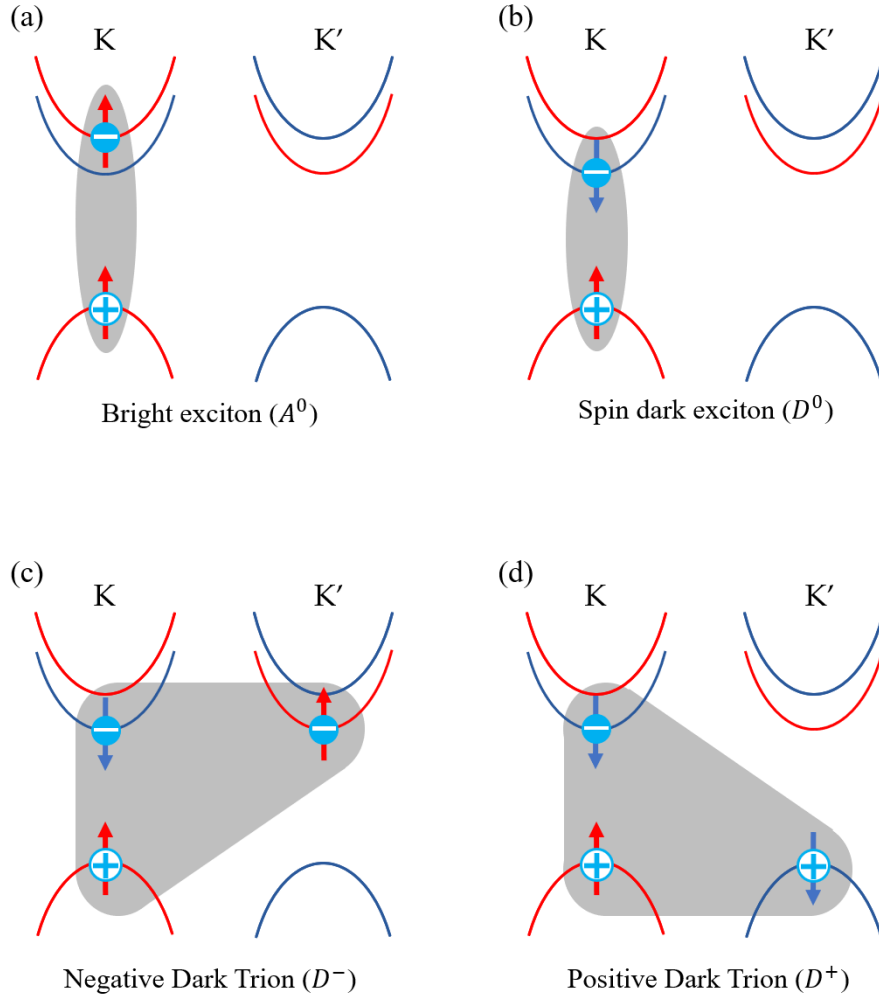


Figure 4.1: Schematic configurations of the (a) bright neutral exciton  $A^0$ , (b) spin-forbidden dark neutral exciton  $D^0$ , (c) negative (electron) dark trion  $D^-$ , and (d) positive (hole) dark trion  $D^+$  in monolayer WSe<sub>2</sub>. In contrast to the bright electron trion which shows observable reflectance and photoluminescence for the intervalley  $A_1^-$  and intravalley  $A_2^-$  configurations, the dark trion exhibits only a intervalley configuration. The intravalley configuration is unfavorable due to Pauli blocking as the dark-exciton-forming electron occupies the lower  $K$ -valley conduction subband.

## 4.1 Optical Selection Rules for the Dark Trion in Monolayer WSe<sub>2</sub>

We ignored this state previously because our analysis of the optical selection rules indicated that this transition is not dipole allowed with absorption of normally-incident light. If we re-examine that analysis more closely, we find that the transition between the lower conduction subband and valence band is actually dipole allowed for linearly polarized light which propagates along the 2D plane ( $\hat{P}_z$ ).

$$\langle C_3\psi_{c_{1,\downarrow}} | C_3\hat{P}_z C_3^{-1} | C_3\psi_{v_{1,\uparrow}} \rangle = e^{-i\frac{\pi}{3}} e^{i\frac{\pi}{3}} \langle C_3\psi_{c_{1,\downarrow}} | C_3\hat{P}_z C_3^{-1} | C_3\psi_{v_{1,\uparrow}} \rangle \quad (4.1)$$

$$= \langle \psi_{c_{1,\downarrow}} | \hat{P}_z | \psi_{v_{1,\uparrow}} \rangle \quad (4.2)$$

$$\langle \sigma_h\psi_{c_{1,\downarrow}} | \sigma_h\hat{P}_z\sigma_h^{-1} | \sigma_h\psi_{v_{1,\uparrow}} \rangle = (-i)(-1)(i) \langle \sigma_h\psi_{c_{1,\downarrow}} | \sigma_h\hat{P}_z\sigma_h^{-1} | \sigma_h\psi_{v_{1,\uparrow}} \rangle \quad (4.3)$$

$$= \langle \psi_{c_{1,\downarrow}} | \hat{P}_z | \psi_{v_{1,\uparrow}} \rangle \quad (4.4)$$

However, the two bands are still of opposite spin. To excite an electron between the bands its spin must be flipped which cannot be accomplished by absorption of a linearly polarized photon. The exciton state should therefore be optically dark, despite the symmetry analysis. Previously, this spin dark exciton was brightened and measured by out-of-plane optical spectroscopy through the use of large in-plane magnetic field [27, 67]. In this scheme, the magnetic field alters the spin of the bands such that they are no longer strictly spin up or down. The transition is then spin-allowed. However, ours and previous measurements without magnetic field show a faint dark exciton PL with out-of-plane detection [36–39, 68, 69] and strong dark exciton PL using more complicated in-plane detection techniques [70–73].

We can again understand this activity by symmetry analysis: the next highest conduction band,  $c_2$ , has  $d_{-1}$  orbital symmetry as compared to the  $d_0$  orbital symmetry of  $c_1$ . Thus when we include the spin splitting,  $c_{1,\downarrow}$  has identical symmetry to the opposite spin  $c_{2,\uparrow}$  (similarly,  $c_{1,\uparrow}$  and  $c_{2,\downarrow}$ ). These bands with identical symmetry can mix through the spin-orbit coupling.

$$|\bar{c}_{1,\downarrow}\rangle = |c_{1,\downarrow}\rangle + \frac{\langle c_{2,\uparrow} | \hat{\alpha}_{soc} | c_{1,\downarrow} \rangle}{E_{c_{1,\downarrow}} - E_{c_{2,\uparrow}}} |c_{2,\uparrow}\rangle \quad (4.5)$$

Here,  $\bar{c}_{1,\downarrow}$  is the modified lowest conduction subband in the  $K$ -valley which is majority spin down but has a small spin up component.  $\hat{\alpha}_{soc}$  represents the spin orbit coupling operator between the  $c_1$  and  $c_2$  bands. As the conduction bands are no longer pure spin (up, down) states, the electronic transition from the valence band is not completely spin-forbidden. Thus, the transition is allowed with the absorption of a photon with  $\hat{P}_z$  polarization.

#### 4.1.1 Optical Detection of In-Plane-Emission Photoluminescence

The derived in-plane optical selection rules do not obviously explain our detection of the spin dark exciton emission using an out-of-plane (primarily  $\hat{P}_{\pm}$ ) detection scheme. For this measurement, we use an objective lens with large numerical aperture ( $N.A. \sim 0.6$ ) [68, 69]. The in-plane emission of the spin dark exciton truly radiates from the center in the 2D plane with some non-zero solid angle, some of which overlaps with the solid angle of the objective lens detection cone. Therefore, we can detect a small percentage of the total in-plane emission from the dark exciton using our out-of-plane detection scheme. In principle, we can also excite the spin dark exciton transition directly with similarly low efficiency; however, it does not appear in our absorption measurement. As the PL intensity

is proportional to both the detection efficiency and the steady-state exciton population, we thus conclude that the spin dark exciton accumulates a large steady-state population due to non-radiative relaxation from higher energy states and the long lifetime of the dark states as compared to the bright states ( $> 100$  ps compared to  $< 10$  ps [68, 71, 74]). This allows the spin dark exciton to have measurable intensity despite the low detection efficiency.

## 4.2 Gate-Tunable Dark Trions in Monolayer WSe<sub>2</sub>

We have argued for the detectability of the spin dark exciton and corresponding trions in our measurement scheme - in the remainder of this section we show experimental results and analysis which substantiate this argument and further characterize the spin dark exciton,  $D^0$ , and trions.  $D^-$ ,  $D^+$ .

### 4.2.1 Methodology

The data in this section is steady-state and time-resolved photoluminescence of BN-encapsulated monolayer WSe<sub>2</sub> gating devices. The devices were fabricated using the dry transfer process described in Chapter 2. All steady-state data shown was measured at  $T = 4$  K using the resistive magneto-optical cryostat system (Cell 9, NHMFL) described in Chapter 2, except the temperature dependent data (Figure 4.3) which was measured using the optical microscope system described in Chapter 2.2. In both cases, we use an excitation laser with 532-nm wavelength. The time-resolved PL data (Figure 4.5) was measured using the single-photon-counting TRPL system with 76 MHz, 515-nm excitation laser described in Chapter 2.

### 4.2.2 Gate-Dependent Photoluminescence at Zero-Field

Figure 4.2(a) shows a gate-dependent photoluminescence data of our monolayer WSe<sub>2</sub> device. We plot the PL intensity (counts) with a logarithmic false color map. At the charge neutrality point ( $V_g = -0.50$  V) we observe the bright A exciton ( $A^0$ ) at 1.712 meV. With electron doping ( $V_g = -0.25 - 0.5$  V) the  $A^0$  exciton is quickly suppressed and two negative bright trions ( $A_1^-, A_2^-$ ) appear. Similarly, a positive bright trion ( $A^+$ ) appears with hole doping ( $V_g < -1.0$  V). The bright trion binding energies are 21 meV, 29 meV, and 35 meV, respectively, which is in good agreement with previous studies [7].

In addition to the bright exciton at charge neutrality, we observe another weak PL feature at 1.671 eV,  $\sim 41$  meV below the  $A^0$  PL energy. According to prior research, we identify this feature as the dark exciton ( $D^0$ ) [27, 70]. Similar to the bright exciton, the  $D^0$  line is quickly suppressed upon electron or hole injection at which point two new peaks appear – one on the electron side at 16 meV below the  $D^0$  energy and the other on the hole side at 14 meV below  $D^0$ . We label these features as  $D^-$  and  $D^+$ , respectively. Both new features exhibit approximately linear PL intensity with increasing excitation power which excludes any association with biexcitons which exhibit quadratic power dependence [36–39]. In the rest of this chapter we will discuss further evidence that the  $D^-$  and  $D^+$  features are properly identified as dark trions.

We first examine the gate-dependence of the  $D^0$ ,  $D^-$ , and  $D^+$  PL lines. For quantitative analysis, we fit the photoluminescence spectra with a series of Lorentzian functions which correspond to each observed PL line. We plot the gate-dependent integrated intensity, PL energy, and full width at half maximum (FWHM) of each exciton feature in

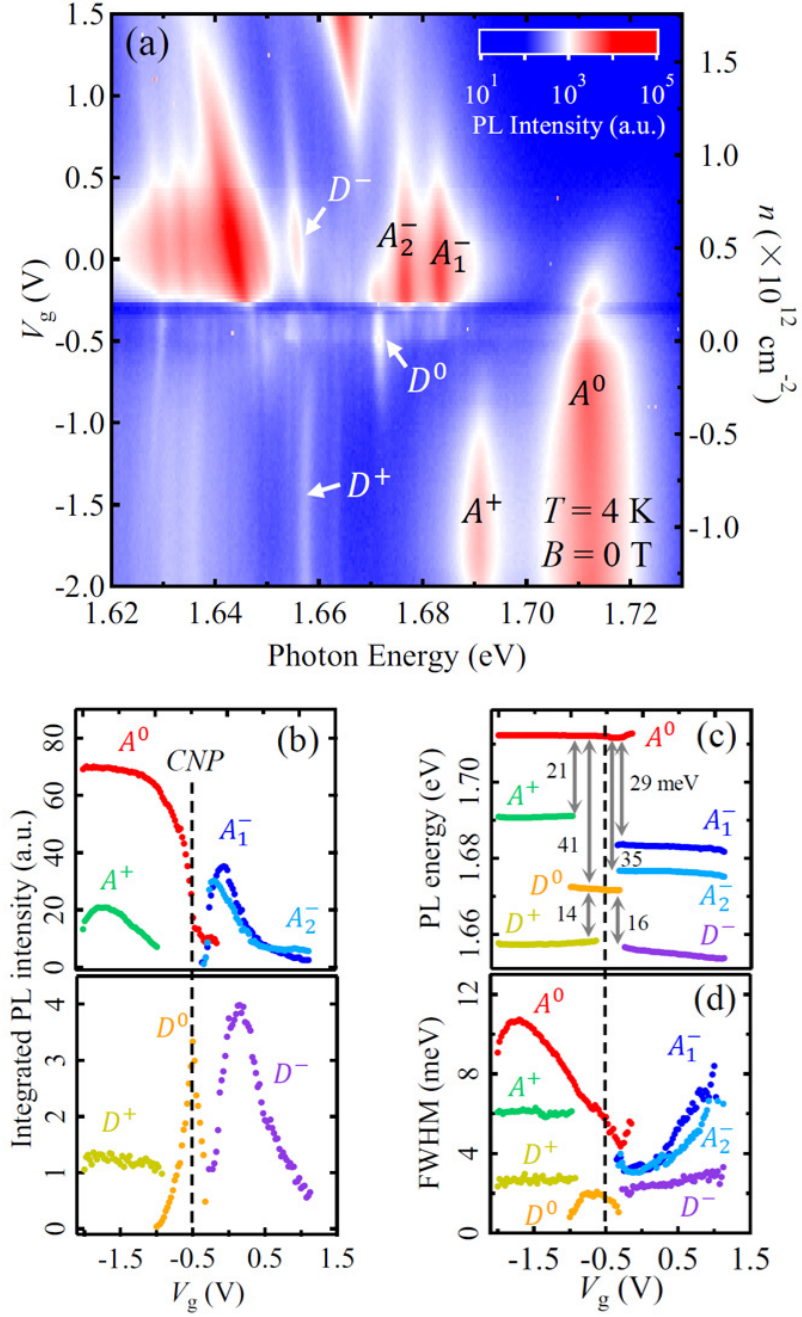


Figure 4.2: (a) Gate-dependent PL map of BN-encapsulated monolayer WSe<sub>2</sub> (device 1) at  $T = 4 \text{ K}$  and  $B = 0 \text{ T}$  under 532-nm continuous laser excitation. (b) The extracted PL integrated intensity, (c) PL energy, (d) PL full width at half maximum (FWHM) of both dark and bright excitons and trions as a function of gate voltage. The numbers in (c) denote the energy separation in units of meV. The dashed lines denote the charge neutrality point (CNP)

Figure 4.2(b-d). The dark species ( $D^0$ ,  $D^-$ ,  $D^+$ ) exhibit approximately analogous behavior to their bright counterparts ( $A^0$ ,  $A^-$ ,  $A^+$ ) in each respect. For example, the intensities of  $D^-$ ,  $A_1^-$ , and  $A_2^-$  each rise quickly to maxima near  $V_g = 0.2$  V and then rapidly fall. Likewise,  $D^+$  and  $A^+$  appear at a similar voltage  $V_g = -0.75$  V. Such parallel behavior suggests that  $D^+$  and  $D^-$  are approximately the dark analogs of the bright trions. We note, as well, that the energy separation between the dark trion,  $D^0$ , and the  $D^-$  and  $D^+$  features are 14 meV and 16 meV, respectively. This is in good agreement with both previously reported [27] and the theoretically predicted [75] binding energy of dark trions in monolayer WSe<sub>2</sub>.

### 4.2.3 Temperature Dependent Photoluminescence

Second, we investigate the temperature dependence of the dark and bright trion species. Figure 4.3 shows temperature dependent photoluminescence for  $T = 5 - 75$  K at fixed gate voltage,  $V_g = -2.0$  V. The  $D^+$  and  $A^+$  PL lines exhibit nearly opposite temperature dependence. When the sample temperature is decreased, the bright trion PL intensity drops sharply – in agreement with previous studies [76]. In contrast, the dark trion PL is initially unobserved but appears at  $T < 50$  K and continues to brighten with temperature reduction. We attribute this behavior to the different energy levels of the bright and dark trion species. The fundamental dark trion energy level lies below that of the bright trion. At low temperature, where the thermal energy is much less than the energy difference between the bright and dark exciton states, non-radiative relaxation processes will result in large population transfer to the dark state. In particular, the bright exciton population may be efficiently funneled to the dark state before it is able to relax radiatively. Thus, the dark state will accumulate a large steady-state population and produce intense PL. Despite

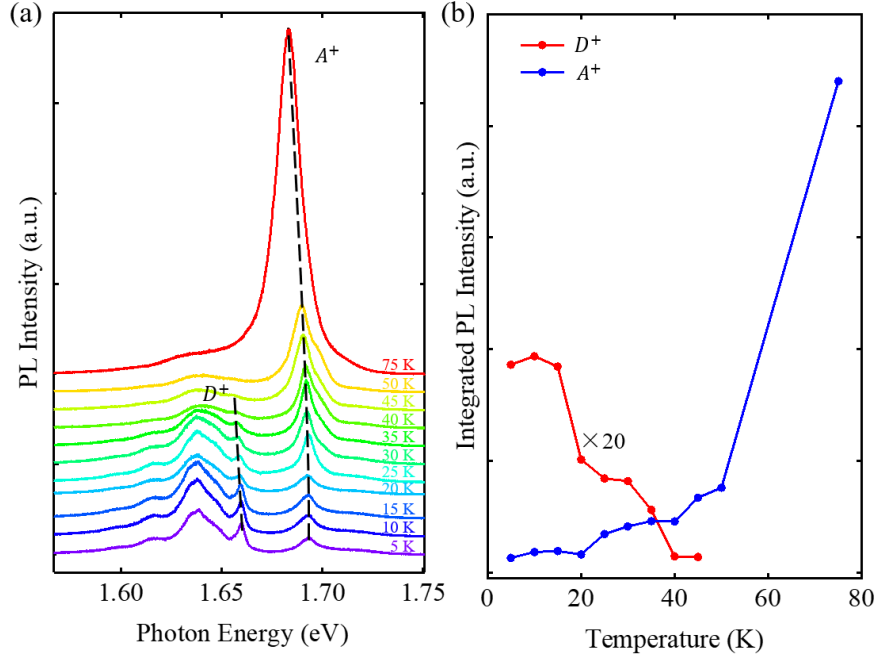


Figure 4.3: Temperature-dependent PL of bright and dark triions in monolayer  $\text{WSe}_2$ . (a) PL spectra at different temperatures from 5 to 75 K. (b) The integrated PL intensity of dark triion ( $D^+$ ) and bright triion ( $A^+$ ) as a function of temperature. The gate voltage is  $V_g = -2$  V.

this large population, we still observe comparable PL intensity from the bright and dark states at 5 K. We attribute this to inherent inefficiency of our measurement geometry. As noted above, our high N.A. objective lens can collect only a small percentage of the dark exciton's in-plane emission. Regardless, the low-temperature PL enhancement of the dark triion is in line with our expectations.

#### 4.2.4 Gate-dependent Magnetophotoluminescence

We expect the dark triion to inherit two further properties of its parent state - linearly-polarized photoluminescence from both valleys due to the optical selection rules

and an enhanced  $g$  factor relative to the bright exciton ( $\sim 8$  vs.  $4$ ) due to the spin-triplet configuration of the dark exciton. To confirm these characteristics, we apply strong out-of-plane magnetic field and examine the relative energy shift of the bright and dark exciton species. As discussed in Chapter 1, the exciton valley degeneracy in WSe<sub>2</sub> is lifted under out-of-plane magnetic field by the valley Zeeman effect. The  $K$ - and  $K'$ -localized excitons will exhibit linear magnetic-field-induced energy split which is proportional to the exciton  $g$ -factor. We illustrate the valley Zeeman shift of the dark exciton schematically in Figure 4.4(a).

Figure 4.4(b) shows the gate-dependent PL map at  $B = -10$  T. As described in Section 4.2.1, we collect only right-circularly polarized PL which corresponds to bright exciton emission from the  $K$ -valley. We observe only one PL line for each of  $A^0$ ,  $A^+$ , and  $A_{1,2}^-$  which are shifted from their  $B = 0$  T energies by the valley Zeeman shift. The dark trions are expected to emit linearly polarized light from both valleys, however, so we should detect PL from both valleys simultaneously.  $D^0$ ,  $D^+$ , and  $D^-$  are split into two PL lines whose intensity is relatively unchanged when detecting right- and left-circularly polarized light. This suggests that  $D^0$ ,  $D^+$ , and  $D^-$  emit linearly polarized PL. We further examine the magnetic-field-dependent PL from  $B = -31$  T -  $31$  T on the electrons side ( $V_g = 0.1$  V) and at the charge neutrality point ( $V_g = -0.5$  V) in Figure 4.4(c,d), respectively. We observe bright exciton (trion) emission from only one valley which shifts linearly with magnetic field intensity. In contrast, we observe a cross-like energy shift of the dark exciton (trion) which indicates PL emission from both the  $K$  and  $K'$  valleys.

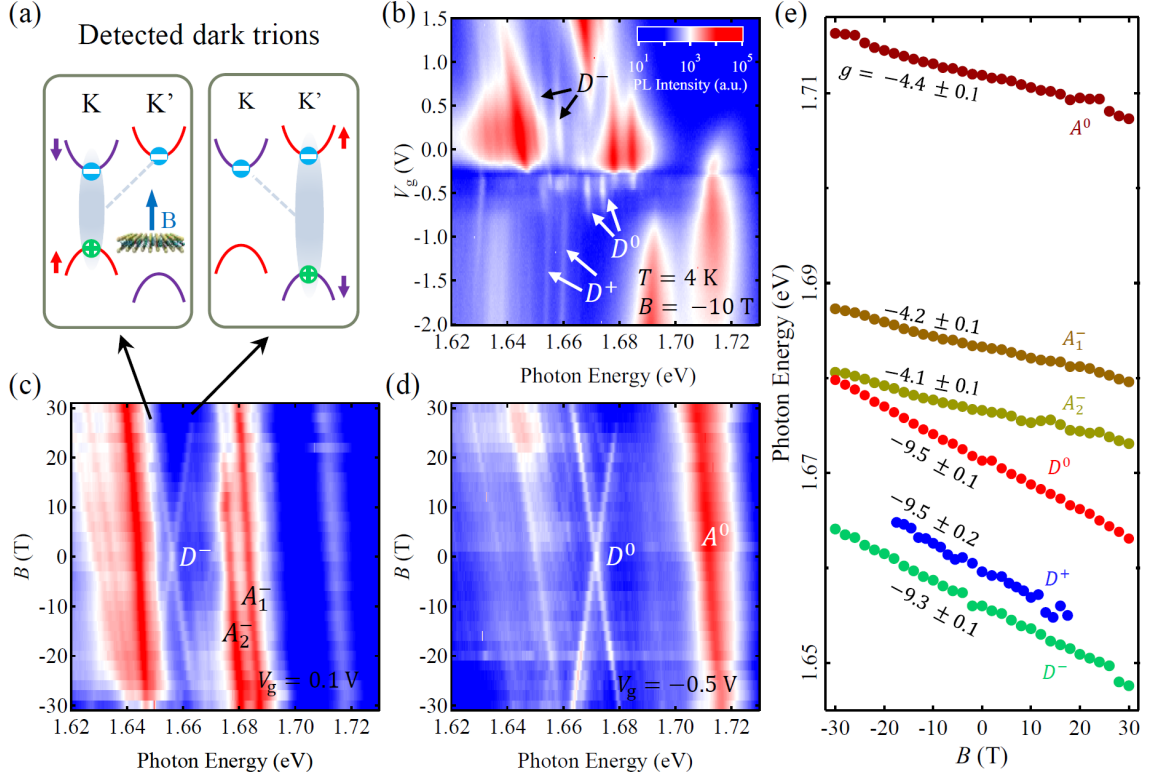


Figure 4.4: (a) Negative dark triions detected in our magneto-PL experiment. (b) The PL map of monolayer WSe<sub>2</sub> (device 1) at  $B = -10$  T under unpolarized optical excitation and right-handed PL detection. Dark excitons and triions are split into two peaks, whereas bright excitons and triions are not. (c),(d) The B-dependent PL map at the electron side ( $V_g = 0.1$  V) and charge neutrality point ( $V_g = -0.5$  V). (b)-(d) share the same color scale bar. (e) The excitons and trion Zeeman shifts. The  $g$ -factors are extracted by linear fits of the energy difference between the positive and negative magnetic field.

#### 4.2.5 Gate-Dependent Photoluminescence Lifetime of Dark Triions

To quantitatively analyze the valley Zeeman shift of the bright and dark exciton (trion) PL lines, we fit each spectra with a series of Lorentzian functions corresponding to each feature of interest (e.g.,  $A^0$ ,  $D^0$ ,  $D^+$ , ...) and extract the center frequency as a function of magnetic field. We plot the extracted peak frequencies for each exciton (trion) state in Figure 4.4(e). Each feature exhibits approximately linear magnetic field dependence. We thus perform a linear fit on each line to determine the experimental  $g$ -factor, which are

shown next to each line in the figure. The bright exciton and trions exhibit  $g$ -factors from  $-4.1$  to  $-4.4$  which matches our prediction ( $g \approx -4$ ) from the spin and orbital configurations and previous research. In contrast, the dark exciton and trion exhibit  $g$ -factors from  $-9.3$  to  $-9.5$ . This enhancement of valley Zeeman shift relative to the bright states is in line with our predictions ( $g \approx -8$ ) and previous study of the dark exciton. We therefore confirm that both the linearly polarized PL emission and enhanced  $g$ -factor characteristics of the dark exciton are inherited by the dark trion.

Finally, the dark exciton and trion are expected to exhibit significantly enhanced lifetime relative to the bright states due to the spin-triplet configuration [68]. The reduced FWHM of the dark trions relative to the bright states (Figure 4.2(d)) is tangential evidence of this lifetime enhancement, but more direct confirmation is needed. To measure the PL lifetime directly, we use time-resolved photoluminescence of the dark trion states *via* the time-correlated single photon counting (TCSPC) method described in Chapter 2. We plot the time-resolved PL traces of  $A^+$ ,  $D^+$ , and instrument response function (IRF) in Figure 4.5(a). After deconvolution with the IRF, each of the trion PL traces is well-fit by a single exponential decay. We first extract a bright trion ( $A^+$ ) lifetime of  $\sim 10$  ps which is in agreement with previous studies [68]. The dark trion,  $D^+$ , exhibits significantly longer lifetime. At  $V_g = -0.8$  V, we extract a  $D^+$  lifetime of 1270 ps - over two orders of magnitude longer than the bright exciton/trion (1 – 10 ps) and one order of magnitude longer than the dark exciton (180 ps).

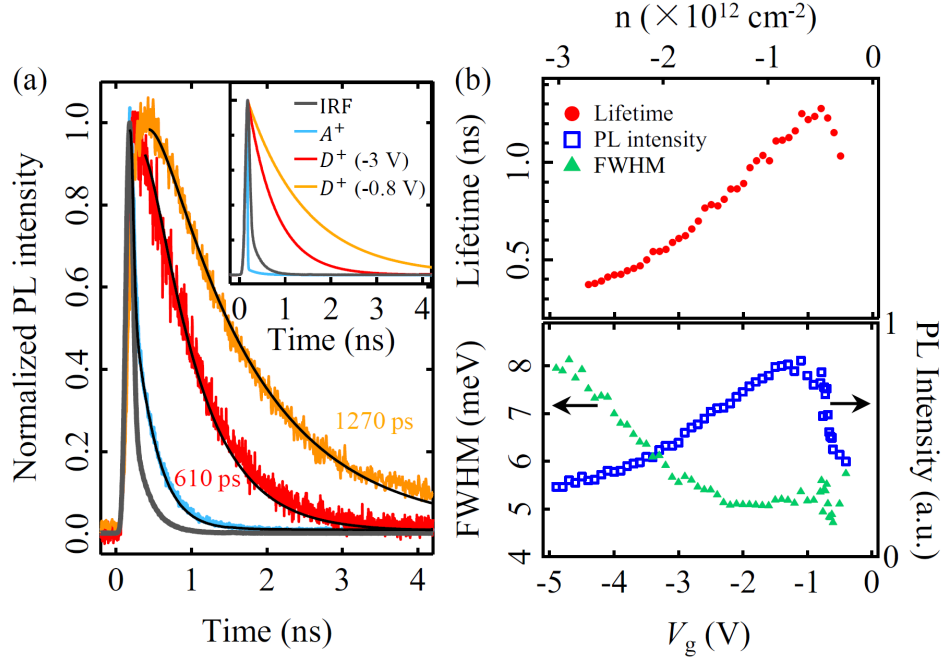


Figure 4.5: (a) Time-resolved PL for the  $A^+$  bright trion and  $D^+$  dark trion in BN-encapsulated monolayer WSe $_2$  (device 2). The black solid line is the instrument response function (IRF). We fit the  $D^+$  and  $A^+$  data, respectively, with single-exponential and bi-exponential functions convolved with the IRF (dashed lines). (Inset) The deconvolved fits. The  $D^+$  lifetime is 1270 and 610 ps at gate voltages  $V_g = -0.8$  V and  $-3$  V, respectively. The  $A^+$  lifetime is  $\sim 10$  ps. (b) The lifetime, PL intensity, and FWHM of the  $D^+$  trion as a function of gate voltage.

We further observe that the PL lifetime of  $D^+$  is tunable with gate voltage. At  $V_g = -3$  V, we extract a  $D^+$  lifetime of 610 ps. To explore this gate-tunability more fully, we systematically measure the  $D^+$  PL lifetime as a function of gate voltage from  $V_g = 0$  to  $-5$  V which we show in Figure 4.5(b) along with the integrated intensity and FWHM. The PL lifetime and intensity of  $D^+$  initially rise with increasing hole concentration from  $V_g = 0$  V to maxima at  $V_g \sim -1$  V. The PL lifetime and intensity are suppressed with further hole injection.  $D^+$  also experiences significant broadening for  $V_g < -2.5$  V as shown by the increase in FWHM from  $\sim 5$  meV at  $V_g = -2.5$  V to  $\sim 8$  meV at  $V_g = -5$

V. We qualitatively understand the gate-dependence of  $D^+$  based on interactions between ambient holes and the exciton / trion. Trion formation requires the presence of ambient carriers - thus, the initial maximum in PL intensity and lifetime is related to the onset of the trion as the dominant state over the neutral exciton. As the hole density increases further, however, the relative density of ambient holes to trions will lead to frequent trion-carrier scattering. This scattering will decrease the trion lifetime, suppress the PL as the primary relaxation pathway, and broaden the PL emission.

#### 4.2.6 Conclusion

In summary, we studied the zero-field and magnetic-field-dependent photoluminescence spectra in high quality monolayer WSe<sub>2</sub> gating devices and observed clear, continuously-tunable *dark trions*  $D^-, D^+$  which we identify as the trions of the spin dark exciton  $D^0$ . At zero magnetic field, we measured the binding energies of the dark exciton (trion) states and demonstrate the exceptionally long and gate-tunable recombination lifetime of the dark trion in comparison to the bright trions (up to 1.2 ns vs. 10 ps). Using magneto-optical PL, we confirmed the spin-triplet configuration of the dark trion by measuring the  $g$ -factors of each dark state  $g \sim 9.5$ .

### 4.3 Valley-selective Chiral Phonon Replicas of Dark Excitons and Trions in Monolayer WSe<sub>2</sub>

The dark excitons and trions discussed above exhibit many attractive properties for fundamental study and future technological application. In comparison to the bright excitonic states with short lifetime and limited valley polarization, the dark exciton (trion) have long lifetimes and strong valley coherence due to the spin-triplet configuration which suppresses intervalley exchange coupling [7]. The dark states also lie at a lower energy than their bright counterparts, and thus can accumulate a relatively large, long-lived steady-state population. Together, these characteristics make the dark excitonic states good candidates to explore multi-body interactions such as exciton condensation and realize exciton manipulation such as excitonic transport.

As shown in the previous section, however, study of the dark exciton states is complicated by their distinct optical selection rules. While the bright exciton states interact strongly with normally-incident light and exhibit optical valley selectivity ( $K$ - and  $K'$ -valley excitons couple to right- and left-circularly polarized light, respectively), the dark excitonic states of both valleys simultaneously couple to vertically-polarized light propagating along the monolayer plane. This lack of optical valley selection is a significant impediment to study and exploitation of valley physics in the dark exciton states. It is therefore of interest to identify alternative pathways to detect the dark exciton (trion) valley polarization.

In this section, we discuss the observation of chiral phonon-mediated radiative relaxation pathways for the dark exciton (trion) in monolayer WSe<sub>2</sub> and establish their

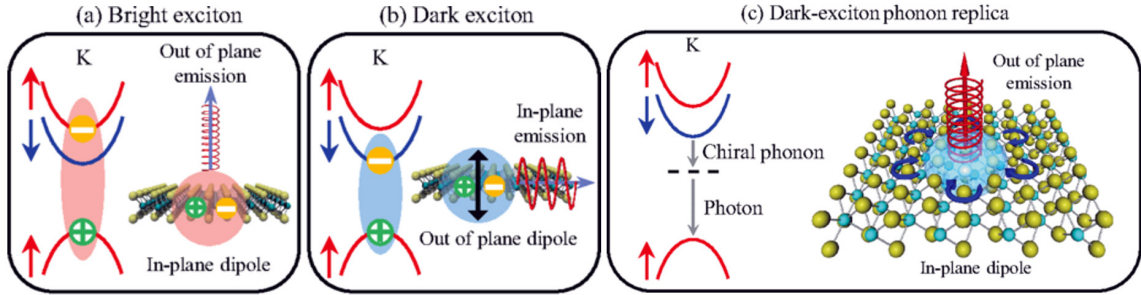


Figure 4.6: (a)–(c) Band configurations, transition dipole, and optical emission of (a) bright exciton, (b) dark exciton, and (c) dark exciton chiral phonon replica at the  $K$ -valley in monolayer  $\text{WSe}_2$ . The arrows denote the electron spin. A dark exciton can decay into a chiral phonon and a photon with opposite chirality.

valley-specific selection rules. We note that this *phonon replica* process was previously observed for the neutral dark exciton ( $D^0$ ) [77] and interband electronic transitions in monolayer  $\text{WSe}_2$  [78, 79]. We expand upon this analysis to comprehensively characterize the phonon replica emission process for  $D^0$ ,  $D^+$ , and  $D^-$ . Altogether, we find that each dark exciton (trion) state has a corresponding *chiral phonon replica* emission in PL which lies  $\sim 21.4$  meV below its parent state and originates from an interband scattering process with a  $\Gamma$ -point  $E''$  optical phonon with energy  $E_{\Gamma, E''} \sim 21.4$  meV [77, 78, 80]. In contrast to the in-plane, linearly polarized emission of the dark exciton, the phonon replicas exhibit out-of-plane, circularly polarized emission with valley-dependent helicity similar to the bright excitons. The relaxation processes of the bright excitons, dark excitons, and chiral phonon replicas are illustrated schematically in Figure 4.6(a,b,c), respectively. We thus identify a method to optically detect the valley index of the dark excitons (trions) and further explore the detailed exciton-phonon interactions in monolayer  $\text{WSe}_2$ .

### 4.3.1 Methodology

The data in this chapter is measured *via* gate-dependent magnetophotoluminescence in BN-encapsulated monolayer WSe<sub>2</sub> gating devices. The devices were fabricated by dry-transfer as described in Chapter 2. All data shown was measured using the 17.5 T superconducting magneto-optical cryostat system (Cell 3, NHMFL) described in Chapter 2 with 532-nm wavelength excitation laser over one week in March 2019.

### 4.3.2 Gate-Dependent Photoluminescence at Zero-Field

Figure 4.7(a) shows a gate-dependent photoluminescence (PL) map of the monolayer WSe<sub>2</sub> device at  $T = 5$  K. The quality of this device is much improved over that shown in Figure 4.2, so we more clearly distinguish the bright ( $A^0$ ,  $A^+$ ,  $A_1^-$ ,  $A_2^-$ ) and the dark ( $D^0$ ,  $D^-$ ,  $D^+$ ) exciton and trions. The PL energy of the dark exciton (trions) relative to the bright states is in good agreement with our previous findings. We observe new PL lines which are situated  $\approx 21.4$  meV below each of the dark exciton (trion) features and mimic their gate-dependent behavior. In Figure 4.7, we label these *replica* PL features as  $D_p^0$ ,  $D_p^+$ , and  $D_p^-$  which are associated with parent states  $D^0$ ,  $D^-$ , and  $D^+$ , respectively. To quantitatively analyze the replica features and their relationship to the dark exciton (trion) states, we fit each PL line and extract the PL energy and integrated intensity of each PL feature. In Figure 4.8(c), we shift the PL energy of each replica feature by +21.4 meV and observe that the shifted replica state PL energies closely match that of the corresponding dark exciton (trion). We plot the integrated intensities in Figure 4.8(b) and observe qualitatively parallel gate dependence of the replicas and corresponding dark states.

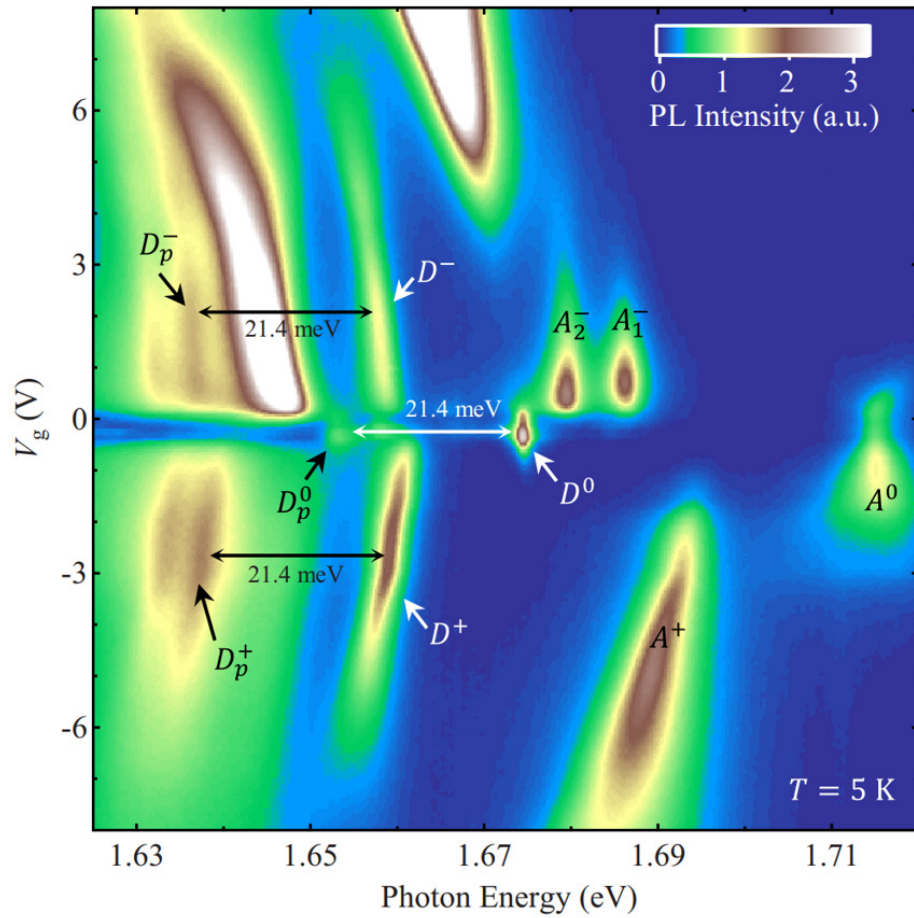


Figure 4.7: Gate-dependent photoluminescence (PL) map of a monolayer WSe<sub>2</sub> device encapsulated by BN. We observe the bright exciton/trions ( $A^0$ ,  $A^+$ ,  $A_1^-$ ,  $A_2^-$ ), dark exciton/trions ( $D^0$ ,  $D^-$ ,  $D^+$ ), and phonon replicas of dark exciton/trions ( $D_p^0$ ,  $D_p^-$ ,  $D_p^+$ ).

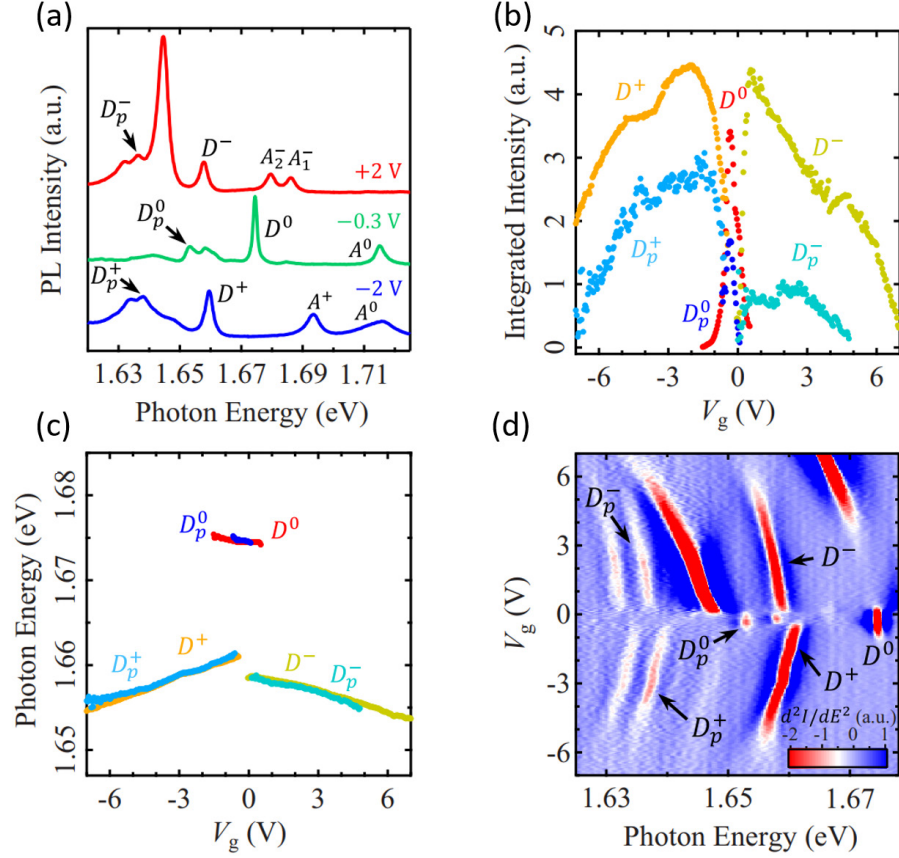


Figure 4.8: (a) The cross-cut PL spectra at the charge neutrality point ( $V_g = -0.3$  V), electron side ( $V_g = 2$  V) and hole side ( $V_g = -2$  V). (b) PL intensity and (c) PL photon energy of the dark excitonic states and replicas as a function of gate voltage. The replica energy is upshifted for 21.4 meV for comparison. (d) The second energy derivative ( $d^2I/dE^2$ ) of the PL map in Figure 4.2.

### 4.3.3 Gate-Dependent Magnetophotoluminescence

To further confirm the replica nature of the observed PL features, we perform magnetic-field-dependent PL measurements.  $K$ -valley (right-circular polarization) PL maps with  $B = 0$  T to  $B = 17.5$  T are shown in Figure 4.9(a,c,e) for electron doping, charge neutrality, and hole doping, respectively.  $K'$ -valley (left-circular polarization) maps are similarly shown in Figure 4.9(b,d,f). As discussed in the previous section, the dark exciton (trion) has a  $g$ -factor of  $\approx -9.5$  which can be measured *via* the valley Zeeman shift of the PL

energy. If the new PL features are indeed replicas of the dark states which radiate through a secondary relaxation pathway, it is reasonable to expect that  $D_p^0$ ,  $D_p^+$ , and  $D_p^-$  should inherit the  $g$ -factor of their parent states. We overlay black dashed lines in Figure 4.9(a-f) to highlight the dark exciton and replica PL lines and immediately see that their Zeeman shift is qualitatively similar. To confirm this, we extract the magnetic-field-dependent PL energy of each feature which is shown in Figure 4.9(g). As above, we shift the replica PL energy by +21.4 meV to highlight the nearly exact overlap with the dark states. The  $g$ -factor for  $D^0$ ,  $D^-$ ,  $D^+$  and their associated replicas are nearly identical, as determined from linear fitting of the PL energy with the valley Zeeman equation. We show the fitted  $g$ -factors for the neutral exciton ( $g = -9.9$ ), electron trion ( $g = -9.2$ ), and hole trion ( $g = -9.9$ ) alongside the PL energies in Figure 4.10(a).

Altogether, the parallel gate- and magnetic-field-dependence of the replica PL lines to those of the corresponding dark exciton (trion) offer compelling evidence to support our identification of the observed PL features as *phonon replicas* of the dark exciton states. The phonon replica process involves relaxation of the exciton through simultaneous emission of a phonon and a photon. The total exciton energy is emitted through the combined phonon and photon energies. Thus, the replica PL line is energetically separated from the parent emission by the emitted phonon energy. Our observed separation of 21.4 meV suggests that phonon which mediates the replica emission is the zone-center ( $\Gamma$ )  $E''$ -mode optical phonon which has energy  $\sim 21.4$  meV in monolayer WSe<sub>2</sub>. [77, 79, 81–84] The previously reported phonon replica of  $D^0$  similarly identified the  $\Gamma$ -point  $E''$  optical phonon [77].

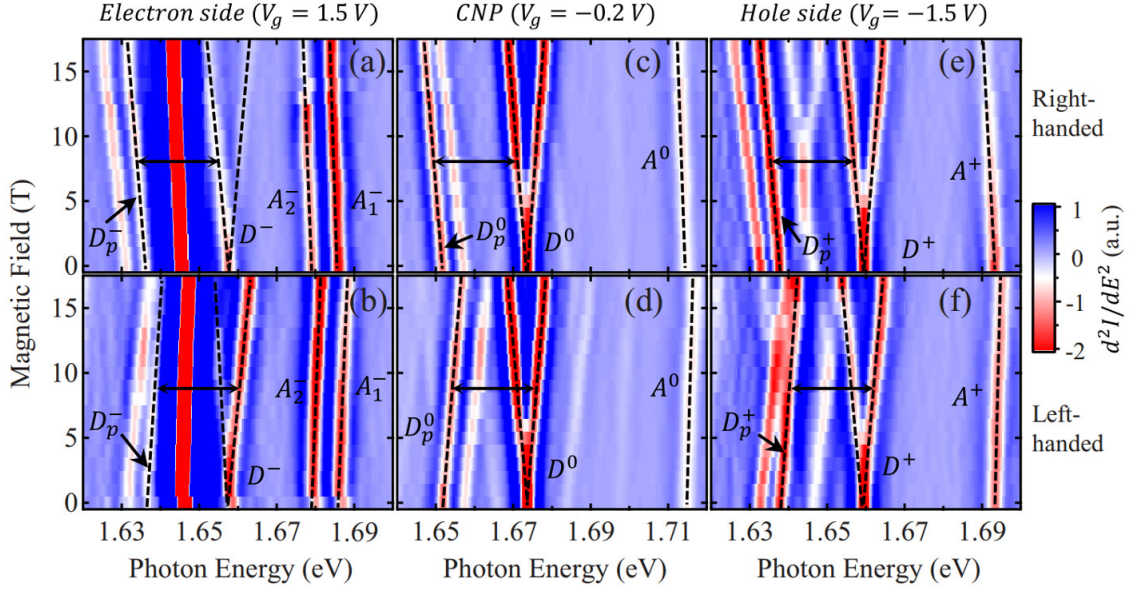


Figure 4.9: (a)–(f) Magnetic-field-dependent second-derivative PL map ( $d^2I/dE^2$ ) of monolayer WSe<sub>2</sub> on the electron side [(a), (b) gate voltage  $V_g = 1.5$  V], near the charge neutrality point (CNP) [(c), (d)  $V_g = -0.2$  V], and on the hole side [(e), (f)  $V_g = -1.5$  V]. We excite the sample with a linearly polarized 532-nm laser and collect the PL with right-handed (top row) or left-handed helicity (bottom row).

Curiously, the phonon replicas do not exhibit the same cross-shaped magnetic field splitting in the circularly polarized PL maps (Figure 4.9) which is characteristic of the linearly polarized dark exciton PL. Each replica instead exhibits a single PL line which redshifts (blue-shifts) under increasing magnetic field intensity for right-handed (left-handed) circular polarized detection. For right-handed circularly polarized detection, the phonon replicas shift in parallel with the lower energy ( $K'$ -valley) dark exciton (trion). For left-handed detection, the replicas shift in parallel to the higher energy ( $K$ -valley) dark exciton (trion). This implies that the phonon replicas emit circularly-polarized PL with helicity corresponding to the dark exciton valley pseudospin. Thus, the replica-mediating phonon interaction allows the dark exciton to luminesce with bright-exciton-light selection rules.

The bright-exciton-like nature of the phonon replica PL in terms of valley selection further suggests out-of-plane light emission (in-plane transition dipole) similar to the bright exciton and thus enhanced detection efficiency in our experimental geometry as compared to the in-plane emission of the dark states. However, the phonon replicas exhibit a lower overall PL intensity than the dark states as shown in Figure 4.7(c). We consider two possibilities to explain this discrepancy. First, our assumption of in-plane transition dipole for the replica PL may be incorrect. The phonon replicas may have unique optical selection which allows valley-specific circular polarization similar to the bright states with in-plane emission similar to the dark states. Second, and more likely, the replica PL intensity may be inherently limited by the rate of phonon emission process.

#### 4.3.4 Measurement of Exciton Dipole-Orientation

To address this question of the phonon replica transition dipole orientation, we examine data obtained by Tang *et al.* [71] using an optical measurement geometry which allows discrimination between in-plane and out-of-plane light emission. The monolayer WSe<sub>2</sub> gating device is deposited on a planar GaSe waveguide with angled edges at which the PL is collected. The waveguide carries both in-plane and out-of-plane oriented PL which will remain perpendicular to one another throughout and can be selectively detected by linear polarization. We extract the integrated PL intensity as a function of linear polarization for the observed bright excitons ( $A^0$ ,  $A^+$ ,  $A^-$ ), dark excitons ( $D^0$ ,  $D^-$ ,  $D^+$ ), and dark state phonon replicas ( $D_p^0$ ,  $D_p^+$ ,  $D_p^-$ ) using this scheme and plot the results in Figure 4.10(b). As the linear polarization detection angle is rotated, we alternate between detecting light

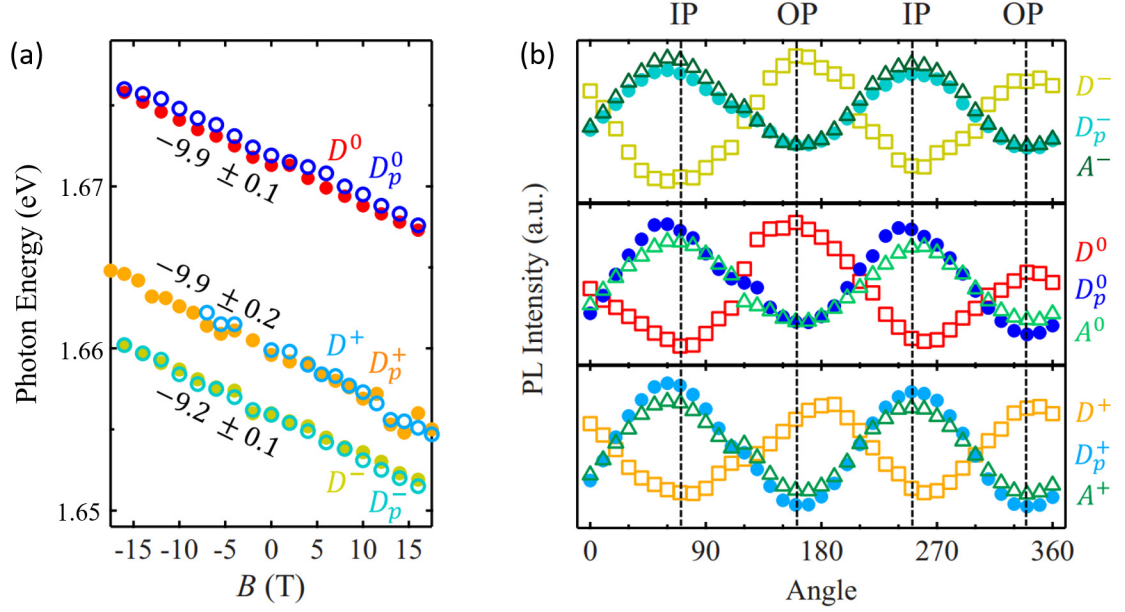


Figure 4.10: (a) The Zeeman energy shift of one branch of the dark states and their replicas from Figure 4.4. The replica energy is upshifted for 21.4 meV for comparison. The Zeeman-splitting  $g$ -factors from linear fits are denoted. (b) The PL intensity of the bright excitonic states (triangle), dark excitonic states (square), and dark-state phonon replicas (dots) as a function of polarization angle in the in-plane collection geometry. The angles corresponding to in-plane (IP) and out-of-plane (OP) dipoles are denoted.

propagating in-plane (out-of-plane transition dipole, labeled OP) and light propagating out-of-plane (in-plane transition dipole, labeled IP). The OP and IP-associated emission are perpendicular to one another. We observe nearly identical behavior of the bright excitons and dark-state phonon replicas, in contrast to the opposite behavior of the direct dark exciton PL. Thus, we confirm that the observed phonon replicas have optical selection rules and transition dipole orientation which wholly mimic those of the bright exciton.

#### 4.3.5 Phonon Replica Optical Selection Rules

For a more comprehensive understanding of the bright-exciton-like phonon replica PL emission and optical selection rules, we perform a symmetry-based analysis of the elec-

tronic and phonon states similar to that shown for the bright excitons in Chapter 1 and dark excitons earlier in this chapter.

We discussed at the beginning of this chapter that the lower conduction band  $c_1$  mixes with higher energy band  $c_2$  through spin-orbit coupling which results in modified, spin-mixed conduction bands. This spin mixing effect allows the dark trions to radiatively relax as the constituent states are no longer purely of opposite spin.

$$|\bar{c}_{1,\downarrow}\rangle = |c_{1,\downarrow}\rangle + \frac{\langle c_{2,\uparrow} | \hat{\alpha}_{soc} | c_{1,\downarrow} \rangle}{E_{c_{1,\downarrow}} - E_{c_{2,\uparrow}}} |c_{2,\uparrow}\rangle \quad (4.6)$$

Because the spin-orbit coupling follows the crystal symmetry, however, it can only mediate interactions between bands which have identical symmetry [17]. In contrast, the electron-phonon coupling breaks the unperturbed crystal symmetry due to the phonon-associated lattice distortion. In other words, the presence of electron-phonon coupling can modify the unperturbed electronic states in a similar fashion without the strict band symmetry requirement. Following the same form, the mixing between conduction subbands ( $\bar{c}_{1,\uparrow}, \bar{c}_{1,\downarrow}$ ) can be expressed as:

$$|\bar{c}_{1,\downarrow}\rangle = |\bar{c}_{1,\downarrow}\rangle + \frac{\langle \bar{c}_{1,\uparrow}, \Omega | \hat{H}_{ep} | \bar{c}_{1,\downarrow} \rangle}{E_{\bar{c}_{1,\downarrow}} - E_{\bar{c}_{1,\uparrow}} - \hbar\Omega} |\bar{c}_{1,\uparrow}\rangle \quad (4.7)$$

where  $\hat{H}_{ep}$  is the electron-phonon coupling operator, and  $|\bar{c}_{1,\uparrow}, \Omega\rangle$  is the conduction subband with a phonon of energy  $\hbar\Omega$  which is mediating the coupling. For the band mixing *via* electron-phonon interaction to be non-zero,  $\langle \bar{c}_{1,\uparrow}, \Omega | \hat{H}_{ep} | \bar{c}_{1,\downarrow} \rangle$  must satisfy the band symmetry as in previous analysis.

$$\langle C_3 \bar{c}_{1,\uparrow}, \Omega | C_3 \hat{H}_{ep} C_3^{-1} | C_3 \bar{c}_{1,\downarrow} \rangle = \langle \bar{c}_{1,\uparrow}, \Omega | \hat{H}_{ep} | \bar{c}_{1,\downarrow} \rangle \quad (4.8)$$

$$\langle \sigma_h \bar{c}_{1,\uparrow}, \Omega | \sigma_h \hat{H}_{ep} \sigma_h^{-1} | \sigma_h \bar{c}_{1,\downarrow} \rangle = \langle \bar{c}_{1,\uparrow}, \Omega | \hat{H}_{ep} | \bar{c}_{1,\downarrow} \rangle \quad (4.9)$$

From our previous knowledge of the conduction band symmetries, we can evaluate the above expressions to determine the phonon selection rules which allow mixing between the spin subbands in  $c_1$ . We note that the interaction Hamiltonian is invariant under the symmetry operations. The following expressions must be satisfied:

$$\langle \bar{c}_{1,\uparrow}, \Omega | \hat{H}_{ep} | \bar{c}_{1,\downarrow} \rangle = \langle C_3 \bar{c}_{1,\uparrow}, \Omega | C_3 \hat{H}_{ep} C_3^{-1} | C_3 \bar{c}_{1,\downarrow} \rangle \quad (4.10)$$

$$= e^{i\frac{2\pi}{3}(1+C_3(\Omega))} \langle \bar{c}_{1,\uparrow}, \Omega | \hat{H}_{ep} | \bar{c}_{1,\downarrow} \rangle \quad (4.11)$$

$$\langle \bar{c}_{1,\uparrow}, \Omega | \hat{H}_{ep} | \bar{c}_{1,\downarrow} \rangle = \langle \sigma_h \bar{c}_{1,\uparrow}, \Omega | \sigma_h \hat{H}_{ep} \sigma_h^{-1} | \sigma_h \bar{c}_{1,\downarrow} \rangle \quad (4.12)$$

$$= -\sigma_h(\Omega) \langle \bar{c}_{1,\uparrow}, \Omega | \hat{H}_{ep} | \bar{c}_{1,\downarrow} \rangle \quad (4.13)$$

where  $C_3(\Omega)$  and  $\sigma_h(\Omega)$  are the respective symmetry operations on the mediating phonon state  $\Omega$ . Thus, to satisfy the above expressions for coupling between  $\bar{c}_{1,\uparrow}$  and  $\bar{c}_{1,\downarrow}$ ,  $\Omega$  must left-handed chirality ( $C_3(\Omega) = -1$ ) and odd parity under out-of-plane reflection ( $\sigma_h(\Omega) = -1$ ). If we perform similar symmetry analysis for the inverse case,  $\langle \bar{c}_{1,\downarrow}, \Omega | \hat{H}_{ep} | \bar{c}_{1,\uparrow} \rangle$ , we find identical results but requiring a right-handed chiral phonon ( $C_3(\Omega) = +1$ ).

#### 4.3.6 Chiral Phonons in Monolayer WSe<sub>2</sub>

Previous work identified the presence of *chiral phonons* in monolayer WSe<sub>2</sub> which are a linear superposition of the energetically-degenerate longitudinal (LO) and transverse (TO) optical phonons with  $E''$  representation at the  $\Gamma$ -point [79, 80]. This superposition can form two *chiral phonon* states with clockwise (counter-clockwise) rotation of the Se atoms around stationary W atoms depending on the relative phase. We refer to these as the right-handed chiral phonon ( $\Omega_+$ ,  $C_3(\Omega_+) = +1$ ) and left-handed chiral phonon ( $\Omega_-$ ,

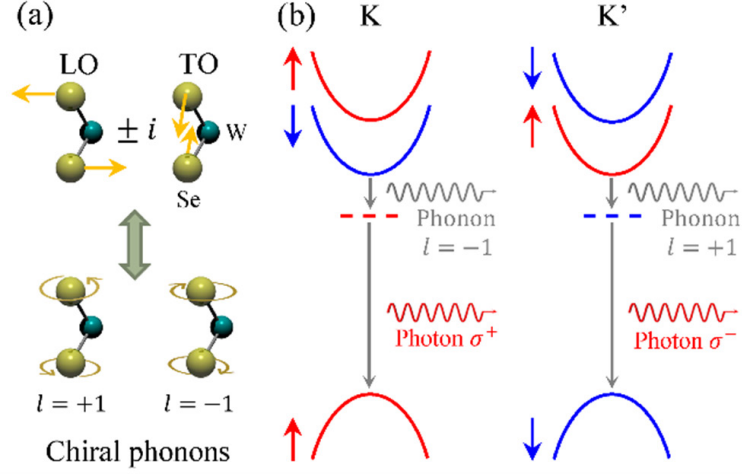


Figure 4.11: (a) The configurations of the doubly degenerate zone-center  $E''$  phonons in monolayer WSe<sub>2</sub>. The W atoms are stationary and the Se atoms move laterally. The vibration can be decomposed into the LO and TO modes with linear Se atomic motion or left-handed and right-handed chiral modes with rotational Se atomic motion. (b) The phonon-assisted radiative recombination of the dark exciton. The dark exciton can decay into a pair of phonon and photon with opposite chirality..

$C_3(\Omega_-) = -1$ ). We show the LO / TO phonon superposition which produces the chiral phonons with  $E''$  symmetry schematically in Figure 4.11(a). Both chiral phonons have odd  $\sigma_h$  parity ( $\sigma_h(\Omega_{\pm}) = -1$ ) as the top and bottom Se atoms counter-rotate in-plane. Therefore, the  $E''$  chiral phonons satisfy the symmetry requirements in our derived phonon selection rules.

The above symmetry-based discussion involves the free particle electronic states in each band; however, the electron and hole which constitute the exciton state inherit the same symmetry as their free particle counterparts. Thus, the results of this symmetry analysis can be directly applied to the dark excitons which are the motivation for this analysis. The electron-phonon interaction with the  $\Gamma$ -point chiral phonon couples the two conduction subbands in the same valley. This suggests mixing of the bright and dark exciton states

in the same valley - the dark exciton can radiate with bright-exciton-like optical selection as the dark exciton electron which resides in the lower conduction subband couples to the higher subband of opposite spin. In this scenario, the  $K$  ( $K'$ ) valley dark exciton electron emits a  $\Omega_-$  ( $\Omega_+$ )  $\Gamma$ -point chiral phonon to couple with the opposite spin conduction band which allows the dark exciton to radiate following the bright exciton selection with out-of-plane right (left) circularly-polarized light. This valley-dependent phonon / photon emission process is shown schematically in Figure 4.11(b). This is the chiral phonon replica process for the dark exciton. We note that the same analysis applies to intravalley relaxation of the dark triions.

For completeness, we calculate the transition rate of the complete dark exciton phonon replica process in the  $K$ -valley from perturbation theory to test the bright-exciton-like optical selection. The electronic transition from the modified lower conduction subband  $\bar{c}_{1,\downarrow}$  to the valence band  $v_{1,\uparrow}$  is given by:

$$|P_{\bar{c}_{1,\downarrow} \rightarrow v_{1,\uparrow}}\rangle \propto \left| \langle v_{1,\uparrow} | \hat{P}_\gamma | \bar{c}_{1,\downarrow} \rangle \right|^2 \delta(E_{v_{1,\uparrow}} - E_{\bar{c}_{1,\downarrow}} - \hbar\Omega - \hbar\omega) \quad (4.14)$$

$$\propto \left| \frac{\langle v_{1,\uparrow} | \hat{P}_\gamma | \bar{c}_{1,\uparrow}, \Omega \rangle \langle \bar{c}_{1,\uparrow}, \Omega | \hat{H}_{ep} | \bar{c}_{1,\downarrow} \rangle}{E_{\bar{c}_{1,\downarrow}} - E_{\bar{c}_{1,\uparrow}} - \hbar\Omega} \right|^2 \delta(\dots) \quad (4.15)$$

where  $\hat{P}_\gamma$  is the momentum operator for an emitted photon with energy  $\hbar\omega$ . This expression is non-zero only when the emitted photon has right-circular polarization ( $\hat{P}_\gamma = \hat{P}_+$ ) and photon energy equal to the dark exciton energy minus the phonon energy ( $\hbar\omega = E_{v_{1,\uparrow}} - E_{\bar{c}_{1,\downarrow}} - \hbar\Omega$ ). Similar analysis for the the  $K'$ -valley dark exciton is the time shows opposite chirality for the emitted photon and phonon.

### 4.3.7 Conclusion

In summary, we have shown comprehensive experimental evidence and group-theory-based analysis which supports the *bright* relaxation of dark excitons (trions) *via* an intravalley chiral phonon replica process. Importantly, we demonstrate that the phonon replica process is valley dependent. The dark exciton (trion) in the  $K$  ( $K'$ )-valley can relax through emission of a left (right)-circularly polarized chiral phonon and right (left)-circularly polarized photon with energy equal to the direct dark exciton PL energy minus the chiral phonon energy ( $\sim 21.4$  meV). This process therefore allows optical detection of the dark exciton (trion) valley degree of freedom.

## 4.4 Multipath Optical Recombination of Intervalley Dark Excitons and Trions in Monolayer WSe<sub>2</sub>

Our optical investigation of the excitons presented thus far (bright, dark, and phonon replica) has been restricted to the constituent electrons and holes which reside in a single valley and thus couple with light through *intravalley* transitions. The initial and final electronic states have almost identical momentum as the mediating photons and  $\Gamma$ -point phonons contribute vanishingly small momentum change. As noted at the beginning of this chapter, however, there is principally a complex landscape of exciton species which forms between states throughout the electronic band structure but which cannot couple directly to light (we note that this is not *strictly* true, as light with special geometries such as twisted light with finite orbital angular momentum can couple to a wider variety of electronic transitions besides those discussed here) [85].

One such example is the *intervalley* exciton which forms between electrons and holes in opposite valleys ( $K \leftrightarrow K'$ ) [86–90]. The intervalley exciton,  $I^0$ , is shown schematically with the bright ( $A^0$ ) and spin dark exciton ( $D^0$ ) in Figure 4.12(a). The intervalley recombination requires a significant change in momentum,  $\Delta p = K - K' = K$ , which cannot be satisfied by the photon or  $\Gamma$ -point phonon interaction. The intervalley exciton therefore cannot couple directly to light. Similar to the intravalley band mixing *via* electron-phonon interaction above, we can imagine that an appropriate phonon in monolayer WSe<sub>2</sub> can allow interaction between valleys, as well. Such an intervalley exciton-phonon scattering process could allow radiative relaxation of the intervalley exciton as shown in Figure 4.12(b)

In this section, we present experimental evidence and group-theory-based symmetry analysis which of radiative intervalley exciton recombination in monolayer WSe<sub>2</sub> and determine the optical and phonon selection rules. We further show that the previously discussed dark excitons ( $D^+$ ,  $D^-$ ) which are illustrated schematically in Figure 4.12(c,d) can relax radiatively through four distinct pathways: in-plane emission, intravalley phonon replica *via*  $\Gamma$ -point phonon emission, intervalley phonon replica *via*  $K$ -point phonon emission, and defect scattering.

#### 4.4.1 Methodology

The majority of data in this chapter is measured *via* gate-dependent magnetophotoluminescence in BN-encapsulated monolayer WSe<sub>2</sub> gating devices. The devices were fabricated by dry-transfer as described in Chapter 2. All magneto-PL data shown was measured using the 17.5 T superconducting magneto-optical cryostat system (Cell 3, NHMFL) de-

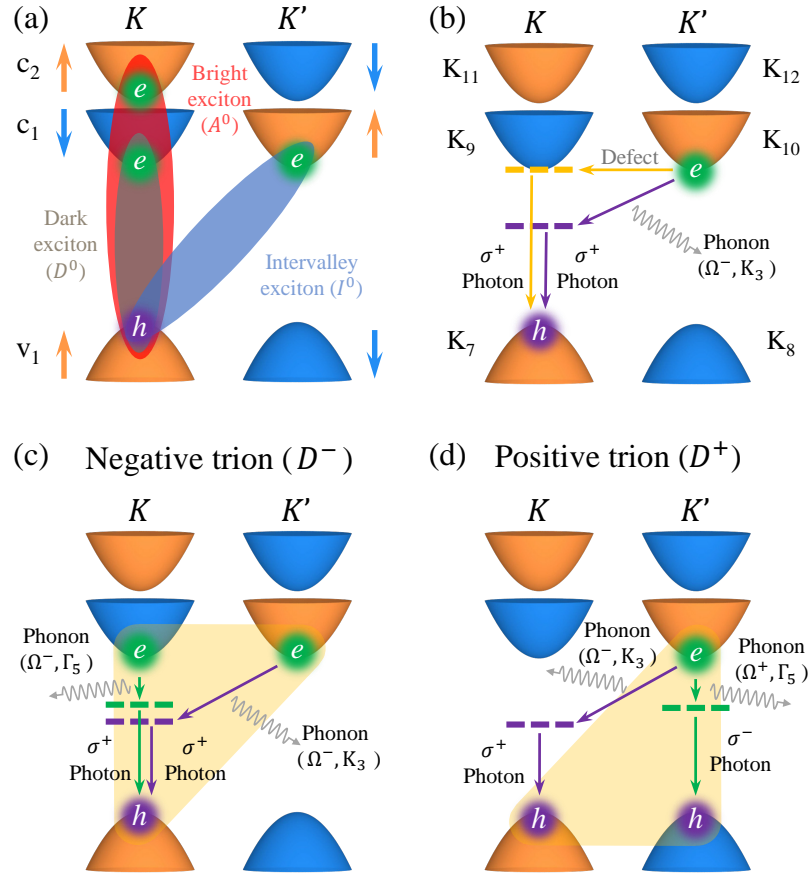


Figure 4.12: Intervalley electron-hole recombination processes in monolayer WSe<sub>2</sub>. (a) Band configurations for the intravalley bright exciton ( $A^0$ ), intravalley spin dark exciton ( $D^0$ ), and intervalley momentum-forbidden dark exciton ( $I^0$ ). The arrows and color denote the electron spin. (b) Recombination of  $I^0$  mediated by defects or zone-corner chiral phonons. We denote the irreducible representations of the electronic states at the  $K$  and  $K'$  points in the  $C_{3h}$  point group. (c),(d) Trion decay through emission of zone-center or zone-corner chiral phonons.  $\Gamma_5$  ( $K_3$ ) is the representation of chiral phonons at the  $\Gamma$  ( $K'$ ) point in the  $D_{3h}$  ( $C_{3h}$ ) point group.  $\Omega_{\pm}$  and  $\sigma_{\pm}$  denote the chirality of the emitted phonons and photons, respectively.

scribed in Chapter 2 with 532-nm wavelength excitation laser over two weeks in March and August 2019. Excitation-power-dependent PL measurement was conducted using the multi-source optical system discussed in Chapter 2.

#### 4.4.2 Observation of the Intervalley Exciton

Figure 4.13(a) shows a gate dependent photoluminescence (PL) map of monolayer WSe<sub>2</sub>. Detailed line cuts showing the linearly scaled PL spectra at the charge neutrality point (CNP,  $V_g = -0.2$  V), electron side ( $V_g = +2$  V), and hole side ( $V_g = -2$  V) are shown in Figure 4.15(a). We can immediately labeled those exciton (trion) PL features which we have discussed earlier in this work: the bright exciton and trions ( $A^0, A^+, A_1^-, A_2^-$ ), spin dark exciton and trions ( $D^0, D^+, D^-$ ), and zone-center chiral-phonon replicas of the spin dark states with  $\sim 21.4$  meV redshift ( $D_p^0, D_p^+, D_p^-$ ). Four previously undiscussed features are labeled in the figure in red:  $I^0$  and  $I_p^0$  at the CNP,  $I_p^-$  on the electron side, and  $I_p^+$  on the hole side which we preliminarily identify as the intervalley exciton, its phonon replica, and intervalley phonon replicas of the dark trion. We will discuss each of these PL features and present evidence and analysis to support this identification, starting with  $I^0$  and  $I_p^0$ .

#### Excitation-power-dependence of Photoluminescence

As an initial, general note, we measure the excitation power dependence of each PL feature to eliminate the possibility that any is attributable to biexciton formation. The PL intensity of biexcitons exhibits quadratic dependence on power, whereas the single exciton (trion) species have approximately linear power dependence [36–39]. For completeness, we

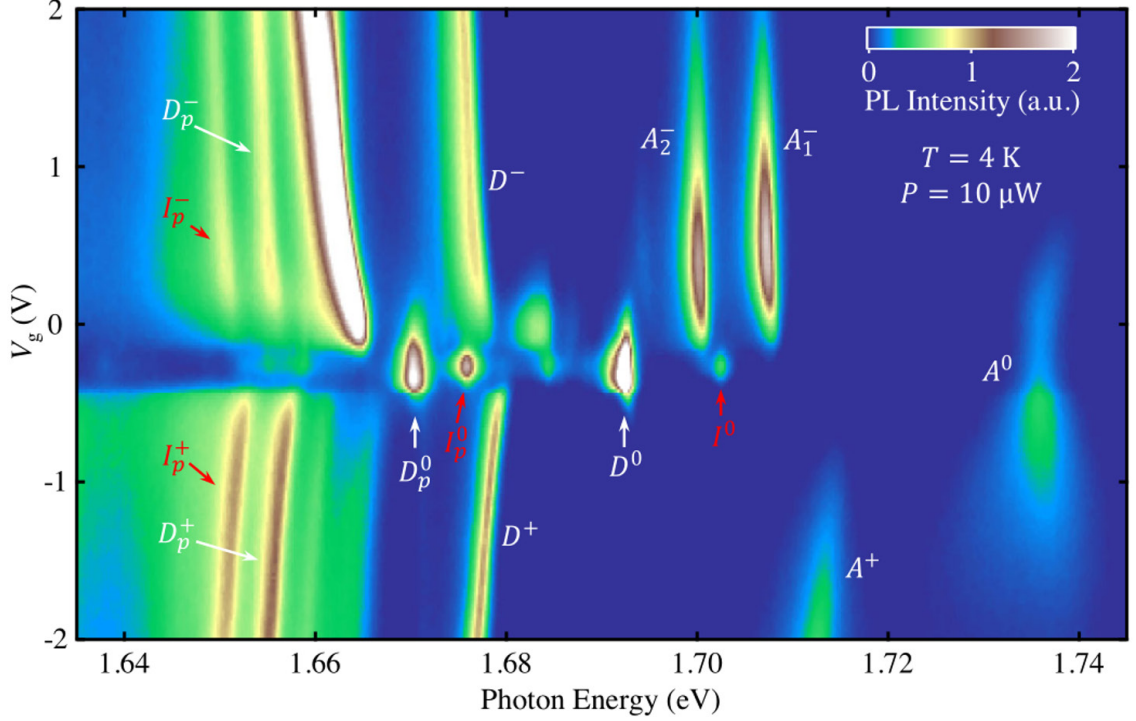


Figure 4.13: Gate-dependent PL map of monolayer WSe<sub>2</sub> at  $T \sim 4$  K and zero magnetic field under 532-nm continuous laser excitation with incident laser power  $P \sim 10 \mu\text{W}$ . We denote the bright exciton and trions ( $A^0, A^+, A_1^-, A_2^-$ ), dark exciton and trions ( $D^0, D^+, D^-$ ), intervalley dark exciton ( $I^0$ ), zone-center chiral-phonon replicas of dark states with  $\sim 21.4$  meV redshift ( $D_p^0, D_p^+, D_p^-$ ), and zone-corner chiral-phonon replicas of dark states with  $\sim 26.5$  meV redshift ( $I_p^0, I_p^+, I_p^-$ ).

show the power dependence for all neutral exciton species discussed thus far. We fit each PL feature with a Lorentzian-type function and plot the integrated intensities as a function of incident laser power in Figure 4.14(a). Each of our observed features shows linear power dependence. We note, as well, that the full-width at half maximum (FWHM) increases for each PL feature increasingly significantly with incident power as shown in Figure 4.14(b). We thus use an incident power of  $\sim 10 \mu\text{W}$  as a reasonable trade-off between detected PL intensity and FWHM to ensure sharp features while maintaining good signal-to-noise ratio in detection.

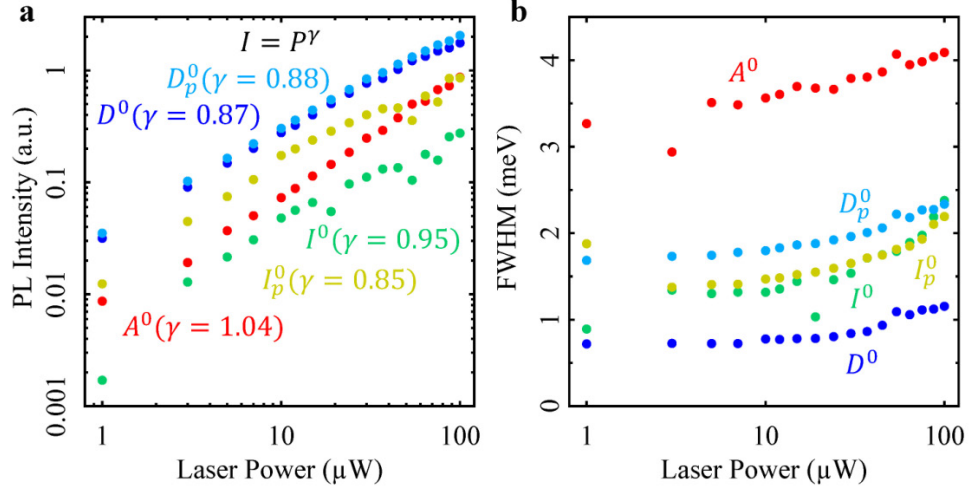


Figure 4.14: (a) Photoluminescence (PL) intensity as a function of incident laser power for the bright exciton ( $A^0$ ), dark exciton ( $D^0$ ) and its phonon replica ( $D_p^0$ ), intervalley exciton ( $I^0$ ) and its phonon replica ( $I_p^0$ ). The coefficients from power law fits ( $I = P^\gamma$ ) of each exciton are shown. (b) Full width at half maximum (FWHM) of these peaks as a function of incident laser power.

#### 4.4.3 Signatures of Intervalley Excitons

We next discuss the  $I^0$  PL feature. We use Lorentzian-type functions to fit the observed exciton features and extract the PL energy, FWHM, and integrated intensity of each as a function of gate voltage, which we plot in Figures 4.15(b-d). It is immediately clear that  $I^0$  exhibits parallel gating behavior to  $D^0$  in each fitted characteristic. Beyond this qualitative similarity, there are two primary attributes which we use to identify this feature as the PL of the intervalley exciton.

First, we measure the PL energy separation between  $I^0$  and  $D^0$  and find that the intervalley exciton lies  $\sim 10$  meV higher in energy. The observation that  $I^0$  has a higher PL energy than  $D^0$  is consistent with our expectations, which we can understand qualitatively from the exciton binding energies. Recall that the PL energy at CNP is equal to the free

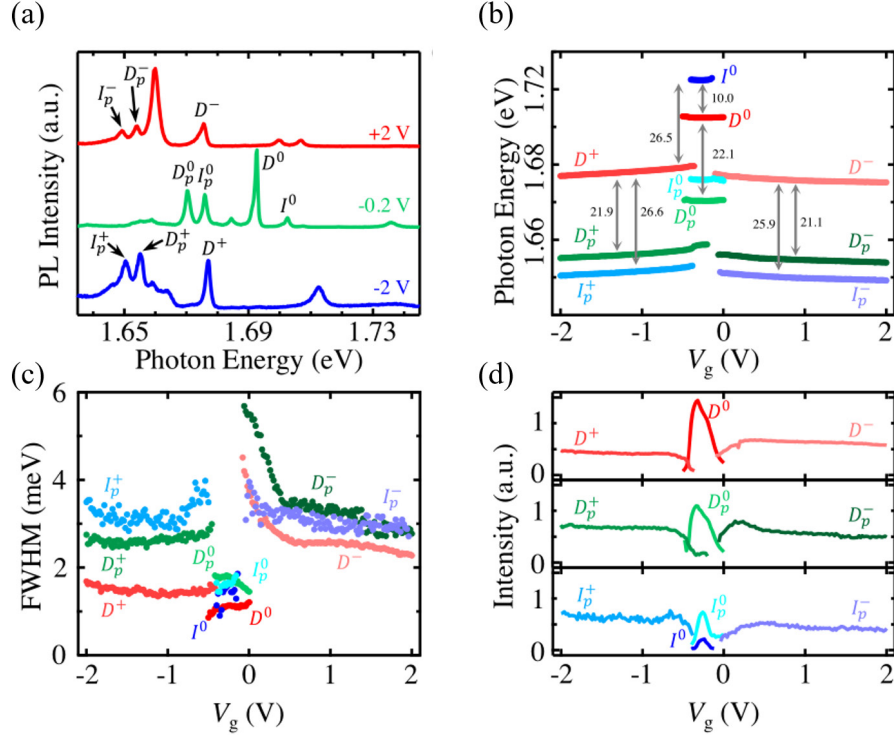


Figure 4.15: Analysis of exciton features in gate-dependent PL map in Figure 4.13. (a) Cross-cut PL spectra on the electron side, charge-neutrality point, and the hole side with respective gate voltages  $V_g = +2, -0.2$ , and  $-2$  V. (b)–(d) The PL energy, full width at half maximum (FWHM), and integrated PL intensity of different excitonic peaks as a function of the gate voltage. The numbers in (b) denote the energy separation in the units of meV.

particle band gap energy minus the exciton binding energy. The band configuration of  $I^0$  and  $D^0$  are energetically degenerate (Figure 4.12(a)), thus  $I^0$  lying at higher energy than  $D^0$  implies that the  $I^0$  binding energy is lower. The binding energy of each exciton arises from two primary interactions: the long range direct Coulomb interaction and the short-range exchange interaction which is related to Pauli exclusion [7]. The long range interaction does not depend on the momentum or spin and is identical between the intravalley and intervalley excitons; the exchange interaction, however, depends strongly on the relative spin of the electron and hole which constitute the exciton.  $D^0$  has opposite electron and hole spin,

while  $I^0$  has parallel spins. Thus, the exciton binding in  $I^0$  should be reduced relative to  $D^0$  as we observe. To quantify this picture, we carried about first-principles calculations which confirm that the binding energy of  $I^0$  should be  $\sim 10$  meV higher than that of  $D^0$ . For details of this calculation, please see the supplemental material of the publication [28].

For finite charge density (electron or hole side), we might naively expect intervalley trions to appear at  $\sim 10$  meV above the dark trions ( $D^-$ ,  $D^+$ ) similar to the relationship between  $D^0$  and  $I^0$ . Careful analysis shows that this should not be the case, however. As shown schematically in Figure 4.12(c,d) for the electron and hole trions, respectively, the intervalley trions are indistinguishable at zero magnetic field from the dark trions discussed earlier in this chapter. The short range exchange interaction which causes the energy splitting between  $D^0$  and  $I^0$  at zero magnetic field is dependent only on the total spin configuration of the constituent electrons and holes and is not sensitive to the recombination pathway [7]. Thus, we require out-of-plane magnetic field to lift the valley degeneracy and distinguish the expected intravalley and intervalley relaxation pathways.

Second, the intervalley exciton has an intervalley configuration and therefore its  $g$ -factor will include a contribution from the valley magnetic moment due to the Berry curvature. As discussed in Chapter 1, the exciton valley Zeeman  $g$ -factor can be estimated from the net azimuthal magnetic moment of the conduction and valence bands which hold its constituent electron and hole, respectively. We show the band configuration with non-zero magnetic field and label the estimated spin, orbital magnetic moment, and Berry curvature contributions to the total  $g$ -factor of each band in Figure 4.16(a). We thus estimate the  $I^0$   $g$ -factor as  $g \sim 13$ . Figure 4.16(b,c) show magnetic-field-dependent PL

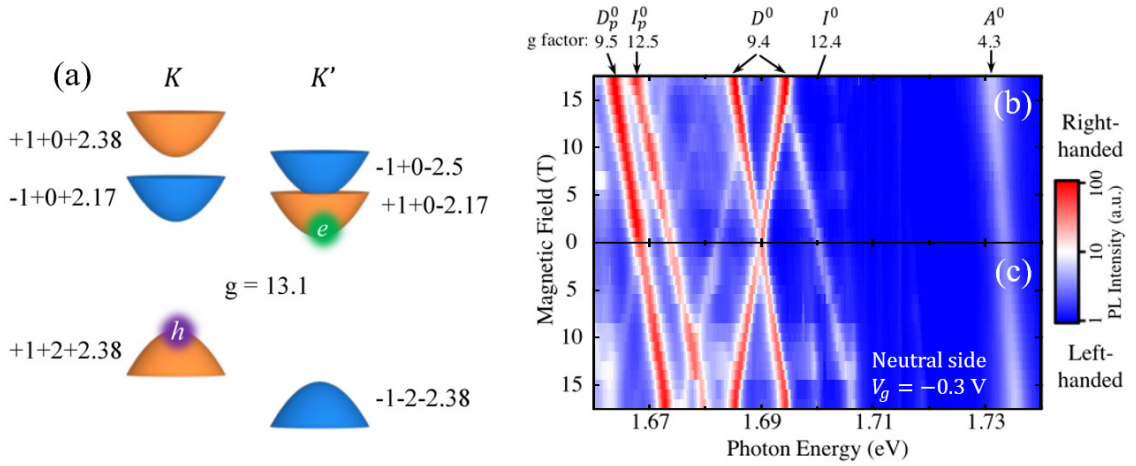


Figure 4.16: (a) Estimation of valley Zeeman splitting  $g$ -factor for intervalley exciton  $I^0$  predicted by the single-particle model described in Chapter 1. The difference of the exciton  $g$ -factors between the two valleys is the Zeeman-splitting  $g$ -factor of the exciton (which is denoted in the middle of each panel). (b,c) Magnetic-field-dependent and helicity-resolved PL map in monolayer WSe<sub>2</sub> at the charge neutrality point for  $B = 0 - 17$  T. The top and bottom rows show PL with right- and left-handed circular polarized detection, respectively. The PL lines and their measured  $g$ -factors are labeled at the top.

maps in monolayer WSe<sub>2</sub> at the CNP ( $V_g = -0.3$  V) for right- and left-circularly polarized detection, respectively. From this map, we perform a linear fit of the Zeeman shift for each PL feature and extract the exciton  $g$ -factors. The  $g$ -factors for the bright exciton ( $A^0 \sim 4$ ), spin dark exciton ( $D^0 \sim 9$ ) and dark exciton phonon replica ( $D_p^0 \sim 9$ ) are in agreement with our previous observations. Importantly, the experimental  $g$ -factor of  $I^0$  ( $g = 12.4$ ) is very close to our estimated value ( $g \sim 13.1$ ).

### Defect-Mediated Intervalley Radiative Relaxation

Together, the energy splitting with  $D^0$  and the distinct valley Zeeman  $g$ -factor provide strong evidence to support our preliminary identification of  $I^0$ . However, it raises the significant question of how  $I^0$  can radiatively relax with unmodified energy. Our stated

expectation is that this relaxation process should only be allowed when the momentum mismatch between electron and hole is satisfied by a  $K$ -point phonon interaction which would necessarily reduce the observed PL energy. It was previously suggested that this intervalley exciton recombination may be mediated by defect interaction, as illustrated in Figure 4.12(b) [91]. We note, however, that the exact mechanism is not clear.

#### 4.4.4 $K$ -point Phonon Replica Photoluminescence

In addition to this defect-mediated relaxation pathway, we observe the  $K$ -point phonon mediated relaxation of  $I^0$  which we label as the intervalley phonon replica,  $I_p^0$ . As discussed in the previous section, the the phonon replica is related to its parent state by several characteristics.

First, the phonon replica PL energy should be equal to that of its parent state minus the energy of the emitted phonon. The neutral phonon replica lies  $\sim 26.6$  meV below  $I^0$ , which is consistent with the energy of the  $K$ -point LO chiral phonon with  $E'$  representation [78]. We observe the same  $\sim 26.6$  meV energy separation between the dark trions ( $D^-, D^+$ ) and the PL features which we preliminarily identified as the intervalley trion phonon replicas ( $I_p^-, I_p^+$ ). Recall that the intervalley trion and dark trion are indistinguishable at zero magnetic field, so we are simply observing three possible decay paths of the same trion state:  $D^-, D_p^-, I_p^-$  arise from the same electron trion depicted in Figure 4.12(c) and  $D^+, D_p^+, I_p^+$  arise from the same hole trion depicted in Figure 4.12(d).

Second, the phonon replicas should exhibit parallel gate dependence to their parent state. As shown in Figures 4.13(c-e),  $I^0$  and  $I_p^0$  both appear in a very narrow gate voltage range immediately surrounding the CNP and exhibit qualitatively parallel intensity change.

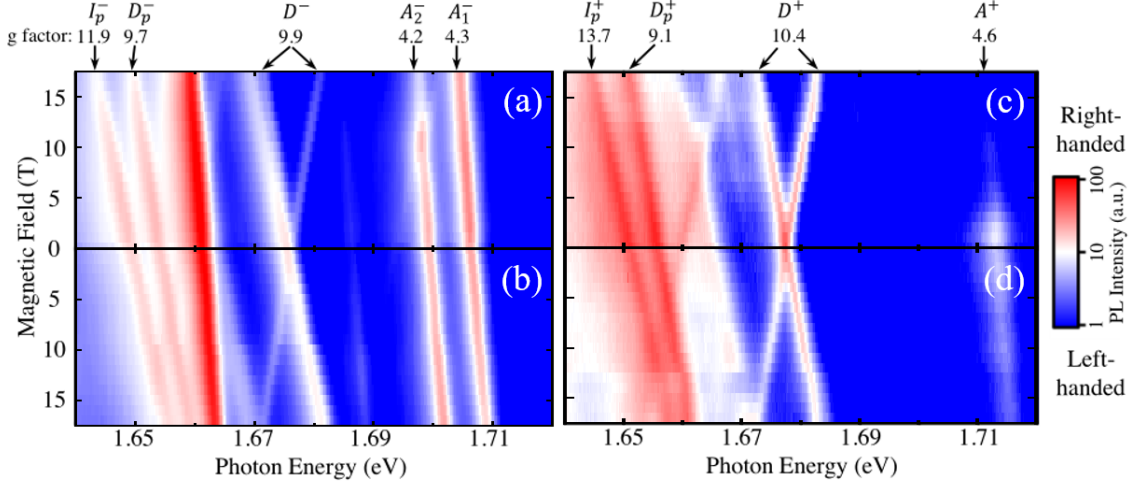


Figure 4.17: Magnetic-field-dependent, helicity-resolved PL map in monolayer WSe<sub>2</sub> with (a,b) electron doping ( $V_g = +1$  V) and (c,d) hole doping ( $V_g = -1$  V) for  $B = 0 - 17$  T. The top and bottom rows show PL with right- and left-handed circular polarized detection, respectively. The PL lines and their measured  $g$ -factors are labeled at the top.

Similarly, the intervalley trion replicas ( $I_p^-, I_p^+$ ) exhibit parallel gating dependence to the corresponding dark trions ( $D^-, D^+$ ) in PL energy, FWHM, and integrated intensity.

Third, the phonon replicas should exhibit the same valley Zeeman  $g$ -factor as their parent states. Returning to the magnetic-field-dependent PL at the CNP in Figure 4.16(b), we see that  $I_p^0$  has nearly identical  $g$ -factor (12.5) to its parent state  $I^0$  (12.4). We also measure the magnetic-field-dependent PL for the electron trions ( $V_g = +1$  V) and hole trions ( $V_g = -1$  V) in Figure 4.17(a,b; c,d), respectively. We extract  $g$ -factors for  $I_p^-$  (11.9) and  $I_p^+$  (13.7) which are comparable to that for  $I^0$  (12.4). Similar to the spin dark trions and dark trion replicas, we note that the  $g$ -factors for the trion states differ noticeably from the corresponding neutral excitons and therefore the  $g$ -factors predicted by the single-particle picture. This further suggests the significance of Fermi sea interactions at finite charge density which modify the character of the excitons and/or constituent electronic states.

Finally, the  $K$ -point LO phonons which mediate the intervalley phonon replicas are chiral, similar to those involved in  $D_p^0$ , etc. The intervalley replica PL should therefore follow similar chiral, valley-dependent selection rules. As shown in Figure 4.16(b) and Figure 4.17, the intervalley phonon replicas ( $I^0, I_p^-, I_p^+$ ) all exhibit single-valley, circularly polarized PL similar to the bright exciton optical selection rules. For completeness, we can derive the intervalley replica phonon and optical selection rules with similar symmetry-based analysis to those used in earlier sections.

#### 4.4.5 Intervalley Phonon Replica Selection Rules

As discussed in the previous section, we can consider the electron-phonon-interaction-mediated conduction band mixing for the intervalley exciton whose hole resides in the  $K$ -valley valence band (Figure 4.12(a)):

$$|\bar{c}'_{1,\uparrow}\rangle = |\bar{c}_{1,\uparrow}\rangle + \frac{\langle \bar{c}_{1,\downarrow}, \Omega | \hat{H}_{ep} | \bar{c}'_{1,\uparrow} \rangle}{E_{\bar{c}'_{1,\uparrow}} - E_{\bar{c}_{1,\downarrow}} - \hbar\Omega} |\bar{c}_{1,\uparrow}\rangle \quad (4.16)$$

where  $|\bar{c}'_{1,\uparrow}\rangle$  is the lower conduction subband with majority spin up in the  $K'$ -valley,  $|\bar{c}_{1,\downarrow}\rangle$  is the lower conduction subband with majority spin down in the  $K$ -valley.  $\Omega$  represents an emitted  $K$ -point chiral phonon with phonon energy  $\hbar\Omega$ . The transition rate for the intervalley recombination with  $K$ -valley hole is thus:

$$P_{\bar{c}'_{1,\uparrow} \rightarrow v_{1,\uparrow}} = \frac{2\pi}{\hbar} \left| \langle v_{1,\uparrow}, \omega, \Omega | \hat{H}_{el} | \bar{c}'_{1,\uparrow} \rangle \right|^2 \delta \left( E_{\bar{c}'_{1,\uparrow}} - E_{v_{1,\uparrow}} - \hbar\Omega - \hbar\omega \right) \quad (4.17)$$

$$= \frac{2\pi}{\hbar} \left| \frac{\langle v_{1,\uparrow}, \omega, \Omega | \hat{H}_{el} | \bar{c}_{1,\downarrow}, \Omega \rangle \langle \bar{c}_{1,\downarrow}, \Omega | \hat{H}_{ep} | \bar{c}'_{1,\uparrow} \rangle}{E_{\bar{c}'_{1,\uparrow}} - E_{\bar{c}_{1,\downarrow}} - \hbar\Omega} \right|^2 \delta(\dots) \quad (4.18)$$

where  $\omega$  represents an emitted photon with energy  $\hbar\omega$ . Using the symmetries of each band as discussed earlier in this chapter and Chapter 1, we have evaluated the above expression

and find that it is non-zero (the transition is allowed) only when the emitted phonon has left-handed chirality ( $C_3(\Omega) = -1$ ) and the emitted photon has right-circular polarization ( $\hat{P}_+$ ). Similarly, the intervalley exciton with hole in the  $K'$ -valley will emit a right-handed chiral phonon and left-circularly polarized photon ( $\hat{P}_-$ ). Thus, the intervalley replica follows the optical selection rules of the bright exciton with identical hole. Together, the gate-dependence, magnetic-field-induced Zeeman shift, and optical selection rules consistent with our analysis and previous theory [83, 84] provide compelling evidence to support our identification of  $I_p^0$  and the intervalley trion replicas  $I_p^-, I_p^+$ .

#### 4.4.6 Multipath Radiative Relaxation of Dark Trions

Finally, we consider the detailed relaxation processes for the dark trions ( $D^+, D^-$ ). In this chapter, we have already observed three distinct relaxation pathways of the dark trion *via* PL at zero magnetic field - the direct dark trion states ( $D^+, D^-$ ), the intravalley phonon replicas ( $D_p^+, D_p^-$ ), and the intervalley phonon replicas ( $I_p^+, I_p^-$ ). As discussed above, however, and illustrated in Figure 4.12(b-d), the dark trion has at least *four* possible relaxation pathways. We cannot distinguish the defect-mediated intervalley trion PL ( $I^\pm$ ) and the direct dark trion PL ( $D^\pm$ ) as the two pathways should be energetically degenerate at zero magnetic field. To resolve this issue, we carefully examine the hole dark trion configuration under strong out-of-plane magnetic field. The magnetic field breaks the exciton / band valley degeneracy as illustrated in Figure 4.18(a) such that the intravalley and intervalley relaxation are no longer energetically degenerate and will instead shift in energy with their respective valley Zeeman  $g$ -factors ( $\sim 9$  and  $\sim 13$ , respectively). Both the direct dark trion ( $D^+$ ) and defect-mediated intervalley trion ( $I^+$ ) emit linearly polarized PL. Therefore,

we expect to observe a four-fold splitting of the dark trion ( $I_K^+, D_K^+; D_{K'}^+, I_{K'}^+$ ) to appear in magneto-PL, which is shown schematically in Figure 4.18(b). We note that the two higher energy branches originate from dark trions with electrons in the  $K'$ - and  $K$ -valley, respectively, as illustrated in Figure 4.18(a). Likewise, the two lower energy branches originate from dark trions in opposite valleys.

To explore this intravalley and intervalley splitting of the dark exciton, we measure the hole side PL at high magnetic field. Although the four-fold splitting should be observable for any PL detection polarization due to the valley-independent linearly polarized emission of  $I^+$  and  $D^+$ , it is nonetheless experimentally preferable to use circularly polarized detection to simplify the remainder of the spectrum and observe just one branch of each phonon replica PL. Figure 4.18(c) shows a hole-side gate-dependent PL map ( $V_g = 0$  V to  $-5$  V) at  $B = 15$  T. We can immediately identify those PL features previously discussed in this chapter:  $D_K^+, D_{K'}^+, D_p^+, I_p^+$ . At intermediate gate voltage, however, we observe an apparent splitting of  $D_{K'}^+$ , and the appearance of a higher energy PL feature which we label as  $I_K^+$ . We verify this assignment of  $I_K^+$  by performing a magnetic-field-dependent measurement at  $V_g = -5$  V, shown in Figure 4.19(a), to observe the magnetic-field-induced splitting of  $D_{K'}^+$  and  $I_K^+$ . We extract the PL energy of both features and plot the energy difference,  $\Delta E$ , in Figure 4.19(b). By performing a linear fit of  $\Delta E$ , we estimate a relative  $g$ -factor for the trion splitting ( $g = 2.35$ ). As illustrated in Figure 4.18(a), the magnetic-field-induced energy splitting between  $D_{K'}^+$  and  $I_K^+$  is simply the Zeeman splitting of the lower conduction subband. Thus, we can directly measure the  $g$ -factor of that band assuming that the electron in the dark trion follows the free-particle band energy at finite charge density. As

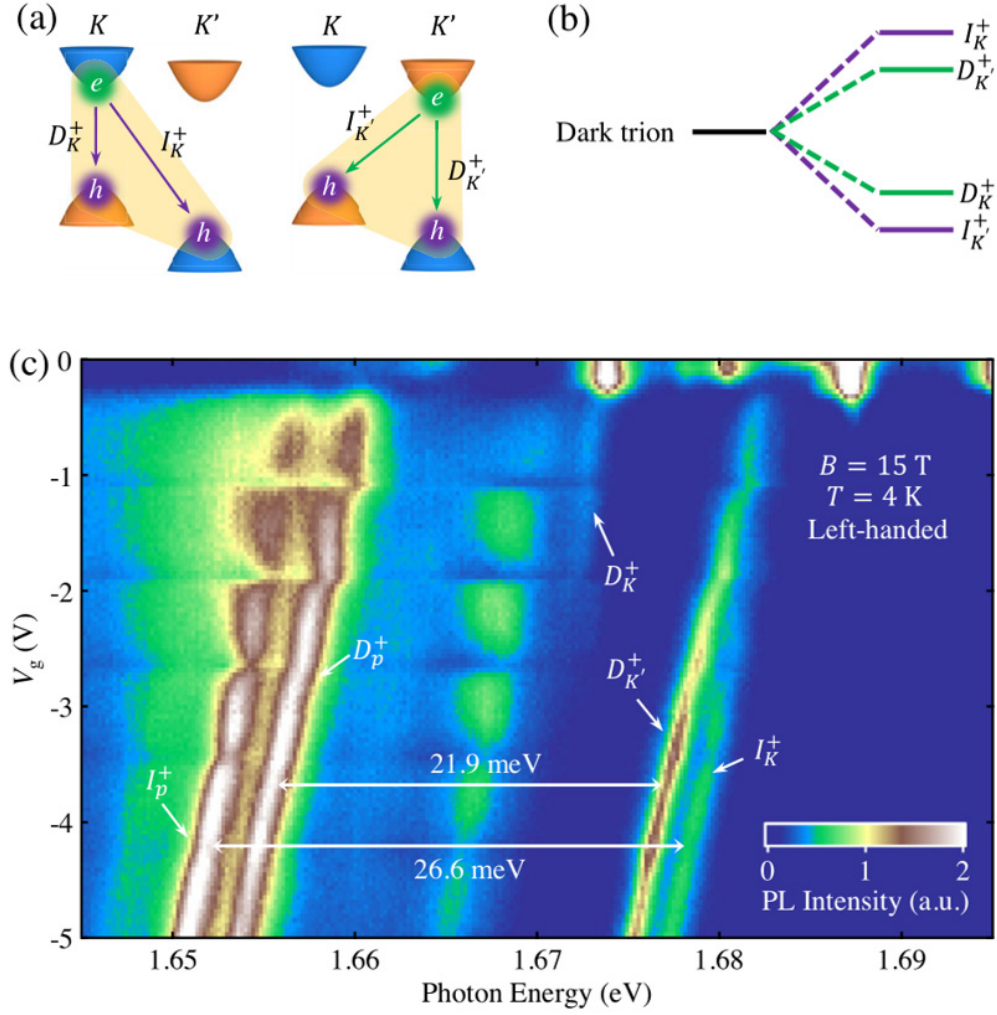


Figure 4.18: Splitting of intra- and inter-valley trion emission under a magnetic field. (a,b) Schematic configurations and energy levels of different trion transitions. The application of a magnetic field splits the fourfold degenerate trion emission into four distinct emission lines, labeled as  $I_K^+$ ,  $D_{K'}^+$ ,  $D_K^+$ , and  $I_{K'}^+$  from high to low energy.  $D$  and  $I$  denote intra- and inter-valley transitions, respectively; the  $K$  and  $K'$  subscripts denote the valley of the electron in the trion. (c) The left-handed PL map on the hole side of monolayer WSe<sub>2</sub> at  $B = 15$  T. The different transitions and energy separations are denoted. The gate-dependent oscillations of PL intensity come from Landau quantization.

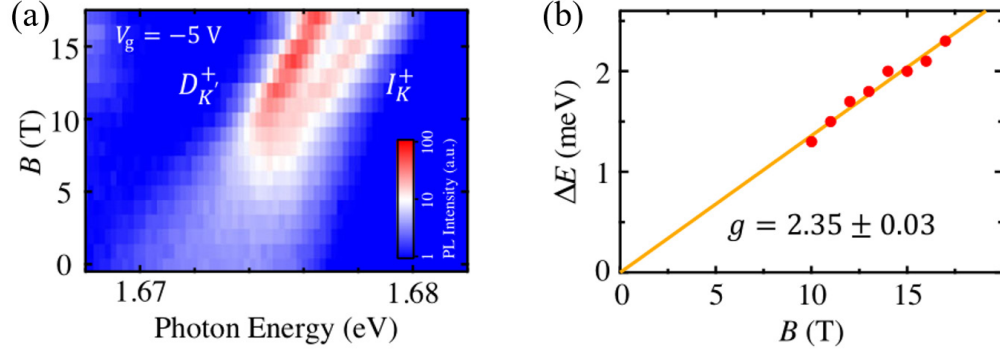


Figure 4.19: (a) Log-scale magnetic-field-dependent PL map of positive dark trions ( $D_{K'}^+$ ,  $I_K^+$ ) for  $B = 0$  to 17 T at  $V_g = -5$  V. (b) Energy separation between the  $D_{K'}^+$  and  $I_K^+$  as a function of magnetic field. The line is a linear fit from which we extract an effective  $g$ -factor of  $2.35 \pm 0.03$ .

discussed in Chapter 1, the final term in the single-particle valley Zeeman shift expression is arises from the Berry curvature, which has opposite sign in the  $K$ - and  $K'$ -valleys. Thus, including the spin-magnetic moment component, the total Zeeman of the lower conduction subband is:

$$\Delta E = g_{band}\mu_B B = 2\mu_B B \left(2 + 2\frac{m_0}{m^*}\right) \quad (4.19)$$

where  $g_{band}$  is the band  $g$ -factor,  $\mu_B$  is the Bohr magneton,  $m_0$  is electron mass, and  $m^*$  is the carrier effective mass. We therefore estimate the electron effective mass in the lower conduction subband as  $m^* = 0.46m_0$ , which is consistent with theoretical predictions [26].

#### 4.4.7 Conclusion

In summary, we examined the complex landscape of intra- and intervalley radiative relaxation pathways for excitons and trions in monolayer WSe<sub>2</sub> using photoluminescence spectroscopy of high-quality BN-encapsulated gating devices. We observed the PL of the neutral intervalley exciton and determined that it can relax either through defect-mediated

or phonon-mediated replica pathways which we label as  $I^0$  and  $I_p^0$ . Using a group-theory-based symmetry analysis, we derive the optical and phonon selection processes for both relaxation pathways. We further apply strong out-of-plane magnetic field to measure the intervalley exciton (replica)  $g$ -factors. The magnetic field also breaks the degeneracy of the intra- and intervalley relaxation pathways for the dark trion - the former is the previously studied dark trion  $D^+, D^-$ , while the latter is relaxation of the dark trion following the defect-mediated pathway which we established for  $I^0$ . We thus demonstrate four distinct radiative relaxation pathways of the dark trion:  $D^\pm, I^\pm$ , the intravalley  $\Gamma$ -point chiral phonon replica ( $D_p^\pm$ ) and the  $K$ -point intervalley chiral phonon replica ( $I_p^\pm$ ).

Totally, we demonstrated in this chapter a more complete experimental and theoretical picture of the complex excitonic landscape in monolayer WSe<sub>2</sub> at the charge neutrality point and under moderate electron (hole) doping.

## Chapter 5

# Interlayer Phonons in Transition Metal Dichalcogenides

To build a more complete understanding of the 2D materials and how they can be arranged to produce desirable properties, it is important to investigate the interlayer coupling and effects of layer-by-layer stacking in addition to the properties of each monolayer material itself. In this section, we directly study the interlayer coupling in two TMD material homostructures - NbSe<sub>2</sub> and MoS<sub>2</sub> - through their interlayer phonons *via* ultralow-frequency Raman Spectroscopy. We examine the interlayer phonon spectra in 2H-NbSe<sub>2</sub> and two stacking configurations (3R and 2H) of MoS<sub>2</sub> from the monolayer to bulk crystal from which we determine the stacking-dependent elastic properties. We further develop an analytical model based on bond polarizability to calculate the interlayer phonon Raman intensities. Together with our experimental results, we demonstrate an efficient method to efficiently identify the thickness and stacking configuration of 2D materials *via* Raman spectroscopy.

## 5.1 Stacking-Dependent Interlayer Phonons in 3R- and 2H-MoS<sub>2</sub>

Besides graphene, molybdenum disulfide (MoS<sub>2</sub>) is a likely the most studied 2D material. Monolayer MoS<sub>2</sub> was successfully isolated only a short time after graphene and has since become a backbone of 2D semiconductor research. In monolayer form, MoS<sub>2</sub> exhibits a non-centrosymmetric trigonal prismatic (1H) structure with alternating layers of sulfur and molybdenum atoms as illustrated in Figure 5.1(a). The lack of inversion symmetry, coupled with intrinsic 2D quantum confinement and strong spin-orbit coupling, produces a remarkable array of electronic properties such as its direct band-gap, room-temperature excitonic effects [92, 93], spin-valley coupling [94], and strong optical harmonic generation [95–97]. Upon adding a second layer, however, MoS<sub>2</sub> commonly adopts a hexagonal 2H configuration Figure 5.1(c) in which adjacent layers are inversion partners. For even-layered systems, this results in a restoration of inversion symmetry which suppresses the most interesting valleytronic [94] and nonlinear optical properties [95, 96]. Odd-layered systems lack inversion symmetry as a whole; however, alternating layers are still inversion symmetric. While those properties which require symmetry breaking can reemerge in odd-layered samples, alternating layers contribute destructively [95, 97]

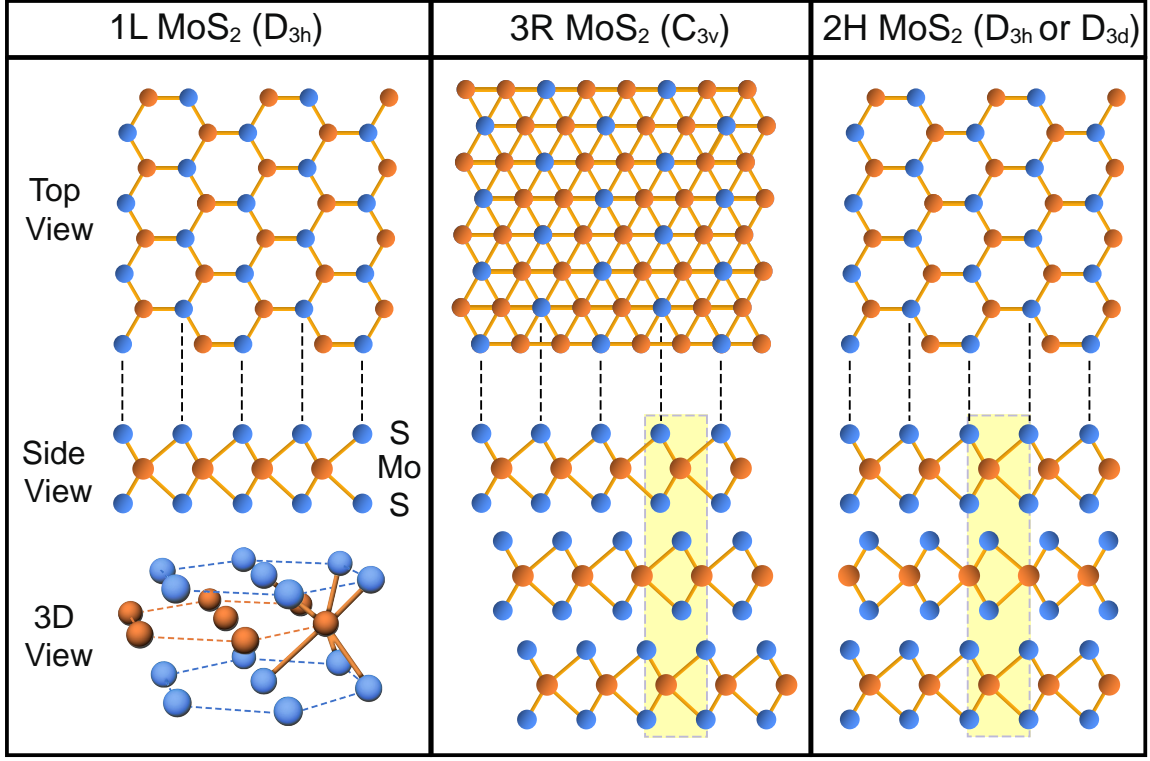


Figure 5.1: The crystalline structure of monolayer MoS<sub>2</sub>, few-layer 3R- and 2H-MoS<sub>2</sub> polytypes. The top (bottom) column shows the top (side) view of the crystals. The dashed boxes highlight the interlayer atomic alignment. 3R-MoS<sub>2</sub> has the non-centrosymmetric point group  $C_{3v}$  for all layer numbers. 2H-MoS<sub>2</sub> has the  $D_{3h}$  ( $D_{3d}$ ) point group for odd (even) layer numbers.

### 5.1.1 Rhombohedral (3R) MoS<sub>2</sub>

MoS<sub>2</sub> exhibits a second stable stacking order which remains non-centrosymmetric for arbitrary layer number. As shown in Figure 5.1(b), adjacent layers are only translated slightly with regard to their neighbors in the rhombohedral 3R stacking order. Thus, 3R-MoS<sub>2</sub> lacks inversion symmetry for all layer numbers and preserves the desirable valleytronic and nonlinear optical properties into the bulk limit [97–100]. Theory predicts that the 3R crystal may also host distinct inter-layer hybridized excitonic states [101]. Notably, 3R-MoS<sub>2</sub> is naturally occurring and constitutes  $\sim 1\%$  of naturally formed MoS<sub>2</sub> crystals.

Although 3R-MoS<sub>2</sub> has many technologically attractive properties which avoid the practical requirement of monolayer fabrication, we lack an efficient, non-destructive method with which to characterize the thickness and stacking configuration of MoS<sub>2</sub> crystals. Standard characterization methods such as electron microscopy, x-ray or electron diffraction, and scanning probe microscopy cannot simultaneously determine the thickness and stacking order. Further, these methods are practically difficult to apply to large scale samples and require significant initial investment and setup. Thus, we turn to Raman spectroscopy as a rapid, non-destructive, and comparatively simple tool to effectively characterize multilayer 2D material samples. The in-plane phonon modes have been used to identify the thickness of few-layer graphene samples, for example, but these spectral features evolve subtly with increasing thickness and quickly converge towards a “bulk” limit beyond  $\sim 5L$ . Thus, Raman spectroscopy of the high-energy in-plane phonons is not an ideal tool for characterizing multilayer structures.

### 5.1.2 Interlayer Phonons

In contrast, the behavior of the interlayer phonons – collective layer-by-layer vibrations of the multilayered crystal – is largely determined by the crystal thickness and detailed stacking configuration. If we consider the 2D layers as approximately rigid sheets, the system should exhibit vibrations which involve either in-plane or out-of-plane displacement. These are the interlayer *shear* and *breathing* phonon modes, respectively. The multilayer structure can be considered a system of nearest-neighbor coupled oscillators where the coupling arises entirely from the weak van der Waals interaction whose normal vibration modes are highly sensitive to the number of layers, interlayer coupling geometry, and surface en-

environment (e.g., adsorbates). By virtue of the weak coupling, the interlayer phonons have exceptionally low energy ( $\sim 0.5 - 5$  meV) as compared to the intralayer phonons composed of strong covalent interatomic bonds ( $\sim 20 - 400$  meV). To measure the interlayer vibrations, we must use specialized *ultralow-frequency* Raman spectroscopy. This technique is well-established and has been widely used to characterize the interlayer phonons and associated properties in a variety of 2D materials [102–111].

In this section, we conduct ultralow-frequency Raman spectroscopy on 2H and 3R MoS<sub>2</sub> sample with varied thickness to study the thickness- and stacking-order-dependence of the interlayer phonons and thus interlayer coupling. From these spectra, we derive the material elastic properties (shear, bulk moduli) and develop a complementary analytical model of the low-frequency Raman spectra.

### 5.1.3 Methodology

We fabricated both 2H- and 3R-MoS<sub>2</sub> flakes with layer number  $N = 1L-13L$  by mechanical exfoliation of bulk crystals onto SiO<sub>2</sub>(285 nm)/Si substrates. We grew bulk 3R-MoS<sub>2</sub> crystals by chemical vapor transport using the method detailed by J. Shi *et al.* [99]. Bulk natural We used natural bulk 2H crystals (HQ Graphene). We measured all Raman spectra shown using a commercial LabRam HR Raman microscope (Horiba) in a backscattering geometry. With this system, we are able to resolve Raman spectra to within  $\sim 5$  cm<sup>-1</sup> of the excitation laser energy with spectral resolution of 0.5 cm<sup>-1</sup>. For all measurements, we use a 532-nm continuous laser with incident on-sample power  $\leq 1$  mW and spot diameter  $\sim 1$   $\mu$ m. In addition to unpolarized Raman spectra, we measure both co- (VV) and cross-linear-polarized (HV) Raman spectra. We vary the linear polarization of the

incident laser using a variable-rotation half-wave plate and detect only scattered light with vertical polarization using a fixed linear polarizer. We note that the shear modes (which feature perpendicular in-plane displacements) are energetically degenerate due to the in-plane isotropy of MoS<sub>2</sub> but are only Raman active for cross-polarized and co-polarized geometries, respectively. Thus, the shear mode appears equally in both polarization schemes. The breathing mode, however, is Raman active only in the co-polarized scheme.

#### 5.1.4 Experimental Low-Frequency Raman Spectra

We first examine the low-frequency Raman spectra of bilayer 2H- and 3R-MoS<sub>2</sub>. Our experimental results are shown in Figure 5.2(a, c) for each stacking order, respectively. In both, we identify two low-frequency Raman features which we assign to the doubly degenerate interlayer shear (S) mode and the breathing (B) mode. For ease of comparison, we normalize the Raman spectra to the shear mode height. The shear features are remarkably similar for both stacking configurations ( $\omega = 22 \text{ cm}^{-1}$ ). In contrast, the 3R breathing mode ( $37 \text{ cm}^{-1}$ ) is lower in energy than the 2H breathing mode ( $40 \text{ cm}^{-1}$ ). The interlayer phonon frequency serves as a measure of interlayer coupling strength, so this difference in breathing mode energy suggests that 3R layers may be less strongly bound than 2H. The relative intensities of the shear and breathing modes also differ between the stacking configurations – the 2H breathing mode has significantly lower relative intensity ( $\sim 25\%$ ) as compared to 3R ( $\sim 70\%$ ).

For comparison, we calculated unpolarized low-frequency Raman spectra for both stacking orders via density functional theory (DFT). The calculated spectra are plotted

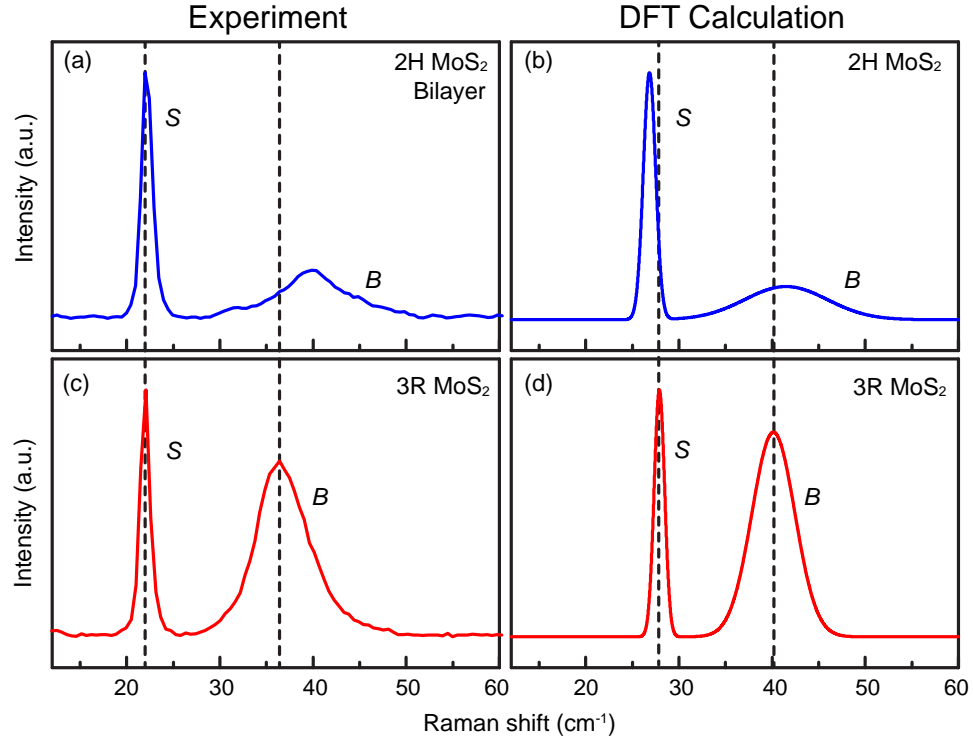


Figure 5.2: Experimental (a, c) and calculated (b, d) Raman spectra of the interlayer shear (S) and breathing (B) modes for 2H- (a, b) and 3R- (c, d) MoS<sub>2</sub> bilayer. The theoretical spectra are obtained by first-principle calculations based on density functional theory (DFT); they are presented as Gaussian functions of the same line width as the experimental spectra. The dashed lines highlight the different frequency separation between the shear and breathing modes in the 2H and 3R polytypes.

in Figure 5.2(b, d). For details of this calculation, see the supplementary material [112].

Although the absolute frequency of each feature is shifted, the calculated spectra nonetheless reproduce the two primary experimental results. The frequency separation between the shear and breathing modes is  $3 \text{ cm}^{-1}$  greater in 3R as compared to 2H, which is identical to our experimental findings. Further, the relative intensities of the breathing and shear modes are in good agreement with experiment. Thus, we have demonstrated a quantitative distinction between the low frequency Raman spectra of 2H- and 3R-MoS<sub>2</sub>.

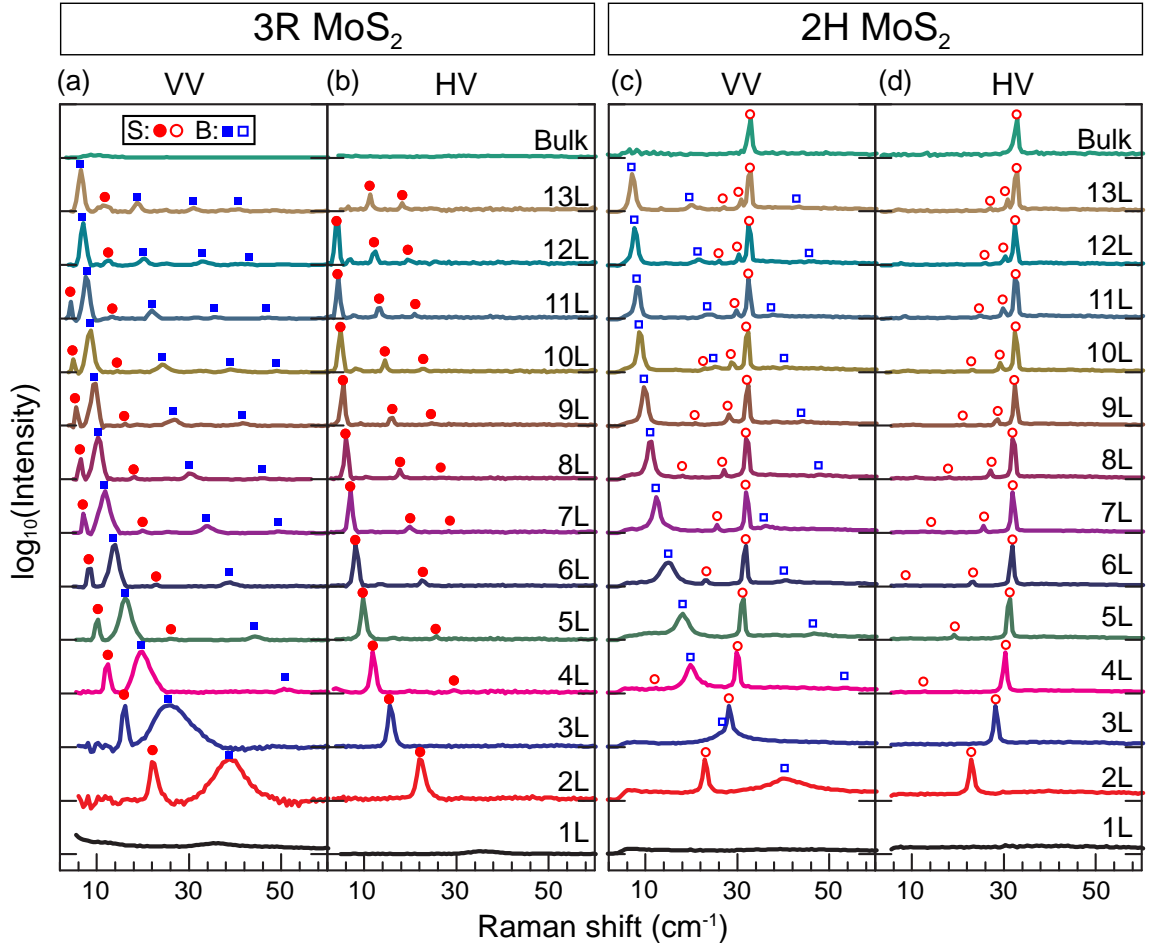


Figure 5.3: (a)–(d) Parallel-polarized (VV) and cross-polarized (HV) Raman spectra of the shear modes (S; red dots) and breathing modes (B; blue squares) for 3R-MoS<sub>2</sub> (solid symbols) and 2H-MoS<sub>2</sub> (open symbols) with layer number  $N = 1L - 13L$ . The breathing modes appear only in the VV geometry, whereas the shear modes appear in both the VV and HV geometries. We have subtracted the broad Raman background and plot the spectra in the logarithmic scale to display the weak interlayer modes.

## Layer-Dependent Low-Frequency Raman Spectra

Expanding on this investigation of bilayer MoS<sub>2</sub>, we examine the low-frequency Raman spectra for thicker 2H and 3R samples. Figure 5.3 shows log-scaled spectra with parallel polarization (VV) and cross-polarization (HV) for 3R and 2H samples with layer number 2L – 13L and bulk. For clarity, we systematically subtracted a broad Raman background from each spectrum to highlight the interlayer Raman features. As in a classical model of nearest-neighbor coupled oscillators, a system of  $N$  masses will host  $N - 1$  normal modes. Thus, for an  $N$ -layered sample there are  $N - 1$  breathing modes and  $N - 1$  doubly degenerate shear modes due to the in-plane isotropy of MoS<sub>2</sub>. We note, however, that not all interlayer vibration modes are observable in our experiment. We discuss the detailed Raman activity of the interlayer phonons later in this section. Nonetheless, we observe up to three shear mode branches (labeled in red) and four breathing mode branches (labeled in blue) in thick MoS<sub>2</sub> samples. The observed breathing modes of both stacking orders exhibit qualitatively similar behavior – each breathing branch redshifts with increasing layer number. In contrast, the observed shear modes of 2H and 3R crystals exhibit distinct behavior. To isolate the shear mode features, we measure the cross-polarized (HV) Raman spectra where the breathing mode features are suppressed. The 3R shear mode features redshift with increasing layer number, similar to the breathing modes, whereas the 2H shear modes exhibit qualitatively opposite behavior and blueshift towards a bulk limit of  $\sim 31 \text{ cm}^{-1}$ .

### 5.1.5 Frequency Analysis *via* Linear Chain Model

An  $N$ -layer system of rigid vdW layers is well-described by the classical model of coupled oscillators – a linear chain model. As in literature [102], we assume that each layer is identical and interacts only with its nearest neighbors through an identical restoring force. Thus, the  $N$ -layer system will host  $N - 1$  normal vibration modes for each degree of freedom. In this case of rigid layers, one out-of-plane breathing vibration and two degenerate in-plane shear vibrations with mode frequencies given by:

$$\omega_N^{(j)} = \omega_0 \cos\left(\frac{j\pi}{2N}\right) \quad (5.1)$$

where  $N$  is the layer number,  $j = 1, 2, 3, \dots, N - 1$  is the branch index, and  $\omega_0$  is the frequency of the highest shear (breathing) branch in the bulk limit.  $N$  is known, thus  $\omega_0$  and  $j$  are the free parameters with which to fit our data.

For quantitative analysis, we fit each spectrum in Figure 5.3 with a series of Lorentzian functions and extract the center frequency of each observed Raman feature. The extracted frequencies for 3R- and 2H-MoS<sub>2</sub> are plotted in Figure 5.4 as solid and open shapes, respectively. We fit the complete set of shear modes for each stacking order separately to obtain a single shear bulk frequency,  $\omega_0$ , for each stacking configuration. The fitted shear mode branches are plotted as red lines. Solid and dashed lines indicate shear mode branches which are observed or are unseen, respectively. As suggested by previous research and our symmetry analysis of interlayer Raman modes in the 2H crystal, we find the best fit where alternating shear branches are not observable with our experimental configuration. We note that similar symmetry-group-based analysis is not effective for 3R-MoS<sub>2</sub> due to its reduced symmetry. We discuss two alternative approaches to predict the Raman activity

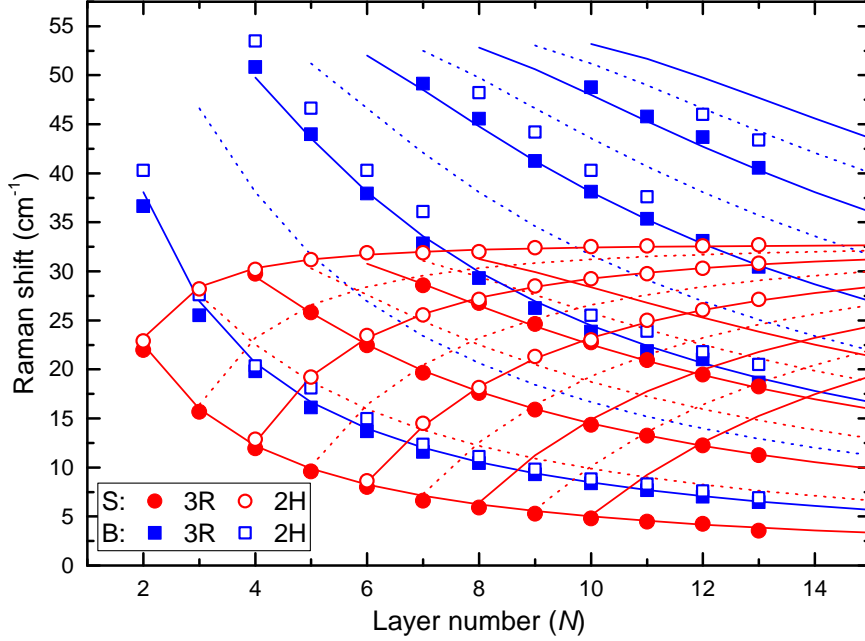


Figure 5.4: Frequencies of the observed shear modes ( $S$ ; red) and breathing modes ( $B$ ; blue) in Figure 5.3 as a function of MoS<sub>2</sub> layer number. The solid (open) symbols are experimental data for 3R- (2H-) MoS<sub>2</sub>. The blue (red) lines are the predicted frequencies of the breathing (shear) modes by the linear chain model, as described in the text. The solid (dashed) lines denote the Raman active (inactive) branches. The 2H breathing modes are consistently higher in frequency than the 3R breathing modes, whereas the shear modes have almost the same frequencies for both polytypes.

of the interlayer phonons later in this section. Regardless, the 3R shear modes appear to follow the trend of alternating Raman activity in successive shear branches.

As alluded to in our qualitative discussion above, we find that the most intense shear mode feature in 2H is the highest-frequency branch whereas the lowest-frequency branch is most intense in 3R. Thus, the shear mode activity in the two stacking orders is distinctly opposite – in 2H the branches  $j = N - 1, N - 3, N - 5, \dots$  are Raman active whereas in 3R the branches  $j = 1, 3, 5, \dots$  are Raman active. Despite the contrasting behavior evident in the Raman activity of the shear modes, we find remarkable similarity

between the fitted  $\omega_{0,S}$  values in 3R (31.85 cm<sup>-1</sup>) and 2H (32.85 cm<sup>-1</sup>) stacking orders. In bulk 2H-MoS<sub>2</sub>, the highest-frequency shear mode is directly observed with frequency 32.9 cm<sup>-1</sup> which is nearly identical to our fitted value.

### 5.1.6 Calculation of Interlayer Force Constant and Elastic Moduli

The interlayer phonon frequencies are intimately tied to the interlayer force constant and related mechanical properties like the elastic moduli. Thus, we may estimate relevant mechanical properties from our low-frequency Raman results. The interlayer force constant,  $K$ , is related to the  $j = 1$  branch bulk phonon frequency,  $\omega_0$ , by:

$$K = (\omega_0 \pi c)^2 \mu \quad (5.2)$$

where  $c$  is the speed of light in vacuum and  $\mu = 3.068 \cdot 10^{-6}$  kg-m<sup>-2</sup> is the mass per unit area of the MoS<sub>2</sub> monolayer [102,103]. Using the fitted bulk shear frequencies,  $\omega_{0,S}$ , we find the shear interlayer force constants for 3R ( $K_x = 2.76 \cdot 10^{19}$  N-m<sup>-3</sup>) and 2H ( $K_x = 2.94 \cdot 10^{19}$  N-m<sup>-3</sup>). In the same way, we estimate the out-of-plane interlayer force constants for 3R ( $K_z = 7.89 \cdot 10^{19}$  N-m<sup>-3</sup>) and 2H ( $K_z = 8.98 \cdot 10^{19}$  N-m<sup>-3</sup>). The elastic force modulus  $C$  is further related to the relevant interlayer force constant,  $K$ :

$$C = Kt \quad (5.3)$$

The interlayer distance,  $t$ , is slightly different for the 3R (6.123 Å) and 2H (6.148 Å). We thus estimate the elastic moduli which correspond to in-plane (shear modulus) and out-of-plane compression (bulk modulus). The calculated elastic moduli, along with the interlayer force constants and bulk interlayer phonon frequencies are summarized in Table 5.1. The mechanical properties of 2H MoS<sub>2</sub> have been studied previously and are in good agreement

Table 5.1: Elastic parameters of 2H- and 3R-MoS<sub>2</sub> calculated from the interlayer phonon frequencies.

|                        | Elastic parameters                         | 3R-MoS <sub>2</sub> | 2H-MoS <sub>2</sub> |
|------------------------|--|---------------------|---------------------|
| Shear properties       | $\omega_{0,S}$ (cm <sup>-1</sup> )         | 31.85               | 32.85               |
|                        | $K_x$ (10 <sup>19</sup> Nm <sup>-3</sup> ) | 2.76                | 2.94                |
|                        | $C_{44}$ (GPa)                             | 16.90               | 18.08               |
| Compressive properties | $\omega_{0,B}$ (cm <sup>-1</sup> )         | 53.85               | 87.40               |
|                        | $K_z$ (10 <sup>19</sup> Nm <sup>-3</sup> ) | 7.89                | 8.98                |
|                        | $C_{33}$ (GPa)                             | 48.32               | 55.19               |

with our results [103,104]. We note, as well, that the 14% reduction in compressive modulus in 3R MoS<sub>2</sub> relative to the 2H stacking is in line with recent theoretical predictions [113].

### 5.1.7 Group-Theory Analysis

Our first approach to understand the Raman activity of each interlayer phonon mode is to examine the symmetry of the crystal and of each vibration [17]. In this way, we can identify the Raman active interlayer phonon modes at the Brillouin zone center ( $\Gamma$ ) which may be detected in our experimental backscattering measurement geometry. From the point group of the crystal ( $D_{3d}$  for even-layered 2H-MoS<sub>2</sub>;  $D_{3h}$  for odd-layered), we can determine the vibrational representation expressed as a sum of irreducible representations:

$$\Gamma_{D_{3d}} = \frac{3N}{2}(E_g + E_u + A_{1g} + A_{2u}) \quad (5.4)$$

$$\Gamma_{D_{3h}} = \frac{3N+1}{2}(E' + A_2'') + \frac{3N-1}{2}(E'' + A_1') \quad (5.5)$$

which indicate the representation of allowed vibrations in the crystal. Consulting the character table for even (odd) layers, we find that only shear modes with  $E_g$  ( $E'$ ) representation and breathing modes with  $A_{1g}$  ( $A_1'$ ) representation are Raman active and detectable in

our measurement configuration. We examine the symmetry of each interlayer vibrational mode to determine the representation. Thus, we find that the shear modes with odd branch number ( $j = 1, 3, 5, \dots$  where  $j = 1$  is the highest frequency mode) are observable for all layer numbers and breathing modes with odd (even) branch number are observable for even (odd) layer numbers. This analysis qualitatively explains the alternating Raman activity observed for 2H-MoS<sub>2</sub> in Figure 5.4. The 3R-MoS<sub>2</sub> crystal, however, has reduced symmetry for which this group-theory-based approach is not effective.

### 5.1.8 Qualitative Description of Raman Activity

Although the standard group-theory-based approach described above fails for the 3R stacking configuration, we can directly examine the symmetry of each interlayer phonon mode to gain a qualitative understanding of its Raman tensor elements and thus the Raman activity. The Raman intensity of a phonon mode,  $k$ , is proportional to: [114,115]

$$I_k = \frac{(n_k + 1)}{\omega_k} |\hat{e}_i \cdot \tilde{R}_k \cdot \hat{e}_s^T|^2 \quad (5.6)$$

where  $\omega_k$  is the phonon frequency,  $n_k$  is the phonon population from the Bose-Einstein distribution,  $\hat{e}_i$  and  $\hat{e}_s$  are the polarization unit vectors of the incident and scattered light, respectively, and  $\tilde{R}_k$  is the Raman tensor. Classically,  $\tilde{R}_k$  is given by:

$$\tilde{R}_k = \frac{\partial \tilde{\alpha}}{\partial Q_k} \Big|_{Q_k=0} \Delta Q_k \quad (5.7)$$

where  $\tilde{\alpha}$  is the polarizability tensor,  $Q_k$  is the normal coordinate of the vibration mode, and  $\partial \tilde{\alpha} / \partial Q_k$  is the derivative of the polarizability tensor at the equilibrium lattice position ( $Q_k = 0$ ). Thus, the change in polarizability of the lattice between the positive ( $Q > 0$ )

and negative ( $Q < 0$ ) normal displacements of a vibration is related to the magnitude of the Raman tensor element.

Figure 5.5(a) illustrates the interlayer atomic configurations of the shear modes in 3L MoS<sub>2</sub> ( $S_3^1$  and  $S_3^2$ ) at positive and negative normal displacement,  $Q$ . Immediately, we see that the 3R and 2H stacking configurations have distinct relative layer position during the vibration. In 3R-MoS<sub>2</sub>, the highest frequency shear mode ( $S_3^1$ ) exhibits identical total layer displacement for  $Q > 0$  and  $Q < 0$ . The differential polarizability  $\partial\tilde{\alpha}/\partial Q_k$  is thus zero which indicates that the vibration mode is Raman inactive. In 2H-MoS<sub>2</sub>, however, the same  $S_3^1$  mode exhibits distinct total layer displacement under normal vibration. It therefore has a non-zero  $\tilde{R}_k$  and is Raman active. For the lower frequency shear mode ( $S_3^2$ ), our qualitative analysis indicates opposite activity -  $S_3^2$  is Raman active in 3R-MoS<sub>2</sub> and Raman inactive in 2H-MoS<sub>2</sub>. Similar analysis of Raman activity is applicable to interlayer vibrations in other vdW materials (e.g., graphene). [105,116]

### 5.1.9 Quantitative Bond Polarizability Model

We can quantify the above qualitative analysis using the so-called bond polarizability model which allows general calculation of the Raman tensor elements given knowledge of the relevant bond strengths and geometries [114,115]. The model considers the distortion (change in polarizability) of the interlayer bonds by the interlayer vibration modes. As alluded to in Equation 5.7, the Raman tensor elements are related to the change in bond polarizability. In a multi-bond system, each Raman tensor element is the sum of all relevant bond distortions. In relation to our experiment, the diagonal tensor element  $R_{xx}$

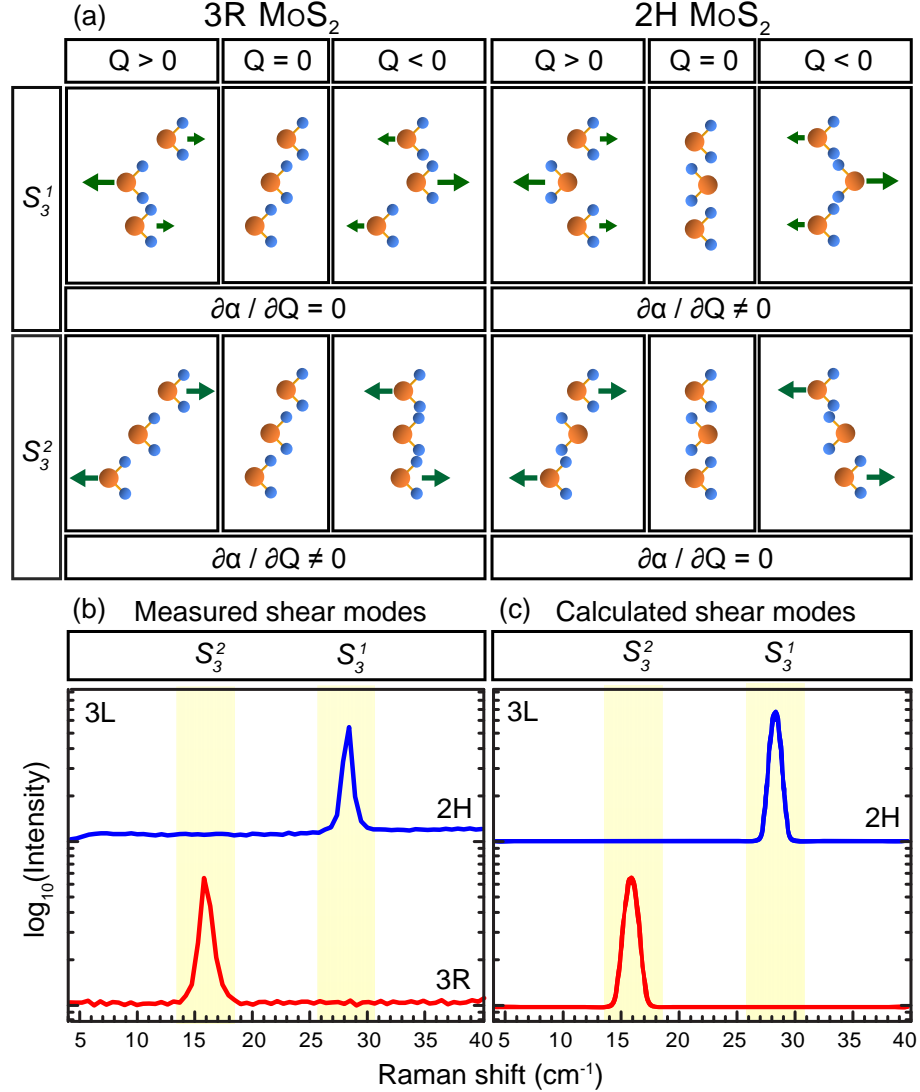


Figure 5.5: (a) Layer displacement of the two shear modes in 3R- and 2H-MoS<sub>2</sub> trilayers. By comparing the atomic configuration at opposite normal displacements ( $Q > 0$  and  $Q < 0$ ) near the equilibrium position ( $Q = 0$ ), we can deduce whether the differential polarizability ( $\partial\tilde{\alpha}/\partial Q$ ) (hence, the Raman tensor) is zero or finite. (b) and (c) The experimental and simulated cross-polarized Raman shear modes for trilayer 2H- and 3R-MoS<sub>2</sub>. In the simulation, the shear-mode frequency is predicted by the linear chain model (highlighted by the yellow bars) and the relative mode intensity is determined by the bond polarizability model. The high and low shear modes appear exclusively in the 2H and 3R trilayer, respectively.

is responsible for the parallel-polarized Raman response and the off-diagonal element  $R_{xy}$  is responsible for the cross-polarized Raman response. For a shear mode  $k$  with  $x$ -direction layer displacement in an  $N$ -layer structure, we can express the Raman tensor elements  $R_{\mu\nu}$  ( $\mu, \nu = x, y, z$ ) as:

$$R_{\mu\nu}(k) = \sum_{l=1}^{N-1} \alpha'_l(x_l - x_{l+1}) \quad (5.8)$$

where  $l$  is the layer index,  $x_l$  is the layer displacement of the layer from the equilibrium position, and  $\alpha_l$  is the  $\mu\nu$ -element of the polarizability tensor of the interlayer bond between adjacent layers.  $\alpha'_l = \partial\alpha_l/\partial x_l$  denotes the derivative of  $\alpha_l$  with respect to  $x_l$ . For shear vibration  $S_N^j$  of an  $N$ -layered system, the layer displacement  $x_l$  is estimated as:

$$x_l \propto \cos \left[ \frac{(N-j)(2l-1)}{2N} \pi \right] \quad (5.9)$$

We note that the 3R and 2H stacking configurations have the same relative layer displacements for each vibration mode, but the interlayer bond geometries are distinct. The interlayer bond structure of 3R-MoS<sub>2</sub> is shown schematically in Figure 5.6(a). Each of the layers have the same orientation and identical interlayer bonds relative to their neighbors -  $\alpha'_l$  is the same for all layers. From Equation 5.8, then, the 3R-MoS<sub>2</sub> Raman tensor elements for shear vibration depend only on the displacement of the top and bottom layers.

$$R_{\mu\nu}(k) = \alpha'_R [(x_1 - x_2) + (x_2 - x_3) + \dots + (x_{N-1} - x_N)] = \alpha'_R(x_1 - x_N) \quad (5.10)$$

In contrast, adjacent layers in 2H-MoS<sub>2</sub> have opposite orientation as illustrated in Figure 5.6(b). The interlayer bonds thus have alternating lateral orientation for neighboring layer pairs such that  $\alpha'_l = -\alpha'_{l+1}$ . If we define the differential bond polarizability of the

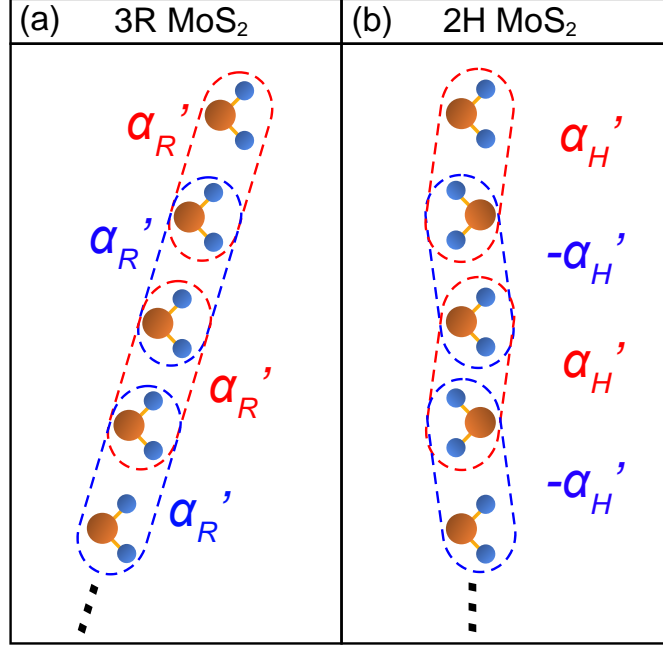


Figure 5.6: Schematic representation of interlayer bonds for (a) 3R- and (b) 2H-MoS<sub>2</sub>. The interlayer bonds have the same lateral orientation for 3R stacking, but alternate lateral orientation for 2H stacking, resulting in their distinct shear-mode Raman response. The blue/red dashed lines highlight the interactions between adjacent layers.

bottom layer pair as  $\alpha'_{l-1} = \alpha'_H$ , the general bond polarizability for layers  $l$  and  $l+1$  is thus  $(-1)^{l+1}\alpha'_H$ . From Equation 5.8, the 2H-MoS<sub>2</sub> Raman tensor elements for shear vibration:

$$R_{\mu\nu}(k) = \sum_{l=1}^{N-1} (-1)^{l+1} \alpha'_H (x_l - x_{l+1}) = \alpha'_H [(x_1 - x_2) - (x_2 - x_3) + \dots (x_{N-1} - x_N)] \quad (5.11)$$

Finally, we can combine the three above equations with Equation 5.6 to calculate the Raman intensity for each shear vibration mode. We thus find general analytic expressions for the Raman intensities of the 3R and 2H shear modes,  $k$ :

$$I_{3R}(k) \propto \frac{n_k + 1}{\omega_k} |\alpha'_R|^2 \sin^2 \left[ \frac{(N-j)(N-1)}{2N} \pi \right] [1 - (-1)^{N-j}] \quad (5.12)$$

$$I_{2H}(k) \propto \frac{n_k + 1}{\omega_k} |\alpha'_H|^2 \sin^2 \left( \frac{N-j}{2N} \pi \right) \tan^2 \left( \frac{N-j}{2N} \pi \right) [1 - (-1)^j] \quad (5.13)$$

We note that in Equation 5.12, the final term  $1 - (-1)^{N-j}$  is zero when  $N - j$  is even leading to non-zero Raman intensity of the shear modes in 3R-MoS<sub>2</sub> for branch indices  $j = N - 1, N - 3, N - 5, \dots$ . Similarly, the final term in Equation 5.13 is zero when  $j$  is even. Thus, we expect non-zero Raman intensity of the shear modes in 2H-MoS<sub>2</sub> for branch indices  $j = 1, 3, 5, \dots$ . Both predictions are accurately reflected in our experimental data as shown in Figure 5.4.

### Quantitative Calculation of Relative Raman Intensity

Beyond qualitatively accounting for the observed activity of the interlayer phonon modes, Equation 5.12 and Equation 5.13 allow us to quantitatively model the Raman intensity of shear vibrations for each layer number and stacking order. To simulate the complete low-frequency Raman spectra, we use the linear chain model (Equation 5.1) to determine the mode frequencies and the bond polarizability model to determine the relative Raman intensity of each phonon mode. Each Raman mode contributes to the total spectrum as a Gaussian function whose width is matched to the corresponding experimental feature. For direct comparison, we plot the experimental and calculated cross-polarized Raman spectra for 2H- and 3R-MoS<sub>2</sub> in Figure 5.5 and Figure 5.7. To illustrate the good agreement with experiment, we show data for samples with 3L, 5L, and 9L thickness. In each case, the experimental relative Raman intensities are accurately reflected in the model calculation.

We can further extend the model calculation to include the out-of-plane breathing modes by redefining the differential polarizability as that of the out-of-plane bonding ( $\alpha'_l = \partial\alpha_l/\partial z_l$ ) where  $z_l$  is the vertical displacement of layer  $l$  during the course of vibration. The

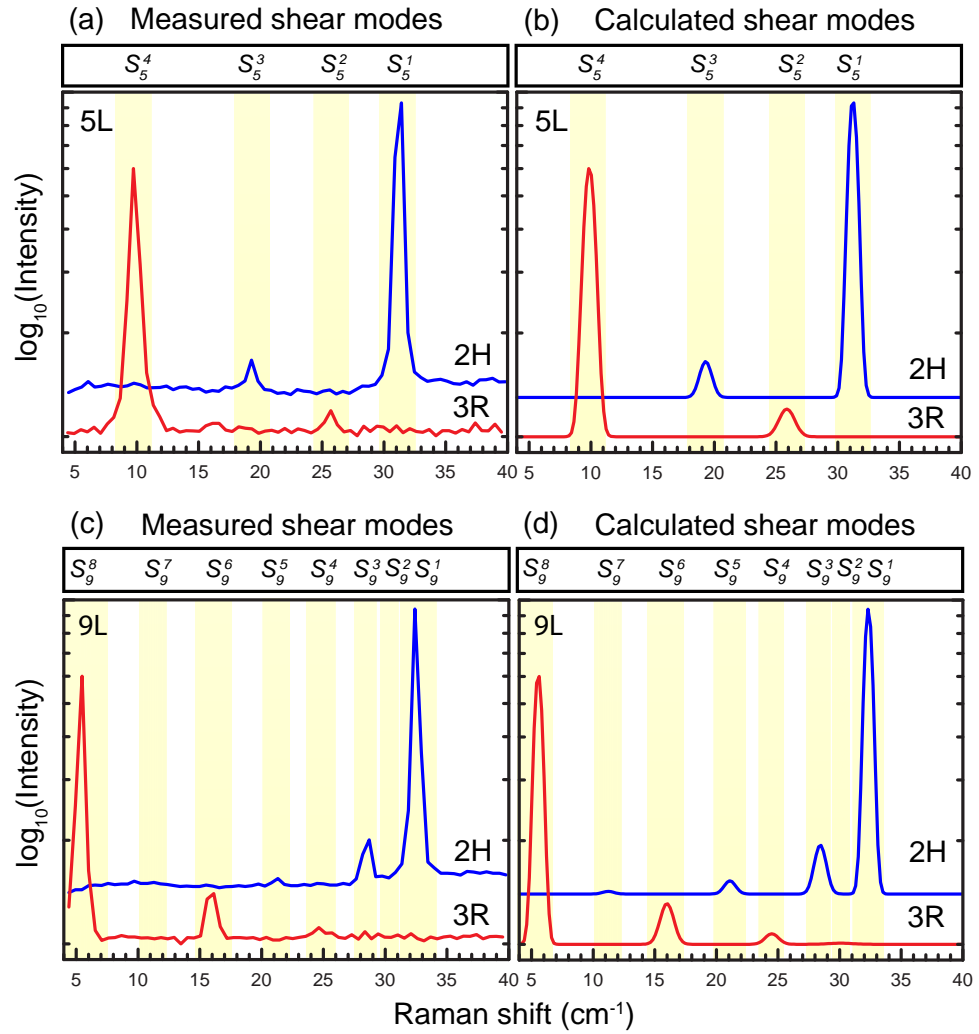


Figure 5.7: Comparison of the cross-polarized (HV) experimental and simulated shear-mode Raman spectra for 5L and 9L MoS<sub>2</sub> in both 3R and 2H phases. In the simulation, the shear-mode frequency is predicted by the linear chain model (highlighted by the yellow bars) and the relative mode intensity is determined by the bond polarizability model.

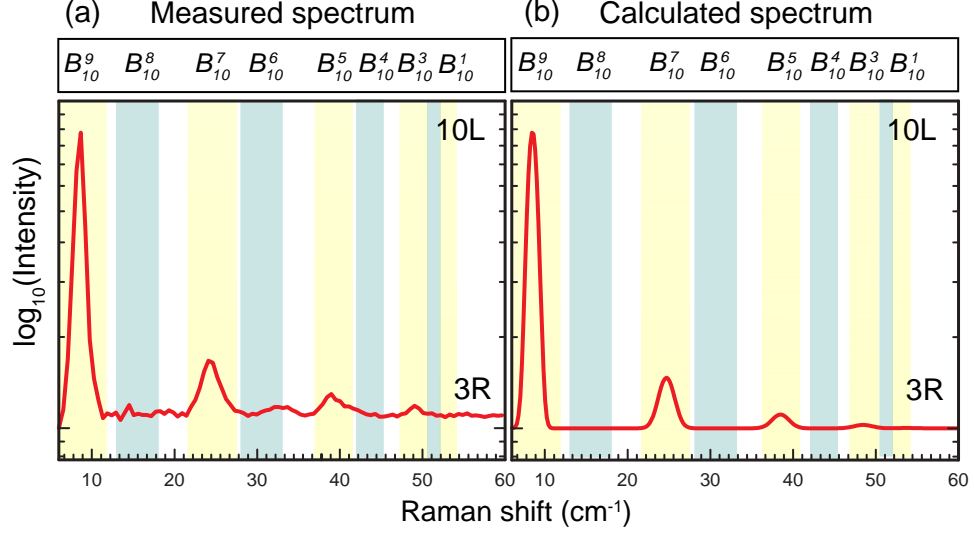


Figure 5.8: (a) The experimental parallel-polarized spectrum of 10L 3R MoS<sub>2</sub>. The four major peaks are the breathing modes. (b) The simulated breathing-mode spectrum for 10L MoS<sub>2</sub> by the linear chain model and the bond polarizability model. The yellow (blue) bars denote the Raman active (inactive) breathing modes.

out-of-plane bond symmetry is identical for both 2H- and 3R-MoS<sub>2</sub> as it does not depend on the lateral layer orientation. Thus,  $\alpha'_i$  is the same for all layer pairs for both stacking orders. This is similar to the symmetry of  $\alpha'_i$  for the 3R shear modes, so the breathing mode Raman intensity expression follows the form of the 3R shear modes with modified value of  $\alpha'_i$ .

$$I_Z(k) \propto \frac{n_k + 1}{\omega_k} |\alpha'_Z|^2 \sin^2 \left[ \frac{(N-j)(N-1)}{2N} \pi \right] [1 - (-1)^{N-j}] \quad (5.14)$$

For clarity, the magnitude of the out-of-plane bond polarizability  $\alpha'_Z$  is an empirical material property that may be different for different stacking orders. We compare the experimental and model parallel-polarized Raman spectra for 10L 2H- and 3R-MoS<sub>2</sub> in Figure 5.8. As with the shear modes, we find that the model quantitatively reproduces the experimental spectrum.

### 5.1.10 Conclusion

In summary, we conducted a comprehensive experimental investigation of the interlayer phonons in 3R- and 2H-MoS<sub>2</sub> *via* ultralow-frequency Raman spectroscopy. We measured the layered dependent Raman spectra and used a linear chain model to extract the interlayer coupling constants and elastic moduli of each stacking order. We find that the in-plane coefficients are similar, but the 2H-MoS<sub>2</sub> is  $\sim 14\%$  stiffer to out-of-plane compression than 3R-MoS<sub>2</sub>. We next examine the Raman activity of both crystals *via* symmetry analysis and implement a bond-polarizability-based model to calculate the Raman tensor elements and thus Raman intensities of the interlayer phonons. Together, our results provide experimental comparison of the mechanical properties of the 3R and 2H stacking configurations in MoS<sub>2</sub> and a simple experimental and numerical approach to simultaneously characterize the thickness and stacking order of 2D materials with layer number  $\lesssim 20$ .

## 5.2 Interlayer Breathing and Shear Modes in NbSe<sub>2</sub> Atomic Layers

Like MoS<sub>2</sub>, Niobium diselenide (NbSe<sub>2</sub>) is another transition metal dichalcogenide (TMD). In contrast to semiconducting MoS<sub>2</sub>, however, NbSe<sub>2</sub> is a conductor which undergoes two electronic phase transitions as it is cooled to low temperature. In the bulk, NbSe<sub>2</sub> undergoes a charge-density-wave (CDW) transition at 33.5 K and becomes superconducting at 7.2 K. [117, 118] Our motivation to study the interlayer interactions in this material stems from the distinct thickness dependence of these phase transitions [119–121], as well as the emergence of new properties (e.g., Ising superconductivity [121]) in the monolayer

limit. Counter-intuitively, the CDW transition is enhanced with decreasing thickness but the superconducting phase appears to be suppressed. Such a significant layer-dependence of the electronic properties suggests that interlayer interactions play a crucial role in the electronic phase transitions in this material.

In this section, we conduct a similar layer-dependent measurement to the previous section of the interlayer phonons in 2H-NbSe<sub>2</sub> *via* ultralow-frequency Raman spectroscopy. Using a linear chain model, we extract the interlayer coupling coefficient and force constants for in-plane and out-of-plane displacement. We under the observed Raman activity of shear and breathing modes using group theory, qualitative symmetry analysis, and comparison to DFT-calculated interlayer phonon frequencies.

### 5.2.1 Methodology

NbSe<sub>2</sub> samples with layer number  $N = 1 - 15L$  were fabricated by mechanical exfoliation of high-quality bulk NbSe<sub>2</sub> crystals onto polydimethylsiloxane (PDMS) stamps and then transferred onto clean SiO<sub>2</sub>/Si substrates [120]. Sample thickness was preliminarily determined *via* optical contrast and confirmed by the interlayer phonon frequency analysis presented below. NbSe<sub>2</sub> is susceptible to degradation with exposure to ambient conditions. To minimize this degradation, we capped some samples with thick BN flakes (10–20 nm) and stored all samples in vacuum aside from short inter-chamber transfer time. We measured all Raman spectra shown using a commercial LabRam HR Raman microscope (Horiba) in a backscattering geometry. With this system, we are able to resolve Raman spectra to within  $\sim 5 \text{ cm}^{-1}$  of the excitation laser energy with spectral resolution of  $0.5 \text{ cm}^{-1}$ . For all measurements, we use a 532-nm continuous laser with incident on-sample power  $\leq 5 \text{ mW}$

and spot diameter  $\sim 2 \mu\text{m}$ . Through measurement, the samples were contained within a helium-cooled optical cryostat with controllable temperature  $T = 8 - 300 \text{ K}$ .

### 5.2.2 Crystal Structure of $\text{NbSe}_2$

We first analyze the crystal structures of 2H- $\text{NbSe}_2$  using the convention by Wilson and Yaffe [122]. We present similar analysis of 2H- $\text{MoS}_2$ , for comparison. As with  $\text{MoS}_2$ , each  $\text{NbSe}_2$  monolayer is composed of three layers (chalcogen, transition metal, chalcogen), the relative arrangement of which can be specified. In this convention, the relative positions of the chalcogen layers are denoted by upper case characters (A,B,C) where “B” indicates linear translation by one unit length relative to “A” and “C” indicates linear translation of two unit lengths. Relative positions of the middle transition metal layer is similarly represented by lower case characters (a,b,c). Thus, the monolayer structure AbA indicates that the chalcogen layers are aligned and the transition metal layer is offset by one unit length. Figure 5.9 shows a schematic of the crystal structures of bilayer  $\text{MoS}_2$  (b) and  $\text{NbSe}_2$ . The bilayer  $\text{MoS}_2$  has structure AbA BaB (2Hc), while bilayer  $\text{NbSe}_2$  has structure AcA BcB (2Ha). Thus, the crystal structures differ only in the relative placement of the transition metal layer.

Despite the differing crystal structure, symmetry analysis shows that bilayer 2H- $\text{NbSe}_2$  and 2H- $\text{MoS}_2$  belong to the same symmetry group. Indeed, the crystals share symmetry group for all thicknesses:  $D_{3d}$  with inversion symmetry for even layer numbers and  $D_{3h}$  with planar mirror symmetry for odd layer numbers.

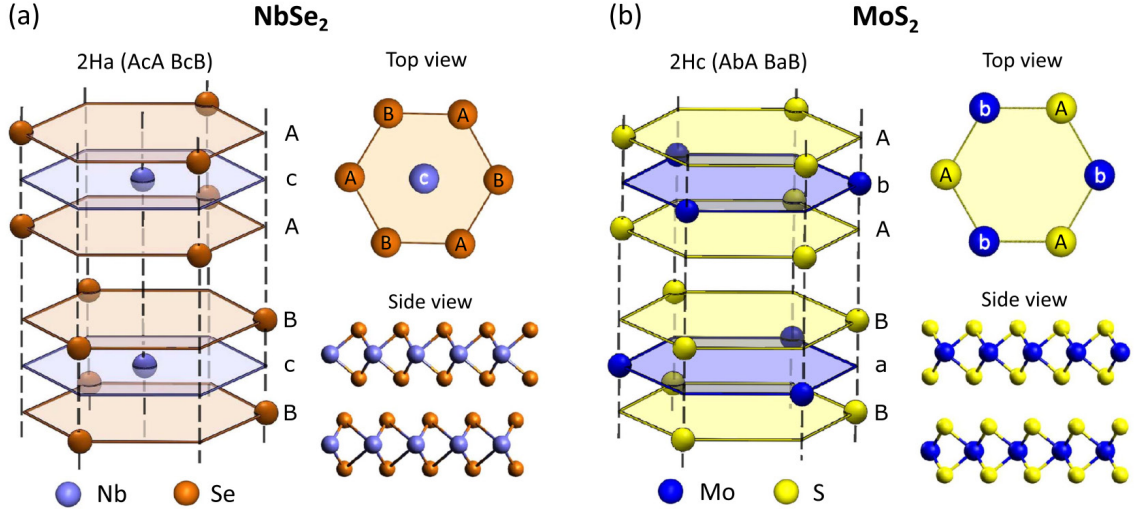


Figure 5.9: Comparison of the crystal structure of bilayer NbSe<sub>2</sub> and MoS<sub>2</sub>. (a) The schematic of 2Ha-NbSe<sub>2</sub>, with both top and side views. The atom location is specified by a, b, c (or A, B, C) points of a triangular lattice, as denoted in the top view. The 2Ha structure is thus (AcA BcB), where the upper and lower cases denote the chalcogen and transition metal atoms, respectively. (b) The schematic 2Hc structure of MoS<sub>2</sub>.

### Interlayer Phonons in NbSe<sub>2</sub>

Figure 5.10(b) shows representative Raman spectra of bilayer (2L) and monolayer (1L) NbSe<sub>2</sub> in the ultralow frequency range 10–50 cm<sup>-1</sup> (1–12 meV). Both spectra display a broad feature at the lowest energies which we attribute to Rayleigh scattering, but the bilayer exhibits two additional peak-like features. We identify these as the doubly degenerate interlayer shear mode (19.5 cm<sup>-1</sup>) and interlayer breathing mode (33 cm<sup>-1</sup>), labeled as S and B, respectively. The inset shows a schematic side-view of 2L NbSe<sub>2</sub> which illustrates the motion of the shear and breathing modes. To emphasize the interlayer phonon modes, we systematically subtract the broad background in each Raman spectrum as illustrated by the dashed line in Figure 5.10(b).

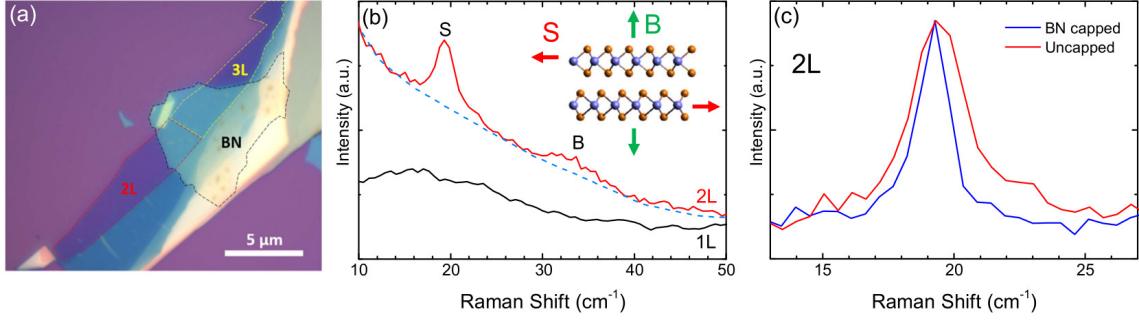


Figure 5.10: (a) Optical image of an exfoliated NbSe<sub>2</sub> flake on a SiO<sub>2</sub>/Si substrate. The sample is partially covered by a boron nitride (BN) flake. The 2L and 3L NbSe<sub>2</sub> regions and the BN-capped region are indicated by red, yellow, and black dashed lines, respectively. (b) Low-frequency Raman spectra of 1L and 2L uncapped NbSe<sub>2</sub>. The dashed baseline is subtracted from the 2L spectrum to highlight the weak breathing mode (B). The inset displays schematic interlayer shear (S) and breathing (B) modes. (d) Comparison of the shear mode of 2L NbSe<sub>2</sub> with and without BN-capping.

### 5.2.3 Broadening of Interlayer Phonon Raman from Sample Degradation

As mentioned in Section 5.2.1, NbSe<sub>2</sub> is susceptible to environmental degradation under ambient conditions. To examine the influence of atmosphere exposure to the interlayer coupling in NbSe<sub>2</sub>, we measure the shear mode in two bilayer NbSe<sub>2</sub> flakes, one of which is capped with a protective BN layer immediately after exfoliation. The shear mode Raman features from both flakes are shown in Figure 5.10(c). We fit both features with Lorentzian functions and find that, although the center frequencies are nearly identical, the shear mode of the exposed flake has a larger full width at half maximum (2.7 cm<sup>-1</sup>) as compared to the flake capped with BN (1.6 cm<sup>-1</sup>). We attribute this spectral broadening of the exposed flake to significant exposure-induced defect formation. While BN is helpful to maintain crystal quality and thus spectral resolution of the interlayer shear mode, we note that BN capping and encapsulation have been shown to suppress the breathing mode [106], likely due to damping effects. There is thus competition in experimental design between the desire

to preserve intrinsic properties via encapsulation and the need for strong breathing mode Raman features which are sufficiently observable given experimental considerations such as excitation intensity, detector efficiency, and noise. For this reason, we use both capped and bare NbSe<sub>2</sub> samples for this study. We note that the magnitude of this damping effect may be reduced through use of less massive capping material (e.g., thinner BN flakes), but further study is necessary.

### Layer-dependent Interlayer Raman Spectra

Figure 5.11(a) shows low frequency Raman spectra for uncapped NbSe<sub>2</sub> samples with thickness from  $2L - 15L$  and bulk, measured at room temperature. We use bare NbSe<sub>2</sub> flakes to avoid suppression of the breathing modes from BN capping. The broad background feature shown in Figure 5.10(b) is systematically subtracted from each spectrum to better highlight the shear and breathing modes. Immediately, we see contrasting energy shift of the observed breathing and shear modes with increasing layer number. The shear mode blueshifts and converges towards the bulk frequency at  $28 \text{ cm}^{-1}$  whereas the breathing mode dramatically red shifts with increasing layer number such that its central frequency falls below our minimum detection energy and is not observed in the bulk.

Our thickness-dependent data is well-described by a classical model of nearest-neighbor coupled oscillators – a so-called linear chain model. In such a model, a system of  $N$  layers hosts  $N - 1$  normal modes with frequencies:

$$\omega_N^{(n)} = \omega_0 \cos\left(\frac{n\pi}{2N}\right) \quad (5.15)$$

where  $n = 1, 2, \dots, N - 1$  is the normal mode index order from high to low frequency and

$\omega_0$  is the highest frequency ( $n = 1$ ) bulk mode at the Brillouin zone center ( $\Gamma$ -point). As noted above, we directly observe one shear mode in bulk NbSe<sub>2</sub> at  $\omega = 28 \text{ cm}^{-1}$ . We do not observe a breathing mode in bulk NbSe<sub>2</sub>. We note, however, that the shear mode observed in the bulk is not necessarily the bulk shear mode  $\omega_0$ . We resolve this issue by again examining the bilayer shear (breathing) features – the bilayer hosts only one vibrational branch and thus we can unambiguously identify the observed interlayer mode. From Equation 5.15 with  $N = 2$ , the bulk frequency  $\omega_0$  is related to the mode frequency:

$$\omega_2^{(1)} = \omega_0 \cos(\pi/4) \rightarrow \omega_0 = \sqrt{2}\omega_2^{(1)} \quad (5.16)$$

We thus estimate the  $n = 1$  bulk shear ( $\omega_{0,S}$ ) and breathing ( $\omega_{0,B}$ ) frequencies as  $27.6 \text{ cm}^{-1}$  and  $46.7 \text{ cm}^{-1}$ , respectively. The estimated frequency,  $\omega_{0,S}$ , is nearly identical to that of the observed bulk shear mode. This suggests that the observed bulk shear feature belongs to the  $n = 1$  branch and preliminarily confirms the above estimation of  $\omega_{0,S}$ . Using the the bulk phonon frequencies we calculate the NbSe<sub>2</sub> interlayer force constants. We estimate  $k_{xy} = 27 \cdot 10^{18} \text{ N-m}^{-3}$  and  $k_z = 78 \cdot 10^{18} \text{ N-m}^{-3}$  for in-plane and out-of-plane motion, respectively. Remarkably, our results for metallic NbSe<sub>2</sub> are similar to interlayer force constants previously reported in semiconducting 2H-MoS<sub>2</sub> ( $k_{xy} = 28 \cdot 10^{18} \text{ N-m}^{-3}$  and  $k_z = 87 \cdot 10^{18} \text{ N-m}^{-3}$  for in-plane and out-of-plane vibration, respectively).

We expand this analysis to include all measured sample thicknesses to more conclusively identify the branch(es) to which our observed interlayer phonons belong. The observed shear (breathing) features evolve smoothly with increasing thickness, which suggests that they belong to the same branch. To test this suspicion, we fit the thickness-dependent shear (breathing) frequency with Equation 5.15 using the integer branch index,  $n$ , as the

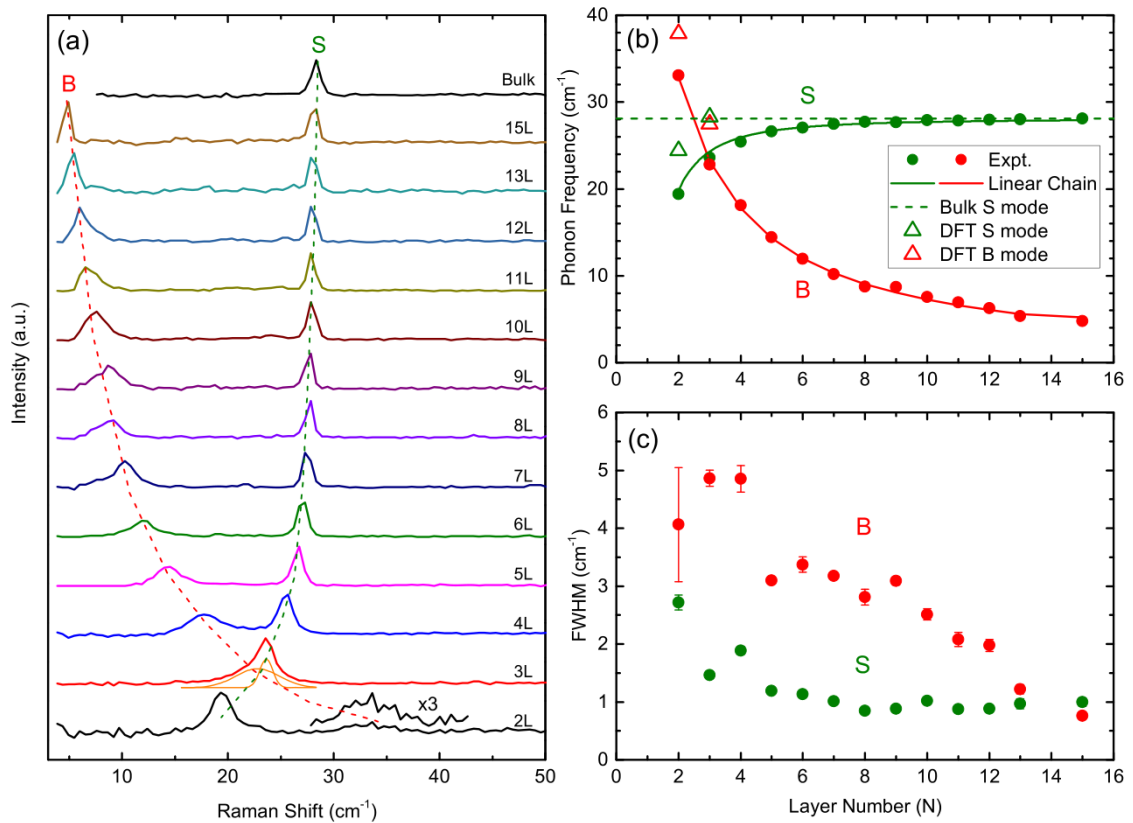


Figure 5.11: (a) Low-frequency Raman spectra of NbSe<sub>2</sub> with layer number  $N = 2 - 15$  and bulk NbSe<sub>2</sub>. For clarity, the spectra are vertically displaced with the broad background subtracted. The green and red dashed lines highlight the evolution of the shear (S) and breathing (B) modes, respectively. The 2L breathing mode is magnified by a factor of three. The orange curves in the 3L spectrum denote the fitted shear and breathing modes which overlap with each other. (b) Fitted frequency of the shear and breathing modes as a function of layer number. The solid lines are the predicted phonon frequencies from the linear chain model. The open triangles are the predicted phonon frequencies from DFT calculation. (c) The full-width at half-maximum (FWHM) of the shear and breathing modes as a function of layer number.

fitting parameter. We use the bulk frequencies  $\omega_0$  estimated above. The observed shear (breathing) mode frequencies and best fit lines are shown in Figure 5.11(b) in green (red). We find good agreement with the linear chain fitting where all observed shear features belong to the highest-frequency ( $n = 1$ ) branch and all observed breathing features belong to the lowest-frequency ( $n = N - 1$ ) branch.

### **Comparison with DFT-calculated Interlayer Phonon Frequencies**

To further confirm this assignment, we calculate the phonon frequencies for NbSe<sub>2</sub> crystals with thickness  $1L - 3L$  by density functional theory (DFT). The calculations were carried out using QuantumESPRESSO code with the Perdew-Wang local density approximation exchange-correlation function [123]. For details of this calculation, please see supporting material of the publication [124]. We plot the calculated interlayer shear and breathing frequencies in Figure 5.11(b) as open triangles. The calculated results exhibit similar layer dependence to the observed shear and breathing frequencies but appear at consistently higher frequency. Nonetheless, the calculations agree remarkably well (within  $4 \text{ cm}^{-1}$ ) with our experimental Raman data given the computational difficulties associated with metallic systems like NbSe<sub>2</sub>.

### **Symmetry Analysis of Raman Activity**

Previous Raman study of interlayer phonons in 2D materials shows the remarkable sensitivity of low-frequency Raman spectra to the layer-by-layer stacking configuration in otherwise chemically identical materials. The ABA and ABC polytypes of graphene, for example, share a nearly identical phonon spectrum at the Brillouin zone center but exhibit

distinct Raman spectra [105]. Although similar phonons are present in both crystals, the Raman scattering intensity, or Raman activity, of a particular phonon mode is intimately tied to the symmetries of both the vibration itself and that of its host crystal. [17]

In Section 5.2.2, we compared bilayer 2Ha-NbSe<sub>2</sub> and 2Hc-MoS<sub>2</sub> and found that their crystal structures differ somewhat, as indicated by the structural prefix. We would assume, then, that each crystal will exhibit distinct Raman activity of its interlayer phonons. However, our results are remarkably similar to previous low-frequency Raman study of MoS<sub>2</sub> and other group IV TMDs. [103, 104, 108, 109]. Despite the structural difference between 2Ha-NbSe<sub>2</sub> and 2Hc-MoS<sub>2</sub>, both crystals share the same symmetry group – inversion symmetric  $D_{3d}$  group for even layer numbers and  $D_{3h}$  group with out-of-plane mirror symmetry for odd layer numbers. Thus, the overall Raman activity of the interlayer phonon modes should be identical for both materials as reflected in our experiment. The group-theory-based analysis of Raman activity in the previous section can therefore be directly applied to NbSe<sub>2</sub> with the same results: we find that the shear modes with odd branch number ( $j = 1, 3, 5, \dots$  where  $j = 1$  is the highest frequency mode) are observable for all layer numbers and breathing modes with odd (even) branch number are observable for even (odd) layer numbers. We observe no more than one shear (breathing) mode feature per sample thickness and thus cannot directly verify this prediction. However, this analysis confirms that the highest-frequency ( $n = 1$ ) shear mode branch and lowest frequency breathing mode branch ( $n = N - 1$ ) are indeed observable in our experiment.

Such symmetry analysis can indicate if a particular phonon mode is Raman active, but provides no information about its scattering intensity relative to other Raman active phonons. Fundamentally, the Raman scattering intensity is proportional to the change in the relevant polarizability of the system during the course of the vibration period. We qualitatively examine the layer displacement patterns associated with each interlayer phonon mode and confirm that the highest-frequency shear mode and lowest-frequency breathing mode have the largest change in polarizability and thus highest Raman activity. A more detailed treatment of Raman intensity calculation is discussed in the previous section.

#### 5.2.4 Layer-dependent Interlayer Raman Peak Broadening

In addition to the central frequency of each Raman feature, we also extract a full width at half maximum (FWHM) as defined by a best fit Lorentzian function. FWHM of the shear and breathing modes are plotted in Figure 5.11(c). For samples of  $5L$ – $15L$  the breathing mode exhibits progressive broadening with decreasing layer number, whereas the FWHM of the shear mode is relatively constant. In the few-layer limit, both shear and breathing features are noticeably broadened. We attribute the thickness-dependent FWHM to two mechanisms.

Previous studies have shown that the anharmonic decay rate of optical phonons to lower energy acoustic phonons is positively related to the optical phonon energy and, further, that phonon lifetime enhancement results in sharper Raman features. Thus, the significant redshift of the breathing mode with increasing thickness should suppress anharmonic decay and ultimately result in a reduction of FWHM at higher layer number. We expect modest broadening of the shear mode with increasing layer number due to the observed blue shift,

for the same reason. Contrary to this assumption, the shear mode has relatively constant FWHM for  $N \geq 5L$  but increases significantly for thinner samples. We attribute the significant broadening of both shear and breathing mode features in the few-layer limit to exposure-induced defect formation.

As discussed in the bilayer, the shear mode of bare NbSe<sub>2</sub> exhibits noticeable broadening as compared to BN capped samples, which we attribute to ambient-exposure-induced defect formation. We further assume that some component of this defect-producing reaction (e.g., oxygen, water vapor) is unable to efficiently penetrate into the bulk crystal. Under these assumptions we expect the formation of a defect-density gradient near the crystal surface upon exposure, where the top-most surface layer is most affected. Interior layers are increasingly shielded from defect formation with further separation from the surface. Thus, both layers of a 2L sample may be similarly defected whereas the interior layers of a thicker crystal (e.g.,  $N = 10L$ ) may be near-intrinsic. The total Raman spectrum collected from a multilayer sample includes diminishing contributions from interior layers up to roughly the penetration depth of the excitation wavelength. If the penetration depth of the Raman probe is much greater than that of the defect formation process, we would expect significant exposure-induced broadening in the thinnest samples which diminishes with increasing thickness. We note that this is one possible explanation for the observed trend and further study is necessary.

### 5.2.5 Conclusion

In summary, we measured the interlayer phonon spectra of 2H-NbSe<sub>2</sub> for layer numbers  $1L - 15L$  and bilayer samples with and without hexagonal boron nitride (BN) capping. From the layer dependence, we used the linear chain model to estimate the interlayer force constant for shear and out-of-plane layer displacement. We found signatures of environmental degradation of the NbSe<sub>2</sub> layers due to ambient exposure in the interlayer phonon Raman spectra. In the bilayer, the full width at half maximum (FWHM) of the interlayer shear mode Raman peak was noticeably broadened in as-exfoliated samples as compared to those with BN capping. We further measured the shear mode FWHM for uncapped NbSe<sub>2</sub> with layer number  $N = 2L$  to  $15L$  and observed notable broadening of the shear mode Raman for  $N \leq 4L$ . We attribute this to increased contribution of the degraded surface layer(s) to the total Raman intensity in thin samples as compared to thicker samples.

## Chapter 6

# Conclusion

Throughout this work we presented our results in three major chapters, the results of which we summarize here.

First, we used high-quality monolayer WSe<sub>2</sub> gating devices under quantizing out-of-plane magnetic field ( $B \leq 31$  T) to study the internal energy levels of the bright  $A^0$  exciton and the Landau-quantization-related oscillatory behavior of the bright  $A^0$  exciton and bright trions ( $A^+$ ,  $A^-$ ). In the former, we measured the exciton Rydberg series PL from which we determined the exciton (and excited state)  $g$ -factors, binding energies, and r.m.s. radii. In the latter, we observed step-like gate-dependent shift of the  $A^0$  absorption energy under high magnetic field where we identified the transition region between plateaus as the Landau level half-filling voltage. This was supported by the simultaneous observation of local maxima in the oscillatory  $A^0$  absorption full-width at half-maximum (FWHM). We thus unambiguously identified the Landau level filling factors *via* optical reflectance. We also observed Landau-level-associated intensity oscillations in the trion,  $A^+$ , PL intensity where

the local intensity maxima correspond to the Landau level half-filling. Together, these results gave us insight into the charge-density-dependent excitonic behavior by condensing it into the quantized density of states and further illustrated a significant enhancement of the valence band  $g$ -factor compared to the single-particle model prediction. This divergence implies the influence of many-body interactions on the magnetic-field-induced energy shift of the electronic bands in monolayer WSe<sub>2</sub> with finite charge density. We suggest that this enhancement may be related to an interaction-induced renormalization of the carrier effective mass but this requires further research.

Second, we conducted a detailed study in three parts of the complex collection of dark exciton species in monolayer WSe<sub>2</sub> and the associated radiative relaxation pathways. We identified the gate-tunable dark trion which we observed to have exceptionally long radiative lifetime, approximately 100x that of the bright trion. The dark trion lifetime was also shown to be tunable with gate voltage. Although available elsewhere, we also derived the optical selection rules for the dark exciton (trion) which illustrate its out-of-plane dipole and resultant in-plane, linearly polarized light coupling without valley optical selection. As a partial remedy to the lack of valley access in the dark trion, we identified radiative relaxation pathway for the dark exciton and trion mediated by a chiral phonon with non-zero angular momentum - the dark exciton (trion) chiral phonon replica. This replica luminescence exhibits valley selectivity in both the phonon and photon emission process; thus, the dark trion valley index can be detected by this pathway. Finally, we identified the momentum-indirect intervalley exciton in this system which cannot luminescence without a mediating interaction. We identify two such processes; the defect-mediated relaxation and

the intervalley chiral phonon replica process.

Finally, we used ultralow-frequency Raman spectroscopy to study the influence of layer-by-layer stacking on the interlayer phonon spectra in 3R- and 2H-MoS<sub>2</sub> and NbSe<sub>2</sub>. In the former, we conducted comprehensive layer-dependent Raman measurement and observed up to five shear (breathing) mode Raman features in one layer. This allowed us to conduct detailed frequency analysis, extract the elastic moduli of both stacking configurations, and implement an analytic model based on bond polarizability to calculate the Raman tensor elements. We found that the 2H stacking order is slightly stiffer to out-of-plane compression than the 3R configuration but that they share a similar shear force constant. Together with the analytical model, our experimental results demonstrate a method for simultaneous, non-destructive identification of layer number and stacking configuration for 2D materials.

# Bibliography

- [1] A. C. Neto, F. Guinea, N. M. Peres, K. S. Novoselov, and A. K. Geim. The electronic properties of graphene. *Reviews of Modern Physics*, 81(1):109, 2009.
- [2] K. S. Novoselov, A. Mishchenko, A. Carvalho, and A. C. Neto. 2D materials and van der Waals heterostructures. *Science*, 353(6298), 2016.
- [3] A. K. Geim and I. V. Grigorieva. van der Waals heterostructures. *Nature*, 499(7459):419–425, 2013.
- [4] Y. Cao, V. Fatemi, S. Fang, K. Watanabe, T. Taniguchi, E. Kaxiras, and P. Jarillo-Herrero. Unconventional superconductivity in magic-angle graphene superlattices. *Nature*, 556(7699):43–50, 2018.
- [5] P. Rivera, H. Yu, K. L. Seyler, N. P. Wilson, W. Yao, and X. Xu. Interlayer valley excitons in heterobilayers of transition metal dichalcogenides. *Nature Nanotechnology*, 13(11):1004–1015, 2018.
- [6] G.-B. Liu, D. Xiao, Y. Yao, X. Xu, and W. Yao. Electronic structures and theoretical modelling of two-dimensional group-vib transition metal dichalcogenides. *Chemical Society Reviews*, 44(9):2643–2663, 2015.
- [7] G. Wang, A. Chernikov, M. M. Glazov, T. F. Heinz, X. Marie, T. Amand, and B. Urbaszek. Colloquium: Excitons in atomically thin transition metal dichalcogenides. *Reviews of Modern Physics*, 90(2):021001, 2018.
- [8] K. F. Mak and J. Shan. Photonics and optoelectronics of 2D semiconductor transition metal dichalcogenides. *Nature Photonics*, 10(4):216–226, 2016.
- [9] K. F. Mak, C. Lee, J. Hone, J. Shan, and T. F. Heinz. Atomically thin MoS<sub>2</sub>: a new direct-gap semiconductor. *Physical Review Letters*, 105(13):136805, 2010.
- [10] A. Splendiani, L. Sun, Y. Zhang, T. Li, J. Kim, C.-Y. Chim, G. Galli, and F. Wang. Emerging photoluminescence in monolayer MoS<sub>2</sub>. *Nano Letters*, 10(4):1271–1275, 2010.

- [11] T. Cao, G. Wang, W. Han, H. Ye, C. Zhu, J. Shi, Q. Niu, P. Tan, E. Wang, B. Liu, et al. Valley-selective circular dichroism of monolayer molybdenum disulphide. *Nature Communications*, 3(1):1–5, 2012.
- [12] D. Xiao, G.-B. Liu, W. Feng, X. Xu, and W. Yao. Coupled spin and valley physics in monolayers of MoS<sub>2</sub> and other group-vi dichalcogenides. *Physical Review Letters*, 108(19):196802, 2012.
- [13] E. J. Sie. *Coherent light-matter interactions in monolayer transition-metal dichalcogenides*. PhD thesis, Massachusetts Institute of Technology, 2017.
- [14] K. He, N. Kumar, L. Zhao, Z. Wang, K. F. Mak, H. Zhao, and J. Shan. Tightly bound excitons in monolayer WSe<sub>2</sub>. *Physical Review Letters*, 113(2):026803, 2014.
- [15] A. V. Stier, N. P. Wilson, K. A. Velizhanin, J. Kono, X. Xu, and S. A. Crooker. Magneto-optics of exciton Rydberg states in a monolayer semiconductor. *Physical Review Letters*, 120(5):057405, 2018.
- [16] E. Liu, J. van Baren, T. Taniguchi, K. Watanabe, Y.-C. Chang, and C. H. Lui. Magnetophotoluminescence of exciton Rydberg states in monolayer WSe<sub>2</sub>. *Physical Review B*, 99(20):205420, 2019.
- [17] M. S. Dresselhaus, G. Dresselhaus, and A. Jorio. *Group theory: Application to the Physics of Condensed Matter*. Springer, New York, 2008.
- [18] G.-H. Jung, S. Yoo, and Q.-H. Park. Measuring the optical permittivity of two-dimensional materials without a priori knowledge of electronic transitions. *Nanophotonics*, 8(2):263–270, 2018.
- [19] A. Chernikov, T. C. Berkelbach, H. M. Hill, A. Rigosi, Y. Li, O. B. Aslan, D. R. Reichman, M. S. Hybertsen, and T. F. Heinz. Exciton binding energy and nonhydrogenic Rydberg series in monolayer WS<sub>2</sub>. *Physical Review Letters*, 113(7):076802, 2014.
- [20] D. K. Efimkin and A. H. MacDonald. Many-body theory of trion absorption features in two-dimensional semiconductors. *Physical Review B*, 95(3):035417, 2017.
- [21] M. Sidler, P. Back, O. Cotlet, A. Srivastava, T. Fink, M. Kroner, E. Demler, and A. Imamoglu. Fermi polaron-polaritons in charge-tunable atomically thin semiconductors. *Nature Physics*, 13(3):255–261, 2017.
- [22] Y.-C. Chang, S.-Y. Shiau, and M. Combescot. Crossover from trion-hole complex to exciton-polaron in n-doped two-dimensional semiconductor quantum wells. *Physical Review B*, 98(23):235203, 2018.
- [23] D. K. Efimkin and A. H. MacDonald. Exciton-polarons in doped semiconductors in a strong magnetic field. *Physical Review B*, 97(23):235432, 2018.

- [24] C. Fey, P. Schmelcher, A. Imamoglu, and R. Schmidt. Theory of exciton-electron scattering in atomically thin semiconductors. *Physical Review B*, 101(19):195417, 2020.
- [25] P. V. Nguyen, N. C. Teutsch, N. P. Wilson, J. Kahn, X. Xia, A. J. Graham, V. Kandyba, A. Giampietri, A. Barinov, G. C. Constantinescu, et al. Visualizing electrostatic gating effects in two-dimensional heterostructures. *Nature*, 572(7768):220–223, 2019.
- [26] A. Kormányos, G. Burkard, M. Gmitra, J. Fabian, V. Zólyomi, N. D. Drummond, and V. Fal’ko.  $k \cdot p$  theory for two-dimensional transition metal dichalcogenide semiconductors. *2D Materials*, 2(2):022001, 2015.
- [27] X.-X. Zhang, T. Cao, Z. Lu, Y.-C. Lin, F. Zhang, Y. Wang, Z. Li, J. C. Hone, J. A. Robinson, D. Smirnov, et al. Magnetic brightening and control of dark excitons in monolayer WSe<sub>2</sub>. *Nature Nanotechnology*, 12(9):883–888, 2017.
- [28] E. Liu, J. van Baren, C.-T. Liang, T. Taniguchi, K. Watanabe, N. M. Gabor, Y.-C. Chang, and C. H. Lui. Multipath optical recombination of intervalley dark excitons and trions in monolayer WSe<sub>2</sub>. *Physical Review Letters*, 124(19):196802, 2020.
- [29] C. R. Dean, A. F. Young, I. Meric, C. Lee, L. Wang, S. Sorgenfrei, K. Watanabe, T. Taniguchi, P. Kim, K. L. Shepard, et al. Boron nitride substrates for high-quality graphene electronics. *Nature Nanotechnology*, 5(10):722–726, 2010.
- [30] L. Wang, E.-M. Shih, A. Ghiotto, L. Xian, D. A. Rhodes, C. Tan, M. Claassen, D. M. Kennes, Y. Bai, B. Kim, et al. Correlated electronic phases in twisted bilayer transition metal dichalcogenides. *Nature Materials*, pages 1–6, 2020.
- [31] L. Wang, I. Meric, P. Huang, Q. Gao, Y. Gao, H. Tran, T. Taniguchi, K. Watanabe, L. Campos, D. Muller, et al. One-dimensional electrical contact to a two-dimensional material. *Science*, 342(6158):614–617, 2013.
- [32] A. Castellanos-Gomez, M. Buscema, R. Molenaar, V. Singh, L. Janssen, H. S. Van Der Zant, and G. A. Steele. Deterministic transfer of two-dimensional materials by all-dry viscoelastic stamping. *2D Materials*, 1(1):011002, 2014.
- [33] Y. Cao. Electronic transport in low-angle twisted bilayer graphene. Master’s thesis, Massachusetts Institute of Technology, 2016.
- [34] P. Yeh. *Optical Waves in Layered Media*. Wiley, Hoboken, 2005.
- [35] A. Kuzmenko. Kramers–kronig constrained variational analysis of optical spectra. *Review of Scientific Instruments*, 76(8):083108, 2005.
- [36] Z. Li, T. Wang, Z. Lu, C. Jin, Y. Chen, Y. Meng, Z. Lian, T. Taniguchi, K. Watanabe, S. Zhang, et al. Revealing the biexciton and trion-exciton complexes in BN encapsulated WSe<sub>2</sub>. *Nature Communications*, 9(1):1–7, 2018.

- [37] S.-Y. Chen, T. Goldstein, T. Taniguchi, K. Watanabe, and J. Yan. Coulomb-bound four-and five-particle intervalley states in an atomically-thin semiconductor. *Nature Communications*, 9(1):1–8, 2018.
- [38] Z. Ye, L. Waldecker, E. Y. Ma, D. Rhodes, A. Antony, B. Kim, X.-X. Zhang, M. Deng, Y. Jiang, Z. Lu, et al. Efficient generation of neutral and charged biexcitons in encapsulated WSe<sub>2</sub> monolayers. *Nature Communications*, 9(1):1–6, 2018.
- [39] M. Barbone, A. R.-P. Montblanch, D. M. Kara, C. Palacios-Berraquero, A. R. Cadore, D. De Fazio, B. Pingault, E. Mostaani, H. Li, B. Chen, et al. Charge-tuneable biexciton complexes in monolayer WSe<sub>2</sub>. *Nature Communications*, 9(1):1–6, 2018.
- [40] S. Ulstrup, A. G. Cabo, J. A. Miwa, J. M. Riley, S. S. Grønberg, J. C. Johanssen, C. Cacho, O. Alexander, R. T. Chapman, E. Springate, et al. Ultrafast band structure control of a two-dimensional heterostructure. *ACS Nano*, 10(6):6315–6322, 2016.
- [41] E. A. Pogna, M. Marsili, D. De Fazio, S. Dal Conte, C. Manzoni, D. Sangalli, D. Yoon, A. Lombardo, A. C. Ferrari, A. Marini, et al. Photo-induced bandgap renormalization governs the ultrafast response of single-layer MoS<sub>2</sub>. *ACS Nano*, 10(1):1182–1188, 2016.
- [42] P. D. Cunningham, A. T. Hanbicki, K. M. McCreary, and B. T. Jonker. Photoinduced bandgap renormalization and exciton binding energy reduction in WS<sub>2</sub>. *ACS Nano*, 11(12):12601–12608, 2017.
- [43] H. M. Hill, A. F. Rigosi, C. Roquelet, A. Chernikov, T. C. Berkelbach, D. R. Reichman, M. S. Hybertsen, L. E. Brus, and T. F. Heinz. Observation of excitonic Rydberg states in monolayer MoS<sub>2</sub> and WS<sub>2</sub> by photoluminescence excitation spectroscopy. *Nano Letters*, 15(5):2992–2997, 2015.
- [44] M. Goryca, J. Li, A. V. Stier, T. Taniguchi, K. Watanabe, E. Courtade, S. Shree, C. Robert, B. Urbaszek, X. Marie, et al. Revealing exciton masses and dielectric properties of monolayer semiconductors with high magnetic fields. *Nature Communications*, 10(1):1–12, 2019.
- [45] A. Chernikov, A. M. Van Der Zande, H. M. Hill, A. F. Rigosi, A. Velauthapillai, J. Hone, and T. F. Heinz. Electrical tuning of exciton binding energies in monolayer WS<sub>2</sub>. *Physical Review Letters*, 115(12):126802, 2015.
- [46] A. V. Stier, K. M. McCreary, B. T. Jonker, J. Kono, and S. A. Crooker. Exciton diamagnetic shifts and valley Zeeman effects in monolayer WS<sub>2</sub> and MoS<sub>2</sub> to 65 Tesla. *Nature Communications*, 7(1):1–8, 2016.
- [47] G. Wang, L. Bouet, M. Glazov, T. Amand, E. Ivchenko, E. Palleau, X. Marie, and B. Urbaszek. Magneto-optics in transition metal diselenide monolayers. *2D Materials*, 2(3):034002, 2015.
- [48] G. Aivazian, Z. Gong, A. M. Jones, R.-L. Chu, J. Yan, D. G. Mandrus, C. Zhang, D. Cobden, W. Yao, and X. Xu. Magnetic control of valley pseudospin in monolayer WSe<sub>2</sub>. *Nature Physics*, 11(2):148–152, 2015.

- [49] A. Srivastava, M. Sidler, A. V. Allain, D. S. Lembke, A. Kis, and A. Imamoglu. Valley Zeeman effect in elementary optical excitations of monolayer WSe<sub>2</sub>. *Nature Physics*, 11(2):141–147, 2015.
- [50] S.-Y. Chen, Z. Lu, T. Goldstein, J. Tong, A. Chaves, J. Kunstmann, L. Cavalcante, T. Wozniak, G. Seifert, D. Reichman, et al. Luminescent emission of excited Rydberg excitons from monolayer WSe<sub>2</sub>. *Nano Letters*, 19(4):2464–2471, 2019.
- [51] S. Walck and T. Reinecke. Exciton diamagnetic shift in semiconductor nanostructures. *Physical Review B*, 57(15):9088, 1998.
- [52] A. Laturia, M. L. Van de Put, and W. G. Vandenberghe. Dielectric properties of hexagonal boron nitride and transition metal dichalcogenides: from monolayer to bulk. *npj 2D Materials and Applications*, 2(1):1–7, 2018.
- [53] N. S. Rytova. Screened potential of a point charge in a thin film. *Moscow University Physics Bulletin*, 1967.
- [54] L. V. Keldysh. Coulomb interaction in thin semiconductor and semimetal films. *JETP Letters*, 1979.
- [55] B. Fallahazad, H. C. Movva, K. Kim, S. Larentis, T. Taniguchi, K. Watanabe, S. K. Banerjee, and E. Tutuc. Shubnikov–de Haas oscillations of high-mobility holes in monolayer and bilayer WSe<sub>2</sub>: Landau level degeneracy, effective mass, and negative compressibility. *Physical Review Letters*, 116(8):086601, 2016.
- [56] S. Xu, Z. Wu, H. Lu, Y. Han, G. Long, X. Chen, T. Han, W. Ye, Y. Wu, J. Lin, et al. Universal low-temperature ohmic contacts for quantum transport in transition metal dichalcogenides. *2D Materials*, 3(2):021007, 2016.
- [57] H. C. Movva, T. Lovorn, B. Fallahazad, S. Larentis, K. Kim, T. Taniguchi, K. Watanabe, S. K. Banerjee, A. H. MacDonald, and E. Tutuc. Tunable  $\gamma$ -K valley populations in hole-doped trilayer WSe<sub>2</sub>. *Physical Review Letters*, 120(10):107703, 2018.
- [58] A. Kormányos, P. Rakyta, and G. Burkard. Landau levels and Shubnikov–de Haas oscillations in monolayer transition metal dichalcogenide semiconductors. *New Journal of Physics*, 17(10):103006, 2015.
- [59] T. Cai, S. A. Yang, X. Li, F. Zhang, J. Shi, W. Yao, and Q. Niu. Magnetic control of the valley degree of freedom of massive Dirac fermions with application to transition metal dichalcogenides. *Physical Review B*, 88(11):115140, 2013.
- [60] F. Rose, M. Goerbig, and F. Piéchon. Spin-and valley-dependent magneto-optical properties of MoS<sub>2</sub>. *Physical Review B*, 88(12):125438, 2013.
- [61] Z. Wang, J. Shan, and K. F. Mak. Valley-and spin-polarized Landau levels in monolayer WSe<sub>2</sub>. *Nature Nanotechnology*, 12(2):144, 2017.

- [62] J. Have, G. Catarina, T. G. Pedersen, and N. Peres. Monolayer transition metal dichalcogenides in strong magnetic fields: Validating the Wannier model using a microscopic calculation. *Physical Review B*, 99(3):035416, 2019.
- [63] M. V. Gustafsson, M. Yankowitz, C. Forsythe, D. Rhodes, K. Watanabe, T. Taniguchi, J. Hone, X. Zhu, and C. R. Dean. Ambipolar Landau levels and strong band-selective carrier interactions in monolayer WSe<sub>2</sub>. *Nature Materials*, 17(5):411–415, 2018.
- [64] T. Smoleński, O. Cotlet, A. Popert, P. Back, Y. Shimazaki, P. Knüppel, N. Dietler, T. Taniguchi, K. Watanabe, M. Kroner, et al. Interaction-induced Shubnikov–de Haas oscillations in optical conductivity of monolayer MoSe<sub>2</sub>. *Physical Review Letters*, 123(9):097403, 2019.
- [65] E. Liu, J. van Baren, T. Taniguchi, K. Watanabe, Y.-C. Chang, and C. H. Lui. Landau-quantized excitonic absorption and luminescence in a monolayer valley semiconductor. *Physical Review Letters*, 124(9):097401, 2020.
- [66] M. Yankowitz, J. Jung, E. Laksono, N. Leconte, B. L. Chittari, K. Watanabe, T. Taniguchi, S. Adam, D. Graf, and C. R. Dean. Dynamic band-structure tuning of graphene moiré superlattices with pressure. *Nature*, 557(7705):404–408, 2018.
- [67] M. R. Molas, C. Faugeras, A. Slobodeniuk, K. Nogajewski, M. Bartos, D. Basko, and M. Potemski. Brightening of dark excitons in monolayers of semiconducting transition metal dichalcogenides. *2D Materials*, 4(2):021003, 2017.
- [68] C. Robert, T. Amand, F. Cadiz, D. Lagarde, E. Courtade, M. Manca, T. Taniguchi, K. Watanabe, B. Urbaszek, and X. Marie. Fine structure and lifetime of dark excitons in transition metal dichalcogenide monolayers. *Physical Review B*, 96(15):155423, 2017.
- [69] J. Echeverry, B. Urbaszek, T. Amand, X. Marie, and I. Gerber. Splitting between bright and dark excitons in transition metal dichalcogenide monolayers. *Physical Review B*, 93(12):121107, 2016.
- [70] Y. Zhou, G. Scuri, D. S. Wild, A. A. High, A. Dibos, L. A. Jauregui, C. Shu, K. De Greve, K. Pistunova, A. Y. Joe, et al. Probing dark excitons in atomically thin semiconductors via near-field coupling to surface plasmon polaritons. *Nature Nanotechnology*, 12(9):856, 2017.
- [71] Y. Tang, K. F. Mak, and J. Shan. Long valley lifetime of dark excitons in single-layer WSe<sub>2</sub>. *Nature Communications*, 10, 2019.
- [72] K.-D. Park, T. Jiang, G. Clark, X. Xu, and M. B. Raschke. Radiative control of dark excitons at room temperature by nano-optical antenna-tip purcell effect. *Nature Nanotechnology*, 13(1):59–64, 2018.
- [73] G. Wang, C. Robert, M. Glazov, F. Cadiz, E. Courtade, T. Amand, D. Lagarde, T. Taniguchi, K. Watanabe, B. Urbaszek, et al. In-plane propagation of light in

- transition metal dichalcogenide monolayers: optical selection rules. *Physical Review Letters*, 119(4):047401, 2017.
- [74] C. Robert, D. Lagarde, F. Cadiz, G. Wang, B. Lassagne, T. Amand, A. Balocchi, P. Renucci, S. Tongay, B. Urbaszek, et al. Exciton radiative lifetime in transition metal dichalcogenide monolayers. *Physical Review B*, 93(20):205423, 2016.
- [75] T. Deilmann and K. S. Thygesen. Dark excitations in monolayer transition metal dichalcogenides. *Physical Review B*, 96(20):201113, 2017.
- [76] X.-X. Zhang, Y. You, S. Y. F. Zhao, and T. F. Heinz. Experimental evidence for dark excitons in monolayer WSe<sub>2</sub>. *Physical Review Letters*, 115(25):257403, 2015.
- [77] Z. Li, T. Wang, C. Jin, Z. Lu, Z. Lian, Y. Meng, M. Blei, S. Gao, T. Taniguchi, K. Watanabe, et al. Emerging photoluminescence from the dark-exciton phonon replica in monolayer WSe<sub>2</sub>. *Nature Communications*, 10(1):1–7, 2019.
- [78] H. Zhu, J. Yi, M.-Y. Li, J. Xiao, L. Zhang, C.-W. Yang, R. A. Kaindl, L.-J. Li, Y. Wang, and X. Zhang. Observation of chiral phonons. *Science*, 359(6375):579–582, 2018.
- [79] X. Chen, X. Lu, S. Dubey, Q. Yao, S. Liu, X. Wang, Q. Xiong, L. Zhang, and A. Srivastava. Entanglement of single-photons and chiral phonons in atomically thin WSe<sub>2</sub>. *Nature Physics*, 15(3):221–227, 2019.
- [80] L. Zhang and Q. Niu. Chiral phonons at high-symmetry points in monolayer hexagonal lattices. *Physical Review Letters*, 115(11):115502, 2015.
- [81] X. Luo, Y. Zhao, J. Zhang, M. Toh, C. Kloc, Q. Xiong, and S. Y. Quek. Effects of lower symmetry and dimensionality on Raman spectra in two-dimensional WSe<sub>2</sub>. *Physical Review B*, 88(19):195313, 2013.
- [82] S. Kim, K. Kim, J.-U. Lee, and H. Cheong. Excitonic resonance effects and Davydov splitting in circularly polarized Raman spectra of few-layer WSe<sub>2</sub>. *2D Materials*, 4(4):045002, 2017.
- [83] Y. Song and H. Dery. Transport theory of monolayer transition-metal dichalcogenides through symmetry. *Physical Review Letters*, 111(2):026601, 2013.
- [84] H. Dery and Y. Song. Polarization analysis of excitons in monolayer and bilayer transition-metal dichalcogenides. *Physical Review B*, 92(12):125431, 2015.
- [85] A. M. Konzelmann, S. O. Krüger, and H. Giessen. Interaction of orbital angular momentum light with Rydberg excitons: Modifying dipole selection rules. *Physical Review B*, 100(11):115308, 2019.
- [86] E. Malic, M. Selig, M. Feierabend, S. Brem, D. Christiansen, F. Wendler, A. Knorr, and G. Berghäuser. Dark excitons in transition metal dichalcogenides. *Physical Review Materials*, 2(1):014002, 2018.

- [87] J. Lindlau, M. Selig, A. Neumann, L. Colombier, J. Förste, V. Funk, M. Förg, J. Kim, G. Berghäuser, T. Taniguchi, et al. The role of momentum-dark excitons in the elementary optical response of bilayer WSe<sub>2</sub>. *Nature communications*, 9(1):1–7, 2018.
- [88] G.-H. Peng, P.-Y. Lo, W.-H. Li, Y.-C. Huang, Y.-H. Chen, C.-H. Lee, C.-K. Yang, and S.-J. Cheng. Distinctive signatures of the spin-and momentum-forbidden dark exciton states in the photoluminescence of strained WSe<sub>2</sub> monolayers under thermalization. *Nano Letters*, 19(4):2299–2312, 2019.
- [89] M. Selig, F. Katsch, R. Schmidt, S. M. de Vasconcellos, R. Bratschitsch, E. Malic, and A. Knorr. Ultrafast dynamics in monolayer transition metal dichalcogenides: Interplay of dark excitons, phonons, and intervalley exchange. *Physical Review Research*, 1(2):022007, 2019.
- [90] D. Van Tuan, A. M. Jones, M. Yang, X. Xu, and H. Dery. Virtual trions in the photoluminescence of monolayer transition-metal dichalcogenides. *Physical Review Letters*, 122(21):217401, 2019.
- [91] D. Van Tuan and H. Dery. Localization-induced optical properties of monolayer transition-metal dichalcogenides. *arXiv:1904.04959*, 2019.
- [92] K. F. Mak, C. Lee, J. Hone, J. Shan, and T. F. Heinz. Atomically thin MoS<sub>2</sub>: a new direct-gap semiconductor. *Physical Review Letters*, 105(13):136805, 2010.
- [93] A. Splendiani, L. Sun, Y. Zhang, T. Li, J. Kim, C.-Y. Chim, G. Galli, and F. Wang. Emerging photoluminescence in monolayer MoS<sub>2</sub>. *Nano Letters*, 10(4):1271–1275, 2010.
- [94] X. Xu, W. Yao, D. Xiao, and T. F. Heinz. Spin and pseudospins in layered transition metal dichalcogenides. *Nature Physics*, 10(5):343–350, 2014.
- [95] Y. Li, Y. Rao, K. F. Mak, Y. You, S. Wang, C. R. Dean, and T. F. Heinz. Probing symmetry properties of few-layer MoS<sub>2</sub> and h-BN by optical second-harmonic generation. *Nano Letters*, 13(7):3329–3333, 2013.
- [96] L. M. Malard, T. V. Alencar, A. P. M. Barboza, K. F. Mak, and A. M. De Paula. Observation of intense second harmonic generation from MoS<sub>2</sub> atomic crystals. *Physical Review B*, 87(20):201401, 2013.
- [97] E. Mishina, N. Sherstyuk, S. Lavrov, A. Sigov, A. Mitioglu, S. Anghel, and L. Kulyuk. Observation of two polytypes of MoS<sub>2</sub> ultrathin layers studied by second harmonic generation microscopy and photoluminescence. *Applied Physics Letters*, 106(13):131901, 2015.
- [98] R. Suzuki, M. Sakano, Y. Zhang, R. Akashi, D. Morikawa, A. Harasawa, K. Yaji, K. Kuroda, K. Miyamoto, T. Okuda, et al. Valley-dependent spin polarization in bulk MoS<sub>2</sub> with broken inversion symmetry. *Nature Nanotechnology*, 9(8):611, 2014.

- [99] J. Shi, P. Yu, F. Liu, P. He, R. Wang, L. Qin, J. Zhou, X. Li, J. Zhou, X. Sui, et al. 3R MoS<sub>2</sub> with broken inversion symmetry: a promising ultrathin nonlinear optical device. *Advanced Materials*, 29(30):1701486, 2017.
- [100] M. Zhao, Z. Ye, R. Suzuki, Y. Ye, H. Zhu, J. Xiao, Y. Wang, Y. Iwasa, and X. Zhang. Atomically phase-matched second-harmonic generation in a 2D crystal. *Light: Science & Applications*, 5(8):e16131–e16131, 2016.
- [101] X. Zhang, W.-Y. Shan, and D. Xiao. Optical selection rule of excitons in gapped chiral fermion systems. *Physical Review Letters*, 120(7):077401, 2018.
- [102] P. Tan, W. Han, W. Zhao, Z. Wu, K. Chang, H. Wang, Y. Wang, N. Bonini, N. Marzari, N. Pugno, et al. The shear mode of multilayer graphene. *Nature Materials*, 11(4):294–300, 2012.
- [103] Y. Zhao, X. Luo, H. Li, J. Zhang, P. T. Araujo, C. K. Gan, J. Wu, H. Zhang, S. Y. Quek, M. S. Dresselhaus, et al. Interlayer breathing and shear modes in few-trilayer MoS<sub>2</sub> and WSe<sub>2</sub>. *Nano Letters*, 13(3):1007–1015, 2013.
- [104] X. Zhang, W. Han, J. Wu, S. Milana, Y. Lu, Q. Li, A. Ferrari, and P. Tan. Raman spectroscopy of shear and layer breathing modes in multilayer MoS<sub>2</sub>. *Physical Review B*, 87(11):115413, 2013.
- [105] C. H. Lui, Z. Ye, C. Keiser, E. B. Barros, and R. He. Stacking-dependent shear modes in trilayer graphene. *Applied Physics Letters*, 106(4):041904, 2015.
- [106] C. H. Lui, Z. Ye, C. Keiser, X. Xiao, and R. He. Temperature-activated layer-breathing vibrations in few-layer graphene. *Nano Letters*, 14(8):4615–4621, 2014.
- [107] A. C. Ferrari and D. M. Basko. Raman spectroscopy as a versatile tool for studying the properties of graphene. *Nature Nanotechnology*, 8(4):235–246, 2013.
- [108] G. Plechinger, S. Heydrich, J. Eroms, D. Weiss, C. Schüller, and T. Korn. Raman spectroscopy of the interlayer shear mode in few-layer MoS<sub>2</sub> flakes. *Applied Physics Letters*, 101(10):101906, 2012.
- [109] S.-Y. Chen, C. Zheng, M. S. Fuhrer, and J. Yan. Helicity-resolved Raman scattering of MoS<sub>2</sub>, MoSe<sub>2</sub>, WS<sub>2</sub>, and WSe<sub>2</sub> atomic layers. *Nano Letters*, 15(4):2526–2532, 2015.
- [110] G. Froehlicher, E. Lorchat, F. Fernique, C. Joshi, A. Molina-Sánchez, L. Wirtz, and S. Berciaud. Unified description of the optical phonon modes in N-layer MoTe<sub>2</sub>. *Nano Letters*, 15(10):6481–6489, 2015.
- [111] C. H. Lui, Z. Ye, C. Ji, K.-C. Chiu, C.-T. Chou, T. I. Andersen, C. Means-Shively, H. Anderson, J.-M. Wu, T. Kidd, et al. Observation of interlayer phonon modes in van der Waals heterostructures. *Physical Review B*, 91(16):165403, 2015.
- [112] J. Van Baren, G. Ye, J.-A. Yan, Z. Ye, P. Rezaie, P. Yu, Z. Liu, R. He, and C. H. Lui. Stacking-dependent interlayer phonons in 3R and 2H MoS<sub>2</sub>. *2D Materials*, 6(2):025022, 2019.

- [113] F. P. N. Antunes, V. S. Vaiss, S. R. Tavares, R. B. Capaz, and A. A. Leitao. Van der waals interactions and the properties of graphite and 2H-, 3R-and 1T-MoS<sub>2</sub>: A comparative study. *Computational Materials Science*, 152:146–150, 2018.
- [114] X. Luo, X. Lu, C. Cong, T. Yu, Q. Xiong, and S. Y. Quek. Stacking sequence determines Raman intensities of observed interlayer shear modes in 2D layered materials—a general bond polarizability model. *Scientific Reports*, 5(1):1–13, 2015.
- [115] L. Liang, A. A. Puretzy, B. G. Sumpter, and V. Meunier. Interlayer bond polarizability model for stacking-dependent low-frequency Raman scattering in layered materials. *Nanoscale*, 9(40):15340–15355, 2017.
- [116] X. Zhang, W.-P. Han, X.-F. Qiao, Q.-H. Tan, Y.-F. Wang, J. Zhang, and P.-H. Tan. Raman characterization of AB-and ABC-stacked few-layer graphene by interlayer shear modes. *Carbon*, 99:118–122, 2016.
- [117] J. Wilson, F. Di Salvo, and S. Mahajan. Charge-density waves and superlattices in the metallic layered transition metal dichalcogenides. *Advances in Physics*, 50(8):1171–1248, 2001.
- [118] F. Soto, H. Berger, L. Cabo, C. Carballeira, J. Mosqueira, D. Pavuna, P. Toimil, and F. Vidal. Electric and magnetic characterization of NbSe<sub>2</sub> single crystals: Anisotropic superconducting fluctuations above T<sub>c</sub>. *Physica C: Superconductivity*, 460:789–790, 2007.
- [119] M. M. Ugeda, A. J. Bradley, Y. Zhang, S. Onishi, Y. Chen, W. Ruan, C. Ojeda-Aristizabal, H. Ryu, M. T. Edmonds, H.-Z. Tsai, et al. Characterization of collective ground states in single-layer NbSe<sub>2</sub>. *Nature Physics*, 12(1):92–97, 2016.
- [120] X. Xi, L. Zhao, Z. Wang, H. Berger, L. Forró, J. Shan, and K. F. Mak. Strongly enhanced charge-density-wave order in monolayer NbSe<sub>2</sub>. *Nature Nanotechnology*, 10(9):765–769, 2015.
- [121] X. Xi, Z. Wang, W. Zhao, J.-H. Park, K. T. Law, H. Berger, L. Forró, J. Shan, and K. F. Mak. Ising pairing in superconducting NbSe<sub>2</sub> atomic layers. *Nature Physics*, 12(2):139–143, 2016.
- [122] J. A. Wilson and A. Yoffe. The transition metal dichalcogenides discussion and interpretation of the observed optical, electrical and structural properties. *Advances in Physics*, 18(73):193–335, 1969.
- [123] J. P. Perdew and Y. Wang. Accurate and simple analytic representation of the electron-gas correlation energy. *Physical Review B*, 45(23):13244, 1992.
- [124] R. He, J. van Baren, J.-A. Yan, X. Xi, Z. Ye, G. Ye, I.-H. Lu, S. Leong, and C. Lui. Interlayer breathing and shear modes in NbSe<sub>2</sub> atomic layers. *2D Materials*, 3(3):031008, 2016.